UNIVERSIDADE FEDERAL DE SANTA CATARINA

PROGRAMA DE PÓS-GRADUAÇÃO EM ENGENHARIA MECÂNICA

ESTUDO TEÓRICO E EXPERIMENTAL DA APLICAÇÃO DE MEIOS POROSOS CERÂMICOS EM LHP E CPL

Tese

PAULO HENRIQUE DIAS DOS SANTOS

Florianópolis, SC

2010

UNIVERSIDADE FEDERAL DE SANTA CATARINA

PROGRAMA DE PÓS-GRADUAÇÃO EM ENGENHARIA MECÂNICA

ESTUDO TEÓRICO E EXPERIMENTAL DA APLICAÇÃO DE MEIOS POROSOS CERÂMICOS EM LHP E CPL

Tese submetida à Universidade Federal de Santa Catarina para obtenção do grau de Doutor em Engenharia Mecânica

PAULO HENRIQUE DIAS DOS SANTOS

Florianópolis, Dezembro de 2010

Catalogação na fonte pela Biblioteca Universitária
da
Universidade Federal de Santa Catarina

S237e Santos, Paulo Henrique Dias dos
Estudo teórico e experimental da aplicação de meios porosos cerâmicos em LHP e CPL [tese] / Paulo Henrique Dias dos Santos ; orientador, Edson Bazzo, co-orientador, Amir Antonio Martins de Oliveira Junior. - Florianópolis, SC, 2010.
175 p.: il., grafs., tabs.

Tese (doutorado) - Universidade Federal de Santa Catarina, Centro Tecnológico. Programa de Pós-Graduaçao em Engenharia Mecânica.

Inclui referências

1. Engenharia mecânica. 2. Água. 3. Tubos de calor. 4. Evaporadores. I. Bazzo, Edson. II. Oliveira Junior, Amir Antonio Martins de. III. Universidade Federal de Santa Catarina. Programa de Pós-Graduação em Engenharia Mecânica. IV. Título.

CDU 621

UNIVERSIDADE FEDERAL DE SANTA CATARINA

PROGRAMA DE PÓS-GRADUAÇÃO EM ENGENHARIA MECÂNICA

ESTUDO TEÓRICO E EXPERIMENTAL DA APLICAÇÃO DE MEIOS POROSOS CERÂMICOS EM LHP E CPL

PAULO HENRIQUE DIAS DOS SANTOS

Esta tese foi julgada adequada para a obtenção do título de

DOUTOR EM ENGENHARIA MECÂNICA

ESPECIALIDADE ENGENHARIA MECÂNICA
Área de concentração em Engenharia e Ciências Térmicas

sendo aprovada em sua forma final.

Prof. Edson Bazzo, Dr. – Orientador

Prof. Amir Antônio Martins de Oliveira Jr., Ph.D. – Co-orientador

---

Prof. Eduardo Alberto Fancello, D.Sc. – Coordenador do curso

BANCA EXAMINADORA

Prof. Edson Bazzo, Dr. – Presidente

Prof. Paulo Couto, Dr. – Relator

Prof. Carlos Antonio Cabral dos Santos, D.Sc.

Prof. Sérgio Colle, D.Sc.

Prof. Jader Riso Barbosa Jr., Ph.D.

Resumo

Título: Estudo Téorico e Experimental da Aplicação de Meios Porosos Cerâmicos em LHP e CPL

Palavras Chave: Elemento Poroso Cerâmico, LHP, CPL, Água

Motivação

A indústria eletrônica tem crescido a um ritmo acelerado visando a miniaturização e o melhor desempenho dos seus componentes. Em virtude desse crescimento, o controle térmico de equipamentos eletrônicos tem se tornado um assunto de importância para a indústria de eletrônicos. Existe atualmente uma necessidade para desenvolver dispositivos de transferência de calor que sejam capazes de transferir grandes quantidades de calor à uma queda de temperatura mínima. Neste contexto, os Heat Pipes (HP), os Loop Heat Pipes (LHP) e os Capillary Pumping Loops (CPL) são alternativas confiáveis e viáveis para a dissipação de calor gerado. Eles são trocadores de calor, que utilizam a evaporação e condensação de um fluido de trabalho para transferir calor de forma mais eficiente. A circulação de fluido é realizada pelas forças capilares geradas em uma estrutura porosa. Portanto, o bombeamento do fluido de trabalho não consome energia elétrica. Nesta tese, apenas os LHPs e o CPLs serão estudados.

Nas últimas décadas, a aceitação destes sistemas na comunidade aeroespacial vem crescendo devido a suas vantagens de desempenho, características únicas de funcionamento e ao sucesso obtido nos recentes experimentos testados no espaço. Por consequência, as pesquisas têm se intensificado a fim de compreender melhor os fenômenos que ocorrem nestes sistemas térmicos. Ku & Kroliczek (1987), Maydanik *et al.* (1991), Ku (1994), Maydanik (1999), Ku (1999), Nikitkin & Cullimore (1998), Chernysheva *et al.* (2007), Santos & Bazzo (2007), entre outros, publicaram avanços passados e recentes na pesquisa desses sistemas de controle térmico.

Objetivo

Os principais objetivos desta tese são dois. O primeiro é o desenvolvimento de um modelo matemático para o problema da transferência de calor e de massa, que ocorre dentro do meio poroso de evaporadores de sistemas de bombeamento capilar. O segundo é a aplicação de meios porosos cerâmicos em sistemas de bombeamento capilar (LHPs e CPLs) seguido pela avaliação de seus comportamentos térmicos durante a partida e em condições de regime permanente. Água e acetona são utilizados como fluidos de trabalho.

Introdução

Classificação e Operação Básica dos CPLs e LHPs

Os CPLs e LHPs operam dentro de um intervalo de temperatura, basicamente, definido pelas propriedades do fluido de trabalho. A escolha do fluido de trabalho envolve vários fatores associados à operação, disponibilidade e segurança. A amônia é freqüentemente usada em sistemas de bombeamento capilar, mas outros fluidos de trabalho, tais como água, etanol, acetona, propileno, metanol, butano, isobutano e propano também apresentam um bom funcionamento (PETERSON, 1994). A faixa de temperatura de operação determina a condição preliminar para a seleção do fluido de trabalho para uma determinada aplicação. A faixa máxima está compreendida entre os pontos triplo e crítico, porque abaixo do ponto triplo e acima do ponto crítico não há circulação do fluido de trabalho por ação capilar.

A capacidade de bombeamento capilar depende da tensão superficial do fluido de trabalho e das propriedades do meio poroso. Até agora, os fluidos de trabalho foram classificadas de acordo com o limite capilar, ou seja, de acordo com a pressão máxima de bombeamento que o meio poroso pode prover. Existe outro limite chamado de limite de ebulição, mas por falta de uma melhor estratégia, os fluidos que apresentam este problema têm sido evitados. O limite de ebulição está relacionado com o processo de evaporação do fluido de trabalho no canal de alimentação de líquido e/ou no meio poroso devido à alta temperatura do líquido que escoa através do evaporador. Ku (1994) estudou o funcionamento de um CPL, baseando a sua análise no diagrama de pressão e temperatura (PT), e em suas conclusões justifica a necessidade de um alto grau de sub-resfriamento na entrada do evaporador capilar exigido por alguns fluidos de trabalho, tais como água e tolueno. Ou seja, quanto maior a exigência de sub-resfriamento de um determinado fluido de trabalho, menor o limite de ebulição. Uma análise similar realizada para o LHP, utilizando o diagrama PT, foi também publicada por Maydanik *et al.* (1991), Ku (1999) and Maydanik (2005). A ocorrência destes dois limites operacionais serão analisados neste trabalho.

Os modos de operação dos sistemas de bombeamento capilar pode ser classificado como condutância fixa ou variável. No modo de condutância variável, a temperatura de saturação do sistema pode ser controlada para diferentes cargas térmicas. Por outro lado, no modo de condutância fixa, quanto maior a carga térmica, maior será a temperatura de saturação do sistema. Nikitkin & Cullimore (1998) apresentou gráficos qualitativos da temperatura do vapor para um CPL e um LHP, ambos operando nos modos de condutância fixa e variável. De forma semelhante, Chernysheva *et al.* (2007) apresentou gráficos quantitativos para um LHP. A próxima seção resume os principais resultados das recentes pesquisas desenvolvida envolvendo a aplicação dos sistemas de bombeamento capilar (CPLs e LHPs) no controle térmico de equipamentos eletrônicos em geral.

Revisão dos Experimentos Realizados com CPL e LHP

O controle térmico tem crescido em importância na indústria eletrônica (computadores modernos) devido à contínua diminuição de tamanho e ao aumento na potência dos seus componentes. De acordo com Nikitkin & Cullimore (1998) and Maydanik (2005), os LHPs e os CPLs, que foram desenvolvidos anteriormente para o controle térmico aeroespacial (satélites), são alternativas confiáveis e viáveis para transferir calor em grandes

quantidades com alto desempenho também para aplicações em condições atmosféricas. Vários autores (CHEN; LIN, 2001; HOANG *et al.*, 2003; PASTUKHOV *et al.*, 2003; MAYDANIK, 2005; CHEN *et al.*, 2006; PASTUKHOV; MAYDANIK, 2007) publicaram resultados experimentais relativos à aplicação dos LHPs, mini-LHPs e CPLs na dissipação de calor em CPUs de computadores modernos, mostrando que eles são trocadores de calor eficientes e confiáveis para a próxima geração de microprocessadores.

É comum expressar a qualidade dos LHPs e CPLs através da resistência térmica R (^{o}C/W) dada por,

$$R = \frac{\Delta T}{Q},$$

onde Q é a taxa de transferência de calor dissipada pelo sistema de bombeamento capilar e ΔT é a diferença de temperatura entre as fonte quente e fria.

O desempenho térmico e a confiabilidade dos LHPs e CPLs têm sido extensivamente estudados experimentalmente. Ku (1999), Chen & Lin (2001), Pastukhov *et al.* (2003), Chuang (2003), Ku *et al.* (2004), Pastukhov & Maydanik (2007), Maydanik & Vershinin (2009) analisaram a partida e o comportamento térmico dos sistemas de bombeamento capilar (CPL e LHP) com relação à razão de preenchimento do fluido de trabalho, à inclinação dos sistemas, ao material do meio poroso (níquel, aço inoxidável, cobre, polietileno), ao material do invólucro do evaporador (cobre e aço inoxidável), ao sistema de refrigeração do condensador (água e ar em convecção forçada e ar em convecção natural), com multi-evaporadores e multi-condensadores. Os testes foram realizados em condições atmosféricas e de microgravidade para uma série de cargas térmicas. Os resultados mais recentes são descritos a seguir.

Hoang *et al.* (2003) desenvolveram e testaram três mini-LHPs que utilizavam propileno, amônia e água como fluidos de trabalho. Todos os LHPs foram assistidos por um sistema de resfriamento secundário na câmara de compensação a fim de diminuir a transferência de calor da zona de evaporação para o canal de entrada de líquido. Dois sistemas de resfriamento na câmera de compensação foram testados: um sistema termo-elétrico (TEC) e um tubo de calor feito de cobre com 3 mm de diâmetro, que utilizava água como fluido de trabalho. Dois dos LHPs foram capazes de transportar calor até 60 W (amônia) e 15 W (propileno) à temperatura ambiente de 25 ^{o}C. O LHP que utilizou água (principal objetivo do trabalho) foi testado com e sem o tubo de calor na câmara de compensação. O LHP que utilizou água foi feito de cobre e o meio poroso foi feito de teflon com diâmetro de poro de 7 μm e permeabilidade de 1×10^{-13} m^2. Este LHP foi capaz de transportar calor até 220 W à uma temperatura de operação de 82 ^{o}C com o tubo de calor na câmara de compensação e 90 ^{o}C sem o tubo de calor. A resistência térmica total variou de $2,0$ a $0,2$ ^{o}C/W. A utilização do tubo de calor na câmara de compensação teve uma grande influência na capacidade de transferência de calor dos LHPs.

Seis mini-LHPs foram desenvolvidos e testados por Pastukhov *et al.* (2003) para o resfriamento de componentes eletrônicos e processadores de computadores portáteis. Amônia e acetona foram utilizadas como fluido de trabalho. Meios porosos feitos de aço inoxidável e titânio foram utilizados como estruturas porosas. O ar foi usado em convecção forçada para o resfriamento do condensador e do diâmetro dos evaporadores cilíndricos variou de 5 a 6 mm. Os LHPs foram capazes de transportar calor até 40 W com resistência térmica total variando de $1,0$ a $2,4$ ^{o}C/W. A temperatura do processador se manteve entre 83 e 90 ^{o}C. Eles concluíram que uma maior diminuição da resistência térmica total deve

ser obtida pela otimização do projeto do LHP e do resfriamento do condensador. Eles mostraram ainda que a amônia apresentou melhores resultados quando comparado com os resultados obtidos usando acetona.

Chen *et al.* (2006) realizaram uma série de testes com um mini-LHP, o qual foi desenvolvido para refrigeração de CPUs de computadores portáteis. Amônia foi utilizada como fluido de trabalho e o material do meio poroso foi feito de titânio com raio de poro de $17,2$ μm, porosidade de 78% e permeabilidade de $11,5 \times 10^{-12}$ m^2. Eles testaram o mini-LHP em diversas posições (na horizontal, condensador acima do evaporador, evaporador acima do condensador, câmara de compensação acima do evaporador e evaporador acima da câmara de compensação), com destaque para a posição com o evaporador acima do condensador em 10^o e vice-versa. O comportamento térmico do mini-LHP foi avaliado durante a partida do sistema e para diferentes temperaturas do banho termostático utilizado no condensador. À temperatura do banho de 25 ^{o}C e na posição horizontal, o mini-LHP foi capaz de transportar calor até 70 W a uma temperatura de operação limite de 80 ^{o}C e a resistência térmica total variou de $0,2$ a $0,85$ ^{o}C/W. Eles concluíram que o mini-LHP testado na posição horizontal operou de maneira satisfatória.

Maydanik & Vershinin (2009) desenvolveram e testaram nove mini-LHPs com evaporadores capilares cilíndricos. Três mini-LHPs tinham diâmetros externos de 5 mm e seis mini-LHPs tinham diâmetros externos de 6 mm. Eles utilizaram amônia como fluido de trabalho para todos os mini-LHPs e materiais diferentes para o meio poroso (titânio, com raios médios de poro de $9,5$ e $17,2$ μm e porosidades de 70 e 78%, e níquel com raios médios de poro variando entre $13,5$ e $10,0$ μm e porosidades de 71, 66 e 65%). Os invólucros dos evaporadores cilíndricos foram feito de titânio e níquel. Vários testes foram realizados com o objetivo de avaliar o comportamento térmico dos mini-LHPs levando em consideração a inclinação dos dispositivos, a temperatura de resfriamento na seção do condensador e o tipo de fluido utilizado para o resfriamento do condensador (ar e água em convecção forçada). Eles apresentaram uma metodologia para estimar as resistências térmica e os coeficientes de transferência de calor dos mini-LHPs. As resistências térmicas mínimas foram $0,53$ ^{o}C/W e $0,14$ ^{o}C/W para o resfriamento do condensador com ar e com água, respectivamente. A capacidade máxima foi de 230 W para o resfriamento do condensador com água.

Como demonstrado, a maioria dos meios porosos foram feitos de metais ou polímeros. No entanto, esses materiais apresentam algumas dificuldades de usinagem (meios porosos metálicos) e uma baixa capacidade de bombeamento capilar (meios porosos de polímero). A usinagem dos meios porosos metálicos pode obstruir os poros na superfície, diminuindo, desta forma, a permeabilidade do meio poroso. A próxima seção apresentará alguns trabalhos nos quais foram realizadas a produção, a caracterização e a aplicação de meios porosos em sistemas de bombeamento capilar.

Aplicação de Meios Porosos Cerâmicos em Sistemas de Bombeamento Capilar

Embora a capacidade de transferência de calor dos LHPs e CPLs seja alta, a produção complicada desses dispositivos é ainda uma desvantagem. A montagem adequada da estrutura capilar no interior do invólucro do evaporador é o primeiro desafio a ser superado. A montagem é relativamente complexa, porque para o bom funcionamento do evaporador capilar se requer um micro-espaçamento entre as paredes internas do invólucro metálico e a superfície externa do meio poroso. Este espaçamento deve ser adequado a fim de

minimizar a resistência térmica e qualquer vazamento de vapor do evaporador para a câmara de compensação (LHP) ou para o canal de alimentação de líquido (CPL). A fim de se obter esses micro-espaçamentos, um processo de usinagem confiável é necessário para as estruturas porosas metálicas, porque há a possibilidade de obstrução dos poros na sua superfície devido à deformação plástica. Os meios porosos cerâmicos não apresentam essa deformação plástica durante a usinagem. Portanto, eles podem ser usinados utilizando máquinas convencionais (JANSSEN *et al.*, 2008).

De acordo com o conhecimento do autor desse trabalho, existem poucos sistemas de bombeamento capilar usando meios porosos cerâmicos (RASSAMAKIN *et al.*, 2002; RHI, 2006). A maioria dos LHPs e CPLs usam meios porosos de polietileno ou de metal. Espera-se que os meios porosos cerâmicos se tornem mais vantajosos porque eles são menos onerosos e de fácil usinagem, pois não corre o risco de obstruir os poros da superfície externa da estrutura por deformação plástica. Além disso, a baixa condutividade térmica pode minimizar a transferência de calor radial para o canal de alimentação de líquido, evitando que o limite de ebulição seja atingido.

Reimbrecht (2004) desenvolveu uma metodologia para a fabricação de meios porosos para aplicação em sistemas de bombeamento capilar. Várias técnicas - análise de imagem, porosimetria através da intrusão de mercúrio e outros métodos experimentais - foram empregadas para determinar as propriedades estáticas e de transporte dos meios porosos estudados. Ele produziu meios porosos metálicos (níquel e aço inoxidável) e cerâmicos.

Camargo (2004) testou e analisou todos os meios porosos fabricado por Reimbrecht (2004) em CPLs. Duas bancadas experimentais foram construídas para avaliar os CPLs produzidos. Ele testou os CPLs com acetona e amônia como fluido de trabalho. Os resultados apresentados por Camargo (2004), mostraram que o CPL com o meio poroso cerâmico obteve sucesso na partida apenas para a carga térmica de 10 W, entretanto ele não operou de forma estável. Além disso, o CPL com o meio poroso cerâmico apresentou os piores resultados de desempenho quando comparados com os outros meios porosos testados (níquel, aço inoxidável e polietileno).

Berti (2008) fabricou e testou dois CPLs que utilizaram acetona como fluido de trabalho. Um CPL testado utilizava um meio poroso cerâmico fabricado por colagem por barbotina, que operou com uma carga térmica de 40 W (3.93 W/cm^2). O outro CPL testado que utilizava também um meio poroso cerâmico, mas que foi fabricado por biomodelagem, operou com uma carga térmica de 20 W (11.32 W/cm^2). Os CPLs funcionaram de forma satisfatória, porém Berti (2008) relatou que ele teve muitos problemas em relação à montagem do evaporador capilar e à transferência de calor através da parede do evaporador para o canal de alimentação de líquido, devido à geometria usada para os evaporadores capilares planos.

A seção seguinte apresentará uma breve revisão bibliográfica dos modelos matemáticos propostos para resolver o problema da transferência de calor e de massa em evaporadores capilares.

Descrição e Revisão do Problema

O principal componente de sistemas de bombeamento capilar (CPL e LHP) é o evaporador capilar. Durante a operação dos evaporadores capilares, calor é aplicado a superfície externa do evaporador e do fluido de trabalho dentro do meio poroso muda de fase. O vapor gerado no evaporador escoa através das ranhuras. A evaporação do fluido de tra-

balho dentro dos evaporadores capilares depende da carga térmica aplicada ao sistema e pode ocorrer em três regimes distintos: (1) evaporação em microfilme (2), evaporação na superfície externa do meio poroso e (3) evaporação dentro do meio poroso.

A incerteza com relação à localização da frente de evaporação e à determinação dos limites capilares para a operação do meio poroso têm motivado tentativas para se resolver o problema da transferência de calor e de massa em meios porosos de sistemas de bombeamento capilar. Alguns dos modelos teóricos são analisados a seguir.

Cao & Faghri (1994a) estudaram a evaporação em meios porosos supondo condições de contornos restritivas, que, no entanto, resultou em soluções analíticas para os campos de velocidade e temperatura. Eles assumiram que o meio poroso estava completamente saturado de líquido e a frente para a evaporação estava localizada na superfície externa. Seu modelo também assume que o campo de velocidade é uniforme na entrada de líquido e na saída de vapor. Eles fizeram uma análise paramétrica direcionada, principalmente, para mostrar que a sua solução analítica é precisa para a maioria das aplicações. Eles concluíram que os resultados obtidos são de relevância para o projeto de evaporadores capilares.

Cao & Faghri (1994b) publicaram uma extensão de seu trabalho anterior fazendo uma análise da geometria tridimensional. Um estudo numérico foi desenvolvido para estudar o fluxo do líquido através do meio poroso (bidimensional) e o fluxo de vapor através das ranhuras (tridimensional). Uma comparação entre os resultados é apresentada para três fluidos de trabalho (água, freon e amônia). Em ambos os trabalhos publicados por Cao e Faghri, eles afirmam que os resultados obtidos são de relevância para o projeto de evaporadores capilares, porém eles não apresentam um critério para a secagem do meio poroso, ou seja, eles não determinam qual seria o fluxo de calor crítico antes da falha do evaporador capilar.

Demidov & Yatsenko (1994) realizou uma análise teórica sobre o problema da transferência de calor e de massa em meios porosos de um sistema de bombeamento capilar. Em seu modelo, o líquido dentro do meio poroso muda de fase, desenvolvendo uma região de vapor saturado separada da região de líquido saturado por uma frente de evaporação. São aplicadas as equações de conservação da massa e da energia na frente de evaporação. A pressão capilar também é modelada nesta frente. Uma solução numérica do modelo matemático permitiu estudar o deslocamento da frente de evaporação em função da variação da carga térmica aplicada ao sistema.

Eles assumiram que duas condições limites são fisicamente possível. Para fluxos de calor baixos, existe uma pequena região de vapor saturado abaixo da aleta e ocorre a formação de meniscos de liquido na interface meio poroso-aleta. Toda a evaporação do fluido ocorre na interface entre o meio poroso e a ranhura. Com o aumento do fluxo de calor, o líquido evapora no menisco e a evaporação passa a ocorrer tanto na região de vapor saturado quanto na interface da ranhura.

A evaporação no menisco é modelada assumindo um coeficiente global de transferência de calor que inclui uma resistência térmica condutiva através do filme líquido. A transferência de calor por condução na aleta também é resolvida. Seus resultados mostraram que a evaporação é muito mais intensa na interface meio poroso-ranhura do que na frente de evaporação. Isso ocorre porque o fluxo de vapor fora da região abaixo da aleta é dificultada pelo baixo valor da viscosidade cinemática do vapor, em comparação com a viscosidade cinemática do líquido. Os autores apresentam bons resultados, entretanto eles também não determinam o valor crítico de fluxo de calor para a transição entre as duas

condições limites estudadas. Somente uma análise qualitativa é apresentada.

Figus *et al.* (1999) analisaram um problema semelhante e eles tentaram quantificar a mudança entre os regimes de evaporação em função da variação do fluxo de calor. Eles consideraram que a frente de evaporação estava localizada dentro do meio poroso. Foram aplicados dois tratamentos diferentes: modelo do contínuo, semelhante ao usado por Demidov & Yatsenko (1994), e modelo de rede de percolação de poros, semelhantes aos modelos desenvolvidos anteriormente por Prat (1993, 1995) e Laurindo & Prat (1996).

Figus *et al.* (1999) apresentaram soluções para um meio poroso com condutividade térmica efetiva baixa ($\lambda_s = 4$ W/m-K) e para um outro meio poroso com condutividade térmica efetiva alta ($\lambda_s = 10$ W/m-K). Para o meio poroso com condutividade térmica baixa, os resultados mostraram que quando o tamanho dos raios dos poros é constante e igual a 10μm, a frente de evaporação invade o meio poroso apenas para um fluxo de calor $q'' > 4.500$ W/m^2. As soluções do problema podem ser bem determinadas através do modelo do contínuo até o fluxo de calor máximo de 90.000 W/m^2.

Na solução obtida com o modelo de rede de percolação de poros para o meio de maior condutividade térmica e com razão entre o tamanho de poro máximo e mínimo de $R = d_{max}/d_{min} = 2$, a frente de evaporação invadiu o meio poroso para um fluxo de calor de $q'' = 1.000$ W/m^2. Acima deste valor, a frente se desenvolveu com uma superfície irregular. Entre os fluxos 15.000 e 35.000 W/m^2, a frente de evaporação se manteve estável dentro do meio poroso. Acima do fluxo de calor de 35.000 W/m^2, a área da frente de evaporação aumentou progressivamente até a falha do sistema no fluxo de $q'' = 200.000$ W/m^2.

Embora Figus *et al.* (1999) não tenham correlacionado o limite para a falha do meio poroso, eles mostraram claramente a tendência do processo de invasão da frente de evaporação no meio poroso.

Takahashi (2002) analisou a transferência de calor e de massa no meio poroso de um evaporador capilar a fim de determinar o fluxo de calor máximo antes de sua falha por limite capilar. Takahashi assumiu, como Figus *et al.* (1999), que a frente da evaporação estava imersa no meio poroso. Ele resolveu numericamente o problema usando o método de volumes finitos em coordenadas curvilíneas ortogonais. Ele usou um método de rastreamento da frente evaporação combinado com uma malha móvel. Ele analisou a amônia como fluido de trabalho e obteve as propriedades para o meio poroso de níquel fabricado por Reimbrecht *et al.* (1999). Ele apresentou os resultados referentes à localização da frente de evaporação para diferentes fluxos de calor. Os valores dos fluxos de calor críticos foram calculados para diferentes propriedades (fluxo de calor máximo de $13,06 \times 10^4$ W/m^2 para um funcionamento em regime permanente), mas nenhuma tentativa foi feita para a parametrização dos resultados obtidos.

Kaya & Goldak (2006) estudaram numericamente a transferência de calor e de massa na estrutura porosa de um LHP, visando a ocorrência do limite de ebulição. O problema foi basicamente o mesmo estudado por Demidov & Yatsenko (1994) e Figus *et al.* (1999) com uma formulação semelhante. Uma diferença na formulação foi que o modelo leva em conta os termos convectivos da equação da conservação da energia. No entanto, como mostrado por Cao & Faghri (1994a), a contribuição desses termos pode ser negligenciada.

A modelagem apresentada por Kaya & Goldak (2006) permite a estabilização da frente de evaporação, tanto na superfície externa quanto no interior do meio poroso. Depois que a frente invade o meio poroso, formando uma região de vapor saturado abaixo da aleta, os autores consideram que o salto de pressão através da interface deve ser menor do que

a pressão capilar e não exatamente igual, tal como exigido pelo equilíbrio termodinâmico numa interface curva líquido-vapor. Essa violação não se justifica.

Além disso, os autores precisam ainda especificar um superaquecimento da superfície na interface meio poroso-aleta necessário para criar uma região de vapor saturado. Eles assumiram que, se temperatura da superfície da aleta for maior do que temperatura de saturação do fluido à pressão de entrada de líquido em 4 ^{o}C, a frente evaporação entra no meio poroso. Percebe-se que este critério é arbitrário, uma vez que não inclui o tamanho dos poros local, o que modificaria o equilíbrio termodinâmico local, e essa condição pode mudar dependendo do fluido, do grau de pureza dele, da rugosidade da superfície e da técnica de montagem. Portanto, os resultados apresentados por Kaya & Goldak (2006) não são confiáveis com relação ao limite para a formação da região de vapor saturado abaixo da aleta.

Até o momento, percebe-se que há uma falta de informação sobre a localização da frente de evaporação, ou seja, qual seria o fluxo de calor máximo para o qual o meio poroso pode suportar antes que a frente de evaporação passe da superfície externa para o interior do meio poroso. Como mencionado anteriormente, a frente da evaporação pode estabelecer uma posição estável dentro do meio poroso, mas essa condição deve ser evitada. Assim, o modelo aqui desenvolvido permite determinar quando a frente de evaporação invade o meio poroso. Ao contrário do critério assumido por Kaya & Goldak (2006), neste modelo um critério confiável é assumido com relação ao fluxo de calor crítico com base na pressão máxima capilar que o meio poroso pode suportar. No presente modelo, as condições de contorno assumidas por Cao & Faghri (1994a, 1994b) são melhoradas para melhor representar a física do problema.

Em relação aos testes experimentais, a maioria dos LHPs e CPLs utilizam meios porosos feitos de metal e amônia como fluido de trabalho. As poucas aplicações de meios porosos cerâmicos em LHPs e CPLs não obtiveram sucesso. Portanto, nesta trabalho é realizado um estudo experimental do comportamento térmico de dois LHPs e de um CPL que utlizam meios porosos cerâmicos e água como fluido de trabalho.

Resultados e Análise

Foram fabricados e testados dois LHPs, um utilizando acetona e o outro água como fluidos de trabalho. Os testes foram realizados para potências de até 25 W. Além disso, foi fabricado e testado um CPL usando água. Os testes do CPL foram realizados para potências de até 30 W. O meio poroso cerâmico utilizado possui 50% de porosidade, distribuição de raio de poro entre 1 e 3 μm e uma permeabilidade de 1.5×10^{-14} m^2. Considerando uma temperatura de operação limite de 100 ^{o}C e regime permanente, os LHPs foram capazes de transferir até 15 W para água e 25 W para acetona, enquanto que o CPL foi capaz de transferir até 30 W. Apesar do bom desempenho dos sistemas de bombeamento capilar avaliados, observou-se que mais pesquisas ainda são necessárias, buscando otimizar as propriedades termofísicas do meio poroso cerâmico e melhorar o projeto dos LHPs e do CPL.

A qualidade dos sistemas de bombeamento tem sido comumente expressa pela resistência térmica total ($R_{total} = \dfrac{\Delta T}{Q}$), no entanto, percebe-se que R_{total} é dependente do tamanho do sistema, ou seja, não leva em conta a área do evaporador onde a taxa de transferência de calor é aplicada. Assim, uma figura de mérito diferente é aqui proposta,

$$R''_{total} = \frac{\Delta T}{q''},$$

onde: q'' é o fluxo de calor dissipado pelo sistema de bombeamento capilar e $\Delta T = T_{Evap} - T_{HS}$ é a diferença de temperatura entre a superfície quente, onde a carga térmica é aplicada, e o banho térmico no condensador.

A Fig. 1 apresenta os resultados obtidos com R_{total} e R''_{total}. Percebe-se através da Fig. 1(b) que a R''_{total} do CPL (água) é maior do que a R''_{total} dos LHPs. De acordo com os resultados obtidos com R''_{total}, o LHP (acetona) funcionou melhor do que o CPL e o LHP, ambos usando água.

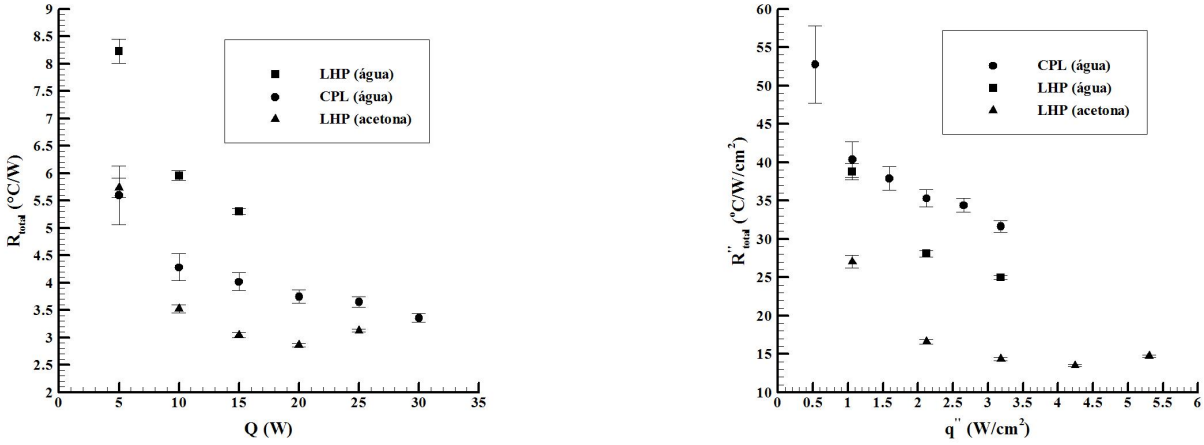

(a) (b)

Figure 1 – Resistência térmica total versus taxa de transferência de calor e (b) a resistência térmica total por centímetro quadrado versus fluxo de calor para os LHPs e o CPL testados.

As Figs. 2 e 3 apresentam uma comparação entre os resultados obtidos experimentalmente nesta tese e os encontrados na literatura para os CPL e LHPs, respectivamente.

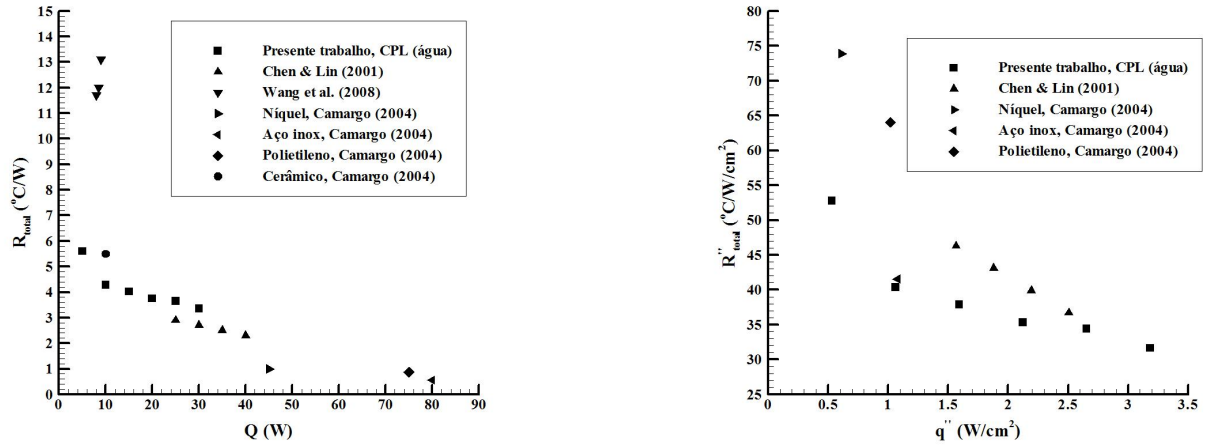

(a) (b)

Figure 2 – (a) Resistência térmica total versus taxa de transferência de calor e (b) a resistência térmica total por centímetro quadrado versus fluxo de calor para o CPL.

Comparando o CPL testado neste trabalho com os encontrados na literatura, percebe-se através da Fig. 2(a) que, de acordo com os resultados calculados através da R_{total}, o CPL testado no presente trabalho apenas operou melhor do que os CPLs apresentados por Wang *et al.* (2008) e por Camargo (2004) (elementos porosos cerâmicos). Entretanto, de acordo com os resultados calculados através da R''_{total} e mostrados na Fig. 2(b), o CPL testado no presente trabalho operou melhor do que os CPLs apresentados na literatura.

Percebe-se através dos resultados mostrados na Fig. 3 que apesar dos LHPs não terem operado tão bem quanto os mini-LHPs, eles apresentaram resultados satisfatórios. Uma das razões para este resultado relativamente fraco, é que os mini-LHPs encontrados na literatura utilizaram amônia como fluido de trabalho que, devido às suas propriedades térmicas, é considerado o melhor fluido de trabalho para sistemas de bombeamento capilar.

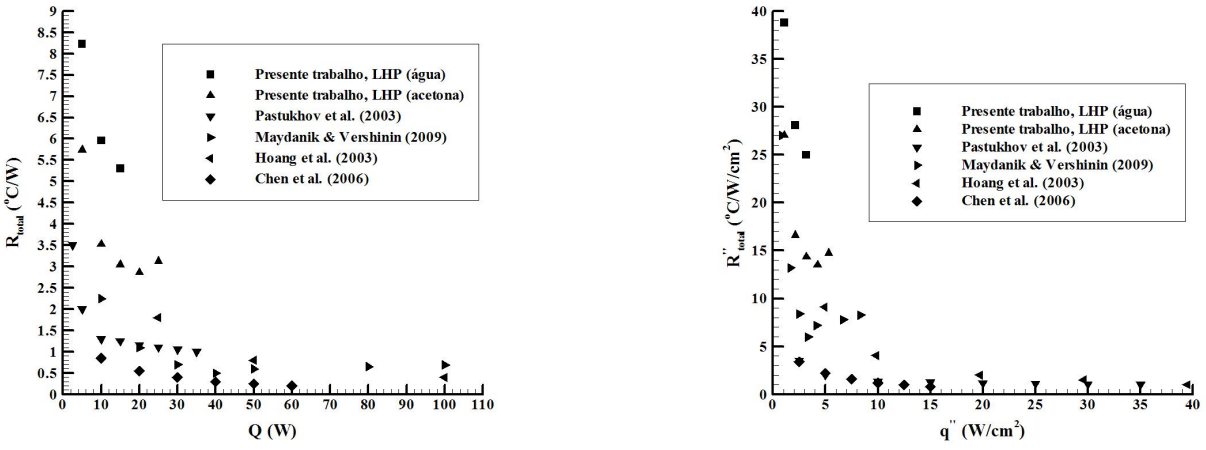

(a) (b)

Figure 3 – (a) Resistência térmica total versus taxa de transferência de calor e (b) a resistência térmica total por centímetro quadrado versus fluxo de calor para os LHPs.

Uma comparação é feita entre os resultados experimentais e teóricos As curvas do raio médio crítico adimensional em função do fluxo de calor de entrada adimensional para um meio poroso com uma ou duas camadas são comparadas com o raio médio adimensional do elemento poroso cerâmico testado neste trabalho para cada fluxo de calor aplicado aos sistemas de bombeamento capilar (Fig. 4).

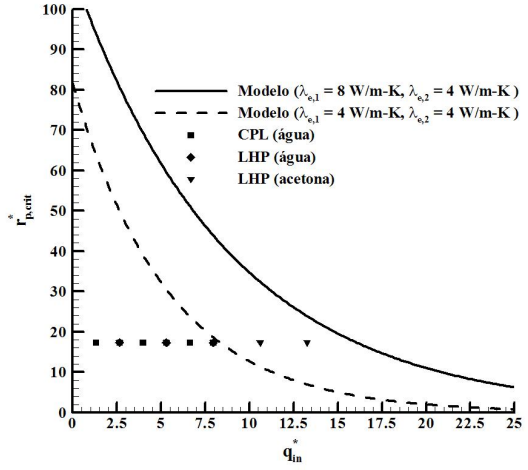

Figure 4 – Comparação entre os resultados experimentais e teóricos.

Percebe-se através da Fig. 4 que apenas o LHP (acetona) atingiu o limite capilar para o meio poroso com uma camada. Apesar do LHP (acetona) ter atingido o limite capilar, ele continuou operando para as taxas de transferência de calor de 20 e 25 W. Desta forma, de acordo com o modelo (apresentado no Capítulo 2), a frente de evaporação invadiu o meio poroso e encontrou uma localização estável dentro dele. No entanto, esta comparação deve ser tomada apenas como uma primeira aproximação, uma vez que o modelo teórico não reproduz completamente a geometria dos sistemas de bombeamento capilar testados. No entanto, as tendências físicas permanecem as mesmas.

Conclusões e Recomendações para Trabalhos Futuros

Quanto à modelagem do problema da transferência de calor e de massa em evaporadores capilares, um critério confiável para o início da secagem do meio poroso foi determinado. Quanto ao desenvolvimento de evaporadores capilares de LHP e CPL, um elemento poroso cerâmico foi proposto como uma alternativa aos elementos porosos feito de metal e polímeros. Estes evaporadores capilares testados operaram de maneira estável e confiável em ambos LHP e CPL.

Os resultados experimentais foram comparados com os resultados teóricos obtidos com o modelo. Apenas o LHP (acetona) atingiu o limite capilar para o meio poroso com uma camada. Apesar do LHP (acetona) ter atingido o limite capilar, ele continuou operando para as taxas de transferência de calor de 20 e 25 W. Desta forma, de acordo com o modelo (apresentado no Capítulo 2), a frente de evaporação invadiu o meio poroso e encontrou uma localização estável dentro dele. No entanto, esta comparação deve ser tomada apenas como uma primeira aproximação, uma vez que o modelo teórico não reproduz completamente a geometria dos sistemas de bombeamento capilar aqui testados. No entanto, as tendências físicas permanecem as mesmas. Se um meio poroso com duas camadas com condutividades térmicas diferentes for usado em vez de um meio poroso com uma camada, foi observado que quanto maior a condutividade térmica abaixo da aleta, maior o limite capilar.

Essas são as principais sugestões para trabalhos futuros:

- Adaptar o modelo para a geometria cilíndrica real dos evaporadores capilares testados.
- Projetar mini-LHPs e mini-CPLs a fim de aplicá-los em computadores portáteis e de mesa.
- Testar o LHP e o CPL em ambiente de micro-gravidade para aplicação aeroespacial.
- Produzir um meio poroso cerâmico com condutividade térmica maior.

FEDERAL UNIVERSITY OF SANTA CATARINA

GRADUATE PROGRAM IN MECHANICAL ENGINEERING

THEORETICAL AND EXPERIMENTAL STUDY OF THE APPLICATION OF A CERAMIC POROUS WICK IN LHP AND CPL

Thesis

PAULO HENRIQUE DIAS DOS SANTOS

Florianópolis, SC

2010

FEDERAL UNIVERSITY OF SANTA CATARINA

GRADUATE PROGRAM IN MECHANICAL ENGINEERING

THEORETICAL AND EXPERIMENTAL STUDY OF THE APPLICATION OF A CERAMIC POROUS WICK IN LHP AND CPL

Thesis submitted in partial fulfillment of the requirements for the degree of Doctor in Mechanical Engineering

PAULO HENRIQUE DIAS DOS SANTOS

Florianópolis, December of 2010

FEDERAL UNIVERSITY OF SANTA CATARINA

GRADUATE PROGRAM IN MECHANICAL ENGINEERING

THEORETICAL AND EXPERIMENTAL STUDY OF THE APPLICATION OF A CERAMIC POROUS WICK IN LHP AND CPL

PAULO HENRIQUE DIAS DOS SANTOS

This doctoral thesis was judged adequate as partial requisite to the degree of

DOCTOR IN MECHANICAL ENGINEERING

and approved on its final version by the Graduate Program in Mechanical Engineering.

Prof. Edson Bazzo, Dr. – Advisor

Prof. Amir Antônio Martins de Oliveira Jr., Ph.D. – Co-advisor

---

Prof. Eduardo Alberto Fancello, D.Sc. – Coordinator of the Graduate Program in Mechanical Engineering - POSMEC/UFSC

REFEREE COMMITTEE

Prof. Edson Bazzo, Dr. – President

Prof. Paulo Couto, Dr. – Relator

Prof. Carlos Antonio Cabral dos Santos, D.Sc.

Prof. Sérgio Colle, D.Sc.

Prof. Jader Riso Barbosa Jr., Ph.D.

"You are the salt of the earth, but if salt has lost its taste, how shall its saltiness be restored? It is no longer good for anything except to be thrown out and trampled under people's feet.

You are the light of the world. A city set on a hill cannot be hidden."

(Matthew 5:13-14)

I dedicate this Thesis to my parents and my parents-in-law
for their constant prayers and faithful support in all of my endeavors.
You are wonderful role models of perseverance.

And especially to my wife, Jamylle, for her constant love, patience,
motivation and prayers during these years.
If I got this degree, if I went to Germany,
if I did not give up, it was because of you.

Acknowledgements

To God for everything, but especially for the gift of faith and perseverance. I also thank the intercession of Holy Mary and Saint Joseph that by it I could have peace and wisdom in difficult moments along these years of my doctorate.

To my parents and parents-in-law for their love and unconditional support. I especially thank my wife for the constant love, patience and motivation along of these years. I am also grateful to all of my family members for their prayers, especially my grandparents, brothers, sisters-in-law, brother-in-law, uncles, aunts and cousins.

To CNPq, DAAD and POSMEC for the financial support.

To Prof. Edson Bazzo and Prof. Amir A. M. Oliveira for my acceptance at LabCET as well as for the guidance and confidence that was fundamental to accomplish this work.

To Dr. Rainer Mertz, Dr. Rudi Kulenovic and Ph.D. student Susanne Becker for their valuable help and collaboration regarding the experiments accomplished during my stay at IKE in Germany.

To members of the referee committee for their provision in evaluating this work and valuable contributions provided.

I especially thank Eng. Edevaldo Reinaldo for his help and dedication regarding the manufacturing of all capillary pumping systems tested in this work.

To students of mechanical engineering Rafael Branco, Renan Galante, Pablo Pelizza and Sérgio Galliza for their valuable contributions regarding the experiments.

Special thanks to friends Pablo Oliveira, Matelli, Fernando, Cirilo, Renzo, Luis Evelio, Lucas Berti and Walber Braga for their attention and discussion regarding the modeling and experimental results of this work.

To friends of LabCET for their companionship, support and encouragement at several moments of this journey which was full of struggles, overcomings and victories.

Special thank to Emaús Moviment (Singers and Shalom groups) and Opus Dei for their prayers, companionship and emotional and faith support.

Contents

List of Figures

List of Tables

List of Symbols

General Symbols

$\dot{m}$	Mass Flow Rate	(kg/s)
A	Area	(m^2)
c_p	Specific Heat	(J/kg-K)
d	Diameter	(m)
E_v	Capillary-Evaporation Number	(-)
f	Darcy (or Moody) Friction Factor	(-)
H	Height	(m)
h	Convection Heat Transfer Coefficient	(W/m^2-K)
h	Enthalpy	(J/kg)
K	Permeability	(m^2)
L	Length	(m)
Nu	Nusselt Number	(-)
P	Perimeter	(m)
p	Pressure	(Pa)
Pe	Peclet Number	(-)
Pr	Prandtl Number	(-)
Q	Heat Transfer Rate	(W)
q	Heat Flux	(W/m^2)
R	Thermal Resistance	(^{o}C/W)
r	Radius	(m)

Ra	Rayleigh Number	(-)
Re	Reynolds Number	(-)
T	Temperature	(^{o}C)
t	Time	(s)
U	Expanded Uncertainty	
u	Standard Uncertainty	
V	Volume	(m^3)
v	Specific Volume	(m^3/kg)
v	Velocity	(m/s)
x	Vapor Fraction	(%)

Greek symbols

α	Thermal Diffusivity	(m^2/s)
ϵ	Porosity	(%)
λ	Thermal Conductivity	(W/m-K)
μ	Dynamic Viscosity	(kg/m-s)
ν	Kinematic Viscosity	(m^2/s)
ρ	Density	(kg/m^3)
σ	Surface Tension	(N/m)
θ	Contact Angle	(rad)

Subscripts

amb	Ambient
app	Applied
c	Combined
cap	Capillary
CC	Compensation Chamber

cond	Condenser
crit	Critical
e	Effective
evap	Evaporator
f	Film
g	Gravity
h	Hydraulic
HS	Heat Sink
in	Inlet
l	Liquid
max	Maximum
MuAl	Mullite and Alumina
Ni	Nickel
out	Outlet
p	Pore
r	Coordinate r
ref	Reference
res	Reservoir
s	Solid
sat	Saturation
SS	Stainless Steel
v	Vapor
w	Wick
z	Coordinate z

Resumo

O controle térmico na indústria eletrônica tem crescido em importância devido à contínua diminuição de tamanho e ao aumento na potência dos componentes. Nestas aplicações, buscam-se dispositivos eficientes de transferência de calor, capazes de transferir grandes cargas de calor com uma diferença mínima de temperatura. Neste contexto, os tubos de calor (Heat Pipes - HPs), os tubos de calor em forma de circuito (Loop Heat Pipes - LHPs) e as bombas capilares (Capillary Pumping Loops - CPLs) são alternativas confiáveis e viáveis para a dissipação de calor. Os evaporadores capilares da maioria dos LHPs e CPLs utilizam meios porosos feitos de metal ou de plástico. Neste trabalho, um meio poroso cerâmico é proposto para aplicações em LHPs e CPLs. O desempenho do meio poroso cerâmico como evaporador capilar é analisado teórica e experimentalmente. Primeiramente, é feita uma análise teórica da transferência de calor e de massa de um evaporador capilar plano com uma estrutura porosa formada por uma ou duas camadas com propriedades diferentes. O meio poroso tem formato de um disco e é instalado entre os canais de líquido e de vapor. Um fluxo de calor externo é aplicado à superfície superior da estrutura porosa onde ocorre a evaporação do fluido de trabalho. A transferência de calor e de massa é modelada usando as equações macroscópicas de conservação da energia e da massa. O fluido é assumido incompressível, prevalece o equilíbrio térmico local e a Lei de Darcy é usada para modelar o fluxo viscoso dentro do meio poroso. Os modelos desenvolvidos permitem verificar o efeito das variáveis de projeto no desempenho do evaporador capilar tais como fluidos de trabalho, dimensões, permeabilidade, raio médio de poros e condutividade térmica do meio poroso. Para as análises experimentais, testes de desempenho de dois LHPs, um utilizando acetona e o outro água como fluidos de trabalho, foram realizados para potências de até 25 W. Além disso, testes de desempenho de um CPL usando água foram realizados para potências de até 30 W. O meio poroso cerâmico utilizado possui 50% de porosidade, distribuição de raio de poro entre 1 e 3 μm e uma permeabilidade de 1.5×10^{-14} m^2. Considerando uma temperatura de operação limite de 100 ^{o}C e regime permanente, os LHPs foram capazes de transferir até 15 W para água e 25 W para acetona, enquanto que o CPL foi capaz de transferir até 30 W. Apesar do bom desempenho dos sistemas de bombeamento capilar avaliados, observou-se que mais pesquisas ainda são necessárias, buscando otimizar as propriedades termofísicas do meio poroso cerâmico e melhorar o projeto dos LHPs e do CPL.

Abstract

Thermal control has become a relevant issue for the electronic industry due to the continuous decrease in size and increase in power of the electronic components. Heat transfer devices capable of transferring large heat loads with a minimal temperature drop are required. In this context, Heat Pipes (HPs), Loop Heat Pipes (LHPs) and Capillary Pumping Loops (CPLs) are reliable and feasible alternatives for heat dissipation. The capillary evaporators of most LHPs and CPLs use porous wicks made of sintered metal and plastic. A ceramic porous wick is proposed in this work as an alternative to wicks made of these common materials for applications in LHPs and CPLs. A theoretical and experimental analysis is presented. First, the heat and mass transfer in a flat capillary evaporator formed by a single or double-layered porous wick is analyzed. The wick has a shape of a flat disc and it is assembled between the liquid and vapor channels. An external heat input is applied in the upper surface of the wick, where the working fluid evaporates. The mass and heat transfer are modeled using the mass and energy macroscopic conservation equations. The fluid is assumed incompressible, local thermal equilibrium prevails and Darcy's Law is used to model the viscous flow within the porous medium. The models developed allow to verify the effect of design variables, such as working fluids, dimensions, permeability, average pore radius and thermal conductivity of the wick, in the performance of the capillary evaporator. For the experimental analysis, performance tests of two LHPs using acetone and water as working fluids were carried out for power inputs up to 25 W and performance tests of one CPL using water were carried out for power inputs up to 30 W. The ceramic porous wick used had 50% of porosity, 1 to 3 μm of pore radius distribution and a permeability of about 1.5×10^{-14} m^2. Limiting the operation temperature at 100 ^{o}C, at steady state, the LHPs were capable to transfer up to 25 W using acetone and 15 W using water, and the CPL was capable to transfer up to 30 W. Despite the good performance of the LHPs and CPL tested, it was observed that further research are still required for the optimization of the properties of the ceramic porous wick and for improving the design of the LHPs and CPL.

1 Introduction

The electronics industry has grown at a rapid pace seeking the miniaturization and better performance of components. At the scales reached nowadays, the thermal control of electronic equipment has become an important issue. There is a need to develop heat transfer devices that are capable of transferring large amounts of heat with a minimal temperature drop. In this context, Heat Pipes (HP), Loop Heat Pipes (LHP) and Capillary Pumping Loops (CPL) are reliable and feasible alternatives as heat transfer devices. They are passive two-phase devices that utilize the evaporation and condensation of a working fluid to transfer heat. The thermal fluid circulation is accomplished by the capillary forces generated in a porous wick. Therefore, the working fluid pumping does not consume electric power. In this thesis, the LHP and the CPL are studied.

In the last decades, there has been an increased acceptance of these systems in the aerospace community because of their performance advantages, unique characteristics of operation and the success in operation in recent flight experiments. As a result, research has been intensified in order to better understand the phenomena that occur in these thermal systems. Ku & Kroliczek (1987), Maydanik *et al.* (1991), Ku (1994), Maydanik (1999), Ku (1999), Nikitkin & Cullimore (1998), Chernysheva *et al.* (2007), Santos & Bazzo (2007), among others, report past and recent advances.

1.1 CPL and LHP Classification and Basic Operation

CPL and LHP operate within a range of temperatures basically defined by the working fluid properties. The choice of working fluid involves several factors associated to the operation, availability and safety. Ammonia is frequently used in capillary pumping systems but other working fluids such as water, ethanol, acetone, propylene, methanol, butane, isobutene and propane also result in good operation (PETERSON, 1994). The range of operation temperatures constitutes the preliminary condition for the selection of the possible thermal fluid for a given application. The maximum range lies between the triple and critical points, because below the triple point and above the critical point there is no circulation of the thermal fluid by capillary action.

The capillary pumping capacity depends on the surface tension of the working fluid and the properties of the porous wick. Up to now, the working fluids have been classified according to the capillary limit, *i.e.*, the maximum pumping pressure that the porous wick can provide. There is another limit called the boiling limit, but for lack of a better strategy, the fluids that present this problem have been avoided. The boiling limit is related to the evaporation process of the working fluid in the liquid feeding channel and/or in the wick due to high temperature of liquid that flows into the evaporator. Ku (1994) studied the operation of a CPL, basing his analysis on the Pressure-Temperature (PT) diagram and his conclusions justified the need for a high state of subcooling in the entrance of the capillary evaporator required by some working fluids such as water and toluene. That is, the greater the subcooling requirement of a determined working fluid, the lower the boiling limit. A similar analysis, using the PT diagram, was also published for LHP by Maydanik *et al.* (1991), Ku (1999) and Maydanik (2005). The occurance of these two operating limits will be analyzed in this work.

The operation modes of the capillary pumping systems can be classified as fixed or variable conductance. In the variable conductance mode, the system saturation temperature can be controlled for different thermal loads. On the other hand, in the fixed conductance mode, the greater the thermal load, the greater the system saturation temperature. Nikitkin & Cullimore (1998) presented qualitative graphs of the vapor temperature for CPL and LHP operating in the fixed and variable conductance modes. Chernysheva *et al.* (2007) presented similar quantitative graphs for LHP.

In the following, an overview of the CPL and LHP theory is presented. The fixed and variable conductance modes and the PT diagrams for CPL and LHP are discussed.

1.1.1 CPL with Fixed Conductance

Figure 1.1 depicts a typical fixed conductance CPL. This device is composed of an evaporator, a condenser, a subcooler and liquid and vapor transport lines. The evaporator possesses a wick that promotes the working fluid circulation in the loop. The fluid circulation occurs in a continuous way and in the same direction, differently of the circulation in the heat pipe, where the liquid and the vapor flow in opposite directions.

Fixed conductance CPLs operate in the following way: heat is supplied to the evaporator and the liquid into the wick evaporates, forming menisci at the liquid-vapor interface. The capillary forces developed by the curvatures of the menisci promote the working fluid circulation along the loop. The vapor formed in the capillary evaporator flows through the vapor transport line to the condenser, where heat is removed. The liquid formed

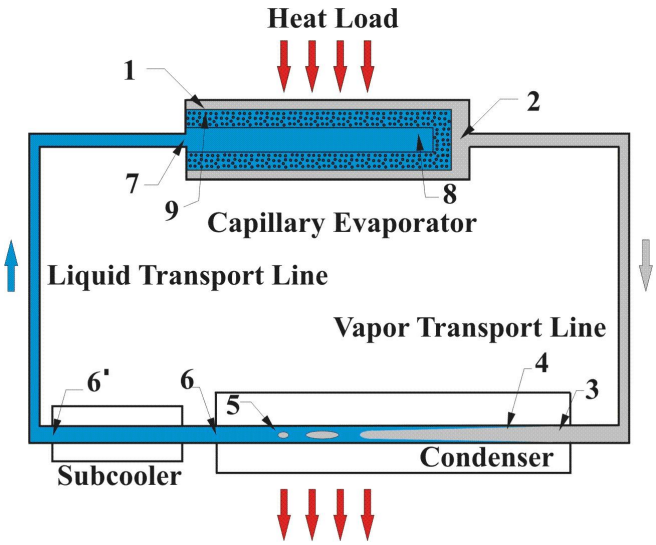

Figure 1.1 – Schematic diagram of a fixed conductance CPL.

in the condenser is subcooled before being transported back to the evaporator. All the pressure losses in the system are supplied by the capillary pressure difference originated in the porous wick of the capillary evaporator.

Fixed conductance CPLs have the following operating characteristics: (i) the subcooler is usually an integral part of the condenser; (ii) they do not have a reservoir that works as a fluid accumulator; (iii) the vapor condensation area in the condenser remains constant as the thermal load varies; (iv) the system operation temperature is dependent on the thermal load, supplied to the evaporator, and on the condenser sink temperature.

At the evaporation front (liquid-vapor interface), the pressure difference between the phases is the capillary pressure, which can be expressed by the Young-Laplace's equation,

$$\Delta p_{cap} = p_v - p_l = \frac{2\sigma \cos\theta}{r}. \tag{1.1}$$

For an averaged radius of curvature r of the liquid-vapor interfaces, the capillary pressure becomes maximum when the contact angle between the liquid and the solid approaches zero, in other words, when the wettability of the working fluid is maximum.

At the evaporation interface, the average radius of curvature of the liquid-vapor interface adjusts itself in order to balance the capillary pressure, as predicted by Young-Laplace's equation above. The minimum possible radius of curvature before dry-out of the pore is the characteristic radius of the pore. This radius depends on the pore topology and is determined by the choice of base material and manufacturing process, *e.g.*, sintering, used to produce the porous wicks. The maximum capillary pressure that the wick can withstand for a zero contact angle is therefore,

$$\Delta p_{cap,max} = \frac{2\sigma}{r_p} \tag{1.2}$$

This characteristic average pore radius r_p for the pore structure is related to the threshold for percolation of the non-wetting phase and is commonly identified, by Young-Laplace, as the wick bubbling pressure. In the operation of a capillary evaporator, when the pressure losses of the system exceed the maximum capillary pressure, the system fails. The capillary limit of a CPL reflects this maximum pumping capacity.

Therefore, the normal CPL operation requires that the sum of the pressure losses in the components and in the transport lines be smaller than the maximum capillary pressure head developed by the wick, *i.e.*,

$$\Delta p_{cap,\max} \geq \Delta p_{\text{evap}} + \Delta p_{\text{cond}} + \Delta p_{\text{v}} + \Delta p_{\text{l}} + \Delta p_{\text{g}} \tag{1.3}$$

In Eq. 1.3 the pressure losses are identified as: Δp_{evap} - pressure loss in the evaporator, Δp_{cond} - pressure loss in the condenser, Δp_{v} - pressure loss in the vapor lines, Δp_{l} - pressure loss in the liquid lines and Δp_{g} - pressure difference due to gravity.

The pressure loss along the lines of liquid (Δp_{l}) and vapor (Δp_{v}) can be approximated by using the Darcy-Weisbach equation:

$$\Delta p_{(l)\,or\,(v)} = f\left(\frac{L}{d_h}\right)\left(\frac{\rho v^2}{2}\right), \tag{1.4}$$

where f is the Darcy (or Moody) friction factor, L is the pipe length, d_h is the hydraulic diameter and v is the average flow velocity.

The most important component of the total pressure loss, accounting for approximately from 40 to 95% of the total pressure loss, is the pressure drop along the porous structure of the capillary evaporator. This pressure loss can be approximated by Darcy's equation,

$$\Delta p_{wick} = \frac{l\mu_l}{\rho_l A_l K_l}\dot{m}_l \tag{1.5}$$

where $\dfrac{A_l}{l}$ is the average area for flow divided by the lenght of the flow path, μ_l is the liquid dynamic viscosity, K_l is the liquid permeability and $\dot{m}_l$ is the liquid mass flow rate accross the porous wick.

This estimate will be further improved when the results are analyzed. For now, it

makes it clear that the permeability of the porous medium, which ranges from 10^{-10} to 10^{-15} m^2 for different porous structures, affects greatly the pressure drop.

The Carman-Kozeny equation provides a simple model that relates permeability to the average pore diameter such that,

$$K_l = \frac{\epsilon^3}{180\,(1-\epsilon)^2} d^2, \tag{1.6}$$

where ϵ is the porosity and d is the average pore diameter of the porous wick. The validity of this equation will not be discussed now. It suffices to say that the permeability scales with the square of the average pore diameter.

The maximum capillary pressure head is a function of the fluid surface tension, the contact angle and the pore radius. On the other hand, the pressure losses on the right side of Eq. 1.3, depend on the system design and the power input to the evaporator. When the total pressure loss in the system exceeds the maximum capillary pressure head, vapor penetrates in the wick causing dry-out and possibly blockage of the liquid inlet. When this occurs, the system fails.

The thermodynamic states of the working fluid may be suitably presented in a p-T diagram such as the one shown in Fig. 1.2. The numbering corresponds to the states identified in Fig. 1.1. In point 1, the liquid vaporizes at a saturation temperature T_1 corresponding to a pressure p_1. The vapor flows along the evaporator grooves and there is a pressure drop due to viscous friction from p_1 to p_2. Point 2 is located closer to the evaporator outlet, where liquid vaporizes at a lower saturation temperature T_2'. Therefore, the liquid vaporizes along the external wick surface at a temperature range between T_1 and T_2', instead of a fixed temperature T_1. The vapor leaves the evaporator in the superheated state (point 2) partly due to the decrease in the saturation pressure and partly due to the proximity of the hot source that supplies heat to the system. The vapor pressure decreases as it flows along the vapor transport line, between points 2 and 3. Since the vapor experiences an adiabatic expansion, its temperature decreases slightly.

The thermodynamic state of the vapor that enters in the condenser is represented by the temperature T_3 and pressure p_3. As shown by Ku (1994), a small area of the condenser is enough to dissipate the sensible heat before the beginning of the vapor condensation in the point 4 at a pressure p_4 (smaller than p_3) and at a saturation temperature T_4. The vapor condensation occurs between points 4 and 5. At point 5 there is no longer vapor. Similar to the liquid vaporization in the evaporator, the vapor condensation occurs at a temperature range between T_4 and T_5. The liquid continues to lose sensible heat until it reaches a subcooled temperature T_6 in the condenser outlet. A further subcooling

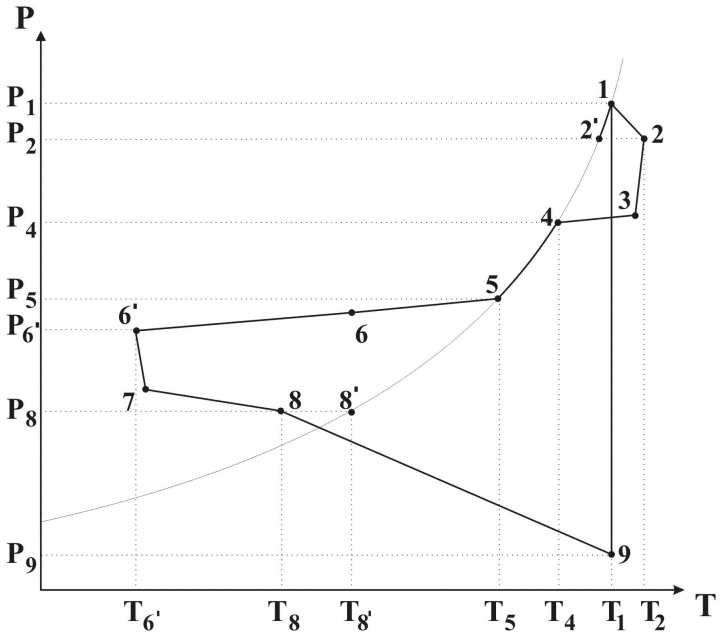

Figure 1.2 – Functional schematic of a fixed conductance CPL (corresponding to Fig. 1.1).

is needed to $T_6^{'}$ to ensure that no vapor bubble reaches in the evaporator. The liquid temperature increases slightly to T_7, while the pressure decreases to p_7 in the liquid feeding channel of the evaporator. Inside the feeding channel, the liquid is heated until temperature T_8. This heating is due to the upstream heat leak from the wick to the fluid. The point $8^{'}$ represents the saturation state corresponding to the local pressure p_8.

From point 8 to point 9 the liquid pressure falls. As the liquid flows through the wick, its temperature is increased until reaching the saturation temperature T_1 corresponding to the pressure p_1 before its evaporation in the external surface of the wick. It is noticed by Fig. 1.2 that the liquid side of the menisci (point 9) is represented as superheated.

The total pressure drop in the system is equal to the difference between p_1 and p_9 which in its turn must be smaller than the maximum capillary pressure head for normal operation. Following Ku (1999), in most of the two-phase capillary pumping systems, the changes of pressure and temperature are extremely small. These changes along a saturation line may be approximated using the Clausius-Clapeyron equation:

$$\left.\frac{dp}{dT}\right|_{T_{sat}} = \frac{h_{lv}}{T_{sat} v_{lv}} \tag{1.7}$$

where h_{lv} is the latent heat of vaporization, T_{sat} is the saturation temperature and v_{lv} is the difference in specific volumes of the liquid and vapor phases.

For instance, the variation of the pressure and temperature between points 1 and 4 are related by

$$\left.\frac{dp}{dT}\right|_{T_4} (T_1 - T_4) \simeq (p_1 - p_4)\,. \tag{1.8}$$

This pressure drop is a function of the mass flow rate which in its turn is a function of the power input to the evaporator.

The heat transfer rate at vaporization is equal to that at condensation ($\dot{Q}_{cond} = \dot{Q}_{evap}$). The heat transfer rate in the condenser can be expressed as:

$$\dot{Q}_{cond} = h_{cond} A_{cond} \left(T_4 - T_0\right), \tag{1.9}$$

where h_{cond} is the heat transfer coefficient, A_{cond} is the heat transfer area in the condenser and T_0 is the temperature of the cold reservoir outside the condenser.

For a CPL with fixed liquid volume, the thermal conductance ($h_{cond}A_{cond}$) remains constant. For a given heat transfer rate rejected by the condenser ($\dot{Q}_{cond}$) and a condenser sink temperature T_0, the vapor in the condenser will condense at the temperature T_4 in agreement with Eq. 1.9 and the liquid will vaporize in the evaporator at the temperature T_1 in agreement with Eq. 1.8. Any change in the input heat to the evaporator and/or in the condenser sink temperature will result in changes of the T_1 and T_4. Therefore, the main characteristic of a fixed conductance CPL is its strong dependence of the operation temperature on the input heat and condenser sink temperature.

1.1.2 CPL with Variable Conductance

In a variable conductance CPL, an online fluid reservoir is added. The function of the reservoir is to control the operation temperature of the system and to accumulate the liquid excess that is not being required in the loop.

The variable conductance mechanism may be explained using Eq. 1.9. If the condenser sink temperature T_0 remains constant and the system thermal load increases, more vapor will be generated in the evaporator and the vapor excess will accumulate in the condenser, causing a local pressure increase. This pressure increase, in its turn, causes a liquid displacement from the condenser to the reservoir, as represented in Fig. 1.3. This occurs because the condensation temperature T_4 remains constant and the heat transfer area A_{cond} increases so that Eq. 1.9 is satisfied.

When the system thermal load decreases and T_0 remains constant, the vapor pressure into the condenser will decrease. An unbalance in the pressure difference between the reservoir and the condenser will force a liquid displacement from the reservoir to the

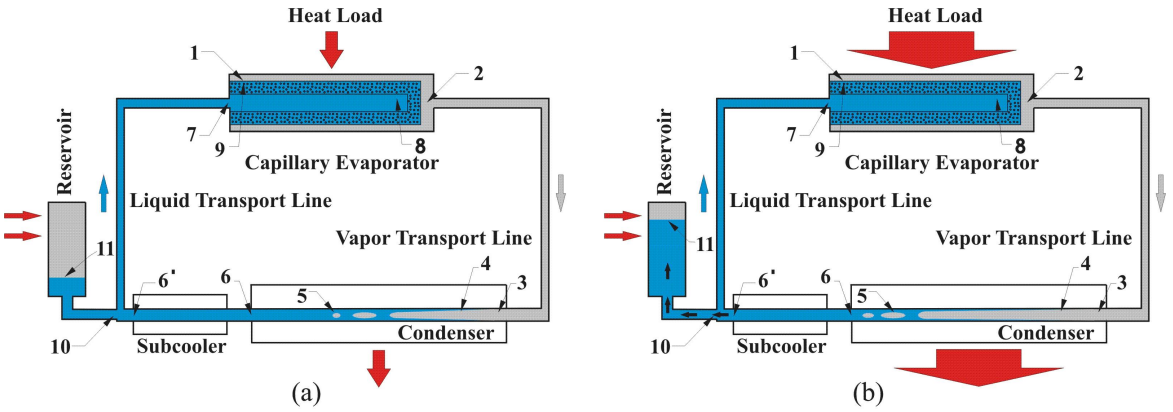

Figure 1.3 – Functional schematic of a fixed conductance CPL.

condenser, reducing the heat transfer area A_{cond} so that Eq. 1.9 is again satisfied. A similar analysis can be made varying the condenser sink temperature T_0.

Figure 1.4 depicts a PT diagram for the variable conductance CPL shown in Fig. 1.3. Point 11 corresponds to the saturation state in the reservoir. The vapor condensation temperature T_4 is related to the reservoir saturation temperature T_{11} by Clausius-Clapeyron and this temperature difference can be approximated by,

$$(T_4 - T_{11}) = \frac{(p_4 - p_{11})\, T_{11} v_{lv}}{h_{lv}}. \tag{1.10}$$

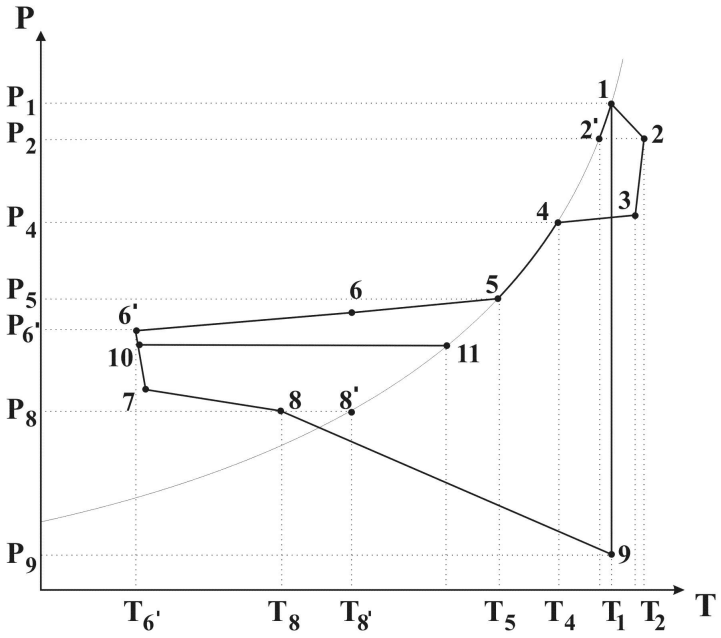

Figure 1.4 – PT diagram for a variable conductance CPL (corresponding to Fig. 1.3).

The variable conductance CPL, represented in Fig. 1.3, operates as follows. Before the system startup, the condenser is submitted to the temperature T_0 and the reservoir is heated up to temperature T_{11} which is higher than the temperatures of the rest of the

loop. Then, the thermal load is supplied to the evaporator. As the evaporator is heated up to the same temperature T_{11} or slightly above that, the liquid is vaporized and flows to the condenser along the vapor transport line. An equilibrium condition is established in the condenser so that the vapor condenses at the temperature T_4 that is very close to the reservoir temperature T_{11}. An equilibrium condition is also established in the evaporator so that the liquid vaporizes at the temperature T_1.

The condensation temperature T_4 is not sensitive neither to the changes in the condenser sink temperature T_0, nor to the changes in the system thermal load. Therefore, the temperature T_4 is controlled by the reservoir saturation temperature T_{11}. This temperature control is only possible if the reservoir is under two phase condition.

1.1.3 LHP

LHP is a kind of variable conductance CPL and was developed to overcome the apparent disadvantage of CPL that requires pre-heating during the startup. In LHP, the reservoir, also denominated hydro-accumulator or compensation chamber, ensures the presence of liquid in the evaporator wick. A secondary wick usually connects the compensation chamber to the evaporator. The compensation chamber is located close to the evaporator, usually in the inlet of the capillary evaporator, as it can be seen in Fig. 1.5; or taking the place of what would be the liquid feeding channel of the evaporator. Thereby, in a LHP the liquid reservoir presents direct thermal contact with the evaporator (hot source), differently of CPL where it is connected to the condenser (cold source). Figure 1.6 depicts a PT diagram for the variable conductance LHP, shown in Fig. 1.5. Point 10 corresponds to the saturation state in the compensation chamber.

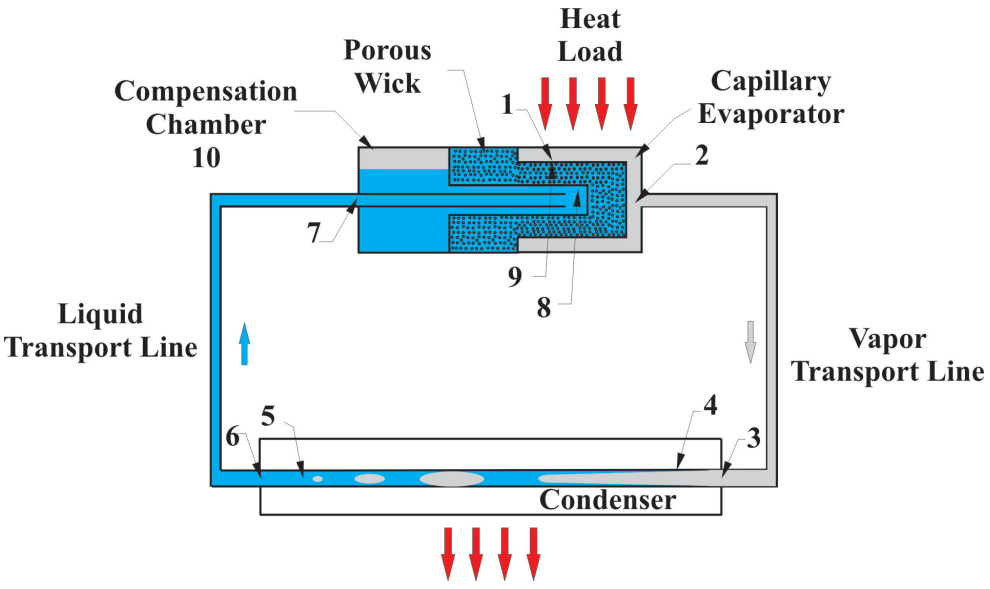

Figure 1.5 – Functional schematic of a LHP.

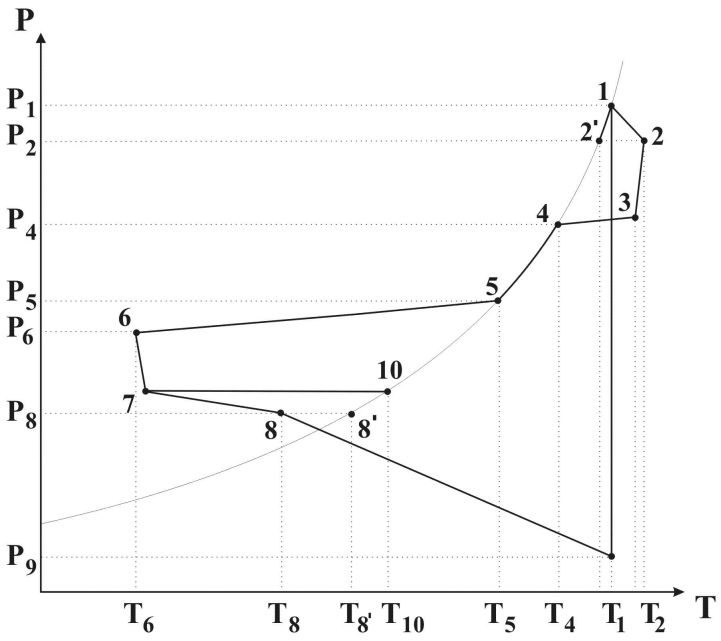

Figure 1.6 – PT diagram for a LHP (corresponding to Fig. 1.5).

The liquid vaporization temperature T_1 is related to the saturation temperature of the compensation chamber T_{10} by Clausius-Clapeyron approximated as,

$$(T_1 - T_{10}) = \frac{(p_1 - p_{10})\, T_{10} v_{lv}}{h_{lv}}. \tag{1.11}$$

The PT diagram, shown in Fig. 1.6, presents an analysis for steady state operation. Therefore, there is no mass flow from the compensation chamber to the liquid feeding channel of the evaporator. Consequently, the saturation pressure p_{10} in the compensation chamber is the same as pressure p_7.

1.1.4 CPL and LHP

The capillary pumping systems in the variable conductance mode, *i.e.*, the CPL and LHP shown in Figs. 1.3 and 1.5, can also work in a binary operation mode. When these systems are operating in a low thermal load condition, the reservoir (CPL) or the compensation chamber (LHP) present stable liquid and vapor regions. As it was already mentioned, when the thermal load increases, the condensation front moves forward, causing a liquid displacement from the condenser to the reservoir (CPL) or to the compensation chamber (LHP). Therefore, as the thermal load increases, these compartments are increasingly filled in with liquid. The evaporation temperature control is only possible if the liquid compartment of the system presents both liquid and vapor. Consequently, if the thermal load increases up to a condition where all the volume of the reservoir (CPL) or the compensation chamber (LHP) is filled with liquid, the saturation temperature control

ceases to be possible.

Figure 1.7 shows qualitatively the variation of the evaporation temperature distribution as a function of the thermal load of CPL and LHP that work in the binary operation mode (fixed and variable conductance). Fig. 1.7(a) depicts that the evaporator temperature of the CPL remains constant in the variable conductance operation mode and starts to increase linearly in the fixed conductance mode. For the LHP, Fig. 1.7(b), even operating in the variable conductance operation mode, the evaporator temperature does not remain constant. The LHP possesses a range of evaporation temperature control in the variable conductance mode. This occurs, according to Chernysheva *et al.* (2007), due to two factors: (i) decrease of the condensation area, caused by the liquid displacement from the condenser to the compensation chamber; and (ii) change in the saturation temperature in the compensation chamber T_{11}, that influences directly the change of the evaporation temperature, due to a complex process of heat and mass transfer. This process develops between the evaporator and the compensation chamber.

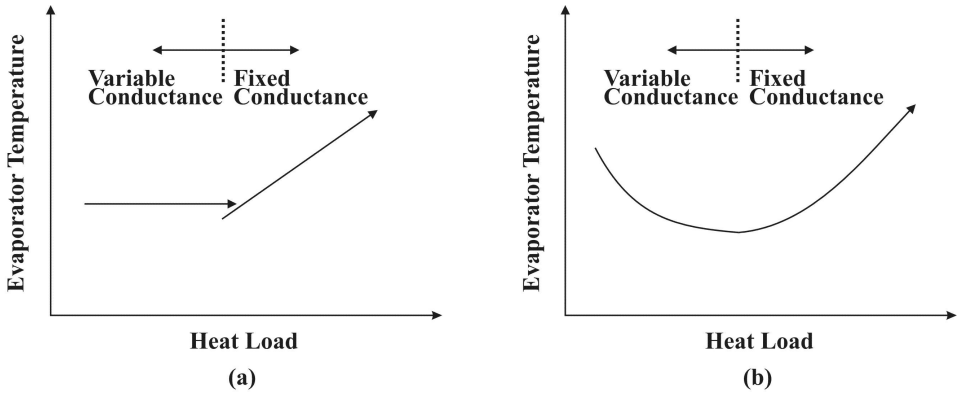

Figure 1.7 – Typical curves of operation for (a) CPL and (b) LHP in the fixed and variable conductance (NIKITKIN; CULLIMORE, 1998).

The thermo and fluid dynamic analysis of capillary pumping systems, presented in these sections, has helped to explain the phenomena that occur in these systems. The next section summarizes the main results of recent research involving the application of capillary pumping systems (CPLs and LHPs) for thermal control in general.

1.2 Overview of CPL and LHP Experiments

Thermal control has become a relevant issue in modern computers due to their continuous size decreasing and power increasing requirements. According to Nikitkin & Cullimore (1998) and Maydanik (2005), the LHPs and CPLs, which were previously developed for spacecraft thermal control, are reliable alternatives and can also transport heat with high performance for terrestrial electronic cooling application. Several authors

(CHEN; LIN, 2001; HOANG *et al.*, 2003; PASTUKHOV *et al.*, 2003; MAYDANIK, 2005; CHEN *et al.*, 2006; PASTUKHOV; MAYDANIK, 2007) have reported experimental results concerning the application of LHPs, mini-LHPs and CPLs for heat dissipation in CPUs of modern computers, showing that they are efficient and reliable heat transfer devices for the next generation of microprocessors.

It has been customary to express the quality of LHPs and CPLs by the thermal resistance $R(^oC/W)$ given by,

$$R = \frac{\Delta T}{Q}, \tag{1.12}$$

where Q is the heat transfer rate dissipated by the two-phase system and ΔT is the temperature difference between the hot surface, where the thermal load is applied, and the cold reservoir.

The thermal resistence is size dependent, but it is the figure of merit usually reported in the literature. A different figure of merit will be proposed when the results of this work are analyzed.

The thermal performance and reliability of the LHPs and CPLs have been extensively tested. Ku (1999), Chen & Lin (2001), Pastukhov *et al.* (2003), Chuang (2003), Ku *et al.* (2004), Pastukhov & Maydanik (2007), Maydanik & Vershinin (2009) analyzed the thermal behavior and startup of the capillary pumping systems (LHP and CPL) regarding the working fluid inventory, slopes of the capillary systems, wick material (nickel, stainless steel, copper, polyethylene), body material of the evaporator (copper and stainless steel), cooling system of the condenser (forced convection using water and air, and natural convection using air), multi-evaporators and condensers, heat sink and environment temperatures at ground and microgravity conditions for a range of power inputs. The most recent and promissing systems are reviewed below.

Hoang *et al.* (2003) have developed and tested three miniature LHPs with ammonia, propylene and water as working fluids for electronics cooling. All LHPs were assisted by a secondary cooling system in the compensation chamber in order to decrease the heat leak. Two cooling systems were tested: a small thermo-electric cooler (TEC) and a heat pipe made of copper with 3 mm of diameter, which uses water as working fluid. Two of the LHPs were capable of transporting heat up to 60 W (ammonia) and 15 W (propylene) at room temperature of 25 ^{o}C in any orientation. The other LHP using water, which was the main objective of the paper, was tested with and without the heat pipe at the compensation chamber. An air cooling fan was used for the cooling of the condenser. This LHP was made of copper and the wick was made of Teflon with pore size of 7 μm

and permeability of 1×10^{-13} m^2. The water LHP was capable of transporting heat up to 220 W for a capillary pump temperature up to 82 ^{o}C assisted by the heat pipe in the compensation chamber and up to 90 ^{o}C without the heat pipe assistence. The total thermal resistance ranged from 2.0 to 0.2 ^{o}C/W. The use of the heat pipe for the controlling of the heat leak had a significant influence on the heat transfer capacity of the LHP.

Six miniature LHPs were developed and tested by Pastukhov *et al.* (2003) for cooling electronics components and CPUs of mobile PCs. Ammonia and acetone were used as working fluid. Porous wicks made of stainless steel and titanium were used as porous structures. Air was used for the condenser cooling and the diameter of the cylindrical evaporators ranged from 5 to 6 mm. The LHPs were capable of heat transfer up to 40 W for cooling the CPU of a notebook with total resistance raging from 1.0 to 2.4 ^{o}C/W. The CPU temperature was kept between 83 and 90 ^{o}C. They concluded that further decrease in total thermal resistance could be obtained by optimization of the LHP design and the condenser cooling, and the ammonia as a working fluid ensured better results when compared to acetone.

Chen *et al.* (2006) performed a series of tests with a miniature loop heat pipe (mLHP) which was developed for cooling CPUs of mobile personal computers. Amonnia was used as working fluid and the material of the wick was titanium with break down pore radius of 17.2 μm, porosity of 78% and permeability of 11.5×10^{-12} m^2. They tested the mLHP at several positions (horizontal, condenser above evaporator, evaporator above condenser, compensation chamber above evaporator and evaporator above compensation chamber), with emphasis to the position with evaporator 10^o above condenser and vice versa. The thermal behavior of mLHP was evaluated during the start-up and for different sink temperatures. At sink temperature of 25 ^{o}C and in horizontal position, the mLHP was capable of transporting heat up to 70 W for a limit temperature of 80 ^{o}C and the total thermal resistance ranged from 0.2 to 0.85 ^{o}C/W. They concluded that for the tested mLHPs, which are targeted at consumer electronics cooling, the overall operating characteristics for horizontal orientation proved to be satisfying.

Maydanik & Vershinin (2009) developed and tested nine mLHPs with cylindrical capillary evaporators. Three mLHPs with external diameter of 5 mm and six mLHPs with external diameter of 6 mm. They used ammonia as working fluid for all mLHPs and different materials for the wick (titanium, with average pore radius of 9.5 and 17.2 μm and porosity of 70 and 78%, and nickel with average pore radius ranging of 13.5 and 10.0 μm and porosity of 71, 66 and 65%). The envelope of the cylindrical evaporator was made of titanium and nickel. Several tests were carried out in order to evaluate the thermal

behavior of mLHPs taking into account the inclination of the devices, the temperature of cooling in the condenser section and the type of the cooling fluid (air and water in forced convection). They presented a methodology for estimating the thermal resistances and the heat transfer coefficients of the mLHPs. The minima total thermal resistances were 0.53 ^{o}C/W and 0.14 ^{o}C/W for air and water cooling, respectively. The maximum capacity was 230 W for water cooling.

As shown, most of porous wicks are made of metals or polymers. However, these materials present some difficulties for machining (metal wicks) and low capillary pumping capacity (polymer wick). The machining of metal wicks may obstruct the surface pores, decreasing the permeability. The next section presents some works that were aimed at manufacturing, characterization and application of porous wick in capillary pumping systems.

1.3 Application of Ceramic Wicks in Capillary Pumping Systems

Although the LHPs and CPLs present high heat transfer capacity, one disadvantage is their complicated manufacture. The proper fitting of the capillary structure inside the envelope of the evaporator is the first challenge to be overcome. The assembly is relatively complex because the metallic envelope requires close contact tolerances at the interface between envelope walls and wick surface. This contact should be fit in order to minimize the thermal resistance and any vapor leak back to the compensation chamber (LHP) and to the liquid feeding channel (CPL). With the aim of obtaining close tolerances, a reliable machining process is required for these wick structures because the possibility of open porosity obstruction due to the plastic deformation. The ceramic wicks do not present plastic deformation during machining. Therefore, they can be machined by conventional machining and the open porosity remains the same (JANSSEN *et al.*, 2008).

To this author knowledge, there are few capillary pumping systems using ceramic porous wick as a porous structure of capillary evaporator (RASSAMAKIN *et al.*, 2002; RHI, 2006). Most LHPs and CPLs use polyethylene or metallic porous wicks. It is expected that ceramic wicks become more advantageous, because they are less expensive and easier to machine without damaging the pores in the external surface of the structure. Also the low thermal conductivity can minimize the radial heat leak to the liquid feeding channel, reducing the possibility of boiling in the liquid inlet.

Reimbrecht (2004) developed a methodology for manufacturing of porous wicks for the application in capillary pumping systems. Several techniques - image analysis, mer-

cury intrusion porosimetry and other experimental methods - were employed to determine static and transport properties of the porous wick such as critical pore diameter, permeability and thermal conductivity. He manufactured metallic (nickel and stainless steel) and ceramic porous wicks and tested them in capillary pumping loops (CPLs). The CPL with the ceramic porous wick was capable of heat transfer up to 40 W (1.4 W/cm^2) using acetone. However this CPL did not work adequately in a second test for a heat load of 20 W (0.7 W/cm^2). The failure was due to the contamination of the working fluid caused by the residual carbon from the organic material that was used to increase porosity in the manufacturing of the ceramic wick.

The wicks obtained by Reimbrecht (2004) had critical pore diameter of 0.9 μm (nickel) and 2.5 μm (stainless steel). The ceramic porous wicks and their pore size distribution obtained by mercury porosimetry are depicted in Fig. 1.8. It can be noted in Fig. 1.8 (b) that the ceramic porous wick has a narrow pore size distribution with 95% of the pore volume being formed by pores with sizes ranging from 0.5 μm to 3.5 μm with average at 1.2 μm.

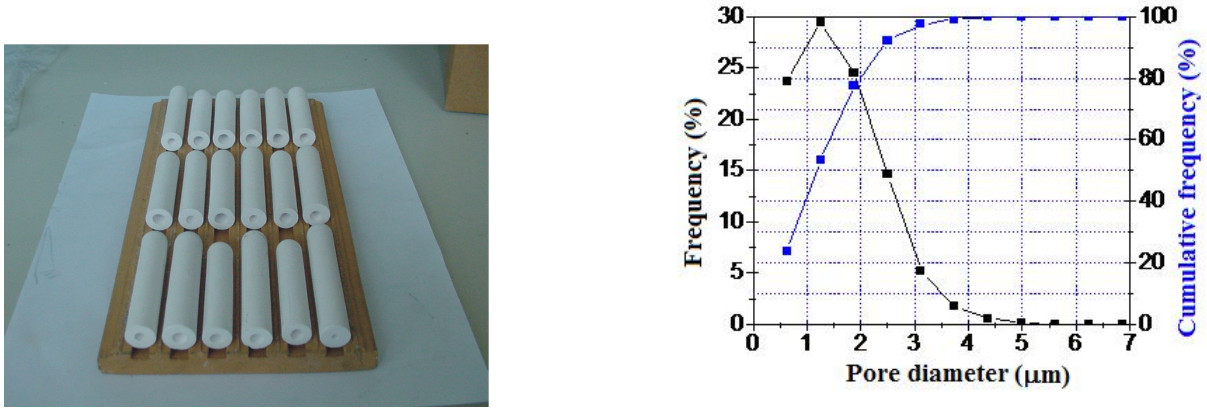

(a) (b)

Figure 1.8 – (a) Ceramic wick samples and (b) pore size distribution obtained by mercury intrusion porosimetry, Reimbrecht (2004).

The objective of the work by Reimbrecht (2004) was to study and optimize the porous samples manufacturing routes, as well as, to evaluate the characterization of these porous structures for the application in capillary pumping systems. With this goal, nickel, stainless steel, mullite and alumina were employed as raw materials. Camargo (2004) aimed at test and analyze all porous wicks manufactured by Reimbrecht (2004), and also another wick made of polyethylene. Two test rigs were built to evaluate the developed CPLs. He tested the CPLs using acetone and ammonia as working fluid, reaching pumping capacity up to 25 kPa. The main results presented by Camargo (2004) for the CPL using ammonia are summarized in Table 1.1.

Table 1.1 – Main results presented in Camargo (2004).

Porous wick	Heat Flux (W/cm^2)	Capillary Pressure[(a)] (kPa)	Pore Diameter (μm)	Permeability (m^2)
Nickel	3.15	12.99	1.0	8.6×10^{-14}
Stainless Steal	3.15	17.34	2.0	5.3×10^{-14}
Polyethylene	3.00	3.09	0.6	26×10^{-14}
Ceramic	0.70	24.90	1.0	3.3×10^{-14}

(a) the capillary pressure was measured using a buble test.

The results presented by Camargo (2004), showed that the CPL with a ceramic wick had a successful started-up only for heat load of 10 W, but even though it did not reach the stabilization. Moreover, the ceramic wick resulted in the worst performance when compared to the other wicks (nickel, stainless steel and polyethylene).

According to the results in Table 1.1, the ceramic wick supplies the greater pumping capacity, however according to Camargo (2004), its low permeability has compromised the performance of the CPL. Camargo (2004) concluded that the permeability of ceramic wicks should be increased for it to become a reliable component in capillary pumping systems. Nevertheless, according to author knowledge of this thesis, the non successfull operation of the CPL was due to the manufacture of the capillary evaporator, mainly in the insertion of the porous wick into the metallic envelop.

Berti (2008) focused his work on the development of manufacturing routes of ceramic wicks in order to improve the ceramic wick manufactured by Reimbrecht (2004) and tested by Camargo (2004) before. The purpose of his work was to manufacture and characterize ceramic wicks for capillary pumping applications. In this way, two manufacturing routes were developed: slip casting and biotemplating. The ceramic wick manufactured by slip casting resulted in porosity of 50%, pore size ranging from 1 to 3 μm providing capillary pressure ranging from 80 to 22 kPa (using acetone) and permeability of 1.5×10^{-14} m^2. The ceramic wick manufactured by biotemplating resulted in porosity of 76% pore size ranging from 33 to 194 μm providing capillary pressure ranging from 0.48 to 3 kPa (using acetone) permeability of 1.5×10^{-10} m^2.

Berti (2008) manufactured and tested two CPLs that used acetone as working fluid. The CPL using ceramic wick manufactured by slip casting worked for heat load of 40 W (3.93 W/cm^2) and the other CPL using ceramic wick manufactured by biotemplating worked for heat load of 20 W (11.32 W/cm^2). The CPLs worked satisfactorily, however Berti (2008) reported that he had many problems regarding the assembly of the capilary evaporator and also heat leak through the wall of evaporator to the liquid feeding channel due to the geometry used for the flat capillary evaporators.

Since the heat and mass transfer required for the working fluid circulation along the loop is the most important phenomenon in capillary evaporators, this is reviewed next. The following section will present some geometries of capillary evaporators, the general description of physical phenomena that take place within the porous wick and the mathematical models proposed to solve the heat and mass transfer in capillary evaporators.

1.4 Description of the Problem Under Investigation

The main component of capillary pumping systems (LHP and CPL) is the capillary evaporator. Micro-grooves or porous wicks are used in the evaporators as capillary structures. Most CPLs and LHPs manufactured nowadays use porous wicks. There are basically two designs for cylindrical capillary evaporators, as shown in Fig. 1.9. A cylindrical evaporator with grooves machined in the metallic envelope is depicted in Fig. 1.9(a), while in Fig. 1.9(b) it is shown a cylindrical evaporator with grooves machined in the porous wick. Figure 1.10 depicts two flat evaporators, one with disk format and the other with square cross-section. In both evaporators shown in Fig. 1.10, the grooves are machined in the metalic envelope.

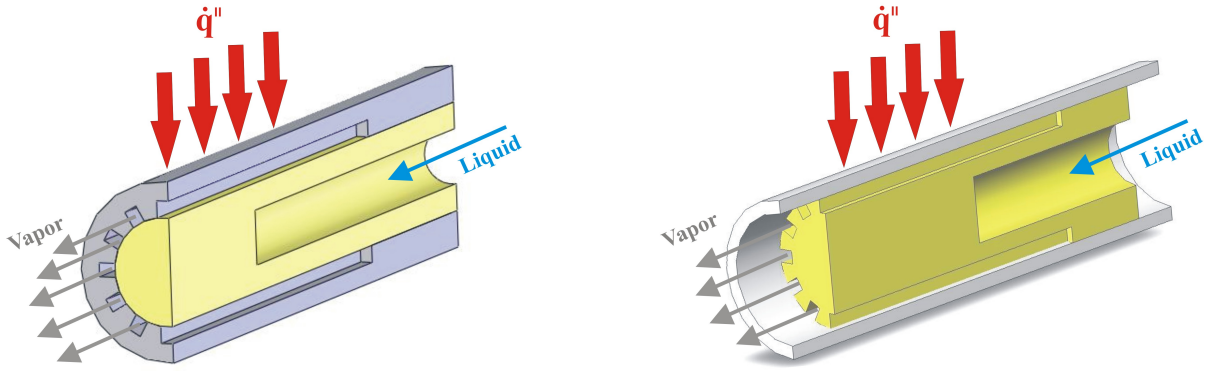

(a) (b)

Figure 1.9 – (a) Cylindrical evaporator with grooves machined in the metallic envelope. (b) cylindrical evaporator with grooves machined in the porous wick.

During operation, heat is applied to the external surface of the evaporator and the working fluid within the wick undergoes evaporation. The vapor flows out of the evaporator along the grooves. The evaporation rate of the working fluid within capillary evaporators depends on the heat load applied to the system and can occur in three different regimes: (1) microfilm evaporation, (2) evaporation at the outer surface and (3) within the porous wick.

The uncertainty regarding the location of the evaporation front and the stablishment of capillary limits for the wick operation has motivated attempts to solve the mass and heat

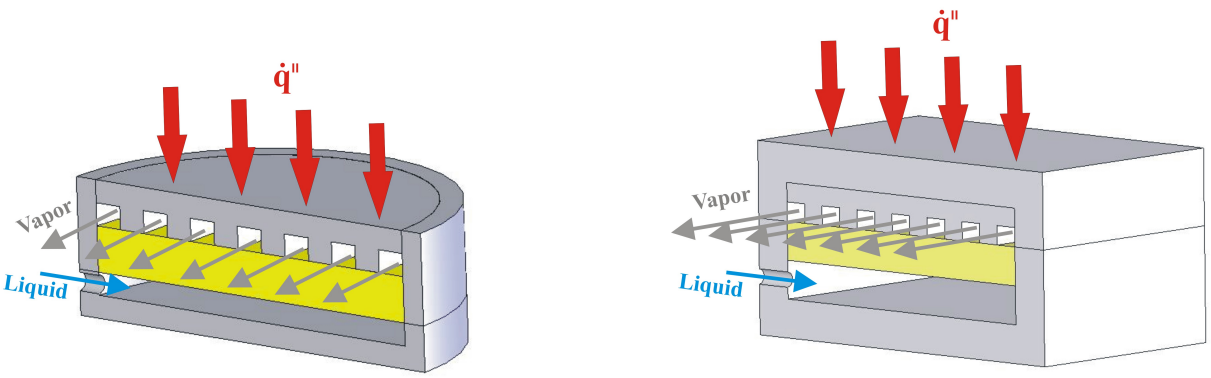

(a) (b)

Figure 1.10 – (a) Flat evaporator with cylindrical cross-section and (b) flat evaporator with square cross-section.

transfer problem within the porous wick. Some of the theoretical modeling is reviewed below.

Cao & Faghri (1994a) studied the evaporation in porous wicks under restrictive assumptions, that nevertheless, provided analytical solutions for the velocity and temperature fields. They assumed that the wick was completely saturated by liquid and the evaporation front was located in the external surface. Their model also assumes that the velocity field is uniform on the boundaries of the wick which is not exactly true as it will be shown bellow. They made a parametric analysis mostly directed to show that their analytical solution is accurate for most applications. Then, they concluded that the results obtained are of relevance for the design of capillary evaporators.

Cao & Faghri (1994b) reported an extension of their previous paper presenting an analysis of a three-dimensional geometry. A numerical investigation was developed for studying the flow of the liquid through the wick (two-dimensional) and the flow of the vapor through the grooves (three-dimensional). A comparison between the results obtained in both models for three working fluids (freon, water and ammonia) is presented and as a consequence they concluded that the working fluid has a strong effect on the difference between the two- and three-dimensional models. For water, the difference was relatively large. For freon and ammonia, however, the differences are generally small, *i.e.*, in this case, the solutions obtained with the two-dimensional model are accurate and reliable. They attribute these differences to the small vapor velocities for freon and ammonia (below 2.5 m/s) in comparison to water vapor velocity (12.5 m/s) for a heat flux of 1.5×10^4 W/m^2. In both works published by Cao and Faghri, they state that the results obtained are of relevance for the design of capillary evaporators, however they do not present a criterion for the dry-out of the porous wick, *i.e.*, there is no information regarding the critical heat flux before the failure of the capillary evaporator or at least a tendency for

that.

Demidov & Yatsenko (1994) made a theoretical investigation of the heat and mass transfer problem in the porous wick of a capillary pumping system. In their analysis, the wick was heated by a heat flux from the fins in contact with the wick. In their model, the fluid within the wick changes phase, developing a vapor-saturated region separated from a liquid-saturated region by a sharp evaporation front. At the evaporation front, the continuity of mass and heat and a jump in pressure due to capillary pressure is applied. A numerical solution of the mathematical model allowed to study the displacement of the evaporation front as the thermal load of the system varies.

They assumed that two limiting conditions are physically possible. For low heat load, there is a small vapor saturated region trapped underneath the fin, Fig. 1.11(a). The continuity of the liquid phase with the groove would then allow for the presence of a curved meniscus at the fin-wick contact line. All evaporation occurs in the wick-groove interface. As the heat load increases, the fluid in the meniscus evaporates and there is continuity of the vapor phase from the vapor-saturated region to the groove. Evaporation occurs both in the vapor-saturated region and in the groove interface, Fig. 1.11(b).

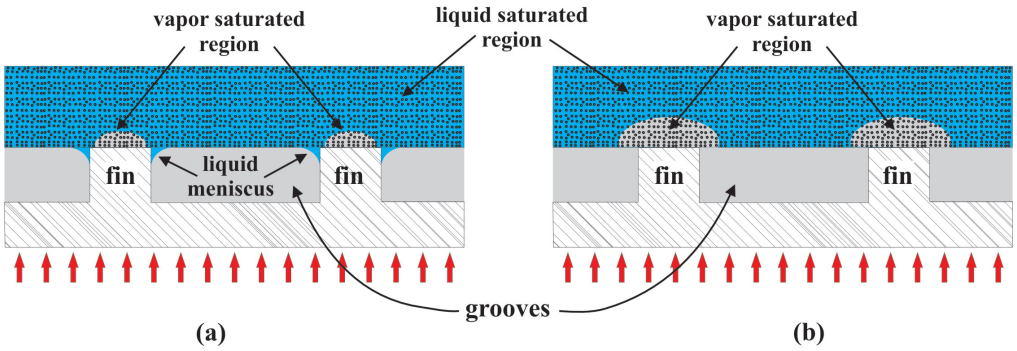

Figure 1.11 – Demidov & Yatsenko (1994) model (a) low heat load and (b) higher heat load.

At the liquid saturated surface in contact with the groove, the same conditions used for the evaporation front applies. The heat transfer to the vapor in the grooves is modeled using a surface convection heat transfer coefficient. All mass flux reaching the surface is suposed to evaporate absorbing the difference between the conductive heat flux from the wick and the convective heat flux to the vapor in the groove. The vapor phase in the groove is assumed to exist under saturated condition $[T_{sat}(p_v)]$.

The evaporation on the meniscus is modeled assuming a global heat transfer coefficient that includes a conductive thermal resistence accross the liquid film. The conduction heat transfer in the fin is also solved. Their results show that the evaporation is far more intense at the wick-groove interface than it is at the evaporation front. This occurs because the

flow of vapor out of the region underneath the fin is hindered by the low value of the vapor kinematic viscosity, as compared to the liquid kinematic viscosity, and the small sections available for flow near the fin-wick-groove triple line.

Maximum heat loads are absorbed at the threshold between the two regimes, exactly when the boundary of the trapped vapor phase reaches the fin-wick-groove triple line. Once the meniscus is dried-out, the heat load that can be absorbed reduces abruptly. The authors do not present results of the value of the critical heat flux at the threshold for the transition between the two limits. Only a qualitative analysis is presented.

Demidov and Yatsenko's work presents a modeling effort that is plenty of physical insights, however they did not quantify the limits of heat load for their porous wick. The effective properties, boundary conditions and dimensions are summarized in the table in Fig. 1.15, but no value of heat load applied has been reported.

Figus *et al.* (1999) analyzed a similar problem and attempted to quantify the change in evaporation regime as the heat load applied increased. In their work, the evaporation front is supposed to be immersed within the porous wick. They applied two different treatments: a continuum model, similar to the one used by Demidov & Yatsenko (1994), and a pore network model, similar to the drying models developed earlier by Prat (1993, 1995) and Laurindo & Prat (1996). The main difference in the formulation of the continuum model when compared to Demidov & Yatsenko (1994) is that Figus *et al.* (1999) did not include the evaporation at the wick-groove interface. All evaporation occurred within the wick. They modeled the heat and mass transfer problem of a cross section of a cylindrical evaporator as shown in Fig. 1.12.

Additional differences in boundary conditions are that T_l is prescribed in the liquid side of the wick, the heat flux is prescribed at the wick-fin interface and the saturation temperature is prescribed at the wick-groove interface. The results show that the fin surface is far from isotherm, presenting a gradient of the order of 60^oC/mm. Then, emphasis was placed on determining the conditions that lead to instability and fingering in the evaporation front. The continuum models do not capture these transitions since they are not appropriate to model phenomena near the threshold for percolation (PRAT, 1995), where small local fluctuations govern the development of the evaporation front.

Figus *et al.* (1999) present solutions for a low effective thermal conductivity medium ($\lambda_s = 4$ W/m-K) and for a high thermal conductivity medium ($\lambda_s = 10$ W/m-K) as summarized in the table in Fig. 1.15. For the low thermal conductivity medium, their results show that when the pore size is constant and equal to 10μm, the vapor phase invades the wick, *i.e.*, forms a vapor-saturated region underneath the fin, only for $q'' >$

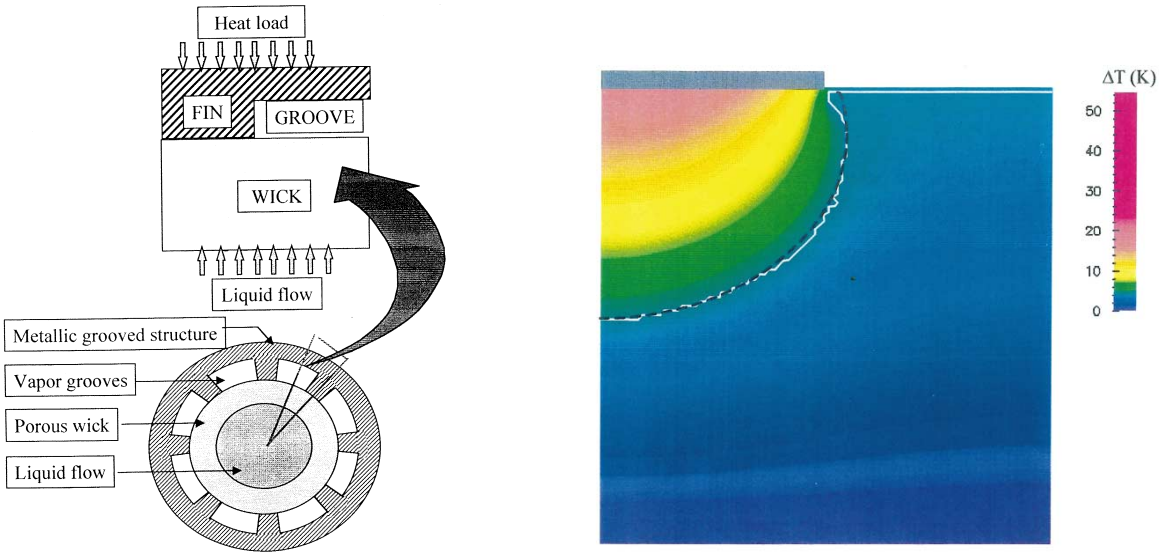

(a) (b)

Figure 1.12 – (a) Cylindrical evaporator and (b) pore network simulation (interface represented by the white line) versus continuum model solution, Figus *et al.* (1999).

$4,500$ W/m^2. The solutions where explored for q'' as high as $90,000$ W/m^2 and all the evaporation front developed with a smooth surface such that they are well predicted by the continuum models.

Then, a pore size distribution was assigned randonly to the pore space with average 10μm and ratio of maximum to minimum pore size denoted by $R = d_{max}/d_{min}$. For the higher thermal conductivity medium and $R = 2$, the vapor phase invades the wick at $q'' = 1,000$ W/m^2. Above this value, the front develops with irregular surface. For q'' from $15,000$ to $35,000$ W/m^2, the front is pinned. After $35,000$ W/m^2, the front area increases steadily until the breakthrough of the vapor accross the wick occurs at $q'' = 200,000$ W/m^2.

The invasion of the pore network occurs when the local vapor pressure overcome the capillary limit for the pore. The final breakthrough occurs when even the smaller pore are overcome by the local vapor pressure. As the ratio $R = d_{max}/d_{min}$ is increased, the final breakthrough occurs for even smaller values of q''. For their model, the position of the evaporation front and, therefore, the breakthrough, does not depend on the wick thermal conductivity. This is a result from their choice of imposing temperature boundary conditions.

Aparently, they also used a constant value for the surface tension, independent of the local temperture. As the heat flux was increased, the fin temperature also increased, reaching values as high as 100 ^{o}C. They conclude discussing that this problem is similar to an invasion-percolation problem characterized by small cappilary number ($C_a = v\mu/\sigma$)

for which, the vapor-liquid front develops as a stable fractal surface. As recomendation for the design of porous wicks, they recomended (i) to use of materials with high thermal conductivity (λ) to limit the fin temperature and high permeability medium as a layer near the fin, followed by (ii) a second layer with low λ material and small pore size near the liquid side.

Although Figus *et al.* (1999) did not correlate the threshold for the wick failure, they showed clearly the trend of the vapor invasion-percolation process. The local vapor pressure depends on the solution of Darcy's equation for the porous wick. The local critical (*i.e.*, maximum) capillary pressure that a given pore can withstand is a function of the pore size and the surface tension, which is calculated locally from the medium temperature. Therefore, the breakthrough criterion can be tested locally and whenever the critical capillary pressure is exceeded, local dry-out occurs.

Takahashi (2002) analyzed the heat and mass transfer with phase change in the cylindrical porous wick of a capillary evaporator (Fig. 1.13) in order to determine the maximum heat flux for steady-state operation of a CPL before its failure based on the capillary limit. Takahashi assumed as Figus *et al.* (1999), that the evaporation front develops within the wick. The differences between his work and the previous analysis (FIGUS *et al.*, 1999) are the inclusion of the capillary pressure jump at the liquid-vapor interface, the modification in a boundary condition and a simplification in the geometry. Takahashi (2002) solved numerically the problem using the finite volume method in orthogonal curvilinear coordinates fitted to the evaporation interface. He used a tracking method of the evaporation front combined with an adaptive mesh to this liquid-vapor interface.

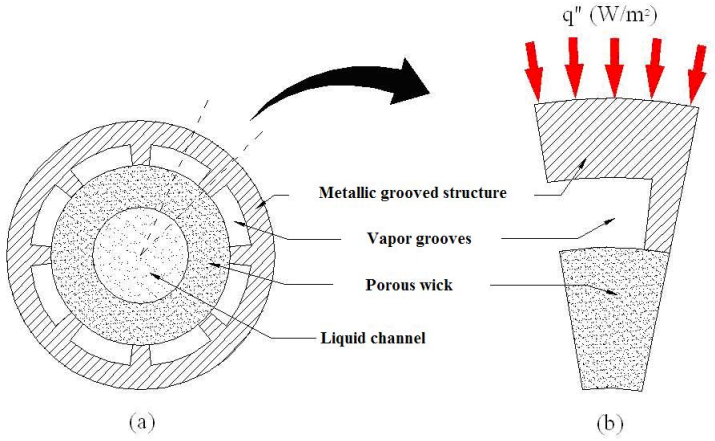

Figure 1.13 – (a) Cross-section of the capillary evaporator and (b) sector used in the analysis, Takahashi (2002)

Takahashi (2002) analized the ammonia as working fluid and obtained the properties for the nickel wick manufactured by Reimbrecht *et al.* (1999). The maximum capillary pressure was obtained from mercury porosimetry and from a drainage experiment. He

presented results regarding the location of the evaporation front for different heat fluxes. Besides, he calculated a maximum heat flux for steady-state operation of 13.06×10^4 W/m^2. At this critical heat flux, the flow of liquid was 2.66×10^{-5} kg/s, the maximum temperature difference (between fin and liquid channel) was 101 ^{o}C and the heat flux to the liquid channel was 0.798×10^4 W/m^2. His results compared well to those of Figus *et al.* (1999). The values of the critical heat flux was calculated for different properties (maximum heat flux of 130613 W/ m^2 for steady-state operation), but no attempt was made of parametrization of the results obtained.

Kaya & Goldak (2006) studied numerically the heat and mass transfer in the capillary porous structure of a loop heat pipe (LHP), presented in Fig. 1.14, with a focus on the occurrence of the boiling limit. The problem was basically the same as Demidov & Yatsenko (1994) and Figus *et al.* (1999) with a similar formulation. One difference in the formulation was that the model takes into account the convective terms in the energy equation. However, as shown by Cao & Faghri (1994a) their contribution is expected to be small. They also included the heat conduction in the fin and the envelope in their solution. The heat load is prescribed as an uniform heat flux at the external surface of the metalic envelope.

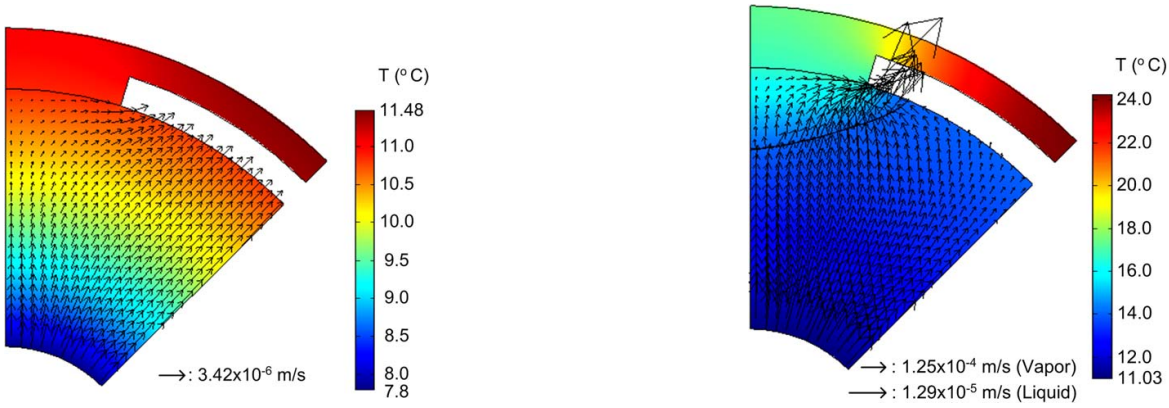

(a) (b)

Figure 1.14 – (a) Evaporation front at the outer surface of the wick and (b) within the porous wick, Kaya & Goldak (2006).

Kaya & Goldak (2006) formulation allows for stabilization of the evaporation front both at the surface as well as within the porous wick. Once the interface penetrates the wick, forming a vapor-saturated region underneath the fin, the authors consider that the pressure jump across the interface must be smaller than the capillary pressure and not exactly equal, as required by the thermodynamic equilibrium at the vapor-liquid interface. This violation is not justified.

Futhermore, the authors needed to specify a surface superheating at the fin-wick

interface necessary to create a vapor-saturated region underneath the fin. They assumed that once the surface temperature reaches 4 ^{o}C above the fluid saturation temperature at the liquid inlet pressure, a vapor region forms under the fin. It is noticed that this criterion is rather arbitrary, since it does not include the local pore size, which alters the local thermodynamic equilibrium, and it may change depending on fluid, fluid purity, surface roughness and assembling technique. This could be used as a resonable nucleation hypothesis only when a gap with size larger than the nucleation bubble diameter for the fin roughness characteristic size would exist separating the wick from the fin, which is clearly not the case for CPLs and LHPs.

Therefore, the results of Kaya & Goldak (2006) are not reliable regarding the threshold for formation of the vapor-saturated region. Once this region is formed, the results are an approximation for the front position, since the pressure jump has been neglected. One interesting result presented is the difference between the outer surface temperature and the saturation temperature in the vapor groove as a function of the applied heat flux. They modeled a stainless-steel casing with thermal conductivity of 14.5 W/m-K and thickness of 2 mm. The calculated temperature difference ranged from 3 to 28 ^{o}C for surface heat flux from $1,254$ to $7,528$ W/m^2.

Kaya & Goldak (2006) attempt to further analyze the occurance of the boiling limit, but this analysis is influenced by the hypothesis assumed. They conclude pointing out that keeping a good thermal contact between the fin and the wick is more beneficial than allowing for small gaps as suggested elsewhere (FIGUS *et al.*, 1999).

From the background discussed above, summarized in the table in Fig. 1.15, some authors assume that the evaporation front is located in the external surface of the wick (CAO; FAGHRI, 1994a, 1994b; KAYA; GOLDAK, 2006). This operation condition was verified experimentally by Li & Ochterbeck (1999), which mentioned also that, in normal operation, the evaporation seldom occurs within the wick. This hypothesis was assumed by Cao & Faghri (1994a, 1994b), but it was not tested theoretically. In both works, there is no information when the vapor invades the wick. In the problem studied by Kaya & Goldak (2006), the formulation allows the stabilization of the evaporation front both at the surface as well as within the porous wick. Once the interface penetrates the wick, they consider that the pressure jump across the interface must be smaller than the capillary pressure and not exactly equal and this violation is not justified. Besides, they assumed that once the surface temperature reaches 4 ^{o}C above the fluid saturation temperature at the liquid inlet pressure, a vapor region forms under the fin. This criterion is also rather arbitrary.

On the other hand some authors assume that the evaporation front is located within

the wick (DEMIDOV; YATSENKO, 1994; FIGUS *et al.*, 1999; TAKAHASHI, 2002). The modeling effort reported by Demidov & Yatsenko (1994) is plenty of physical insights, however they did not quantify the limits of heat load for their porous wick. Figus *et al.* (1999) assumed that evaporation front is immersed within the porous wick. Although Figus *et al.* (1999) did not correlate the threshold for the wick failure, they showed clearly the trend of the vapor invasion-percolation process. Takahashi (2002) assumed as Figus *et al.* (1999), that the evaporation front develops within the wick. The differences between his work and the previous analysis (FIGUS *et al.*, 1999) are the inclusion of the capillary pressure jump at the liquid-vapor interface, the modification in a boundary condition and a simplification in the geometry. He presented results regarding the location of the evaporation front for different heat fluxes.

So far, it is noticed that there is a lack of information regarding the limit of the evaporation front location, *i.e.*, what is the maximum heat flux that the wick can withstand before that the evaporation front passes from external surface to inside the wick. As mentioned before, the evaporation front can stablish a stable position within the wick, but this condition should be avoided. Thus, the model developed here allow to determine when the evaporation front invades the porous wick, unlike the criterion assumed by Kaya & Goldak (2006) (once the surface temperature reaches 4 ^{o}C above the fluid saturation temperature at the liquid inlet pressure, a vapor region forms under the fin). In the present model, a reliable criterion is assumed regarding the critical heat flux based on the maximum capillary pressure that the porous wick can withstand. In the present model, the boundary conditions assumed by Cao & Faghri (1994a, 1994b) are improved to match better with the expected physics of the problem.

Regarding the experimental tests, most LHPs and CPLs used porous wicks made of metal and ammonia as working fluid (which is considered the best fluid), as presented in the previous review. The few applications of ceramic wicks in LHPs and CPLs did not have success. Therefore, in lack of experiemental data regarding the successful application of ceramic wicks and the use of water as working fluid in LHPs and CPLs, in this work, an experimental study of the thermal behaviour of two LHPs and one CPL using water and acetone as working fluid is presented. The ceramic wick manufactured by Berti (2008) is proposed as an alternative to wicks made of metal and polymers for this application.

		Effective Properties					B.C. Liquid		B.C. Vapor		Fin	Wick Dimensions			
References	Material / Manufacturing / Working Fluid	ε	d, μm	K, m^2	λ_e, W/mK		p_l, Pa	T_l, °C	p_v, Pa	T_v, °C	T_f, °C	$L_z, \mu m$	$L_R, \mu m$	$L_{R'}, \mu m$	Observations
Cao and Faghri (1994a)	$h_{lv} = 0.2\times10^6$ J/kg				1 to 10			30				750	750	500	$q"=10000$ to 100000 W/m^2, mostly show the validity of analytical solution. There is no vapor breakthrough.
Cao and Faghri (1994b)	fluid: freon-11 ($h_{lv} = 0.17\times10^6$ J/kg), ammonia and water wick: $\lambda_s = 10$ W/mK	0.6	100	10^{-11}	$\lambda_{e,l} = 4.05$			30				750	750	500	$q"=15000$ to 30000 W/m^2, comparison between the two- and three-dimensional models for different working fluids. There is no vapor breakthrough.
Demidov and Yatsenko (1994)	wick: sintered metal copper fluid: approximates water	0.4 to 0.6	4 to 10	10^{-13}	25		0.8×10^5 to 1.0×10^5	80 to 95	1.0×10^5 to 1.2×10^5	100	105 to 150	200	200	70	Two limiting conditions: (i) $T_f = 107\ ^oC$, small vapor saturated region underneath the fin and a curved meniscus at the fin-wick contact line; (ii) $T_f = 124\ ^oC$, vapor-saturated region within the wick and evaporation in the external surface of the wick. There is no vapor breakthrough.
Figus et al. (1999)	fluid: ammonia $h_{lv} = 1.13\times10^6\ J/kg$ solid: ceramic or polymer material ($\lambda_s = 0.4$ W/mK)	0.4	$d_h \simeq 10$ (narrow)	10^{-13}	$\lambda_{e,l}$ 0.44	$\lambda_{e,v}$ 0.26	p_v - 40 = 1127	26	$p_{sat}(T_v)$ = 1167	30	30 to 91	5000 = 5 mm	5000 = 5 mm	2000 = 2 mm	Smooth front, vapor invaded wick at $q"=45000$ W/m^2 to $q"=90000$ W/m^2 stable operation.
	$\lambda_s = 10$ W/mK (broader)	0.44	$\frac{d_{max}}{d_{\min}} = 2$ ($\overline{d} = 10$)	3.2 to 3.4×10^{-13}	$\lambda_{e,l}$ 6.2	$\lambda_{e,v}$ 6.0	1127	10	1167	30	30 to 36	5000	5000	2000	$q"<10000$ W/m^2 vapor does not invade. $q">10000$ W/m^2 vapor region forms irregular interface from 15000 to 35000 W/m^2 the front is pinned. At 200000 W/m^2 there is vapor breakthrough.
Takahashi (2002)	fluid: ammonia $h_{lv} = 1.13\times10^6\ J/kg$ wick: sintered metal nickel	0.53	6	2 to 10×10^{-14}	$\lambda_{e,l}$ 5.6	$\lambda_{e,v}$ 3.3	728803	15			116	5000 = 5 mm	4500 = 4.5 mm	2500 = 2.5 mm	Maximum heat flux of 130613 W/m^2 for steady-state operation.
Kaya and Goldak (2006)	fluid: ammonia $h_{lv} = 1.22\times10^6\ J/kg$ wick: $\lambda_s = 14.5$ W/mK	0.6		4×10^{-14}	6.07		569538	7.8	569785	10.8		7240 = 7.24 mm	θ_{fin} = 67.5-90°	θ_{groove} = 45-67.5°	Stabilization of the evaporation front at the surface of wick with ($q"=1254$ W/m^2) and within the porous wick with ($q"=2508$ W/m^2 to $q"=7528$ W/m^2). When the liquid temperature underneath the fin is 4 °C higher than T_{sat} there is vapor breakthrough.

Figure 1.15 – Summary of the models.

1.5 Objective

The main objectives of this thesis are twofold. The first is the development of a mathematical model for the heat and mass transfer problem which occurs within the porous wick of evaporators of capillary pumping systems. This model allows to verify the effect of design variables, such as working fluids, dimensions, permeability, average pore radius and thermal conductivity of the wick, in the performance of the capillary evaporator and it allows for establishing a rigorous criterion for the wick dry-out limit. The second is the application of ceramic porous wick in capillary pumping systems such as LHPs and CPLs followed by the evaluation of their thermal behavior during the start up and at steady state conditions for different inclinations. Water and acetone are used as working fluids.

The thesis is divided into five chapters as follows:

1. Chapter 1 (Introduction) describes the operation of capillary pumping systems (LHPs and CPls). It also presents a literature survey about the recent experiments in CPL and LHP, the application of ceramic wick in CPLs and the recent mathematical models for heat and mass transfer in capillary evaporators.

2. Chapter 2 (Theoretical Analisys) deals with the formulation of the heat and mass transfer problem within porous wick of capillary evaporators. Two models are presented. One is solved analytically (Simplified Model) while the other is solved numerically (Improved Model). The solutions aim at verifying the effect of design variables, such as working fluids, dimensions, permeability, average pore radius and thermal conductivity of the wick, in the performance of the capillary evaporators and also in stablishing the criterion for dry-out.

3. Chapter 3 (Experiment) presents the manufacturing of the CPL and two LHPs. Two tests rigs, one at Laboratory of Combustion and Thermal Systems Engineering (LABCET) of UFSC in Brazil and the other at Institute of Nuclear Technology and Energy Systems (IKE) of Stuttgart University in Germany, were built.

4. Chapter 4 (Experimental Results and Analysis) presents the experimental study of the thermal behaviour of two LHPs and one CPL. Performance tests of two LHPs using acetone and water as working fluids were carried out for power inputs up to 25 W and performance tests of one CPL using water were carried out for power inputs up to 30 W. An analysis of the capillary limit of these systems based on their experimental results and a comparison between the theoretical and experimental results are also presented.

5. Chapter 5 (Conclusions and Recommendations for Future Work) presents the general conclusions as well as some suggestion for development of future works in modeling of heat and mass transfer in capillary evaporators and in the design of LHP and CPL systems.

2 Theoretical Analisys

This chapter presents the problem formulation of the heat and mass transfer within porous wick of capillary evaporators. For the modeling, the porous wick is a flat circular disc and is assembled between the liquid feeding channel and the vapor chamber. Figure 2.1 presents a rendering of the porous wick modeled. The upper part of the wick is heated by an external heat flux. The evaporation process that takes place in the wick of the capillary evaporator depends on the applied thermal load on the system and it is assumed that it may occur in three regimes: microfilm evaporation, evaporation at the external surface of the wick and evaporation within the wick.

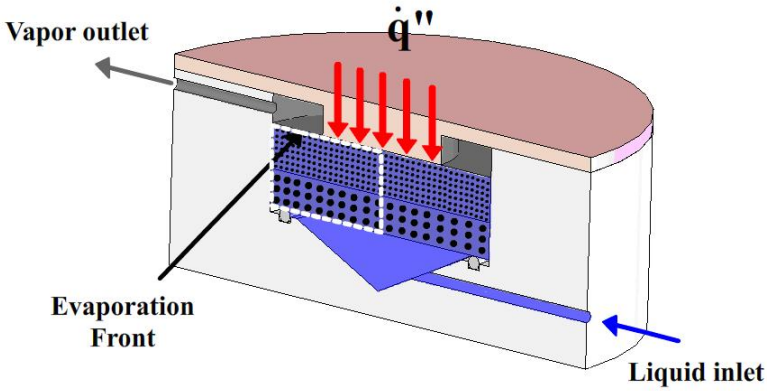

Figure 2.1 – Cross-section view of the flat capillary evaporator with cylindrical geometry.

Figure 2.2 presents a unit cell formed by a half of a single fin and the region of the porous wick bounded by the two symmetry surfaces. In Fig. 2.2(a), an external heat flux is supplied to the capillary evaporator and a liquid microfilm is formed between the external surface of the porous wick and the vapor grooves as modeled by Demidov & Yatsenko (1994). Since the inner surface temperature of the fin is higher than the liquid temperature, the liquid microfilm tends to dry out. After the microfilm dries out, the evaporation interface migrates to the external surface of the porous wick, as depicted in Fig. 2.2(b). If the thermal load continues increasing, a capillary pressure threshold is reached and the evaporation front moves to within the porous wick, as shown in Fig. 2.2(c). Here, only the evaporation regime in the external surface of the wick is studied. Following Li & Ochterbeck (1999), this is the safest operation condition.

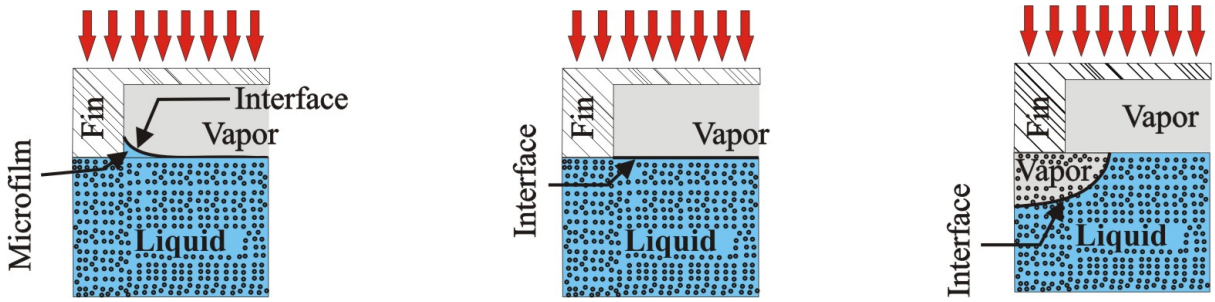

Figure 2.2 – (a) Microfilm evaporation (b) evaporation at the outer surface and (c) evaporation within the porous wick.

The models developed here will be used to simulate the heat and mass transfer within a wick with one and two layers with different thermophysical properties and working fluids. The mass and heat transfer problems are modeled by the volume averaged equations of energy and mass conservation. Further information concerning the the volume averaging method can be found in Appendix A.

Two models are developed. In the first model, the equations are analytically solved using the superposition and variable separation methods. This model is based on the model reported by Cao & Faghri (1994a). An analisys on the limitations of this model is presented. In the second model, the equations are numerically solved using the finite volume method. This second model allows to verify the effect of design variables, dimensions, permeability, average pore radius and thermal conductivity of the wick in the performance of the flat capillary evaporator. Furthermore, the second model also allows the test of the onset of drying underneath the fin, defining the limit for the operation of the capillary evaporator.

For both models, the equations of conservation of energy and mass in volume average were cast in cylindrical coordinates and the following assumptions were made:

- the process is steady state;
- the porous layers forming the wick are isotropic and homogeneous;
- there is a negligible influence of gravity;
- there are no heat transfer by radiation nor energy generation (besides the surface phase change);
- the solid phase is inert and stationary;
- the fluid (liquid and its vapor) is incompressible;

- the thermophysical properties are constant;
- the solid phase is in local thermal equilibrium with the liquid phase;
- there are no chemical reactions.

The volume averaged equation for the conservation of mass of liquid for incompressible fluid in cylindrical coordinates, becomes:

$$\frac{1}{r}\frac{\partial\left(r\,v_r\right)}{\partial r}+\frac{\partial v_z}{\partial z}=0 \tag{2.1}$$

Here, the volume averaged notation is omitted for simplicity. The formulation of the conservation of linear momentum equation depends on the flow velocity. It has been shown before (DEMIDOV; YATSENKO, 1994; CAO; FAGHRI, 1994b; FIGUS *et al.*, 1999) that the flow velocity in the application of interest here is small. The pore Reynolds number can be estimated and ranges from 4.0×10^{-5} to 4.0×10^{-4}. Therefore, macroscopic and microscopic (Forchheimer) inertia terms are negligible when compared to the microscopic viscous terms (KAVIANY, 1995). Also, since boundary effects penetrate distances that are of the order of a few particle diameters, the macroscopic (Brinkman) viscous term is also neglected. Finally, neglecting the influence of gravity, the r and z components of the equation for the conservation of linear momentum reduce to Darcy's Law, *i.e.*,

$$v_r=-\frac{K}{\mu}\frac{\partial p}{\partial r} \tag{2.2}$$

$$v_z=-\frac{K}{\mu}\frac{\partial p}{\partial z} \tag{2.3}$$

where K is the permeability and μ is the dynamic viscosity. Substituting the conservation of momentum equation in the conservation of mass equation, we obtain,

$$\frac{1}{r}\frac{\partial}{\partial r}\left(r\frac{K}{\mu}\frac{\partial p}{\partial r}\right)+\frac{\partial}{\partial z}\left(\frac{K}{\mu}\frac{\partial p}{\partial z}\right)=0 \tag{2.4}$$

which reduces to a Laplace equation for the pressure when the properties are assumed constant.

Since the fluid velocity is relativily small, the dispersion tensor can be neglected. Then, the total energy equation for liquid and solid phases is written as,

$$v_r\frac{\partial T}{\partial r}+v_z\frac{\partial T}{\partial z}=\frac{\lambda_e}{\rho_l c_{p,l}}\left[\frac{1}{r}\frac{\partial}{\partial r}\left(r\frac{\partial T}{\partial r}\right)+\frac{\partial^2 T}{\partial z^2}\right], \tag{2.5}$$

where λ_e is the effective thermal conductivity.

The boundary conditions will be presented in the context of the two models. The first, a simplified model, will employ a set of boundary conditions that allows an analytical solution. The second, a more comprehensive model, will require a numerical solution.

2.1 Simplified Model

In the current section, analytical solutions for the velocity and temperature fields within the porous wick of a flat capillary evaporator are presented. The model developed is based on the model reported by Cao & Faghri (1994a), but the properties of the porous wicks and the working fluids used are more realistic.

The calculation domain and the boundary conditions are represented schematically in Fig. 2.3. Due to the cylindrical symmetry of the evaporator, only a section represented by a dotted line in Fig.2.3(a) is modeled.

The boundary conditions for velocity and temperature are:

$$\text{At} \quad r = 0 \ \text{ and } \ r = R: \quad v_r = 0 \quad \text{and} \quad \frac{\partial T}{\partial r} = 0 \tag{2.6}$$

$$\text{At} \quad z = 0: \quad v_z = v_{z,in} \quad \text{and} \quad T = T_{in} \tag{2.7}$$

$$\text{At} \quad z = L_z \ \text{ and } \ 0 \leq r \leq R': \quad v_z = 0 \quad \text{and} \quad q_{in} = \lambda_e \frac{\partial T}{\partial z} \tag{2.8}$$

$$\text{At} \quad z = L_z \ \text{ and } \ R' \leq r \leq R: \quad v_z = v_{z,out} \ \text{ and } \ q_{out} = -\lambda_e \frac{\partial T}{\partial z}, \tag{2.9}$$

while q_{in} is given, q_{out} is unknown.

Following Cao & Faghri (1994a), the next parameters were used for the parametrization of the conservation equations:

$$r^+ = \frac{r}{R\mathrm{Re}\,\mathrm{Pr}}, \ \ z^+ = \frac{z}{R\mathrm{Re}\,\mathrm{Pr}}, \ \ v_z^+ = \frac{v_z}{v_{z,in}}, \ \ v_r^+ = \frac{v_r}{v_{z,in}}, \ \ T^+ = T - T_{in} \ \text{ and } \ p^+ = \frac{p}{\frac{R\mu v_{z,in}}{K}}$$

Substituting these parameters in Eqs. 2.1 to 2.5, we obtain:

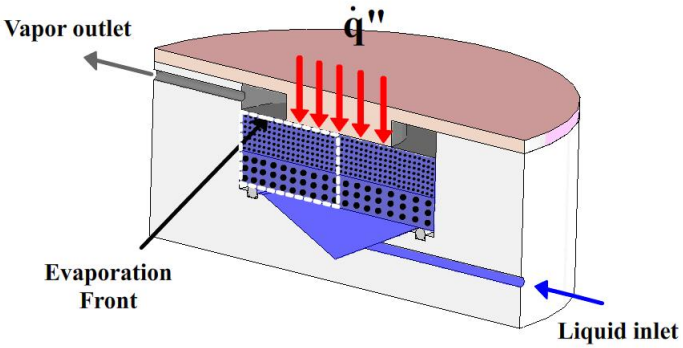

(a)

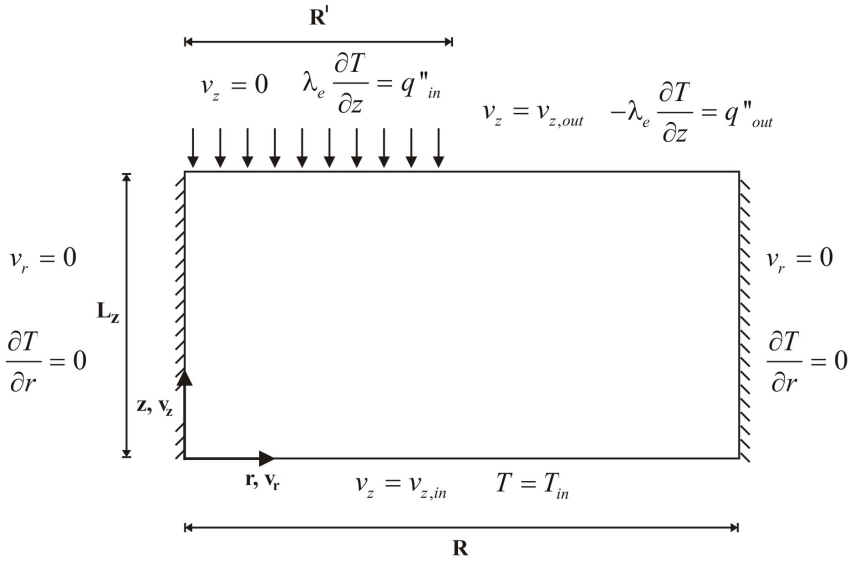

(b)

Figure 2.3 – (a) A cross section of the flat capillary evaporator with a bi-layered wick in the shape of a flat disc and (b) schematic diagram of the calculation domain and the boundary conditions.

$$\frac{\partial v_r^+}{\partial r^+} + \frac{v_r^+}{r^+} + \frac{\partial v_z^+}{\partial z^+} = 0 \tag{2.10}$$

$$v_r^+ = -\frac{1}{(\mathrm{Re}\,\mathrm{Pr})}\frac{\partial p^+}{\partial r^+} \tag{2.11}$$

$$v_z^+ = -\frac{1}{(\mathrm{Re}\,\mathrm{Pr})}\frac{\partial p^+}{\partial z^+} \tag{2.12}$$

$$\frac{\partial^2 p^+}{\partial r^{2+}} + \frac{1}{r^+}\frac{\partial p^+}{\partial r^+} + \frac{\partial^2 p^+}{\partial z^{2+}} = 0 \tag{2.13}$$

$$(\mathrm{Re}\,\mathrm{Pr})^2\left(v_r^+\frac{\partial T^+}{\partial r^+} + v_z^+\frac{\partial T^+}{\partial z^+}\right) = \frac{1}{r^+}\frac{\partial T^+}{\partial r^+} + \frac{\partial^2 T^+}{\partial r^{+2}} + \frac{\partial^2 T^+}{\partial z^{+2}} \tag{2.14}$$

for which the boundary conditions become:

$$\text{At} \quad r^+ = 0 \quad \text{and} \quad r^+ = R^+ : \quad v_r^+ = 0 \quad \text{and} \quad \frac{\partial T^+}{\partial r^+} = 0 \tag{2.15}$$

$$\text{At} \quad z^+ = 0 : \quad v_z^+ = v_{z,in}^+ \quad \text{and} \quad T^+ = 0 \tag{2.16}$$

$$\text{At} \quad z^+ = L_z^+ \quad \text{and} \quad 0 \leq r^+ \leq R'^+ : \quad v_z^+ = 0 \quad \text{and} \quad \frac{\partial T^+}{\partial z^+} = \frac{R\text{Re}\,\text{Pr}\,q_{in}}{\lambda_e} \tag{2.17}$$

$$\text{At} \quad z^+ = L_z^+ \quad \text{and} \quad R'^+ \leq r^+ \leq R^+ : \quad v_z^+ = v_{z,out}^+ \quad \text{and} \quad \frac{\partial T^+}{\partial z^+} = -\frac{R\text{Re}\,\text{Pr}\,q_{out}}{\lambda_e} \tag{2.18}$$

2.1.1 Analytical Solution for the Flow

The equation for the determination of the pressure field in the wick and its respective boundary conditions are repeated here for clarity:

$$\frac{\partial^2 p^+}{\partial r^{2+}} + \frac{1}{r^+}\frac{\partial p^+}{\partial r^+} + \frac{\partial^2 p^+}{\partial z^{2+}} = 0 \tag{2.19}$$

$$\text{At} \quad r^+ = 0 \quad \text{and} \quad r^+ = R^+ : \quad \frac{\partial p^+}{\partial r^+} = 0 \tag{2.20}$$

$$\text{At} \quad z^+ = 0 : \quad \frac{\partial p^+}{\partial z^+} = -\left(\text{Re}\,\text{Pr}\right) v_{z,in}^+ \tag{2.21}$$

$$\text{At} \quad z^+ = L_z^+ \quad \text{and} \quad 0 \leq r^+ \leq R'^+ : \quad \frac{\partial p^+}{\partial z^+} = 0 \tag{2.22}$$

$$\text{At} \quad z^+ = L_z^+ \quad \text{and} \quad R'^+ \leq r^+ \leq R^+ : \quad \frac{\partial p^+}{\partial z^+} = -\left(\text{Re}\,\text{Pr}\right) v_{z,out}^+ \tag{2.23}$$

In this model, it is assumed that the velocity distributions at inlet $v_{z,in}$ and outlet $v_{z,out}$ are known and uniforms. The problem is linear and the boundary conditions suggest the use of the method of separation of variables (ARPACI, 1966). Since the governing equation and boundary conditions are linear, the problem is subdivided into two simpler problems, according to Fig. 2.4.

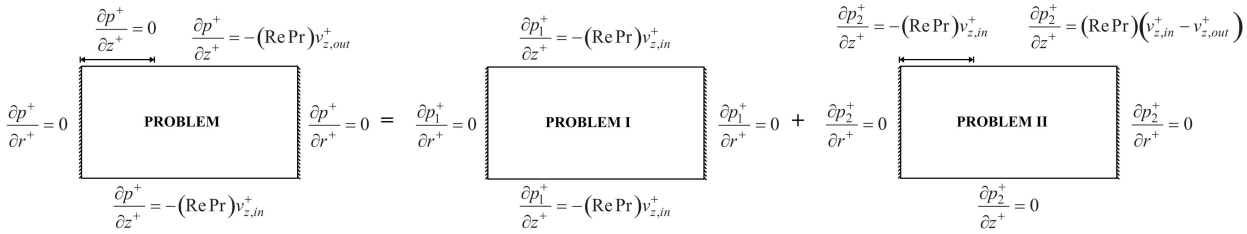

Figure 2.4 – Schematic subdivision of the general problem of the flowing into the wick.

The general solution of the problem is given by the sum of solutions of problems I and II:

$$p^+ = p_1^+ + p_2^+ \rightarrow \nabla^2 p^+ = 0 \rightarrow \nabla^2 p_1^+ = 0 \text{ and } \nabla^2 p_2^+ = 0 \tag{2.24}$$

Problem I:

$$\frac{\partial^2 p_1^+}{\partial r^{2+}} + \frac{1}{r^+}\frac{\partial p_1^+}{\partial r^+} + \frac{\partial^2 p_1^+}{\partial z^{2+}} = 0 \tag{2.25}$$

$$\frac{\partial p_1^+}{\partial r^+} = 0, \quad \left(r^+ = 0 \text{ and } r^+ = R^+\right) \tag{2.26}$$

$$\frac{\partial p_1^+}{\partial z^+} = -\left(\mathrm{Re}\,\mathrm{Pr}\right) v_{z,in}^+, \quad \left(z^+ = 0\right) \tag{2.27}$$

$$\frac{\partial p_1^+}{\partial z^+} = -\left(\mathrm{Re}\,\mathrm{Pr}\right) v_{z,in}^+, \quad \left(z^+ = L_z^+ \text{ and } 0 < r^+ \leq R^+\right) \tag{2.28}$$

An arbitrary solution was admitted for the Problem I that satisfies the general equation and all the boundary conditions:

$$p_1^+ = p_0^+ - \left(\mathrm{Re}\,\mathrm{Pr}\right) v_{z,in}^+ z^+ \tag{2.29}$$

where p_0^+ is a constant.

Problem II:

$$\frac{\partial^2 p_2^+}{\partial r^{2+}} + \frac{1}{r^+}\frac{\partial p_2^+}{\partial r^+} + \frac{\partial^2 p_2^+}{\partial z^{2+}} = 0 \tag{2.30}$$

$$\frac{\partial p_2^+}{\partial r^+} = 0, \quad \left(r^+ = 0 \text{ and } r^+ = R^+\right) \tag{2.31}$$

$$\frac{\partial p_2^+}{\partial z^+} = 0, \quad \left(z^+ = 0\right) \tag{2.32}$$

$$\frac{\partial p_2^+}{\partial z^+} = -\left(\mathrm{Re}\,\mathrm{Pr}\right) v_{z,in}^+, \quad \left(z^+ = L_z^+ \;\text{ and }\; 0 < r^+ \leq R'^+\right) \tag{2.33}$$

$$\frac{\partial p_2^+}{\partial z^+} = \left(\mathrm{Re}\,\mathrm{Pr}\right)\left(v_{z,in}^+ - v_{z,out}^+\right), \quad \left(z^+ = L_z^+ \;\text{ and }\; R'^+ < r^+ \leq R^+\right) \tag{2.34}$$

Problem II is solved by the method of separation of variables. The general solution for the pressure field in the wick, by the sum of the solutions of Problems I and II, is given by:

$$p^+\left(r^+, z^+\right) = p_0^+ - \left(\mathrm{Re}\,\mathrm{Pr}\right) v_{z,in}^+ z^+$$

$$+\sum_{n=1}^{\infty}\left[\frac{2\left(\mathrm{Re}\,\mathrm{Pr}\right) v_{z,out}^+ R'^+ + J_1\left(\frac{R'^+\alpha_n}{R^+}\right)}{\alpha_n^2 \mathrm{sinh}\left(\frac{\alpha_n}{R^+}L_z^+\right) J_0\left(\alpha_n\right)^2}\right] J_0\left(\frac{\alpha_n}{R^+}r^+\right)\cosh\left(\frac{\alpha_n}{R^+}z^+\right) \tag{2.35}$$

where the eigenvalues (α_n) are the roots of the Bessel function J_1. Returning to the originals variables, the solution for the pressure field is:

$$p\left(r,z\right) = p_{in} - \frac{\mu}{K}v_{z,in}\, z + \sum_{n=1}^{\infty}\left[\frac{2\mu v_{z,out} R' J_1\left(\frac{R'\alpha_n}{R}\right)}{K\alpha_n^2 \mathrm{sinh}\left(\frac{\alpha_n}{R}L_z\right) J_0\left(\alpha_n\right)^2}\right] J_0\left(\frac{\alpha_n}{R}r\right)\cosh\left(\frac{\alpha_n}{R}z\right) \tag{2.36}$$

From Darcy's Law, the velocity fields are given by the following expressions:

$$v_r = \sum_{n=1}^{\infty}\left[\frac{2v_{z,out} R' J_1\left(\frac{R'\alpha_n}{R}\right)}{\alpha_n R \mathrm{sinh}\left(\frac{\alpha_n}{R}L_z\right) J_0\left(\alpha_n\right)^2}\right] J_1\left(\frac{\alpha_n}{R}r\right)\cosh\left(\frac{\alpha_n}{R}z\right) \tag{2.37}$$

$$v_z = v_{z,in} - \sum_{n=1}^{\infty}\left[\frac{2v_{z,out} R' J_1\left(\frac{R'\alpha_n}{R}\right)}{\alpha_n R \mathrm{sinh}\left(\frac{\alpha_n}{R}L_z\right) J_0\left(\alpha_n\right)^2}\right] J_0\left(\frac{\alpha_n}{R}r\right)\sinh\left(\frac{\alpha_n}{R}z\right) \tag{2.38}$$

It is noticed that ($v_{z,in}$) and ($v_{z,out}$) still need to be determined, as it will be shown below.

2.1.2 Analytical Solution for the Thermal Problem

For the solution of the thermal problem, q_{in} is known and q_{out} is calculated. The Peclet number relates the convective and diffusive effects, and it can be written as:

$$Pe = \mathrm{Re}\,\mathrm{Pr} = \frac{v_{z,in}R^{'}}{\alpha_e}, \quad \text{where } \alpha_e = \frac{\lambda_e}{\rho_l c_{p,l}} \tag{2.39}$$

In order to evaluate the Peclet number, it is necessary to know the value of $v_{z,in}$. For that, a mass and energy balance is applied in the wick. From this balance represented in Fig.2.5, the following expressions are obtained.

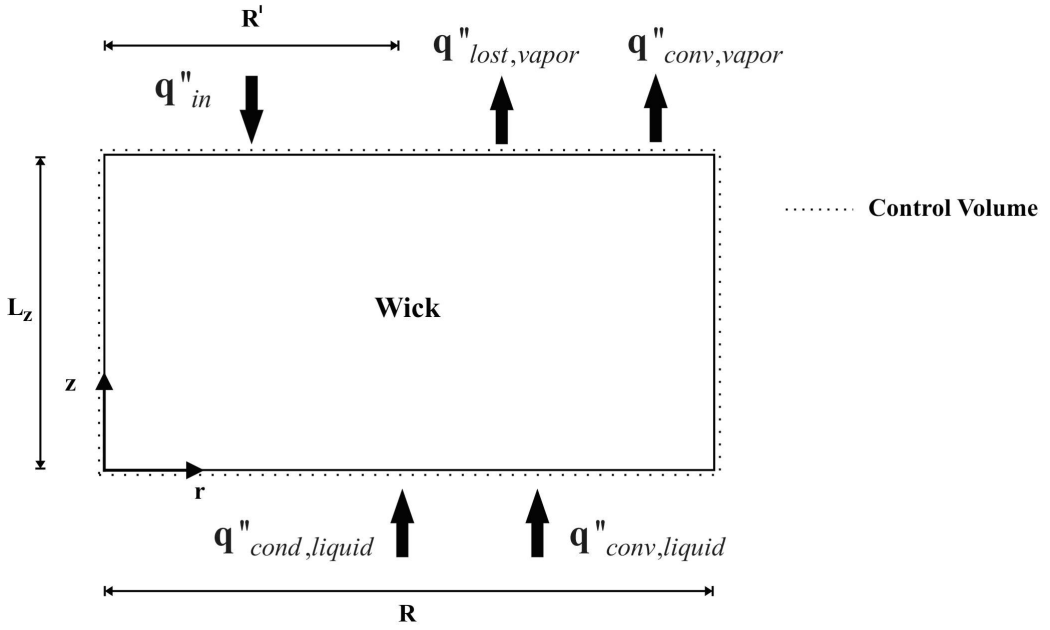

Figure 2.5 – Energy balance within the porous wick.

Energy balance:

$$q_{in}A_{in,fin} + \left[\left(-\lambda_e \left.\frac{\partial T}{\partial z}\right|_{z=0}\right) + \rho_l v_{z,in} h_{l,in}\right] A_{in,l} = \left[q_{lost,vapor} + \rho_l v_{z,out} h_{v,out}\right] A_{out,vapor} \tag{2.40}$$

Mass Balance:

$$\rho_l v_{z,in} A_{in,l} = \rho_l v_{z,out} A_{out,vapor} = \dot{m}_{lv} \tag{2.41}$$

Substituting Eq. 2.41 in 2.40, we obtain,

$$q_{in}A_{in,fin} - \lambda_e \left.\frac{\partial T}{\partial z}\right|_{z=0} A_{in,l} = q_{lost,vapor}A_{out,vapor} + \dot{m}_{lv}\left[\Delta h_{lv} + c_{p,l}\left(T_{v,out} - T_{l,in}\right)\right] \quad (2.42)$$

Assuming that $q_{lost,vapor} = 0$, $-\lambda_e \left.\frac{\partial T}{\partial z}\right|_{z=0} A_{in,l} \ll \dot{m}_{lv}\Delta h_{lv}$ and neglecting the sensible heat, Eq. 2.42 becomes,

$$q_{in}A_{in,fin} \cong \dot{m}_{lv}\Delta h_{lv} \quad (2.43)$$

Assuming the inlet velocity of the liquid is distributed uniformly, we obtain,

$$v_{z,in} \cong \frac{q_{in}A_{in,fin}}{\rho_l \Delta h_{lv} A_{in,l}} \quad (2.44)$$

The velocity and heat flux at the outlet are calculated by the following expressions:

$$q_{in}A_{in,fin} = q_{out}A_{out,vapor} \rightarrow q_{out} = \frac{q_{in}A_{in,fin}}{A_{out,vapor}} \quad (2.45)$$

$$\rho_l v_{z,in}A_{in,l} = \rho_l v_{z,out}A_{out,vapor} \rightarrow v_{z,out} = \frac{v_{z,in}A_{in,l}}{A_{out,vapor}} \quad (2.46)$$

Using Eq. 2.44 to estimate $v_{z,in}$, the Peclet number ($RePr$) is estimated to be of the order of 10^{-1} to 10^{-2} for the inlet heat flux from 10^3 to 10^5 W/m^2 (working fluid is water at the saturation temperature of 50 °C). Therefore, for this range of heat flux, the convective terms in Eq. 2.14 can be neglected. With this approximation, the energy equation is reduced to the Laplace equation,

$$\frac{1}{r^+}\frac{\partial T^+}{\partial r^+} + \frac{\partial^2 T^+}{\partial r^{+2}} + \frac{\partial^2 T^+}{\partial z^{+2}} = 0 \quad (2.47)$$

Using the method of separation of variables, the solution of Eq. 2.47 subjected to the boundary conditions in Eqs. 2.15 to 2.18 is:

$$T^+\left(r^+, z^+\right) = \sum_{m=1}^{\infty} \frac{2R\left(q_{in} + q_{out}\right) J_1\left(\frac{\gamma_m R'^+}{R^+}\right) J_0\left(\frac{\gamma_m}{R^+}r^+\right) sinh\left(\frac{\gamma_m}{R^+}z^+\right)}{\gamma_m^2 \lambda_e sinh\left(\frac{\gamma_m}{R^+}L_z^+\right)\left[J_0\left(\gamma_m\right)\right]^2} \quad (2.48)$$

Finally, returning to the original variables, the solution for the temperature field is:

$$T(r,z) = \sum_{m=1}^{\infty} \frac{2R\left(q_{in}+q_{out}\right) J_1\left(\frac{\gamma_m R'}{R}\right) J_0\left(\frac{\gamma_m}{R}r\right) sinh\left(\frac{\gamma_m}{R}z\right)}{\gamma_m^2 \lambda_e sinh\left(\frac{\gamma_m}{R}L_z\right)\left[J_0\left(\gamma_m\right)\right]^2} + T_{in} \tag{2.49}$$

The application of the solution above follows. First, the properties of the working fluid, the dimensions of the wick and the inlet flux are supplied. Then, the inlet velocity is calculated from Eq. 2.44, the heat flux at the outlet is calculated from Eq. 2.45 and the outlet velocity is calculated from Eq. 2.46. Subsequently, these results are substituted in Eqs. 2.36, 2.37, 2.38 and 2.49 for the calculation of the pressure, velocity components in directions r and z and temperature fields, respectively. The equations are solved using Maple 10 and the properties are obtained from EES (Engineering Equation Solver).

2.1.3 Results and Discussion

Results are presented here for two working fluids, water and acetone, and for three porous wicks, stainless steel, nickel and ceramic. The properties of the wick and the working fluids are presented in Tables 2.1 and 2.2, respectively. The effective thermal conductivity for porous wick saturated with liquid (λ_e) was calculated using the correlation reported by Hadley (1986),

$$\frac{\lambda_e}{\lambda_l} = (1-\alpha_o)\frac{\varepsilon_l f_o + \frac{\lambda_s}{\lambda_l}\left(1-\varepsilon_l f_o\right)}{1-\varepsilon_l\ \left(1-f_o\right)+\frac{\lambda_s}{\lambda_l}\varepsilon_l\ \left(1-f_o\right)} + \alpha_o \frac{2\left(\frac{\lambda_s}{\lambda_l}\right)^2\left(1-\varepsilon_l\right)+\left(1-2\varepsilon_l\right)\frac{\lambda_s}{\lambda_l}}{\left(2+\varepsilon_l\right)\frac{\lambda_s}{\lambda_l}+1-\varepsilon_l}$$

where $f_o = 0,8$ and $log\,\alpha_{\,o} = -1,084 - 6,778\,(\varepsilon - 0,298)$. The α_o is valid in the range of $0.298 \leq \varepsilon\ \leq 0.580$.

Table 2.1 – Wick properties.

Wick	ε (%)	K (m^2)	$\lambda_{e,water}$ (W/mK)	$\lambda_{e,acetone}$ (W/mK)	r_p (μ m)
Nickel*	0.50	86×10^{-15}	6.27	4.02	1.0
Stainless steel*	0.41	53×10^{-15}	2.94	1.34	2.5
Ceramic*	0.52	35×10^{-15}	2.87	1.30	1.1

* The wick properties were obtained from Reimbrecht (2004).

Figure 2.6 presents isobaric lines and velocity vector for the flow within the wick for an inlet heat flux of 2.0×10^4 W/m^2 and $p_{in} = 4260$ Pa, for water and a ceramic wick. This

Table 2.2 – Properties of working fluids.

Working Fluid	σ_l (N/m)	h_{lv} (kJ/kg)	$c_{p,l}$ (kJ/kg-K)	ρ_l (kg/m^3)	λ_l (W/mK)	μ_l (kg/ms)
Water*	0.07119	2382	4.183	995.6	0.6178	0.0007977
Acetone**	0.02250	544	2.161	779.0	0.175	0.0002960

* The properties of the working fluids were obtained by the software Engineering Equation Solver (EES) and ** from Peterson (1994) at $T_{sat} = 40$ ^{o}C.

magnitude of heat flux and pressure are typical of applications. The dimensions of the wick are: $R = 15$ mm, $R^{'} = 7.5$ mm, $L_z = 10$ mm. The velocity vectors, always perpendicular to the isobaric lines, remain pointed upwards until the middle of the structure, where they begin to change the direction toward the outlet of the wick due to the impermeability of the metallic fin.

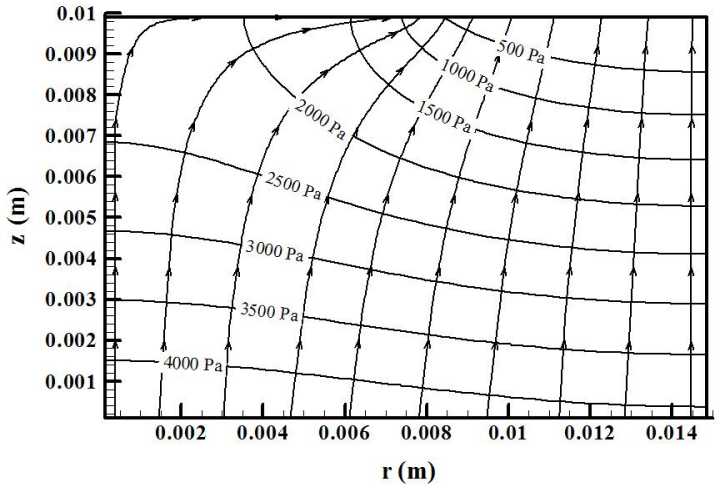

Figure 2.6 – Velocity vectors and isobaric lines in the wick for an inlet heat flux of 2.0×10^4 W/m^2.

Figure 2.7 presents the isothermal and heat flux lines for an inlet heat flux of 2.0×10^4 W/m^2. Note that most of the heat flows to the outlet where evaporation takes place, while the remaining heat flows right to the feeding liquid channel. Note also that there is heat flux from the liquid feeding channel to the vapor channel. This is a limitation of the model which is due to the boundary conditions assumed for solving it. This limitation will be explored further later on in this section.

Figures 2.8 presents the temperature profiles at $z = L_z$ (surface at the vapor channel) for the three types of wicks saturated with water and acetone, for an inlet heat flux of 2.0×10^4 W/m^2. The results for water are shown in Fig. 2.8(a) and for acetone in Fig. 2.8(b) for different solid phases. It is noticed that the smaller the thermal conductivity of the wick, the higher the temperature in the area underneath the fin. This happens

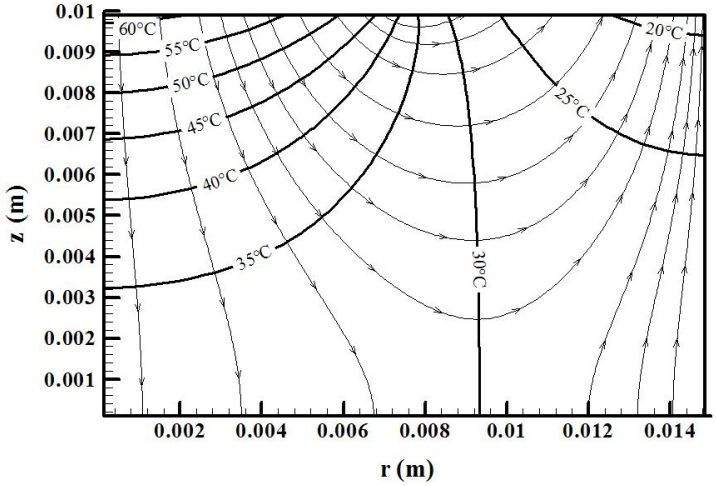

Figure 2.7 – Isotherm lines and heat streamlines for an inlet heat flux of 2.0×10^4 W/m^2.

due to the increase in the heat transfer resistance of the porous structure. This larger temperature can cause the formation of vapor bubbles in the area underneath the fin, causing a possible failure by dryout. Later, a criterion for dryout will be stablished.

Figure 2.9 presents the heat fluxes at $z = 0$ for different thickness (L_z) and radius of the fin ($R^{'}$). For these results, an inlet heat flux of 2.0×10^4 W/m^2, water as a working fluid and a ceramic wick were used. It is noticed that the larger the thickness of the wick, the smaller the heat flux to the liquid channel. Note that here the temperature at the channel has been kept uniform at T_{in}. For lager heat flux there would be a superheating of this surface which could lead to boiling. The onset of the boiling limit in the channel will not be analyzed in this work.

The negative values of the heat fluxes, presented in Fig. 2.9 for $0 \leq r \leq 9$ mm, indicate that there is a heat transfer from the porous wick to the liquid feeding channel. However these values become positive for $r > 9$ mm. This indicates that there is a heat transfer from the liquid feeding channel to the porous wick. This heat transfer is evident in Fig. 2.10(a), in which it is shown that the inlet temperature is larger than the outlet temperature in the vapor outlet of the porous wick for $r > 9$ mm (hatched area). Figures 2.10(a) and (b) were produced using the same conditions as in Figs. 2.9(a) and (b). Figure 2.10(b) shows the heat fluxes lines from the liquid feeding channel to the vapor outlet. Since the fin is the only source of heat in the system, this condition does not represent the physics of the problem and it limits the model for a practical application. This is going to be improved in the following model.

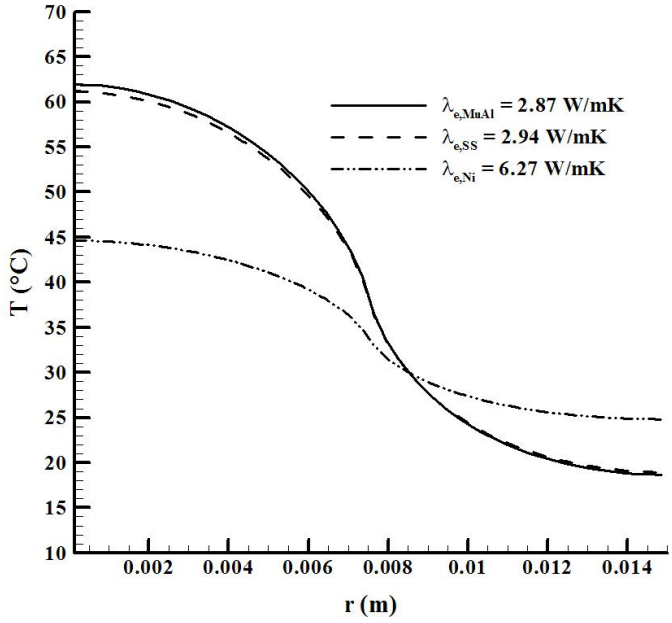

(a)

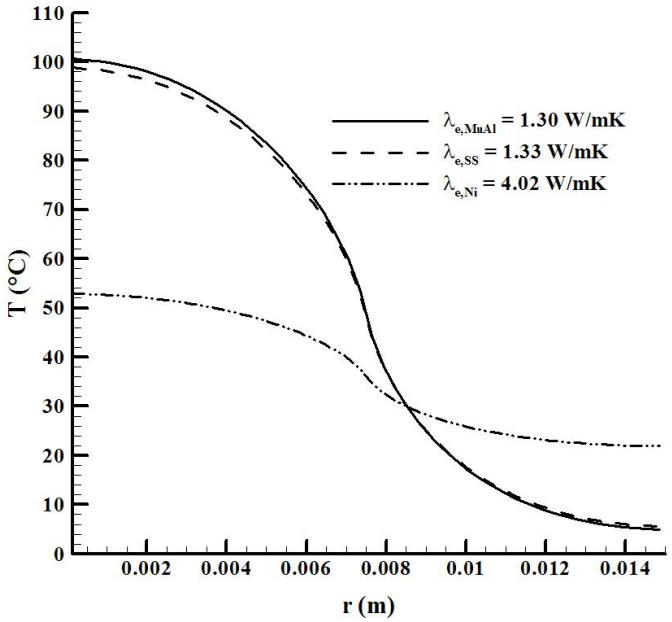

(b)

Figure 2.8 – Temperature profiles at $z = L_z$ for different wicks using (a) water and (b) acetone for an inlet heat flux of 2.0×10^4 W/m^2.

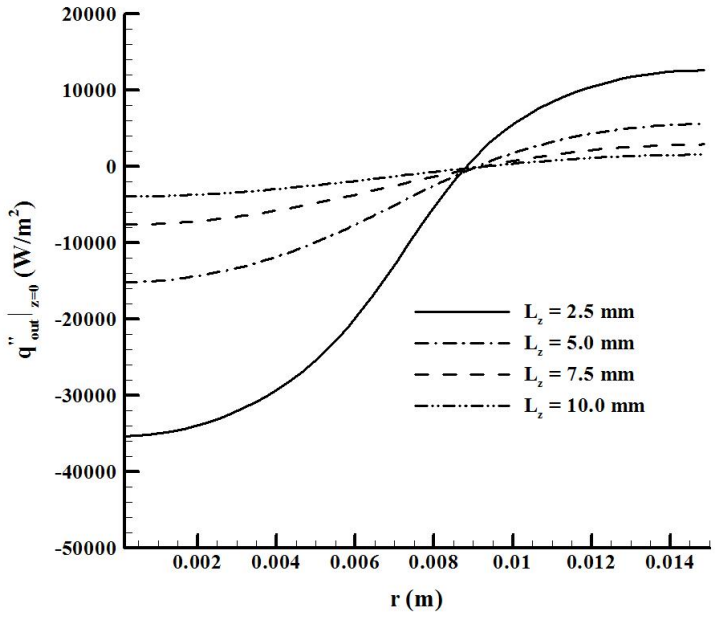

(a)

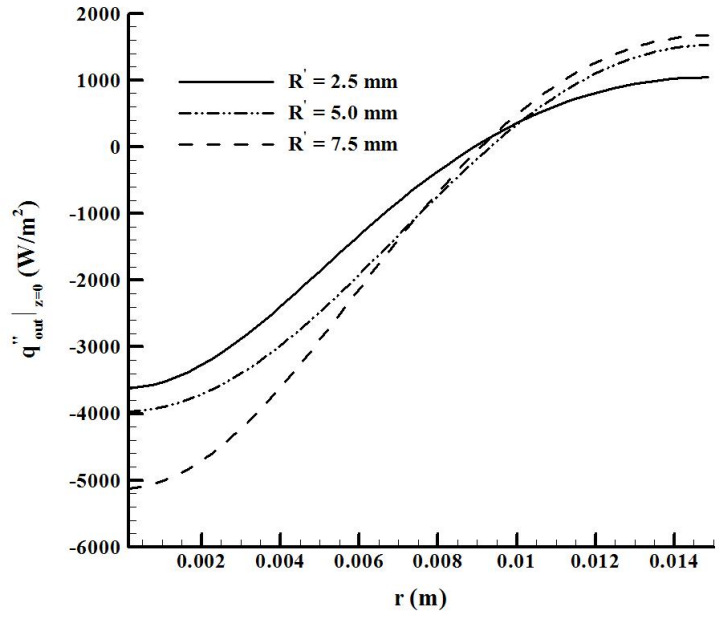

(b)

Figure 2.9 – Heat fluxes at $z = 0$, for (a) different thicknesses of the wick (L_z) and (b) different radii of the fin ($R^{'}$).

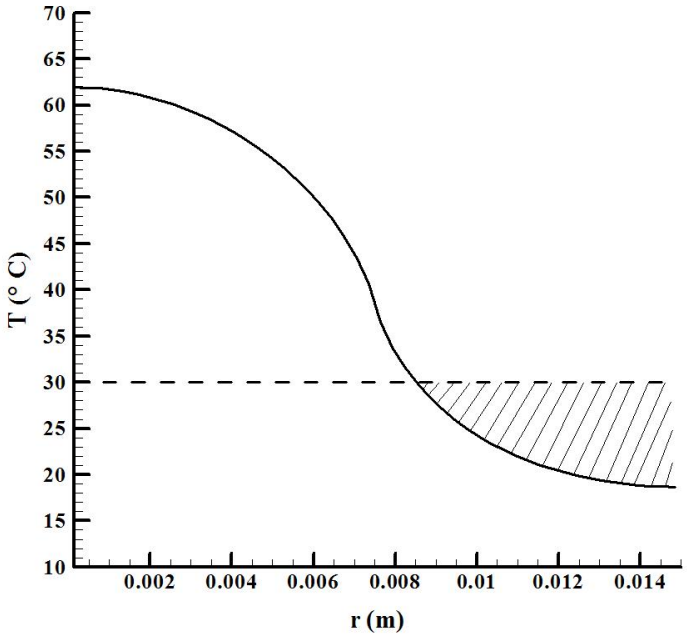

(a)

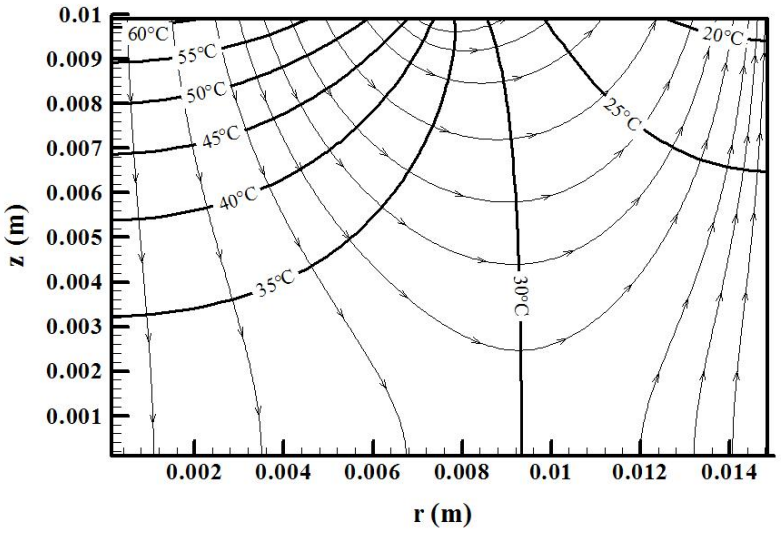

(b)

Figure 2.10 – (a) Temperatures at $z = 0$ and $z = L_z$ and (b) isotherm lines and heat streamlines for an inlet heat flux of 2.0×10^4 W/m^2.

2.1.4 Conclusion

The model developed here allowed to verify the effect of design variables in the performance of a capillary evaporator. The analysis of the different types of wicks, working fluids and the variation of some geometric parameters provided important information such as: the decrease of the wick thickness increased the capillary limit, however increased both the temperature in the area close to the fin and the heat flux to the feeding liquid channel. Also, as expected, it was noticed that the smaller the thermal conductivity of the wick, the greater the temperatures in the area underneath the fin.

Therefore, from the variation of the parameters, thickness and thermal conductivity, we can conclude that for a proper design of a capillary evaporator one must determine:

1. an optimum thickness and a high permeability so that the heat flux to the feeding liquid channel is minimized and the pressure losses remain low;

2. a porous material with optimum thermal conductivity so that the temperature in the area underneath the fin is minimized. While, at the same time, the temperature in the surface of the liquid channel is also limited. This contradictory need was also observed by Figus *et al.* (1999) that recomended the use of a double layered porous wick.

This model allows no conclusions regarding the attainment of a capillary limit and the boundary conditions should be improved to match better with the expected physics of the problem. It is expected that:

1. the outlet velocity field is not uniform but it must result in higher velocities closer to the fin;

2. the liquid channel surface temperature must be smaller than the vapor temperature.

For this improvement, the model proposed in the next section is solved numerically, due to the nonlinearities that will appear. With this improved model, it is possible to simulate the heat and mass transfer within the wick with more than one layer with different thermophysical properties. This improved model will also provide a condition for dryout.

2.2 Improved Model

This section presents an extension of the model developed in the previous section. Here, a numerical evaluation of heat and mass transfer in the porous wick of a flat capillary

evaporator is presented. The model was used to simulate the heat and mass transfer within a wick with two layers with different thermophysical properties. The model allows to verify the effect of design variables, dimensions, permeability, average pore radius and thermal conductivity of the wick in the performance of the flat capillary evaporator. Furthermore, the model allows the test of the onset of drying underneath the fin, defining the limit for the application of the model which considers the wick fully saturated with liquid.

The problem domain and the boundary conditions are represented schematically in Fig. 2.11. Due to the cylindrical symmetry of the evaporator, only the section represented by a dotted line in Fig.2.3 (a) is modeled.

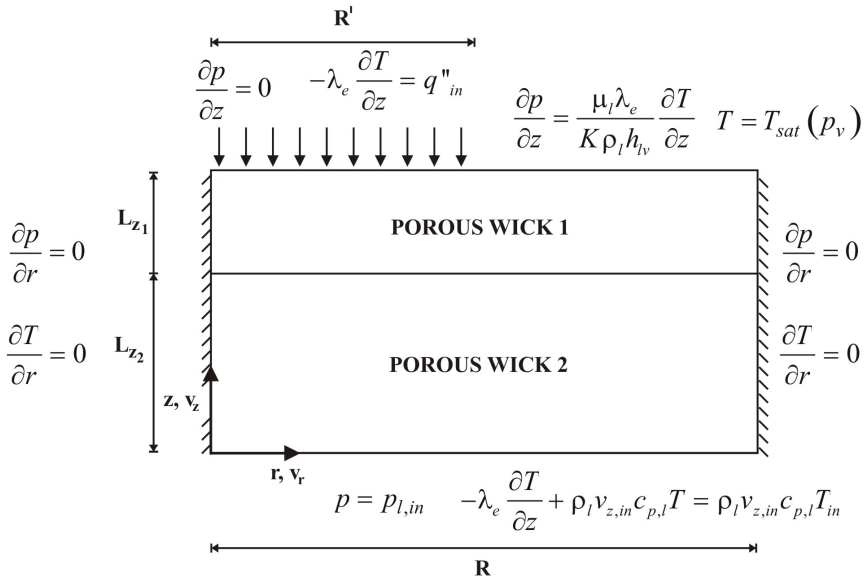

Figure 2.11 – Schematic diagram of the problem domain and the boundary conditions.

In the volume-averaged equation and assuming local thermal equilibrium between the liquid and solid phases, λ_e is the effective thermal conductivity of fully liquid saturated porous medium. For constant property, isotropic media, the conservation of thermal energy equation reduces to a Laplace equation for the temperature. Following the system of coordinates (r,z) depicted in Fig. 2.11, the boundary conditions are as follows.

At the surface at $r = 0$, cylindrical symmetry requires that:

$$\frac{\partial p}{\partial r} = 0 \quad \text{and} \quad \frac{\partial T}{\partial r} = 0 \tag{2.50}$$

At the surface at $r = R$ the boundary is assumed impermeable to liquid flow and adiabatic. Then,

$$\frac{\partial p}{\partial r} = 0 \quad \text{and} \quad \frac{\partial T}{\partial r} = 0 \tag{2.51}$$

At the inlet surface at $z = 0$, the porous wick is fed with a liquid flow with far end temperature $T_{l,in}$, *i.e.*,

$$p = p_{l,in} \text{ and } -\lambda_e \frac{\partial T}{\partial z} + \rho_l v_{z,in} c_p T = \rho_l v_{z,in} c_p T_{l,in} \tag{2.52}$$

This temperature boundary condition reflects the continuity of the total normal component of the heat flux vector. Finally, at the outlet surface, two regions are observed. First, underneath the metallic fin ($z = L_z$ and $0 \leq r \leq R'$),

$$\frac{\partial p}{\partial z} = 0 \quad \text{and} \quad -\lambda_e \frac{\partial T}{\partial z} = q_{in} \tag{2.53}$$

Second, considering the evaporation at the outlet surface, assuming that the pore size is not extremely small, *i.e.*, this is not a hygroscopic porous medium, from Kelvin's Law, the surface temperature is approximately equal to the vapor saturation temperature in the bulk of the vapor channel. Also, the conduction heat transfer from the fin is responsible for the liquid evaporation. Therefore, we have,

$$\frac{\partial p}{\partial z} = \frac{\mu \lambda_e}{K \rho_l h_{lv}} \frac{\partial T}{\partial z} \quad \text{and} \quad T = T_{sat}\left(p_v\right) \tag{2.54}$$

This set of boundary conditions closes the formulation. The pressure difference ($p_v - p_{l,in}$) corresponds to the total pressure loss of the CPL components. In all stable operation points, this pressure difference balances exactly the capillary pressure difference across the medium. The total heat transfer rate at the fin is responsible for the liquid evaporation at the outlet surface and part of it flows to the liquid channel. A total energy balance in the wick provides:

$$Q_{in} = Q_{out,l} + Q_{lv}$$

where Q_{in} is the heat transfer rate at the fin surface,

$$Q_{in} = q_{in} A_{in}$$

The heat transfer rate to the liquid channel $Q_{out,l}$, following Eq. 2.52, is given by,

$$Q_{out,l} = \int_0^R \left(\lambda_e \frac{\partial T}{\partial z}\right) r dr, \quad at \;\; z = 0.$$

This heat transfer is responsible for raising the incoming flow temperature from the

far end value T_{in} to the porous wick surface value $T(z=0)$. Then, the heat transfer rate actually used for the liquid evaporation is,

$$Q_{lv} = \int_{R'}^{R} \left(-\lambda_e \frac{\partial T}{\partial z}\right) r dr, \text{ at } z = L_z.$$

Note that the total liquid mass flow rate is,

$$\dot{m}_{lv} = \left[\int_{R'}^{R} \left(-\frac{K}{\mu}\frac{\partial p}{\partial z}\rho_l\right) r dr\right]_{z=L_z}$$

or

$$\dot{m}_{lv} = \left[\int_{0}^{R} \left(-\frac{K}{\mu}\frac{\partial p}{\partial z}\rho_l\right) r dr\right]_{z=0} \tag{2.55}$$

When $Q_{out,l}$ is large, the liquid in the channel can reach the onset of nucleate boiling which is called a boiling limit for the CPL operation. In the evaporation front (liquid-vapor interface), located in the external surface of the wick, the pressure difference between the phases liquid and vapor is the capillary pressure, which in its turn, can be expressed by the Young-Laplace's equation ($\Delta p_{cap} = p_v - p_l = \frac{2\sigma\cos\theta}{r}$). For an averaged pore radius r_p, the capillary pressure becomes maximum when the contact angle between the liquid and the solid approaches zero, in other words, when the wettability of the working fluid is maximum. Since the objective here is to explore the maximum pumping capacity, the contact angle is considered equal to zero. At the evaporation interface, the capillary pressure is defined by the liquid and vapor pressure. Then, the average radius of curvature of the liquid-vapor interface adjusts itself in order to balance this capillary pressure, as predicted by Young-Laplace's equation above. The minimum possible radius of curvature before drying of the pore is the characteristic radius of the pore (r_p). This radius depends on the pore topology and is determined by the choice of material and manufacturing process, *i.e.*, sintering, used to produce the porous wicks. The maximum capillary pressure that the wick can withstand is therefore,

$$\Delta p_{cap,max} = \frac{2\sigma}{r_p} \tag{2.56}$$

This maximum capillary pressure is related to the threshold for percolation of the non-wetting phase and is commonly identified as the wick bubbling pressure. In the operation of a capillary evaporator, when the pressure losses of the system exceed the maximum capillary pressure, the wick dry-out begins leading to the system failure. Therefore, the

capillary limit of a CPL reflects its maximum pumping capacity. Before moving to the solution, a different nondimensionalization is proposed.

2.2.1 Nondimensional equations

Udell (1983) studied the heat and mass transfer in a problem that resembles the operation of a heat pipe. Following Udell (1983), the nondimensional variables are proposed:

$$p_{ref} = \frac{\sigma}{(K/\varepsilon)^{1/2}}, \qquad v_{ref} = \frac{(K\varepsilon)^{1/2}\sigma}{\mu_l L_z}, \qquad q_{ref} = \frac{\lambda_e(T_v - T_l)}{L_z}$$

$$Pe = \frac{\rho_l c_{p,l}(K\varepsilon)^{1/2}\sigma}{\mu_l \lambda_e}, \qquad E_v = \frac{\lambda_e \left(T_v - T_l\right)\mu_l}{\rho_l h_{lv} \left(K\varepsilon\right)^{1/2}\sigma}$$

$$r^* = \frac{r}{R}, \qquad z^* = \frac{z}{L_z}, \qquad T^* = \frac{T - T_l}{T_v - T_l}$$

$$p^* = \frac{p}{p_{ref}}, \qquad v_r^* = \frac{v_r}{v_{ref}}, \qquad v_z^* = \frac{v_z}{v_{ref}}, \qquad q_{in}^* = \frac{q_{in}}{q_{ref}}$$

This nondimensionalization is based on the assumption that $(K/\epsilon)^{1/2}$ provides a suitable order of magnitude for the average pore size. From this estimative, p_{ref} is a reference value for the liquid pressure, v_{ref} is a reference value for the liquid velocity and q_{ref} is a reference value for the heat flux.

The nondimensional conservation equations and boundary conditions become:

Equation of conservation of thermal energy,

$$\frac{\partial^2 T^*}{\partial z^{*2}} + \frac{L_z^2}{R^2}\frac{1}{r^*}\frac{\partial}{\partial r^*}\left(r^*\frac{\partial T^*}{\partial r^*}\right) = 0, \tag{2.57}$$

Boundary conditions,

$$\begin{aligned}
z^* &= 0, \qquad -\frac{\partial T^*}{\partial z^*} + Pe v_{z,in}^* T^* = 0, \\
z^* &= 1, \qquad 0 \le r^* \le r'^*, \qquad -\frac{\partial T^*}{\partial z^*} = -\frac{q_{in} L_z}{\lambda_e \left(T_v - T_l\right)} = -q_{in}^* \\
z^* &= 1, \qquad r'^* \le r^* \le 1, \qquad T^* = 1 \\
r^* &= 0, \qquad \frac{\partial T^*}{\partial r^*} = 0 \\
r^* &= 1, \qquad \frac{\partial T^*}{\partial r^*} = 0
\end{aligned}$$

Equation of conservation of mass,

$$\frac{\partial^2 p^*}{\partial z^{*2}} + \frac{L_z^2}{R^2}\frac{1}{r^*}\frac{\partial}{\partial r^*}\left(r^*\frac{\partial p^*}{\partial r^*}\right) = 0, \tag{2.58}$$

Boundary conditions,

$$\begin{aligned}
z^* &= 0, \qquad p^* = p^*_{l,in} \\
z^* &= 1, \qquad 0 \le r^* \le r'^*, \qquad \frac{\partial p^*}{\partial z^*} = 0 \\
z^* &= 1, \qquad r'^* \le r^* \le 1, \qquad E_v\frac{\partial T^*}{\partial z^*} = \frac{\partial p^*}{\partial z^*} \\
r^* &= 0, \qquad \frac{\partial p^*}{\partial r^*} = 0 \\
r^* &= 1, \qquad \frac{\partial p^*}{\partial r^*} = 0
\end{aligned}$$

The parameters that controls the solution are: $\frac{L_z}{R}$; $v^*_{z,in}$; q^*_{in}; $\frac{R'}{R}$; $p^*_{l,in}$; E_v.

The capillary-evaporation number (E_v) is the ratio of conduction heat flux to the energy rate consumed by the evaporation of the capillary-driven liquid flow. This number provides the relation between the nondimensional liquid pressure and temperature gradients at the evaporation surface. Also, the capillary pressure and the pore radius can be cast in nondimensional form as,

$$\Delta p^*_{cap} = \frac{\Delta p_{cap}\left(K/\varepsilon\right)^{1/2}}{\sigma} = \frac{\left(p_v - p_l\right)\left(K/\varepsilon\right)^{1/2}}{\sigma} \tag{2.59}$$

and

$$r^*_p = \frac{r_p}{\left(K/\varepsilon\right)^{1/2}} \tag{2.60}$$

2.2.2 Numerical Solution

The conservation equations were solved numerically by the finite volume method (PATANKAR, 1980; MALISKA, 2004). The tri-diagonal matrix algorithm (TDMA) was employed to solve the discretized equations in a segregated form. The numerical algorithm was implemented in FORTRAN 90 and can be summarized as:

1. First, an inlet velocity is estimated to solve the Laplace equation for the temperature. From the solution for T, the outlet velocity is calculated using the boundary condition of Eq. 2.54.

2. Next, the pressure equation is solved using the outlet velocity calculated in step (1). Then, the velocities are calculated and the values are compared to the ones obtained in step (1);

3. Return to step (1) until the converged solution is obtained.

Convergence of the solution was examined by checking the overall mass and energy balances. The coupled equations are assumed to converge when overall energy and mass balances are satisfied within ± 1%. The code verification was developed according to the method reported by Eça & Hoekstra (2008), and it was found that a grid of (150×150) is sufficient to obtain accurate solutions. The uncertainty of the numerical solution was estimated using the method developed by Marchi & Silva (2002). The same grid of (150×150) was chosen and the numerical uncertainty of the solutions for the temperature and pressure fields were ± 0.038 ^{o}C and ± 5.443 Pa, respectively. Further information regarding the code verification and the determination of the numerical uncertainty of the solution can be found in Appendix B.

2.2.3 Results and Discussion

The results are presented as follows. First, the problem was solved for a porous wick with only one layer and the results are presented for a specific inlet heat flux. Then, three analyses are developed: analysis of the effect of the magnitude of the external heat transfer rate in the mass flow rate, analysis of the onset of drying (one-layer) and analysis of the effect of a bi-layered structure on the mass flow rate and onset of drying. For the results presented here, water was used as working fluid. A ceramic wick, initially with one layer and next with two layers with different thermal properties, was used as porous wick. The thermodynamic properties of the wick and the working fluid and the main nondimensional parameters are presented in Table 2.3. In the analysis that follows, the properties were kept constant.

Table 2.3 – Thermophysical properties of the porous wick and working fluid and nondimensional parameters.

	ε (%)	K (m^2)	$\lambda_{e,1}$ (W/m-K)	$\lambda_{e,2}$ (W/m-K)	r_p (μm)
Ceramic	0.5	35×10^{-15}	$4.0 - 8.0$	4.0	$3.0 - 15.0$
	σ (N/m)	$h_l v$ (kJ/kg)	c_p (kJ/kg-K)	ρ (kg/m^3)	μ (kg/m-s)
Water	0.07119	2382	4.18	995.60	0.0007977
	p_{ref} (Pa)	v_{ref} (m/s)	E_v	Pe	L_z/R
	269073	1.181×10^{-3}	0.00143	12.28	0.67

Figure 2.12(a) presents the streamlines and isobaric lines (Pa) for the flow within the wick for an inlet heat flux of 4.0×10^4 W/m^2, for water and a wick with $\lambda_{e,1} = \lambda_{e,2} = 4.0$ W/m-K (a uniform layer). This heat flux applied is representative of typical values found in aeroespacial applications and in cooling electronics components of portable computers. The dimensions of the wick are: $R = 15$ mm, $R^{'} = 7.5$ mm, $L_{z,1} = 4$ mm, $L_{z,2} = 6$ mm. The saturation temperature is $T_{sat} = 40$ °C at the vapor outlet and the pressure at liquid inlet is $P_{l,in} = 4246$ Pa ($T_{l,in} = 30$ °C). The streamlines point upwards up to the middle of the structure, where they begin to change direction towards the outlet surface of the wick. Note that the liquid pressure is not uniform at the outlet surface, but becomes a consequence of the normal heat flux at this surface. There is a strong curvature of the streamlines at the end of the fin at $r = R^{'}$. Figure 2.12(b) presents the inlet and outlet normal velocities. Note the high velocity of the vapor flow at the end of the fin (at $r = R^{'}$). Actually, at $r = R^{'}$, $v_{z,out} \rightarrow \infty$. This result of the velocity at $r = R^{'}$ does not match with the expected physics of the problem. Indeed, there is a no-slip condition at the wall of the fin and would be necessary to include in the momentum equation (Darcy's Law) the macroscopic (Brinkman) viscous term for taking into account this phenomenon. However, to some extend, as the velocities are so low, this contribuition would not affect the temperature and pressure fields obtained with the model.

Figure 2.13(a) presents the isotherm and heat flux lines for an inlet heat flux of 4.0×10^4 W/m^2. Note that part of the heat flows to the outlet where evaporation occurs, while the remaining flows right to the feeding liquid channel. Fig. 2.13(b) presents the temperature distribution at outlet and inlet for the same inlet heat flux used for Fig. 2.11(a). The inlet temperature presents a maximum variation of 0.02 °C for all results obtained. These figures should be compared to Fig. 2.10 for the simplified model. We note a markedly different temperature distribution for the region underneath the channel.

From this general view, more specific aspects will be presented using the nondimensional variables.

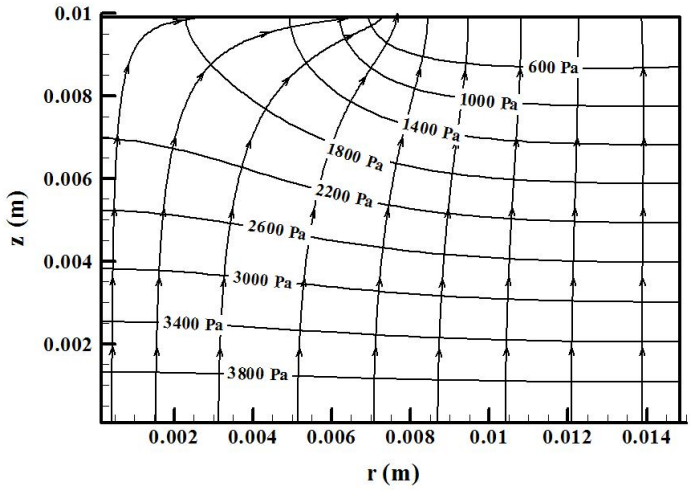

(a)

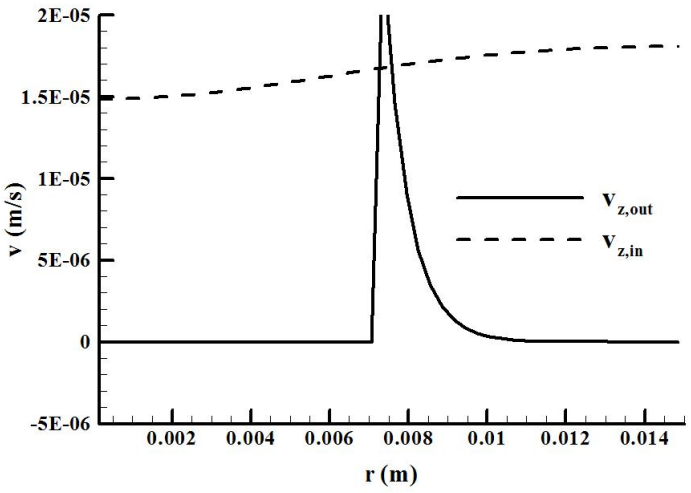

(b)

Figure 2.12 – (a) Streamlines and isobaric lines within the wick for a heat flux of 4.0×10^4 W/m^2; (b) inlet and outlet normal velocities at the outlet of vapor for a heat flux of 4.0×10^4 W/m^2.

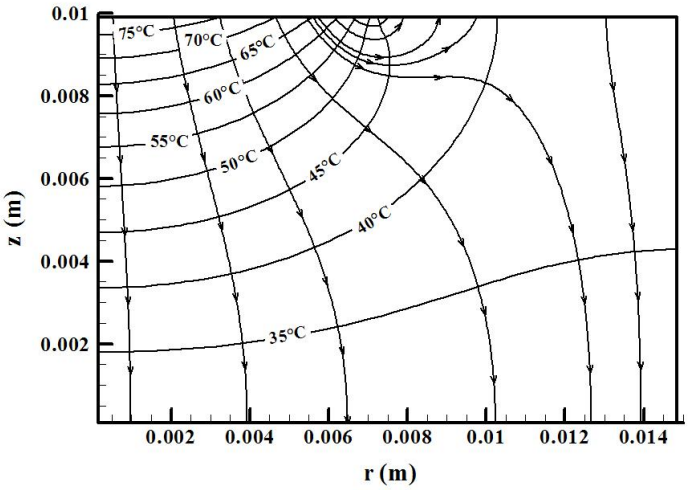

(a)

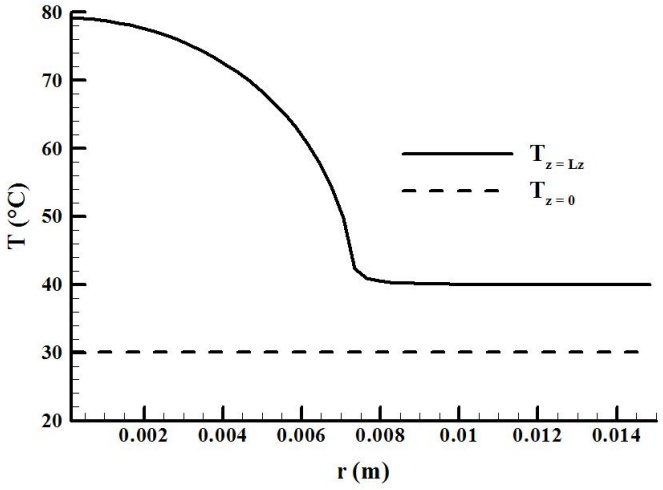

(b)

Figure 2.13 – (a) Isotherm lines and heat streamlines and (b) temperature profiles at the inlet and outlet for a heat flux of 4.0×10^4 W/m^2.

2.2.4 Effect of the magnitude of the external heat transfer rate in the mass flow rate

It is expected that an increase in the heat flux at the fin causes an increase in the mass flow rate. Figures 2.14, 2.15 and 2.16 present the nondimensional isotherm and heat flux lines for three increasing heat fluxes. Fig. 2.14 presents the results for a nondimensional inlet heat flux of 5.0. The fin ends at $r^* = 0.5$. The isotherm with $T^* = 1.0$ ($T = T_v$) is also shown. Note that surface evaporation occurs only in the first few millimeters of the outlet surface, very close to the end of the fin. For the remaining of the fin, the heat flux lines turn around and heat flows right to the liquid channel. As the nondimensional heat flux is increased (Figs. 2.15 and 2.16), an increased amount of heat flows to the outlet surface, causing the liquid evaporation. When the heat flux is increased, the isotherm $T^* = 1.0$ penetrates deeper in the porous wick.

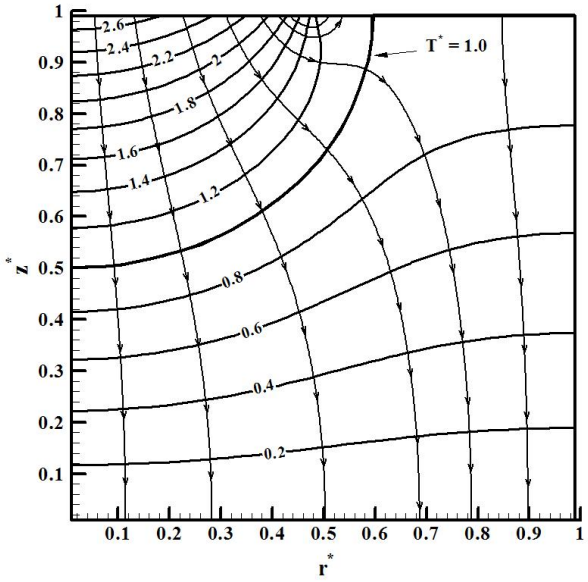

Figure 2.14 – Nondimensional isotherm and heat flux lines for a nondimensional inlet heat flux of 5.0 ($q_{in} = 2.0 \times 10^4$ W/m^2).

This is also evidenced in Fig. 2.17 that presents the normal nondimensional liquid velocity at the outlet surface. The area underneath the curve shown is proportional to the mass flow rate which, given the boudary conditions, is simply calculated by $\frac{q_{in} A_{in}}{h_{lv}}$. Since the normal velocity at the region underneath the fin is zero, Fig. 2.17 shows only the vapor outlet surface ($z^* = 1.0$ and $0.5 \leq r^* \leq 1.0$). Except for a region closer to the fin, the nondimensional liquid velocity at the outlet surface is not very sensitive to the heat flux.

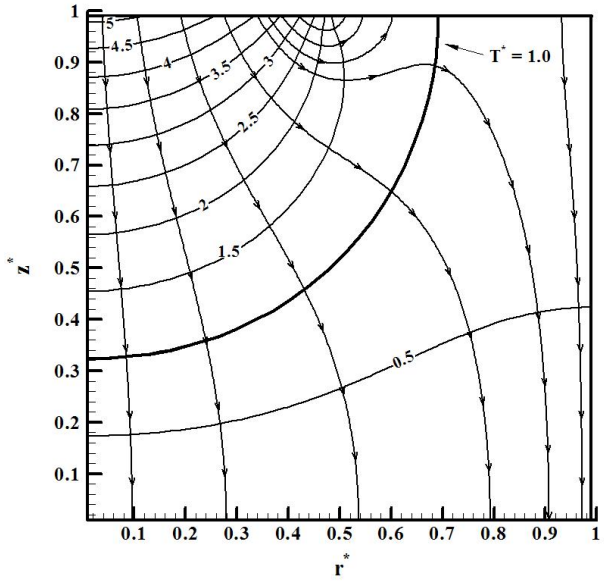

Figure 2.15 – Nondimensional isotherm and heat flux lines for a nondimensional inlet heat flux of 10.5 ($q_{in} = 4.2 \times 10^4$ W/m^2).

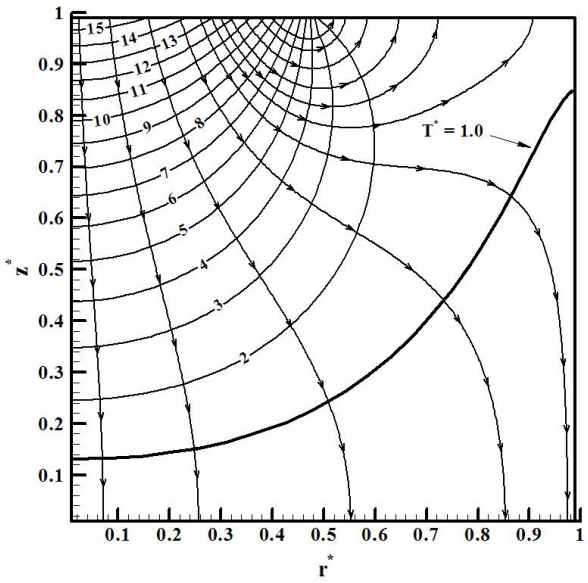

Figure 2.16 – Nondimensional isotherm and heat flux lines for a nondimensional inlet heat flux of 37.5 ($q_{in} = 1.5 \times 10^5$ W/m^2).

2.2.5 Analysis of the Onset of Drying

The heat transfer rate imposed in the fin is transferred to the outlet surface, causing evaporation, and also to the inlet surface, resulting in heating of the liquid channel. Both these heat transfer paths have their characteristic thermal resistances. As a result of these thermal resistances, the fin surface reaches a temperature which can be reasonably large in certain conditions. For instance in Fig. 2.16, we observe that for a nondimensional inlet heat flux of 37.5, the fin surface reaches nondimensional temperatures above 15 which are

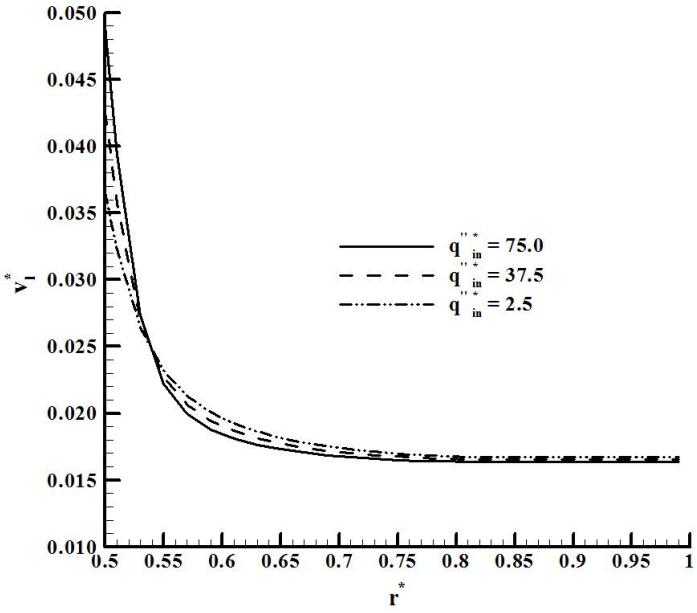

Figure 2.17 – Normal nondimensional liquid velocity at the outlet surface as a function of nondimensional inlet heat flux.

about 14 times above the nondimensional saturation temperature of the fluid (for infinite radius of curvature). Then, a question remains whether the fluid would remain liquid or evaporate under this temperature. This can be tested by observing the capillary pressure at the top surface of the wick and comparing it to the maximum capillary pressure that the wick can sustain.

The maximum capillary pressure that a pore with radius r_p can sustain is,

$$\Delta p_{cap,max} = \frac{2\sigma}{r_p}$$

This can be nondimensionalized using Eq. 2.59 resulting in,

$$\Delta p^*_{cap,max} = \frac{2\sigma \left(K/\varepsilon\right)^{1/2}}{\sigma r_p} = \frac{2\left(K/\varepsilon\right)^{1/2}}{r_p} \tag{2.61}$$

Note that this maximum nondimensional capillary pressure is a purely geometrical parameter. Therefore, the maximum nondimensional capillary pressure is the one that exists for a pore with radius equal to $2\left(K/\varepsilon\right)^{1/2}$. When applied to a porous wick, this means that the maximum capillary pressure is the one that occurs when the average radius of the curvature of all menisci exposed to the vapor phase is equal to r_p.

The local nondimensional capillary pressure at the outlet surface is given by equation Eq. 2.59 (repeated here)

$$\Delta p^*_{cap} = \frac{(p_v - p_l)\,(K/\varepsilon)^{1/2}}{\sigma}$$

where $p_v = p_{sat}(T_v)$ and p_l is the local value of liquid pressure calculated from the improved model, $p_l = p_l(r)$ at $z = L_z$. Here, $\sigma = \sigma(T)$ where T is the porous wick temperature.

Using $p_v = p_{sat}(T_v)$ and p_l obtained from the solution of the improved model, $p_l = p_l(r)$ at $z = L_z$, Δp^*_{cap} can be calculated and compared to $\Delta p^*_{cap,max}$.

Fig. 2.18 presents the nondimensional capillary pressure at the top surface as a function of properties for two heat fluxes, $q^*_{in} = 10.5$ and $q^*_{in} = 5.0$. All properties were kept constant and correspond to the properties of the porous wick with nondimensional average pore radius of 11.34. The horizontal lines represent the maximum nondimensional capillary pressure for each characteristic nondimensional pore size, from 11.34 to 56.69 as shown. We note that for the nondimensional inlet heat flux of 5.0 all media would remain saturated by liquid except those with the larger nondimensional pores of 37.80 and 56.69. For these two sizes, the local capillary pressure exceeds the maximum allowed capillary pressure and, therefore, the region underneath the fin would dry and the evaporation front would seek a new equilibrium position within the wick. This condition in which the front is embedded within the wick has been analyzed by Demidov & Yatsenko (1994), Figus *et al.* (1999), Takahashi (2002) and Kaya & Goldak (2006).

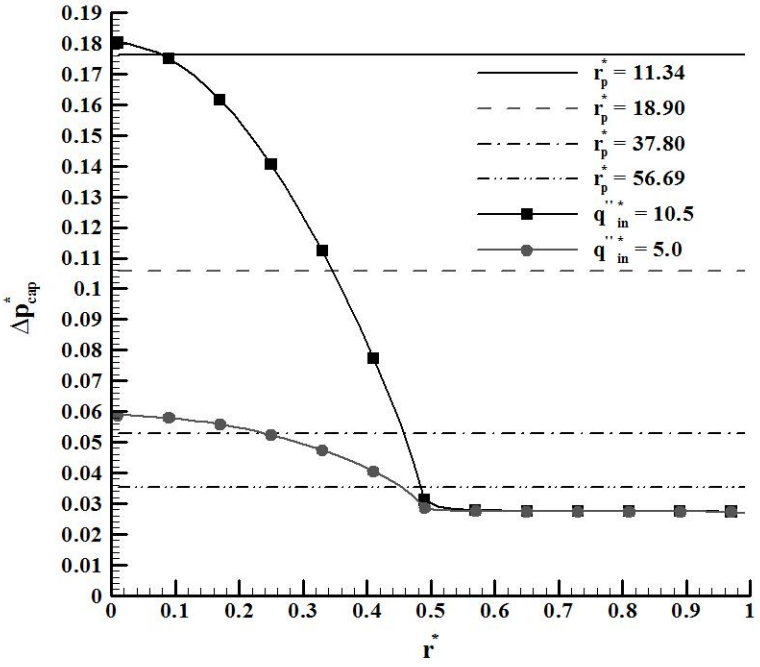

Figure 2.18 – Nondimensional capillary pressure profiles at $z^* = 1.0$ for different nondimensional averaged radius of curvature and nondimensional inlet heat fluxes.

For higher heat fluxes, all media with pore sizes above 11.34 would suffer dry out

underneath the fin. Therefore, there is a relation between the pore size (and all medium properties) and the heat flux at the onset of drying. Note that this drying underneath the fin may not cause the failure by the capillary limit, since there may be a stable condition for operation with the embedded evaporation front according to Demidov & Yatsenko (1994), Figus *et al.* (1999), Takahashi (2002) and Kaya & Goldak (2006). This, however, is not analyzed here. Nevertheless, this test allows the definition of safe operation limits.

2.2.6 Analysis of the Onset of Drying in the Bi-layered Structure

Here, the analysis of the porous wick with two layers is presented. It is expected that this kind of porous structure improves the capillary pumping capacity, avoiding reaching the capillary limit. It is also expected that the heat transfer to the feeding liquid channel is decreased. For the bi-layered porous wick, porous wick 1 and 2 have nondimensional lengths of $L^*_{z,1} = 0.4$ and $L^*_{z,2} = 0.6$, respectively. The porous wick 2 has the effective thermal conductivity constant ($\lambda_{e,2} = 4.0$ W/m − K). The effective thermal conductivity of the porous wick 1 was varied ($\lambda_{e,1}$) from 6.0 W/m-K (two-layers I) to 8.0 W/m-K (two-layers II) in order to evaluate its effect on the onset of drying.

Figure 2.19 presents the nondimesnional capillary pressure at the top surface as a function of properties of the wicks with one and two layers for a nondimensional inlet heat flux of 10.5 and four characteristic nondimensional pore average radius (from 11.34 to 56.69). All properties were also kept constant and correspond to the nondimensional average porous radius of 11.34. Note that for the nondimensional inlet heat flux of 10.5 in the wick with two layers, as the thermal conductivity increase the local capillary pressure decreases and may not exceed the maximum allowed capillary pressure.

For a given nondimensional heat flux there will be a local maximum nondimensional average radius needed to avoid the drying of the wick in the region underneath the fin, which will be called critical nondimensional average radius ($r^*_{p,crit}$). From Eq. 2.59 and 2.60, this is given by,

$$r^*_{p,crit} = \frac{2\sigma}{(p_v - p_l)\,(K/\varepsilon)^{1/2}} \tag{2.62}$$

where $p_v = p_{sat}(T_v)$ and p_l is the local value of liquid pressure calculated from the improved model, $p_l = p_l(r)$ at $z = L_z$. Here, $\sigma = \sigma(T)$ where T is the porous wick temperature.

Figures 2.20 and 2.21 depict curves of critical nondimensional average radius as a function of the nondimensional heat flux in the upper part of the wick ($z^* = 1$). Figure 2.20 presents the nondimensional critical average radius for two nondimensional heat

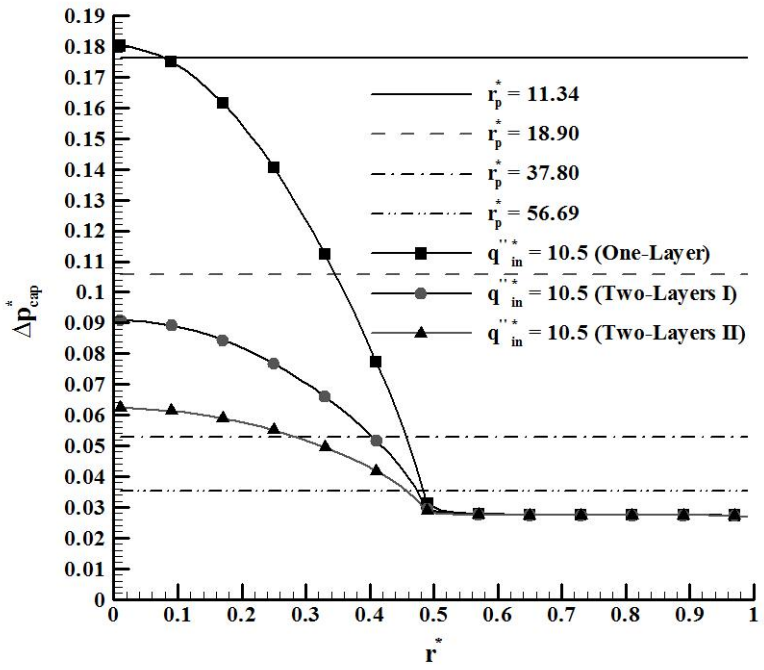

Figure 2.19 – Nondimensional capillary pressure profiles at $z^* = 1.0$ in the bi-layered wick for a nondimensional inlet heat flux of 10.5 and for different nondimensional averaged radius of curvature.

fluxes (5.0 and 10.5) for the porous wick with one layer.

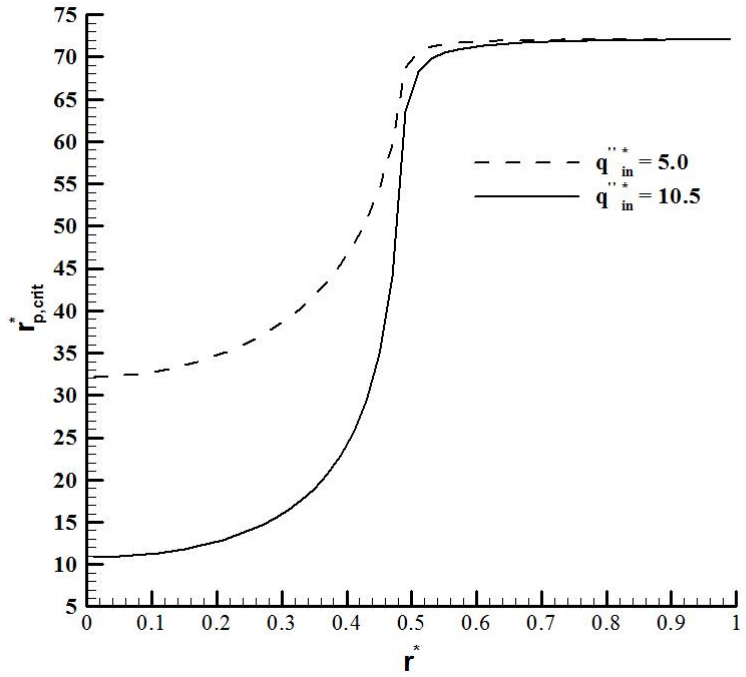

Figure 2.20 – Critical nondimensional average radius profiles at $z^* = 1.0$ for two nondimensional inlet heat fluxes, one layer.

This is the same condition presented in Figs. 2.14 and 2.15. Note that, in the region underneath of the fin, the smaller the nondimensional heat flux the higher the critical nondimensional average radius. That is, the temperatures underneath the fin and the mass

flow rate decrease with the decreasing of heat flux. As a consequence the capillary pressure also decreases. Since the critical average radius is inversely proportional to the maximum capillary pressure according Eq. 2.62, when the nondimensional heat flux is decreased the critical nondimensional average radius increases. For the nondimensional heat flux of 10.5 the porous wick should be manufactured with minimum critical nondimensional average radius of 10.86 ($r_p = 2.87$ μm calculated for the properties from Table 2.3), while for nondimensional heat flux of 5.0 it is sufficient a minimum critical nondimensional average radius of 32.18 ($r_p = 8.51$ μm calculated for the properties from Table 2.3).

It is noted in Fig. 2.21 that for the same nondimensional heat flux of 10.2, as the thermal conductivity of the wick 1 increases, the minimum critical nondimensional average radius also increases in the region underneath the fin. The minimum critical nondimensional average radius is 32.18 (two-layers II - $\lambda_{e,1} = 8.0$ W/m $-$ K), 21.86 (two-layers I - $\lambda_{e,1} = 6.0$ W/m $-$ K) and 10.86 (one-layer). Therefore, these results provide guidelines for the design and manufacture of the porous wicks in order to avoid the drying of the region underneath the fin.

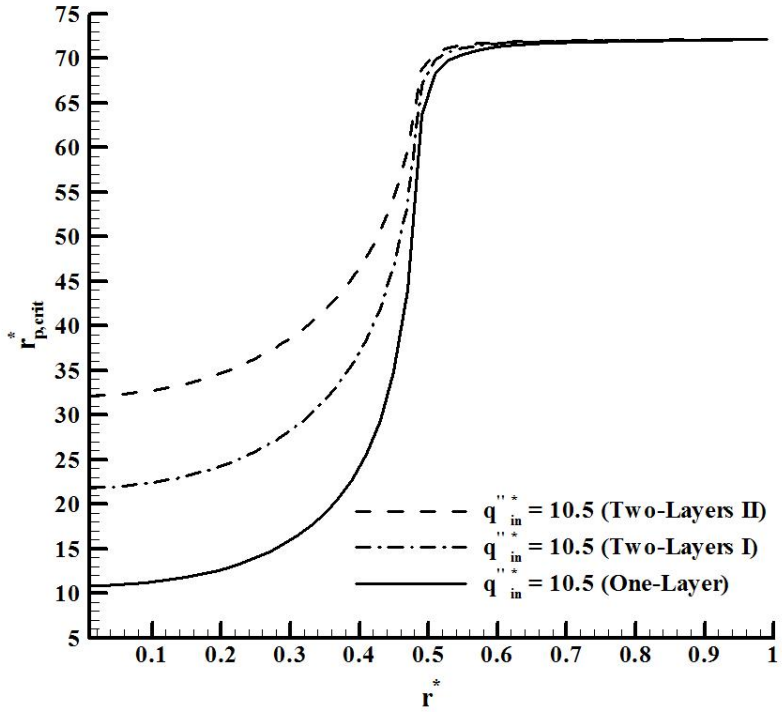

Figure 2.21 – Critical nondimensional average radius profiles at $z^* = 1.0$ in the bi-layered wick for a nondimensional inlet heat flux of 10.5.

It is noticed in Figs. 2.20 and 2.21 that the minimum critical nondimensional average radius is located in the region underneath of the fin at $z^* = 1.0$ and $r^* = 0.0$. Thus, the Fig. 2.22 presents the critical nondimensional average radius as a function of the nondimensional heat flux at $z^* = 1.0$ and $r^* = 0.0$.

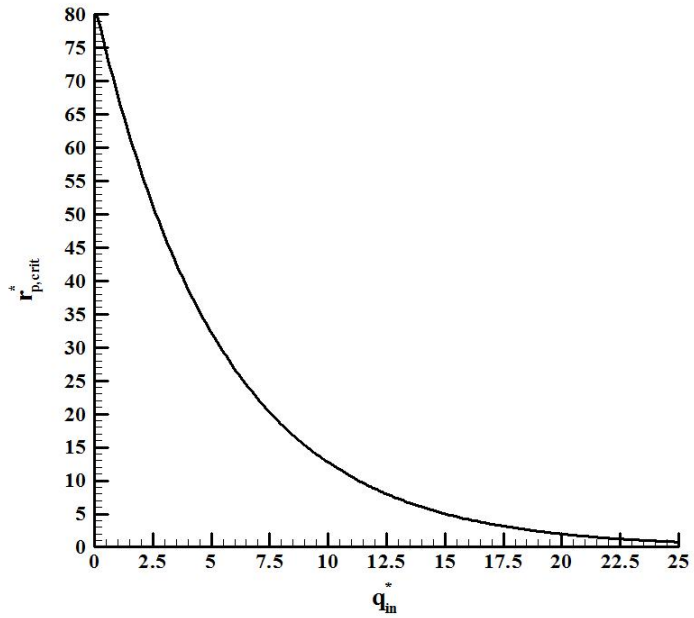

(a)

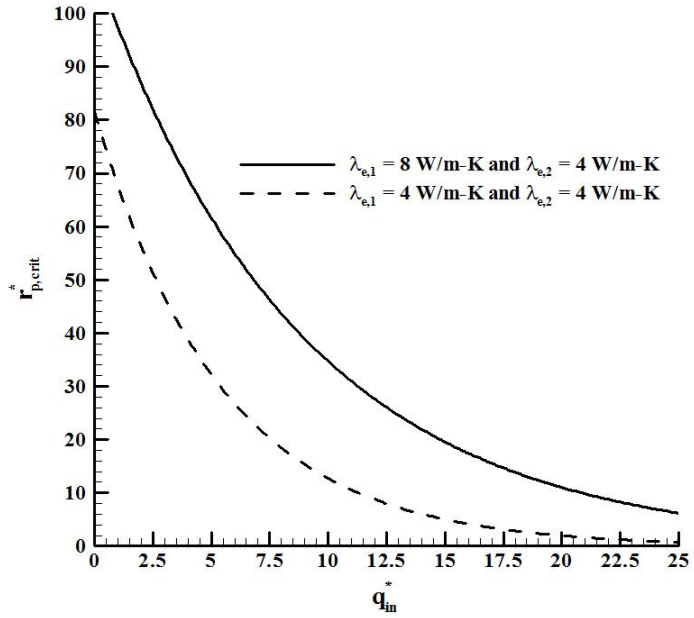

(b)

Figure 2.22 – (a) Critical nondimensional average radius at $z^* = 1.0$ and $r^* = 0.0$ as a function of the nondimensional inlet heat flux for one layer and (b) bi-layered wick.

The curve shown in Fig. 2.22(a) represents the capillary limit, *i.e.*, bellow this curve the capillary limit is not reached and there is no vapor breakthrough and above the curve occurs the vapor invasion of the porous wick. Figure 2.22(b) presents the minimum critical nondimensional average radius as a function of the nondimensional heat flux for a bi-layered wick. Note that, as the thermal conductivity of the wick 1 increases, the capillary limit is displaced and the minimum critical nondimensional average radius also increases. For a minimum critical nondimensional average radius ($r^*_{p,crit}$) of 20, for instance, the nondimensional heat flux increases from 7.5 (one layer) to 15 (bi-layered) which refer to

a heat flux of 3×10^4 W/m^2 and 6×10^4 W/m^2, respectively.

2.2.7 Conclusions

The model developed here allowed to verify the effect of design variables in the steady-state performance of a flat capillary evaporator. The model simulated the heat and mass transfer within a wick with one and two layers with different thermophysical properties. Also, a criterion for the onset of dryout was obtained and calculated for the conditions simulated.

The analysis of the wick with one and two layers showed that the wick with two layers is better than with one layer regarding the onset of drying underneath the fin. Other conclusions are:

1. The capillary limit, or onset drying, stablishes a relation between the pore size (and all medium properties) and the heat flux. If this limit is reached, the evaporation front may penetrate within the wick. This can be used as a criterium for the specification of the maximum heat flux allowed during operation in steady-state.

2. The larger the thermal conductivity of the porous wick 1 (underneath the fin), the smaller is the heat transfer to the feeding channel, causing a smaller increase of the inlet temperature. The increase of the thermal conductivity of the porous wick 1 causes the increase of the capillary limit, avoiding the onset of drying of the region underneath the fin. The increase of the thermal conductivity also decreases the mass flow rate, causing the decrease of the pressure losses through the porous wick.

3. Finally, the dimensions of the bi-layered wick ($R = 15$ mm, $R^{'} = 7.5$ mm, $L_{z,1} = 4$ mm, $L_{z,2} = 6$ mm) and its thermophysical properties can be used for a design of a flat capillary evaporator.

From the understanding developed from the theoretical analysis, two LHPs and one CPL were designed, fabricated and tested under conditions typical of aerospacial applications.

However, the attempts to produce a flat capillary evaporator where not succesful due to sealing difficulties in the region between the wick and the casing. Therefore, it was decided to follow the work producing cylindrical capillary evaporators. Besides the change in geometries, the same general principles described above apply.

3 Experiment

3.1 Introduction

In this work two LHPs and one CPL were manufactured and tested in order to evaluate their thermal performance and their applicability in thermal control of microprocessors and electronic components in general. The surface temperatures at the main part of the systems, *e.g.* evaporator and condenser inlet and outlet, compensation chamber (in case of LHPs) and reservoir (in case of CPL) were measured while the thermal load was varied. The LHPs used acetone and water as working fluid, while the CPL only used water. The LHPs and the CPL used a ceramic porous wick as capillary structure in the evaporator. For the heating of the capillary evaporator of LHPs and CPL, electric resistors (cartridge heaters inside of copper block for the LHPs and heaters in format of wire for the CPL) were used to simulate the heat generation in microprocessors and electronic components. The condensers of the LHPs were cooled using water in forced convection and the condenser of CPL was cooled using air also in forced convection.

The CPL and LHPs used here were manufactured at Federal University of Santa Catarina (UFSC) in Brazil. All tests of the CPL were carried out at Laboratory of Combustion and Thermal Systems Engineering (LABCET) of UFSC in Brazil and all tests of LHPs were carried out at Institute of Nuclear Technology and Energy Systems (IKE) at University of Stuttgart in Germany, under the supervision of Researcher Dr. Rainer Mertz.

3.2 Ceramic Porous Wick Manufacturing

Most porous structures used in the evaporators of LHPs and CPLs are made of metallic sintered powders, such as nickel, titanium and stainless steel. Metallic wicks have lower thermal resistance when compared to polymeric and ceramic porous wicks. Although this comes as an advantage for heat transfer to the evaporation front, they also transfer a considerable quantity of heat from the evaporation zone to the inlet liquid channel, leading

to formation of bubbles that block the liquid feeding channel. Moreover, the machining of porous metal structures can block the external pores and hence reduce the liquid flow. In this work, ceramic porous wicks are proposed as alternative to wicks made of metallic material for all capillary evaporators in order to minimize the bubble formation inside the liquid feed channel and problems in the machining of the wick. According to Janssen *et al.* (2008) ceramic wick structure can be machined by conventional machining processes and the porosity remains opened up to surface.

Here, slip casting was used to produce the porous structures. The following materials were used in the formulation of the ceramic powder: mullite (Treibacher 140F, Brazil) and alumina (Alcoa SG1000, 90% $<$ 44μm, Brazil). Activated carbon (Carbomafra, 90% $<$ 44μm, Brazil) was used as pore forming agent to increase the porosity of the porous elements. Aqueous slurries (67wt% solids content, corresponding to 80wt% mullite and 20wt% of alumina) were prepared. The pore forming agent was then added (10wt% in relation to the solids content). Chemical additives (sodium polyacrylate as dispersant, and poly(vinyl-alcohol) as plasticizer) were used to stabilize the slurries. The slurries were then submitted to a grinding process to decrease particle size and after grinding, the slurries were poured into plaster moulds. Subsequently, the samples were pre-sintered at 1200^{o}C for 1 h to remove the pore forming agent, followed by sintering at 1450^{o}C for 1 h, (BERTI *et al.*, 2010).

Figure 3.1 shows the ceramic wick with vapor channels (grooves) used in the evaporators of LHPs and CPL. Only four grooves were machined in the ceramic wick used for the LHPs, Fig. 3.1(a). Along the work the machining technique was improved and it was possible to machine more vapor channels (12 grooves) in the ceramic wick used for the CPL, Fig. 3.1(b). A thermal cleaning at 800^{o}C for 120 min is applied to remove the oil contamination after the machining.

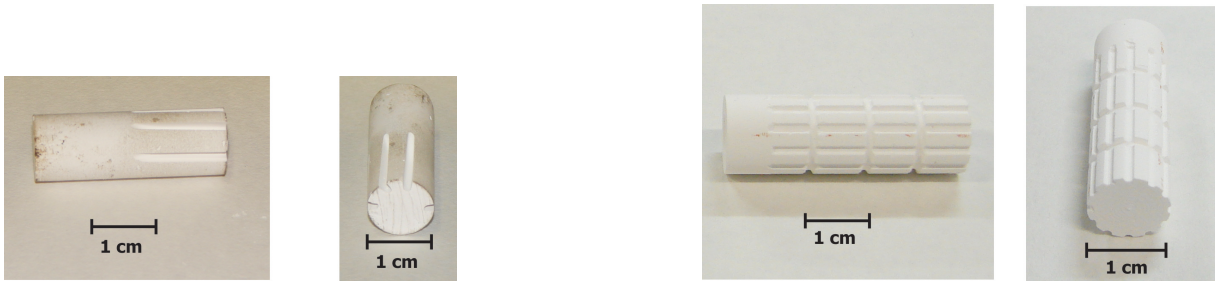

(a) (b)

Figure 3.1 – (a) Ceramic wick with vapor channels (grooves) used in the LHPs and (b) in the CPL.

3.3 Manufacturing of the LHPs and the CPL

During the assembly of the capillary evaporator, the insertion of porous wicks into the metallic envelope must result in close contact tolerances between envelope walls and wick surface. This contact should be tight in order to avoid any vapor leak back to the liquid channel. The assembling of metallic wicks requires at the same time the heating of the metallic tube and cooling of the wick for the insertion into the metallic envelop. The ceramic wick is not cooled due to its low volumetric thermal expansion coefficient when compared to those of metals. Therefore, only the metallic envelop of the evaporator is heated at $\sim 800^o$C for the insertion of the ceramic wick.

Figure 3.2(a) depicts a view of the evaporator, the compensation chamber and the ceramic porous wick of the LHPs. Only the upper side of the capillary evaporator has grooves. Figure 3.2(b) shows a view of the evaporator and the ceramic porous wick of the CPL. Contrary to the wicks for LHPs, all the circumference of capillary evaporator for the CPL has grooves.

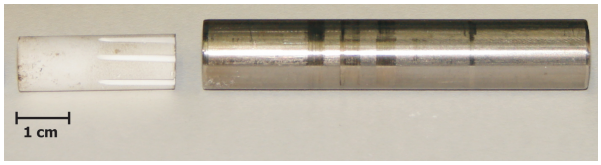

(a)

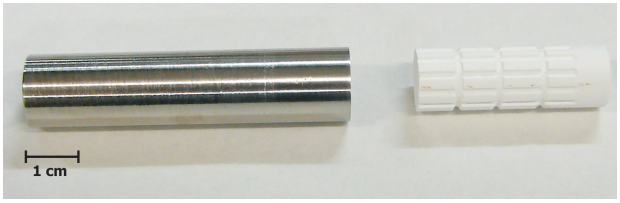

(b)

Figure 3.2 – (a) View of the evaporator, the compensation chamber and the ceramic porous wick of the LHPs and (b) view of the evaporator and the ceramic porous wick of the CPL.

3.4 Description of the LHPs

Two LHPs were manufactured with the same capillary evaporator. Fig. 3.3 shows the LHPs. Both capillary evaporators have 10 mm of inner diameter and 25 mm of length. The ceramic porous wick has 50% of porosity, 1 to 3 μm pore size distribution and permeability of about 1.5×10^{-14} m^2; a compensation chamber with the same diameter of the evaporator and length of 50 mm; transport lines of liquid and vapor with 2.8 mm of inner diameter and the condenser with 120 mm of length. The lengths of the vapor

and liquid transport lines of the two LHPs have small differences, which are presented in the Table 3.1.

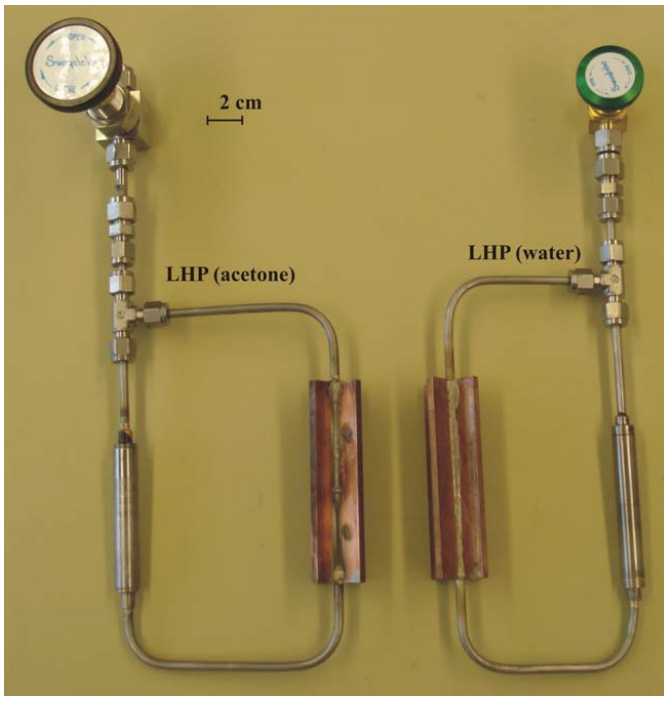

Figure 3.3 – General view of the LHP (acetone) and LHP (water) with cylindrical evaporators.

The properties of the ceramic porous wick, obtained in Berti (2008), and the working fluids are presented in Table 3.2.

3.4.1 Filling Station

The ammount of working fluid has a significant influence on the operation of capillary pumping systems, hence it is necessary to control carefully the amount of fluid inserted in these systems. Figure 3.4 shows the filling station used in the filling of LHPs which is composed by one vaccum pump conection, four valves and one burette. First, the valves 1 and 3 are opened while the valves 2 and 4 are closed. Next the conection between the vaccum pump and the LHP is evacuated. After reaching the required vaccum, the valve 4 is opened in order to evacuate the LHP. After reaching the required vaccum level in the LHP, the valves 1 and 4 are closed and the valve 2 is opened. Again the valve 4 is opened carefully until the desired volume of liquid is fed to the LHP.

The working fluid charge ratio of LHP working with water was varied in the range from 50 to 65% in steps of 5%, while for the LHP working with acetone the working fluid charge ratio was set at $50, 60, 65$ and 70%. A working fluid charge ratio of 60% means that the LHP is filled with 60% of its total volume including the compensation chamber. The

Table 3.1 – Structural characteristics of the LHPs.

Characteristic	LHP (Acetone)	LHP (Water)
Evaporator - $d_{evap,in}$, (mm)	10	10
Evaporator - $d_{evap,out}$, (mm)	12	12
Number of grooves - N_{groove},	4	4
Groove width - w_{groove}, (mm)	1	1
Groove heigth - h_{groove}, (mm)	1	1
Groove length- L_{groove}, (mm)	10	10
Active zone length, (mm)	25	25
Wick - $r_{wick,in}$, (mm)	2.5	2.5
Wick - $r_{wick,out}$, (mm)	4.0	4.0
Wick length - L_{wick}, (mm)	25	25
Vapor transport line, (mm)	260	245
Vapor transport line - $d_{vl,in}$, (mm)	2.8	2.8
Liquid transport line, (mm)	270	260
Liquid transport line - $d_{ll,in}$, (mm)	2.8	2.8
Condenser type	Finning Tube	Finning Tube
Number of fins - N_{fin},	4	4
Fin width - δ_{fin}, (mm)	3.0	3.0
Fin heigth - H_{fin}, (mm)	10	10
Fin length - L_{fin}, (mm)	100	100
Condenser length, (mm)	120	120
Condenser - $d_{cond,in}$, (mm)	2.8	2.8
Condenser - $d_{cond,out}$, (mm)	5.0	5.0
Condenser box - H_{box}, (mm)	50	50
Condenser box - L_{box}, (mm)	50	50
CC and evaporator assembly	80	80
CC - $d_{CC,in}$, (mm)	10	10
CC - $d_{CC,out}$, (mm)	12	12

CC means Compensation Chamber.

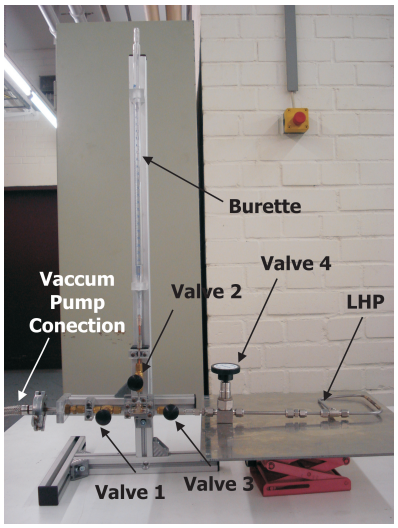

Figure 3.4 – Filling station for the LHPs.

Table 3.2 – Thermodynamic properties of the ceramic wick and working fluid.

Wick material	ε (%)	K (m^2)	λ_s (W/m-K)	r_p (μ m)
Ceramic[a]	50.0	1.5×10^{-14}	11.2	$1-3$
Working fluids	σ (N/m)	h_{lv} (kJ/kg)	ρ (kg/m^3)	μ (kg/m-s)
Water[b]	0.07119	2382	995.6	0.0007977
Acetone[c]	0.02250	544	779.0	0.0002960

[a] ceramic wick properties were obtianed from Berti (2008).
[b] the properties of the water (at saturation temperature of 40 ^{o} C) were obtained by the software Engineering Equation Solver (EES).
[c] the properties of the acetone (at saturation temperature of 40 ^{o} C) were obtained from Peterson (1994).

working fluid charge ratio was varied until the systems started up properly and reached the steady state condition.

3.4.2 Experimental Apparatus

Figure 3.5 shows the instrumentation used for testing the LHPs. The LHP with the heat source, the heat sink and the temperature sensors were fixed to a movable frame in order to adjust the orientation to different angles. The whole construction is embedded into a box made of Plexiglas (1.5 x 1.5 x 0.8 m^3), where different ambient conditions can be set. The box is insulated to avoid as much as possible heat transfer between the box and the ambient. Flanges are employed at the front side and at the top of the box, so that the experimental components inside the box can be set easily to the requested experimental conditions. Several feedthroughs are employed to connect the lines for the measurement sensors and the heating and cooling devices.

The power supply unit is connected to the cartridge heaters and is controlled by the data logger. A thermostat controls the temperature of the coolant at the condenser section. The volumetric flow rate of the coolant working fluid (water) is measured by a magnetic inductive flow meter. Two resistant temperature sensors (Pt100) measure the inlet and outlet coolant temperature. The temperature inside the box is set by a cryostat. A resistant temperature sensor (Pt100) located near the LHP is connected to the cryostat, measuring the input temperature for the loop control of the cryostat. Furthermore there are three more resistant temperature sensors (Pt100) measuring the ambient temperature inside the box placed near the top, in the middle and at the bottom. All signals are measured by a data logger including the room ambient temperature which is measured by a resistant temperature sensor (Pt100). Figure 3.6 depicts the external view of the test rig.

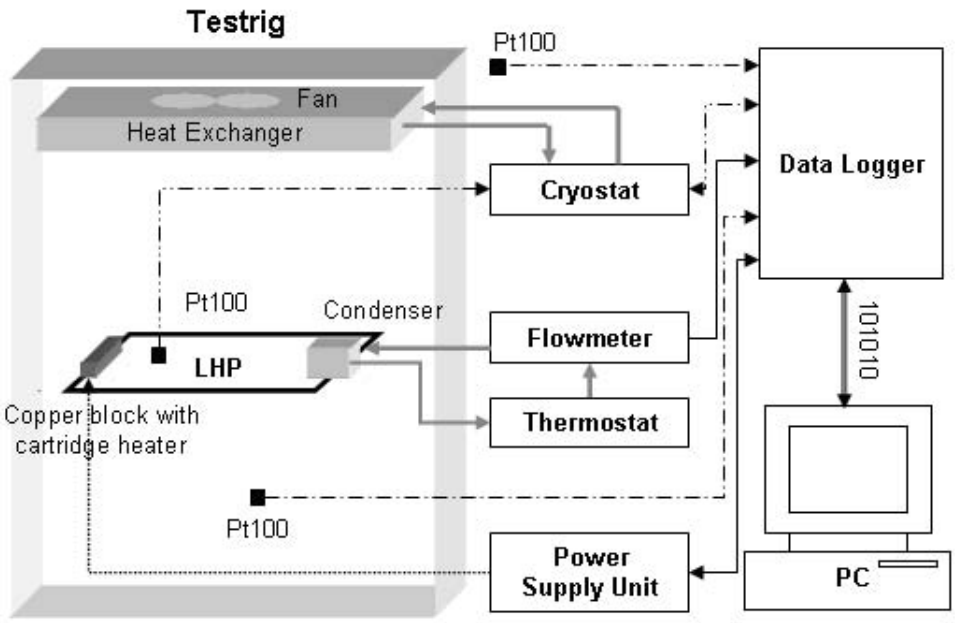

Figure 3.5 – Diagram of the instrumentation of the test rig.

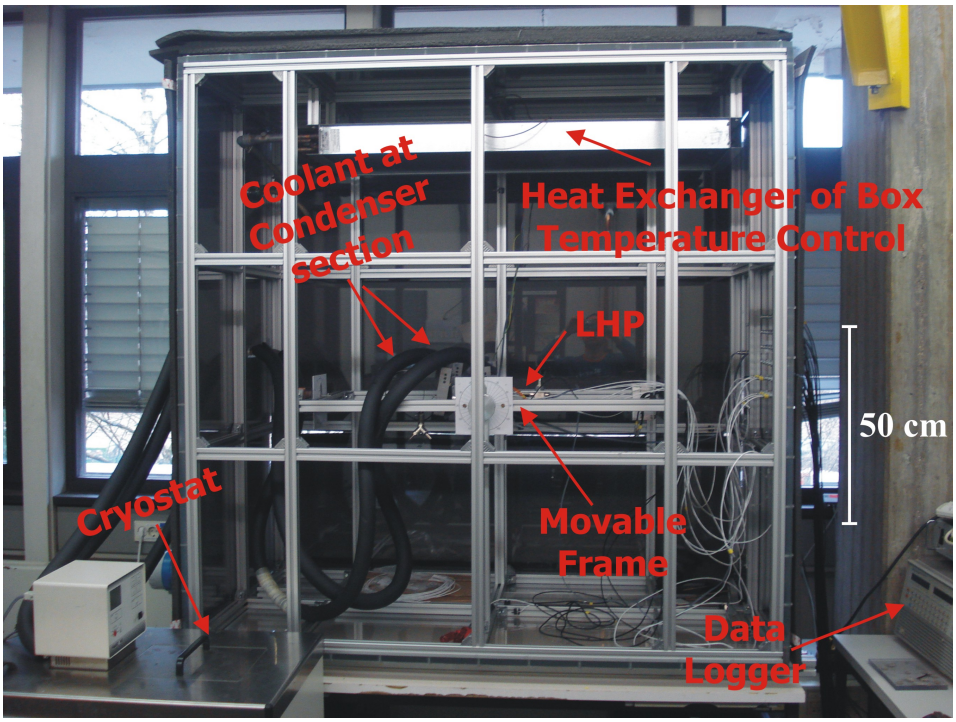

Figure 3.6 – Photo of the test rig with movable frame without front door.

The temperature distribution along the LHP was measured using thermal resistors (Pt100). Figure 3.7 depicts the locations of the temperature sensors: evaporator outlet ($T_{Evap,out}$), condenser inlet ($T_{Cond,in}$), condenser outlet ($T_{Cond,out}$), evaporator inlet ($T_{Evap,in}$) and the compensation chamber (T_{CC}).

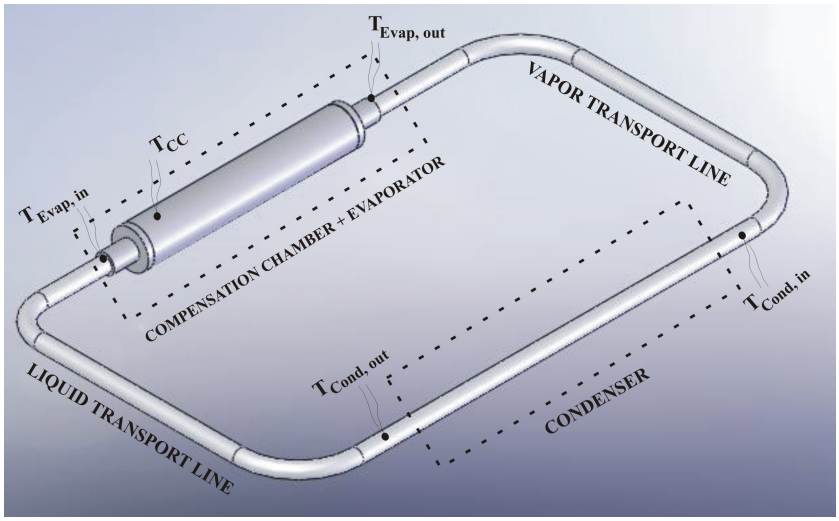

Figure 3.7 – Positions of the thermal sensors along the LHP.

3.4.3 Cooling and Heating Systems

The capillary evaporators of the LHPs were heated using two cartridge heaters inserted into a copper block. The heat sink of the LHPs, which used water as working fluid, were cooled by a thermostat. Figure 3.8 presents the LHP with the condenser box attached to it, the copper block and the cartridge heaters attached to the capillary evaporator of one of the LHPs.

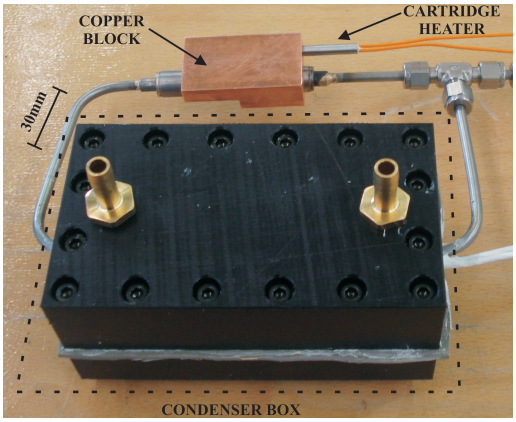

Figure 3.8 – View of one of the LHPs, showing the heating system and the condenser box.

3.4.4 Experimental Procedure

The LHPs were first adjusted to inclinations of interest and the box ambient temperature was set. Once all temperatures of the LHP showed the same value as the box ambient temperature ($\Delta T_{max} = 1^{o}$C), the first power input step of 5 W was applied to the evaporator. Once all temperatures reached a stationary value (or oscillating stationary value), the power input was increased by steps of 5 W. The electrical power (P_{el}) applied

to the cartridge was calculated by measuring the current and the voltage accross it. Assuming no heat losses through the insulation at the heating zone, the applied electrical power is taken as the heat applied to the LHP. The performance tests were carried out for power inputs ranging from 5 to 25 W for the LHP (Acetone) and ranging from 5 to 15 W for the LHP (Water), taking into account the changes in the heat sink temperature and different slopes for the LHPs.

3.4.5 Analysis of Experimental Uncertainties

For LHP, including the accuracy of the temperature sensors and the uncertainties of the data logger, the uncertainty of the temperature is estimated at ± 0.41 ^{o}C. The uncertainty of the electrical power input is estimated at ± 0.12 W including the uncertainty of the power supply unit and the uncertainty of the data logger. Further information concerning the estimative of the experimental uncertainty can be found in Appendix C.

3.5 Description of the CPL

One CPL was manufactured, Fig. 3.9, with the following characteristics: capillary evaporator has 10 mm of inner diameter and 50 mm of length; the same ceramic porous wick used for the LHPs were used; transport lines of liquid and vapor have 2.8 mm of inner diameter and the condenser has 385 mm of length. The main structural characteristics of the CPL are presented in Table 3.3.

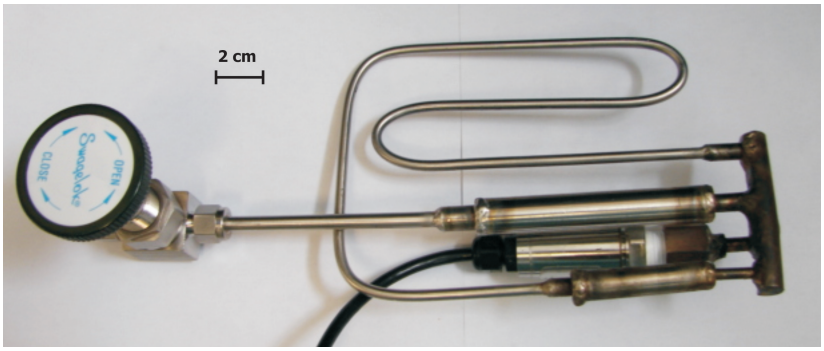

Figure 3.9 – General view of the CPL (water) with cylindrical evaporator, reservoir and pressure sensor.

3.5.1 Filling Station

A similar filling process as for LHP is used for the filling of the CPL using another filling station that is shown in Fig. 3.10.

Table 3.3 – Structural characteristics of the CPL.

Characteristic	CPL (Water)
Evaporator - $d_{evap,in}$, (mm)	10
Evaporator - $d_{evap,out}$, (mm)	12
Number of grooves - N_{groove},	12
Groove heigth - h_{groove}, (mm)	1
Groove width - w_{groove}, (mm)	1
Groove length- L_{groove}, (mm)	25
Active zone length, (mm)	30
Wick - $r_{wick,in}$, (mm)	2.5
Wick - $r_{wick,out}$, (mm)	4.0
Wick length - L_{wick}, (mm)	30
Vapor transport line, (mm)	205
Vapor transport line - $d_{vl,in}$, (mm)	2.8
Liquid transport line, (mm)	140
Liquid transport line - $d_{ll,in}$, (mm)	2.8
Condenser type	Finning Tube
Number of fins - N_{fin},	24
Fin width - δ_{fin}, (mm)	1.0
Fin channel - δ_b, (mm)	2.0
Fin heigth - L_{fin}, (mm)	20
Fin base heigth - L_b, (mm)	10
Fin length - W_{fin}, (mm)	67
Fin base length - W_b, (mm)	77
Condenser length, (mm)	385
Condenser - $d_{cond,in}$, (mm)	2.8
Condenser - $d_{cond,out}$, (mm)	5.0
Reservoir length, (mm)	90

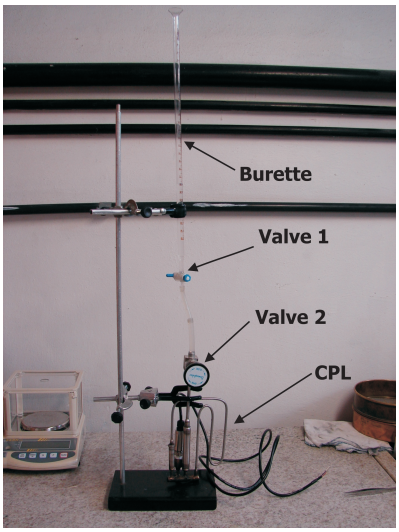

Figure 3.10 – Filling station for the CPL.

For the CPL the total volume does not take into account the reservoir volume, therefore the working fluid charge ratio was tested with 120 and 130%. A working fluid charge ratio of 100% means that only the loop is filled and the reservoir is empty.

3.5.2 Experimental Apparatus

The temperature distribution along the CPL was measured using temperature sensors (thermocouples type T). Figure 3.11 depicts the locations of the temperature sensors: evaporator (T_{Evap}), evaporator outlet ($T_{Evap,out}$), vapor line ($T_{VaporLine}$), condenser inlet ($T_{Cond,in}$), condenser (T_{Cond}), condenser outlet ($T_{Cond,out}$), evaporator inlet ($T_{Evap,in}$), reservoir (T_{Res}) and reservoir outlet ($T_{Res,out}$).

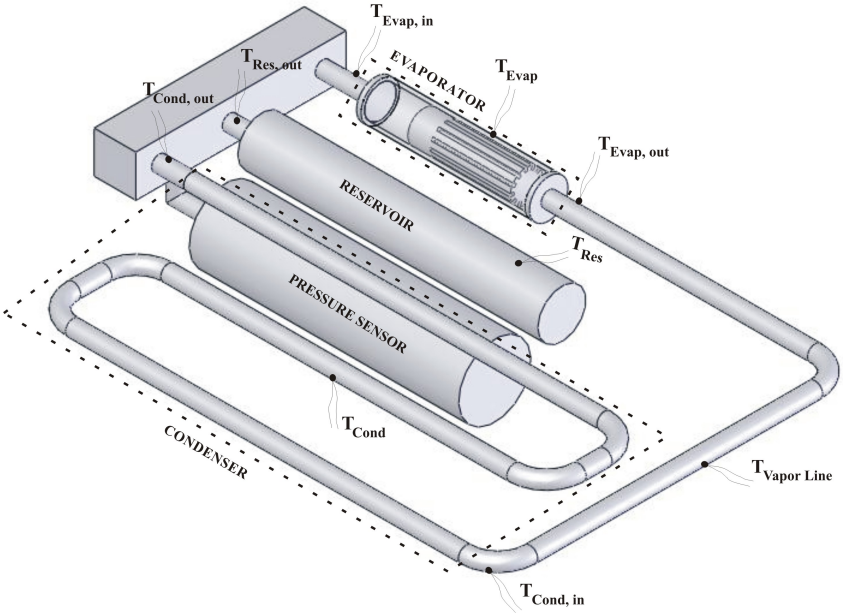

Figure 3.11 – Positions of the thermal sensors along the CPL.

3.5.3 Cooling and Heating Systems

Figure 3.12 presents the CPL with the air cooling system at the condenser section, the heating system of the capillary evaporator and reservoir and the pressure sensor. Two air coolers with fins were used to cool the condenser section as shown in Fig. 3.12(a).

3.5.4 Experimental Procedure

The CPL was adjusted to the orientation of interest (horizontal position) and the room temperature was measured. Once all temperatures of the CPL showed almost the same value as the ambient temperature ($\Delta T_{max} = 1^o$ C), the first power input step of 5 W was applied to the evaporator. Once all temperatures reached a stationary value (or oscillating stationary value), the power input was increased by steps of 5 W. The electrical power (P_{el}) applied to the electric heater was calculated by measuring the voltage and the current which pass through the wire. Assuming no heat losses through the insulation at the heating zone, the applied electrical power is taken as the thermal heat applied to

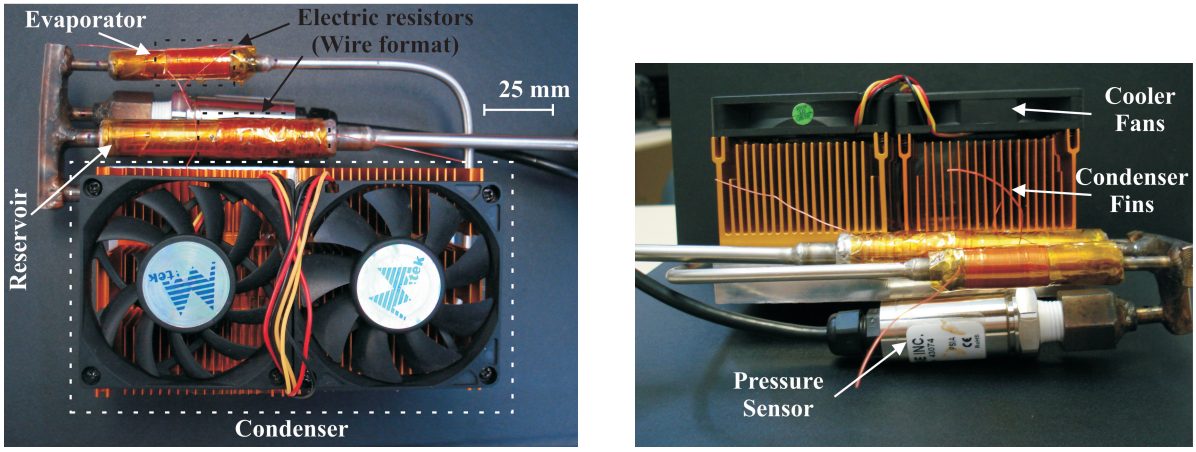

(a) (b)

Figure 3.12 – (a) Top view of the CPL, the heater system and the condenser and (b) side view of the CPL, the coolers fans, the fins of the condenser and the pressure sensor.

the CPL. The performance tests of the CPL were carried out for power inputs ranging from 5 to 30 W.

3.5.5 Analysis of Experimental Uncertainties

For the CPL, the uncertainty of the measurements were estimated for the temperature, power input and pressure. Taking into account the accuracy of the temperature sensors (thermocouples type T) and the uncertainties of the data logger (Agilent 34970A with 20 channels), the uncertainty of the temperature measured was estimated at ± 1.8 ^{o}C. The uncertainty of the electrical power input was estimated at ± 0.28 W including the uncertainty of the power supply unit and the uncertainty of the data logger (Agilent N6700B). The experimental uncertainty of pressure sensor was estimated as ± 345.22 Pa. Further information regarding the estimation of the experimental uncertainties can also be found in Appendix C.

4 Experimental Results and Analysis

This chapter presents the results of the thermal behaviour of two LHPs and one CPL. Performance tests of two LHPs using acetone and water as working fluids were carried out for power inputs up to 25 W and performance tests of one CPL using water were carried out for power inputs up to 30 W. An analisys of the results is developed regarding the startup and operation of the systems for different working fluid inventory, heat sink temperature and inclination. Besides, an analisys of the capillary limit for all systems and a comparison between the experimental and theoretical (modeling presented in Chapter 2) results are also presented.

4.1 Results of LHP with Acetone

4.1.1 The Working Fluid Inventory and Startup

A successful startup is mainly related to the applied heat load, heat sink temperature and working fluid inventory. Figure 4.1 shows the start up for $50, 60, 65$ and 70% working fluid charge ratios, under heat load of 10 W and condenser positioned 90^o above the evaporator. This position is more favorable to the operation of the LHP because the liquid flows to the evaporator due to the capillary and also to the gravity action. Besides, it can be sure that the evaporator is full filled with liquid before start-up.

In Fig. 4.1(a), after approximately 60 s, the inlet condenser temperature ($T_{cond,in}$) increases fast, indicating that the vapor front reached the condenser. At 130 s, however, the temperature starts to decrease, indicating that the system failed to start up. This sudden decrease is caused by lack of working fluid along the loop. So, there is not enough liquid flow to the capillary evaporator. As a consequence of no evaporation of liquid, the outlet temperature of evaporator increases continuously. A similar behavior is presented in Fig. 4.1(b), where the system failed at approximately 275 s.

A successful startup occurred for 65% working fluid charge ratio, shown in Fig. 4.1(c).

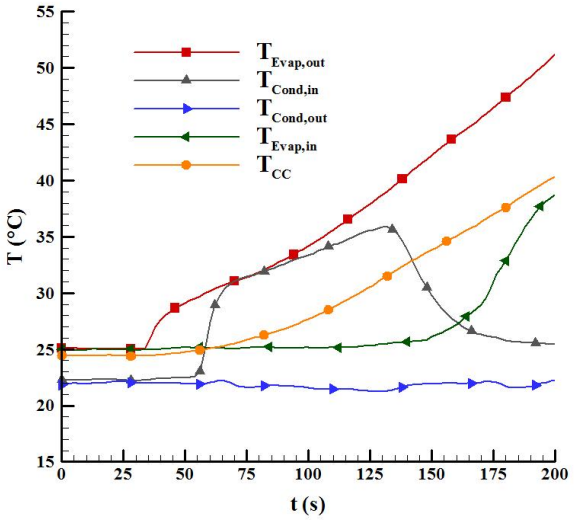

(a) 50%

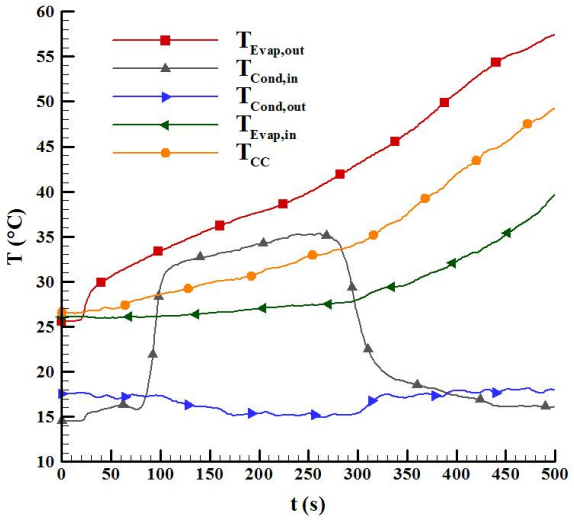

(b) 60%

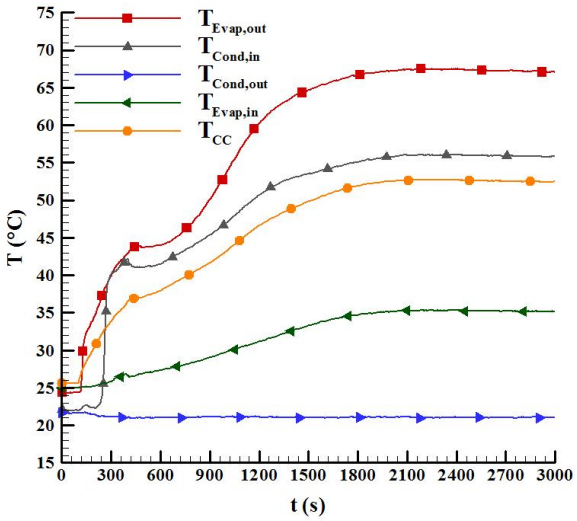

(c) 65%

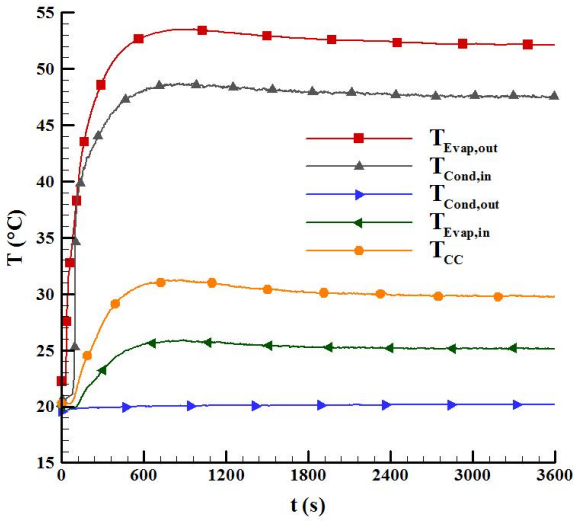

(d) 70%

Figure 4.1 – Startup under heat load of 10 W and condenser positioned 90° above the evaporator for different working fluid charge ratios.

The outlet evaporator and the inlet condenser temperatures reached a steady state condition at 68 and 56 ^{o}C, respectively. A faster start up was achieved for 70% working fluid charge ratio. Now the outlet evaporator and the inlet condenser temperatures reached the steady state condition at 52 and 47 ^{o}C, respectively. Note that there is a temperature difference in the operation temperature ($T_{evap,out}$) of 16^{o}C between the cases (c) and (d). So, the fluid inventory plays also an important role regarding the operating temperature of the LHP. The startup was not successful for working fluid charge ratio smaller than 60% and there was no significant decrease of operation temperature for working fluid charge ratios higher than 70%.

4.1.2 Temperatures of LHP (acetone) as a Function of Heat Load

Figure 4.2 depicts the temperatures of the evaporator outlet ($T_{evap,out}$), condenser inlet ($T_{cond,in}$), condenser outlet ($T_{cond,out}$), evaporator inlet ($T_{evap,in}$) and the compensation chamber (T_{CC}) at horizontal position and heat sink temperature of 20 ^{o}C for stepwise increase in heat flux.

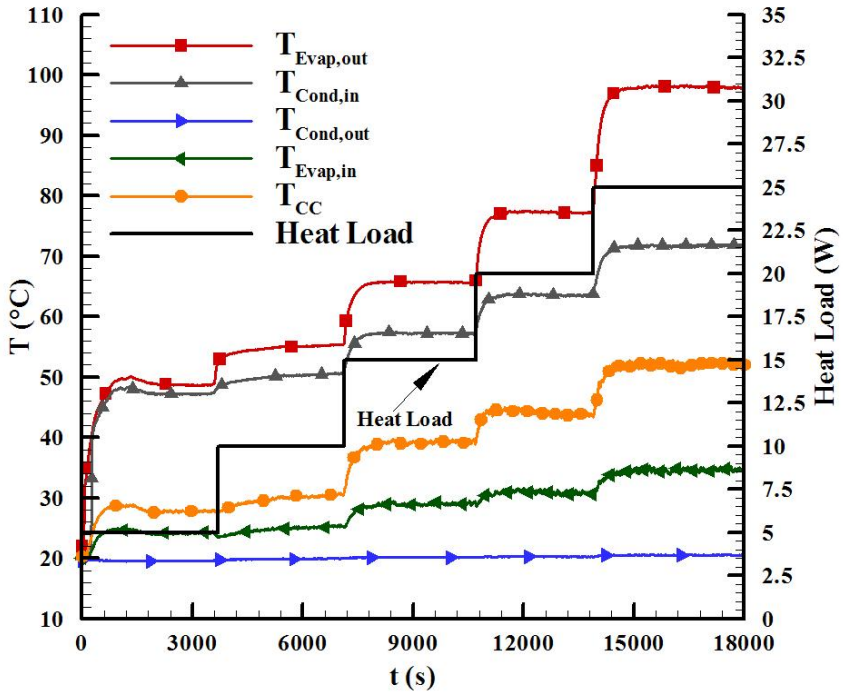

Figure 4.2 – Temperatures of LHP (acetone) for heat loads increasing at horizontal position and at heat sink temperature of 20 ^{o}C.

The LHP (acetone) worked satisfactorily in the power range from 5 to 25 W. The limit temperature of 100 ^{o}C (assumed for safety reasons) was reached for 25 W power input. Contrarily to capillary pumped loops, the temperature of the compensation chamber (T_{CC}) is not constant, as shown in Fig. 4.2, changing from 29 to 51 ^{o}C. The measured outlet evaporator temperature was higher, from 50 to 98 ^{o}C, and the temperature difference to the heat sink temperature (20 ^{o}C) varied from 30 to 78 ^{o}C.

4.1.3 Heat Sink Temperature

For low heat loads the evaporator temperature is high. As the heat load increases, the evaporator temperature decreases until a minimum value is reached. This region is called the variable conductance mode. Afterwards it starts to increase linearly, characterizing the fixed conductance mode. Experimental studies exploring this phenomenon have been reported in Chen *et al.* (2006), Ku (1999) and Chuang (2003). Their results showed that

the heat sink temperature influences the operation temperature of LHP only when it is much lower than the ambient temperature.

Figure 4.3 presents the outlet evaporator temperatures for 10 and 20 W for the LHP in horizontal position, using acetone as working fluid and heat sink temperatures varying from 10 to 40 ^{o}C. With exception the value for heat load of 10 W under heat sink temperature of 10 ^{o}C, there is a small difference, mostly within the uncertainty level, between the outlet evaporator temperatures when the heat sink temperature changes for both heat loads. Since the heat sink temperature is approximately equal to the ambient temperature, it was not possible to state anything concerning the conductance mode.

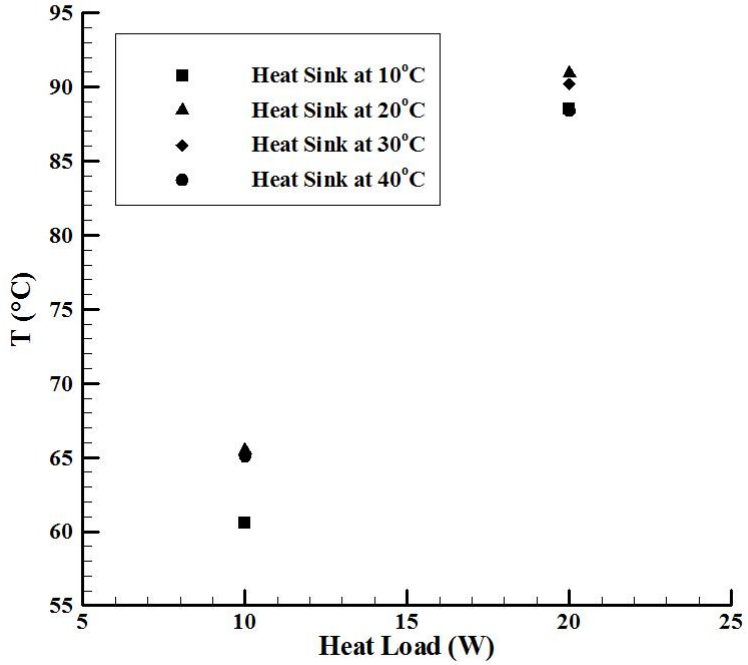

Figure 4.3 – Outlet evaporator temperatures of the LHP (acetone) for heat loads of 10 and 20 W at horizontal position and at heat sink temperatures of 10, 20, 30 and 40 ^{o}C.

4.1.4 Inclination of the LHP

Four different scenarios were analyzed: (i) evaporator positioned 90^{o} above the condenser; (ii) condenser positioned 90^{o} above the evaporator, according to Fig. 4.4; (iii) evaporator positioned 10^{o} above the condenser; (iv) condenser positioned 10^{o} above the evaporator.

Figure 4.5 depicts the outlet evaporator temperature of LHP (acetone) for heat loads ranging from 10 to 20 W. As expected, due to the position effect of thermobuoyancy on the mass flow rate, the lowest outlet evaporator temperature was measured for the condenser positioned 90^{o} above the evaporator. On the other hand, the highest temperature was measured for the evaporator positioned 90^{o} above the condenser.

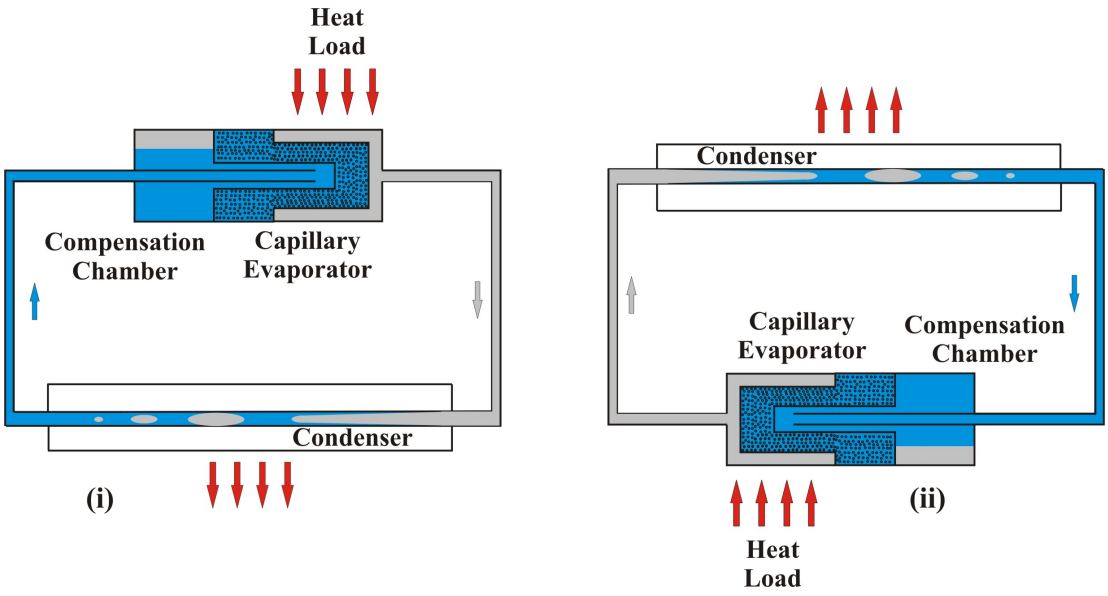

Figure 4.4 – (i) evaporator positioned 90^o above the condenser and (ii) condenser positioned 90^o above the evaporator.

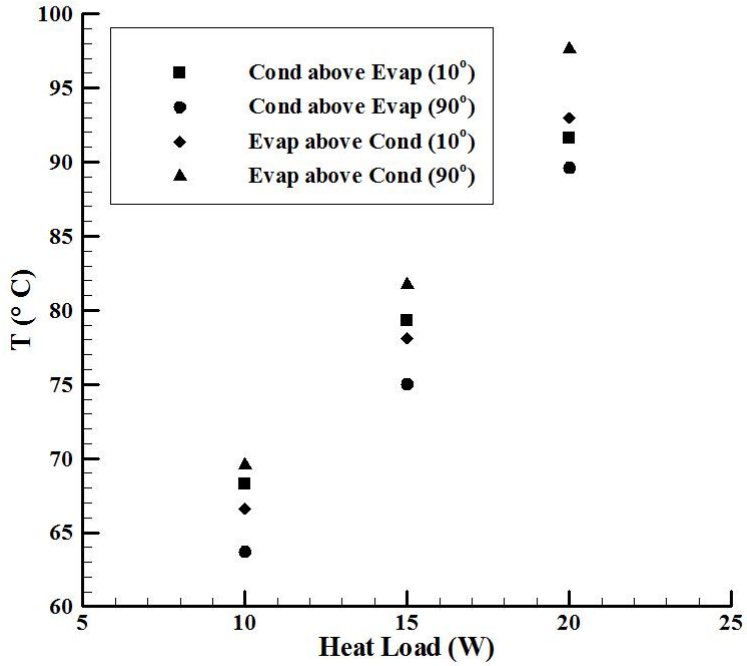

Figure 4.5 – Outlet evaporator temperatures of the LHP (acetone) for heat loads of 10, 15 and 20 W at different slopes and at heat sink temperature of 20 ^{o}C.

4.2 Results of LHP with Water

4.2.1 The Working Fluid Inventory and Startup

Figure 4.6 shows the start up for 50, 55, 60 and 65% working fluid charge ratios, under heat load of 10W and at horizontal position. The startup was successful for working fluid charge ratio of 60%. In Fig. 4.6(a) the temperature of condenser inlet increases but does not reach a stationary state and after 800 s the system fails. This elapsed time until

failure increases as the working fluid charge ratio increases, as it can seen in Figs. 4.6(a) and (b). It took 1500 and 2250 s for system failure in case of 55 and 60% working fluid charge ratios, respectively. Finally, the successful startup was reached for 65% working fluid charge ratio, Fig. 4.6(d).

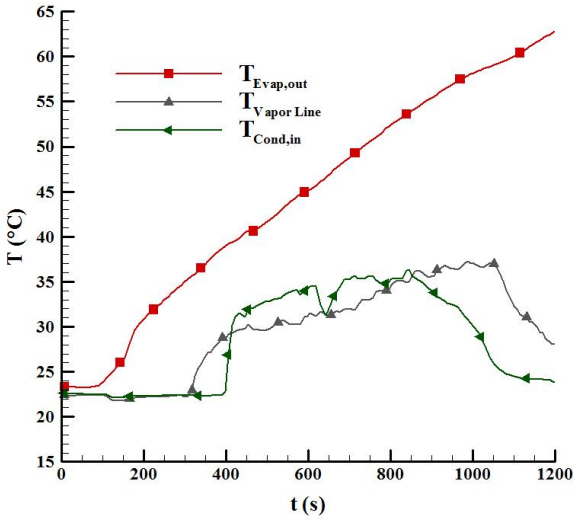

(a) 50%

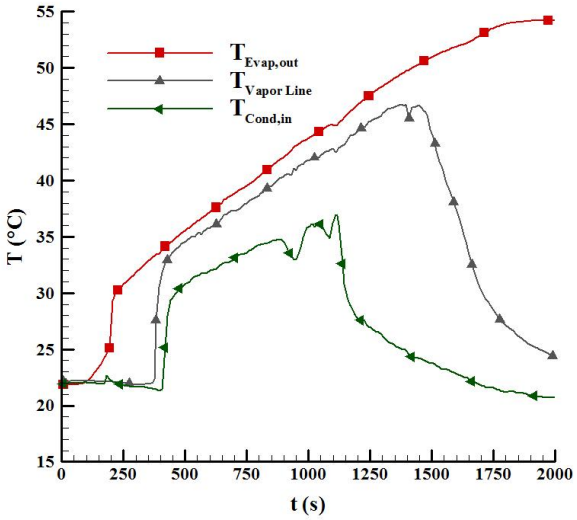

(b) 55%

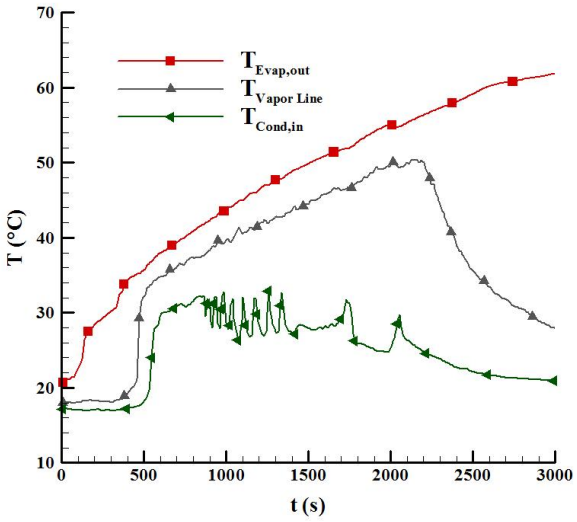

(c) 60%

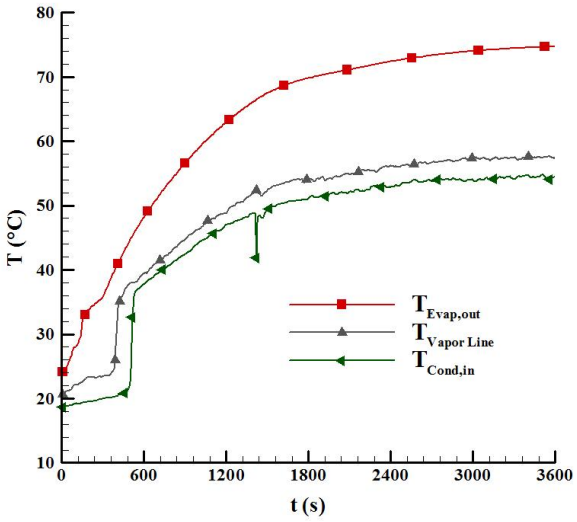

(d) 65%

Figure 4.6 – Startup under heat load of 10 W and condenser positioned 90° above the evaporator for diffrent working fluid charge ratios.

4.2.2 Temperatures of LHP (water) as a Function of Heat Load

Figure 4.7 depicts the loop temperatures, measured in the same positions as in the LHP with acetone, for the LHP with water at horizontal position and at heat sink temperature of 20 °C. The LHP (water) worked satisfactorily in the range from 5 to 15 W, as shown in Fig. 4.7. The maximum operation temperature was again set to 100 °C for safety reasons. The outlet evaporator temperature reached higher temperatures ranging

from 60 to 100 ^{o}C, and the temperature difference to the heat sink temperature (20 ^{o}C), varied from 40 to 80 ^{o}C.

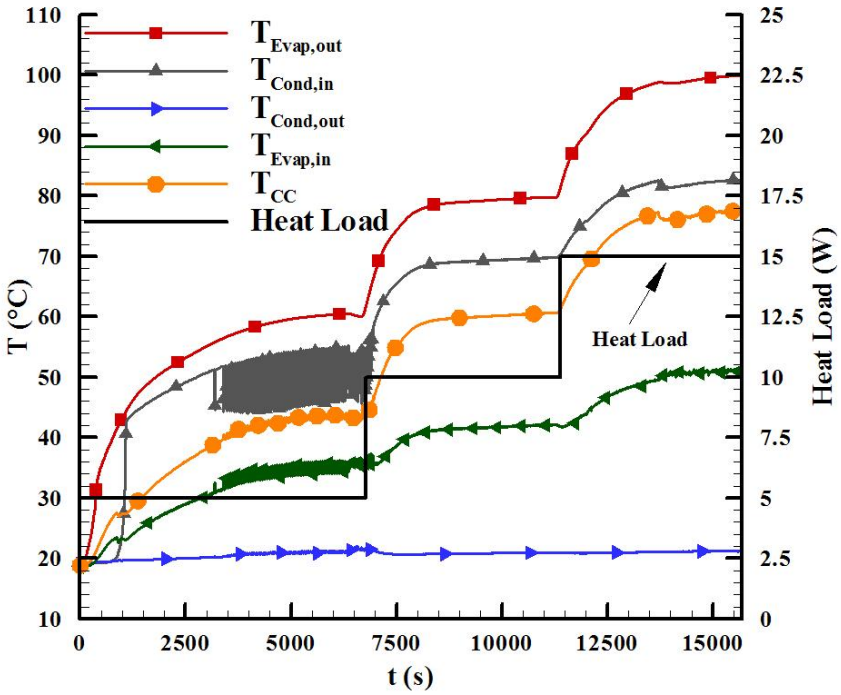

Figure 4.7 – Temperatures of LHP (water) for heat loads increasing at horizontal position and at heat sink temperature of 20 ^{o}C.

4.2.3 Heat Sink Temperature

Figure 4.8 presents outlet evaporator temperatures for 5, 10 and 15 W at horizontal position, considering water as working fluid and heat sink temperatures varying from 10 to 40 ^{o}C. For low heat load (5 W) there is a small difference between the temperatures. As the heat load increases, this difference increases and reaches up to 10.3 ^{o}C. Again, since the heat sink temperature is approximately equal to the ambient temperature, it is not possible to state anything concerning the conductance mode.

4.2.4 Inclination of the LHP

Figure 4.9 shows the outlet evaporator temperature of LHP (water) for heat loads from 5 to 15 W. The lowest outlet evaporator temperature was also measured for the condenser positioned 90^{o} above the evaporator. The highest temperature was measured for evaporator positioned 10^{o} above the condenser and the LHP did not start up for evaporator positioned 90^{o} above the condenser.

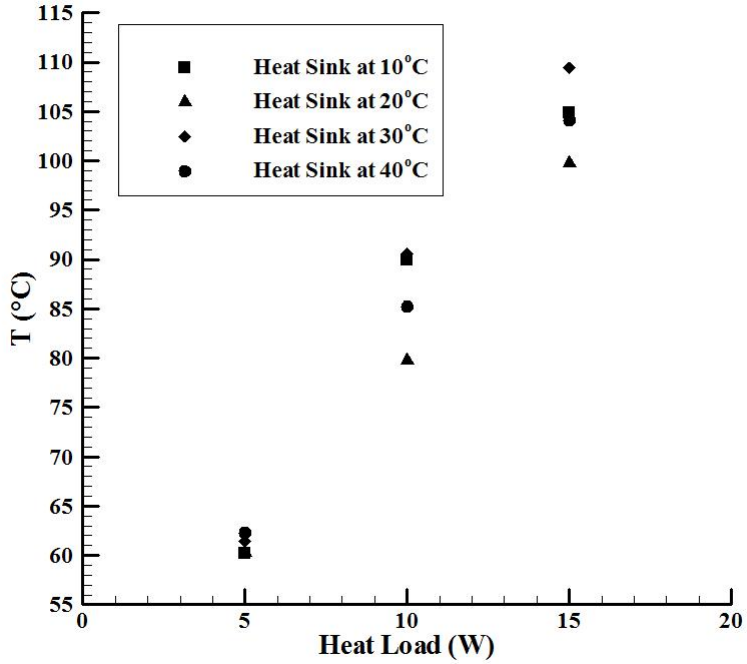

Figure 4.8 – Outlet evaporator temperatures of the LHP (water) for heat loads of 5, 10 and 15 W at horizontal position and at heat sink temperatures of 10, 20, 30 and 40 ^{o}C.

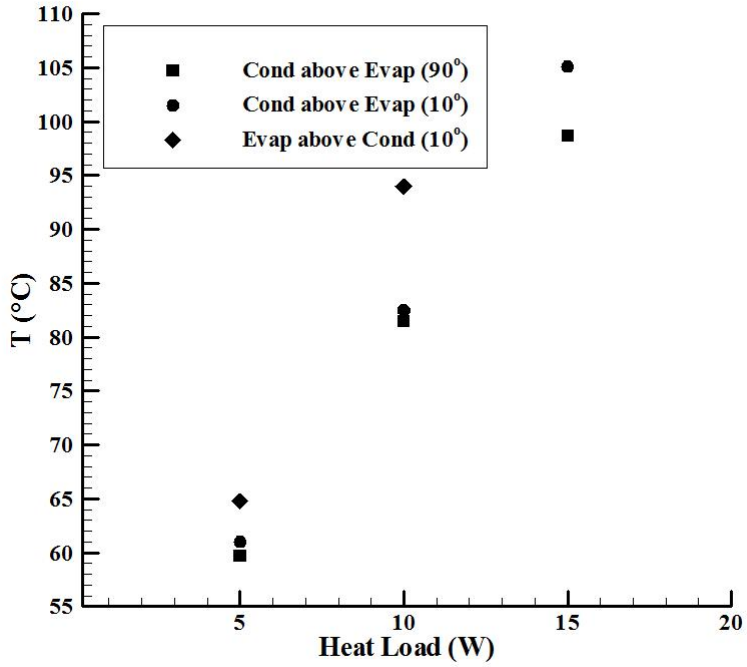

Figure 4.9 – Outlet evaporator temperatures of the LHP (water) for heat loads of 5, 10 and 15 W at different slopes and at heat sink temperature of 20 ^{o}C.

4.3 Comparision between LHP with Water and Acetone

Here, the results of two LHPs using water and acetone are compared. The Tab. 4.3 presents the time for the startup corresponding to the results shown in Figs. 4.1 and 4.6.

It is noticed that the time for startup for the LHP using acetone was lower than the LHP using water. To some extent, this difference between the time for the startup can be due to several factor such as thermal properties and purity of the working fluid, filling and manufactoring of the LHPs and so on.

Table 4.1 – Startup times for the LHPs.

Acetone		Water	
R* (%)	t** (s)	R (%)	t (s)
50	28	50	253
60	78	55	263
65	151	60	371
70	63	65	361

* R is the working fluid charge ratio.
** t is the startup time.

Figure 4.10 presents the temperatures of the evaporator outlet of the LHPs using acetone and water as a function of the heat load in horizontal position. It was observed a difference between the operation temperatures in the experiments using water and acetone varing from 13 ^{o}C at the lowest load to 33 ^{o}C at the highest load. To some extent, this difference can be due to the vapor pressure and/or the thermal inertia (startup time). The vapor pressure of acetone is lower than the water and, as a consquence, the evaporation temperature should be lower. The time of startup for the LHP with acetone is lower than with water, so the LHP with water takes more time to reach the stabilization of its operation temperature, causing an increase in temperatures of the system.

A small temperature difference between the evaporator outlet and the heat sink is required for a successful application of these LHPs. Therefore, high temperature differences claim for changes in the properties of the ceramic porous wick (porosity, pore size and thermal conductivity) or improvements in the original LHP design. A total thermal resistance, following Maydanik & Vershinin (2009), can be defined as,

$$R_{total} = \frac{(T_{Evap} - T_{HS})}{\dot{Q}_{evap}}, \tag{4.1}$$

where T_{HS} is the heat sink temperature, *i.e.*, the average cooling temperature. Here $T_{Evap,out}$ was used instead of T_{Evap}, since it was not possible in the set up developed to fix a thermoresistor at the interface between the copper block heater and the evaporator.

This resistance plays the role of a relative measure of the LHP effectiveness. When the same system operates with two different fluids, the conditions that lead to minimum resistance imply a higher heat transfer capacity per degree of temperature difference.

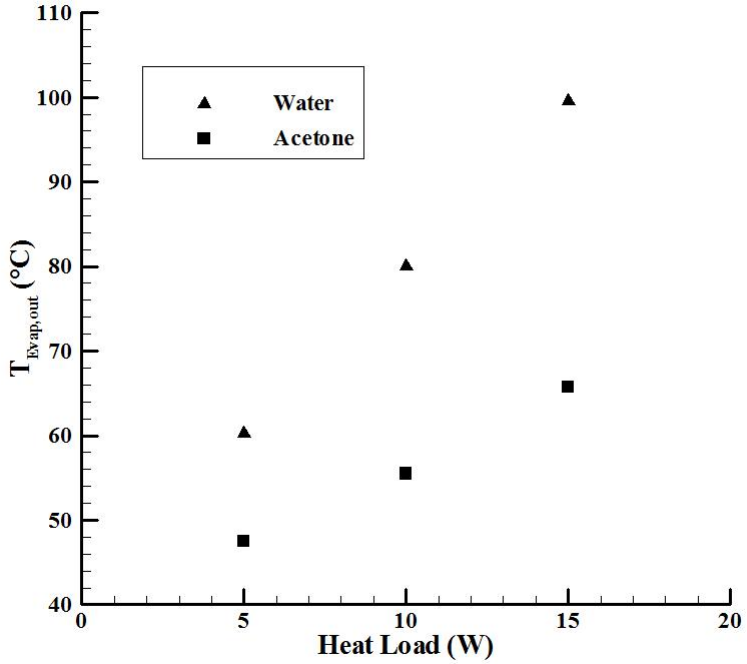

Figure 4.10 – Outlet evaporator temperatures of the LHPs with acetone and water for heat loads of 5, 10 and 15 W at horizontal position and at heat sink temperature of 20 ^{o}C.

Figure 4.11 depicts the total thermal resistance for the LHPs for both water and acetone. It is noticed that the total thermal resistance for the LHP using water is higher than with acetone. This difference is due to the higher temperatures in the evaporator outlet, as it was explained before. For the measurements made, from 5 to 25 W, the total thermal resistance was maximum for a heat load of 5 W (8.2 ^{o}C/W for LHP using water and 5.7 ^{o}C/W for LHP using acetone) and it was minimum for a heat load of 20 W (2.9 ^{o}C/W for LHP using acetone). The operation with water leaded to a minimum total thermal resistance of 5.3 ^{o}C/W for a heat load of 15 W. The smaller the total thermal resistance, the greater the heat transfer between the hot (evaporator surface) and cold (heat sink) sources of the LHP for a given temperature difference.

4.4 Results of CPL with Water

4.4.1 The Working Fluid Inventory and Startup

The set point temperature of the reservoir controls the CPL operating temperature regardless of changes in the heat load or heat sink temperature as long as the reservoir is in a two phase condition. For that, the amount of working fluid in the loop should be sufficient so that at minimum heat load and minimum sink temperature, the condenser is almost completely blocked by liquid. If the system does not contain enough liquid, the

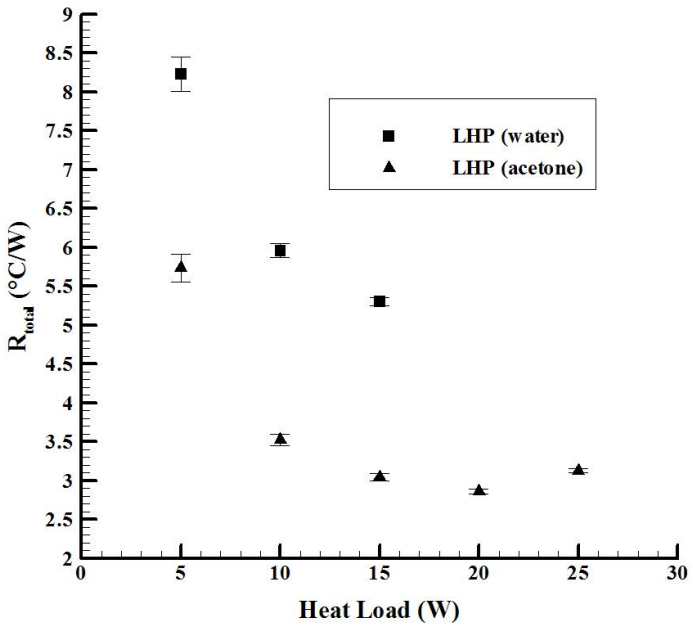

Figure 4.11 – Total thermal resistance vs. heat load for both LHPs.

reservoir empties before the condenser is completely blocked by liquid.

On the other hand, if the system contains too much liquid and the reservoir cannot accommodate the full range of liquid change in the condenser, the CPL will work in the fixed conductance mode and the temperature will not be controlled, (KU, 1994). As a result, the amount of working fluid in the loop is a very important parameter for the proper operation of CPLs. Most of the time, however, it is not trivial to find the ideal working fluid charge ratio. Here, besides varying the working fluid charge ratio, it was also required to change the set point temperature of the reservoir for the proper start up of the CPL. Figure 4.12 shows the start up for three set point temperatures of the reservoir ($40, 50$ and 60 ^{o}C), for 120% working fluid charge ratio, heat load of 10W and CPL positioned at horizontal position. The startup was not successful for set point temperatures of the reservoir of 40 and 50 ^{o}C.

In Fig. 4.12(a) it is shown that after approximately 175 s the inlet condenser temperature ($T_{cond,in}$) increases fast, indicating that the vapor front reached the condenser. At 500 s, however, the evaporator temperature increases continuously, showing that the system failed. A similar thermal behavior is shown in Fig. 4.12(b), where the system failed at approximately 1700 s. The successful startup was reached for the set-point temperature of the reservoir of 60 ^{o}C after a short excursion of the evaporator temperature, as shown in Fig. 4.12(c).

The lower the set point temperature of the reservoir, the lower the saturation temperature of evaporation into the capillary evaporator. Therefore, in order to have startup

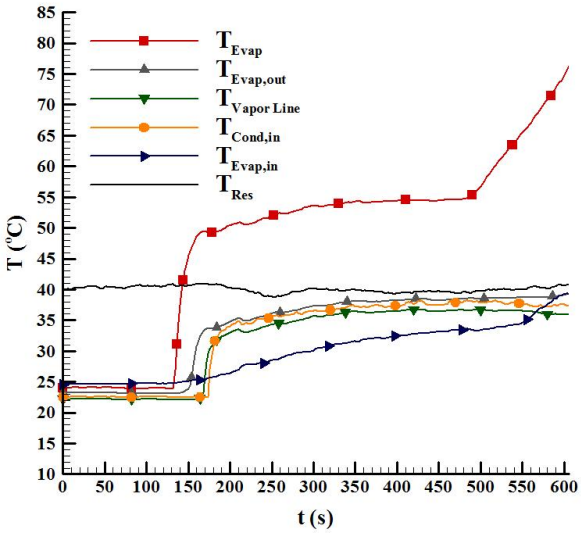

(a) $T_{reservoir} = 40\ ^{o}$C

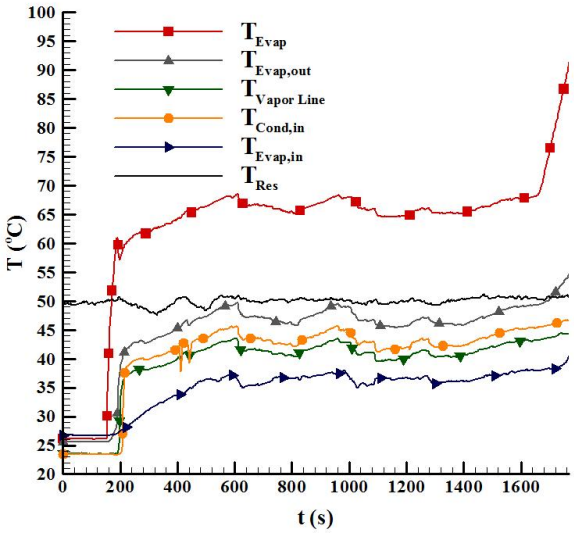

(b) $T_{reservoir} = 50\ ^{o}$C

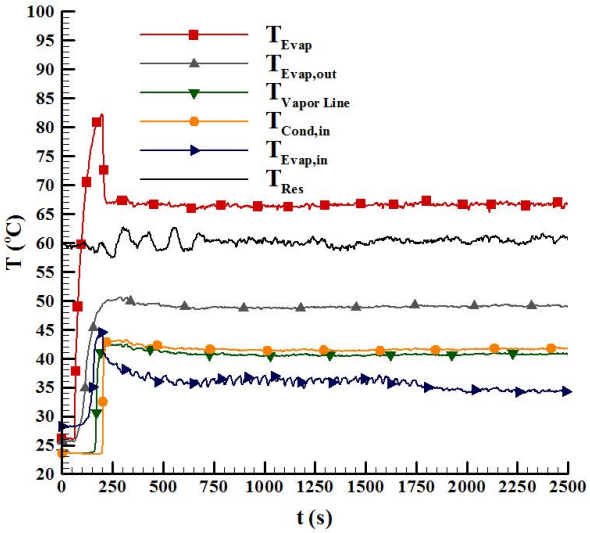

(c) $T_{reservoir} = 60\ ^{o}$C

Figure 4.12 – CPL startup under heat load of 10 W, working fluid charge ratio of 120% and at horizontal position for diffrent set point temperatures of the reservoir.

at lower reservoir temperature, the working fluid charge ratio was increased to 130% and the results are shown in Fig. 4.13 for heat load of 10 W and at horizontal position. Figure 4.13(a) shows that the CPL did not startup successfully for the set point temperature of the reservoir of 40 ^{o}C. The system failed at approximately 1100 s. The successful startup was reached for the set point temperature of the reservoir of 50 and 60 ^{o}C, Figs. 4.13(b) and 4.14. Besides, in the case for the set point temperature of the reservoir of 50 ^{o}C, the CPL only reached the successful startup under heat load equal or smaller than 10 W.

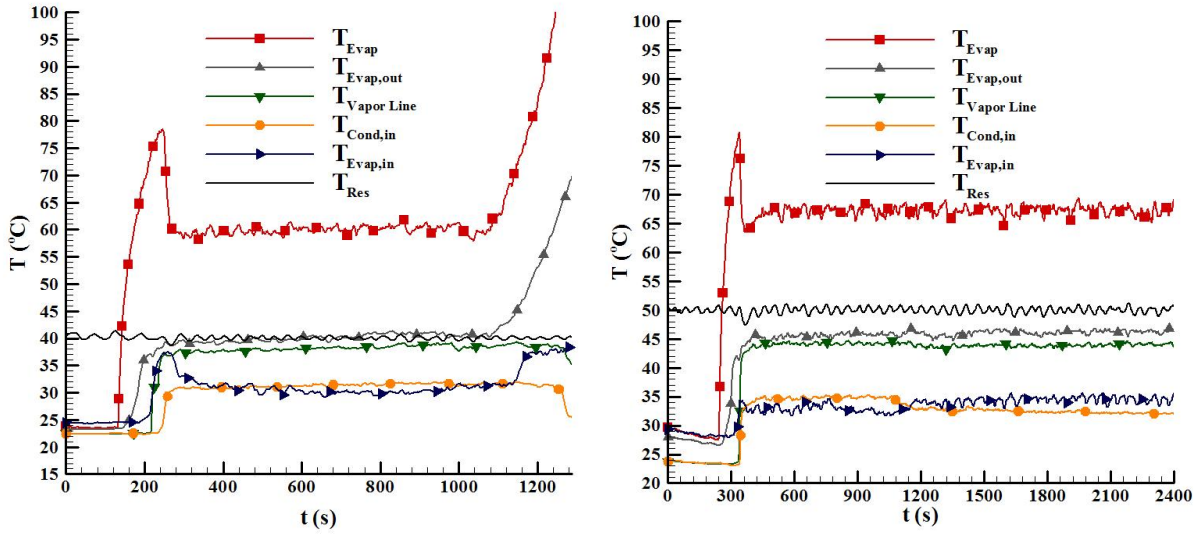

(a) $T_{reservoir} = 40\ ^{o}$C (b) $T_{reservoir} = 50\ ^{o}$C

Figure 4.13 – CPL startup under heat load of 10 W, working fluid charge ratio of 130% and at horizontal position for diffrent set point temperatures of the reservoir.

4.4.2 Temperatures of CPL as a Function of Heat Load

Figure 4.14 depicts the temperatures of the evaporator (T_{evap}), evaporator outlet ($T_{evap,out}$), condenser inlet ($T_{cond,in}$), condenser outlet ($T_{cond,out}$), evaporator inlet ($T_{evap,in}$) and the reservoir ($T_{reservoir}$) at horizontal position with air cooling in the condenser. The charge ratio was 130% and the set-point temperature of the reservoir was 60 ^{o}C. The CPL had a sucessful startup and reached nearly the steady state for the range of heat load from 5 to 30 W.

The temperature of the evaporator outlet for heat loads of 5 and 10 W remained approximately constant and varied only 1^{o}C. For heat loads higher than 10 W the temperature of the evaporator outlet increased. It can be noticed that the temperatures of the evaporator outlet and the condenser inlet are close for heat load up to 10 W. The increased difference observed for higher loads is a consequence of axial heat transfer from the heating surface of the evaporator to its outlet. The higher temperature at the evaporator inlet is also a consequence of axial heat transfer along the tubbing from evaporator surface.

The CPL (water) worked satisfactorily in the range from 5 to 30 W. The limit temperature of 100 ^{o}C (assumed for safety reasons) at evaporator outlet was not reached even for 30 W. However, considering the evaporator temperature as a limiting temperature, the CPL worked properly up to heat load of 20 W.

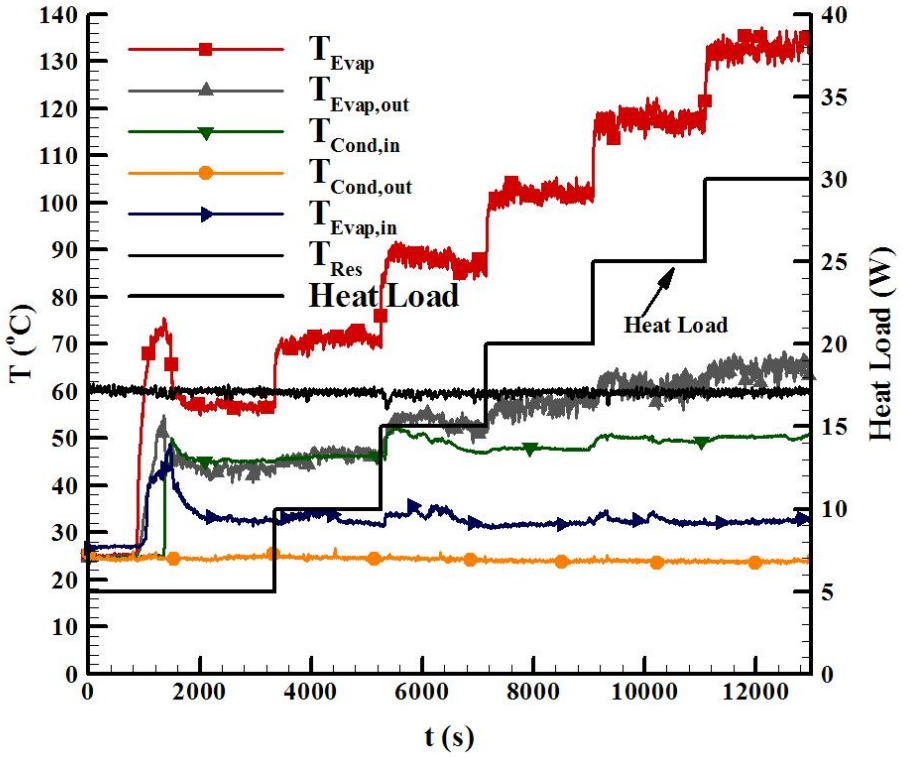

Figure 4.14 – Temperatures of the CPL (water) for heat loads increasing at horizontal position.

4.5 Comparision of the Results

Here, the results of the LHP and CPL are compared. Table 4.2 presents the time for the startup corresponding to the results shown in Figs. 4.6, 4.12 and 4.13 for the LHP and CPL, both using water, respectively. It is noticed that the times of startup for the CPL were lower than for the LHP. To some extent, this difference between the times of startup can be due to the differences between the evaporation areas in the capillary evaporator of both systems. The evaporation area of the CPL (785.4 mm^2) is two time greater than the area of the LHP (392.7 mm^2), and therefore the CPL can pump approximately twice more liquid.

Figure 4.15 presents the temperatures of the evaporator outlet of the LHP using water and acetone, the CPL using water, and the evaporator temperature of CPL using water as a function of the heat load, at horizontal position for charge ratio of 130%. A large difference between the outlet evaporator temperatures ($T_{evap,out}$) of the LHPs using water and acetone, varing from 13 to 33 ^{o}C, is observed. The outlet evaporator temperature of the LHP and the CPL (both with water) varied from 19 to 44 ^{o}C. It is clear from Fig. 4.15 that in the results of the CPL with water, there is a significant difference between the temperature of evaporator (T_{evap}) and its outlet temperature ($T_{evap,out}$), varing from 14 to 66 ^{o}C. This difference occurs because the temperature sensor of the evaporator

Table 4.2 – Startup times for the LHP and CPL operating with water.

LHP		CPL	
R[a] (%)	t[b] (s)	R (%)	t (s)
50	253	120[c]	96
55	263	120[d]	200
60	371	130[c]	114
65	361	130[d]	160

[a] R is the working fluid charge ratio.
[b] t is the startup time.
[c] In this case $T_{res} = 50$ ^{o}C.
[d] In this case $T_{res} = 60$ ^{o}C.

(T_{evap}) was placed very close to the electric resistor (heating system). The existence of this temperature difference indicates the presence of a large heat transfer along the evaporator.

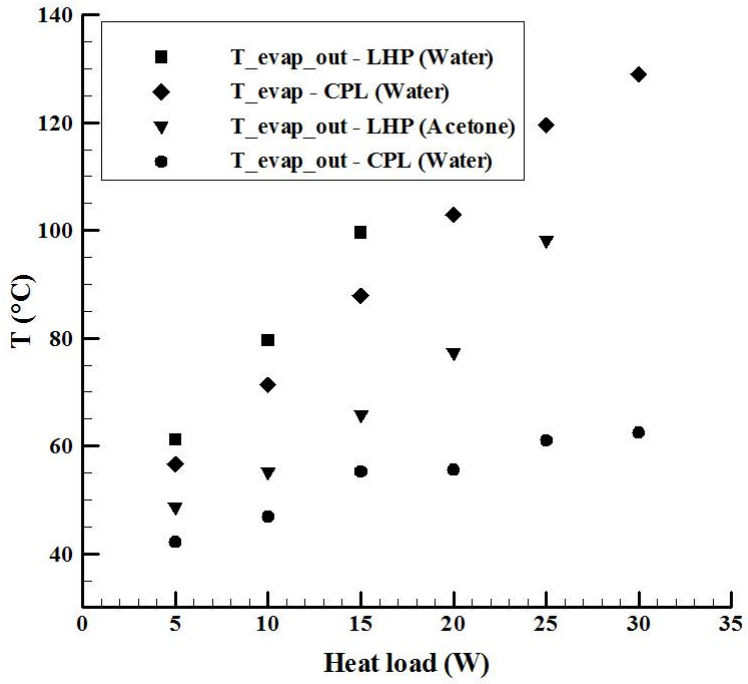

Figure 4.15 – Outlet evaporator temperature of the LHPs with acetone and water and CPL with water, and evaporator temperature of the CPL with water for heat loads from 5 to 30 W at horizontal position, with 130% load.

In order to compare the results obtained for the LHPs and CPL, the total resistance is calculated using Eq. 4.1. For the CPL, the temperature of the evaporator was used instead of the outlet temperature of evaporator and the heat sink temperature is an average temperature between the inlet and outlet of condenser. Figure 4.16(a) depicts the total thermal resistance for the LHPs and CPL. It is noticed that the total thermal resistances for the CPL, even using the evaporator temperature (T_{evap} - CPL), are lower

than LHP(water). According to the results presented in Fig. 4.16(a), the CPL with water worked better than both LHPs for low heat load (5 W). The total thermal resistance was larger for heat load of 5 W (5.6 ^{o}C/W for CPL using water, 8.2 ^{o}C/W for LHP using water and 5.7 ^{o}C/W for LHP using acetone) and it reached the lowest values in the range measured for heat load of 30 W (3.3 ^{o}C/W for CPL using water), heat load of 15 W (5.3 ^{o}C/W for LHP using water) and heat load of 20 W (2.9 ^{o}C/W for LHP using acetone). The total thermal resistance (R_{total}) has been customary to express the quality of LHPs and CPLs, however, it is noticed that R_{total} is size dependent, *i.e.*, the R_{total} does not take into account the area of evaporator where the heat transfer rate is applied. Thus, a different figure of merit is proposed here,

$$R''_{total} = \frac{\Delta T}{q''}, \tag{4.2}$$

where q'' is the heat flux dissipated by the two-phase system and $\Delta T = T_{Evap} - T_{HS}$ is the temperature difference between the hot surface, where the thermal load is applied, and the heat sink.

It is noticed in Fig. 4.16(b) that R''_{total} of the CPL (water) is larger than both LHPs. The R''_{total} was larger for heat flux of 0.53 W/cm^2 (52.8 ^{o}C/W/cm^2 for CPL using water) and heat flux of 1.06 W/cm^2 (38.8 ^{o}C/W/cm^2 for LHP using water and 27.0 ^{o}C/W/cm^2 for LHP using acetone) and it reached the lowest values measured for heat flux of 3.18 W/cm^2 (31.7 ^{o}C/W/cm^2 for CPL and 25.0 ^{o}C/W/cm^2 for LHP, both using water) and heat flux of 4.24 W/cm^2 (13.5 ^{o}C/W/cm^2 for LHP using acetone). Now, according to the results obtained with R''_{total}, the LHP (acetone) worked better than the CPL and LHP, both using water.

Figures 4.17 and 4.18 present a comparison between the results of the present work and the results reported in the literature for R_{total} and R''_{total}. Figure 4.17 shows the results regarding the CPLs and Fig. 4.18 shows the results regarding the LHPs. It is noticed in Fig. 4.17(a), regarding the R_{total}, that the CPL (water) worked only better than the results reported by Wang *et al.* (2008) and Camargo (2004) for ceramic wick. On the other hand, in Fig. 4.17(b), regarding the R''_{total} which takes into account the heat flux instead of the heat transfer rate, the CPL (water) worked better than all CPLs. The result reported by Camargo (2004) for ceramic wick regarding the R''_{total} is not shown because its value reached 406.4 ^{o}C/W/cm^2 and it is out of the scale of the graphic.

It is noticed in Fig. 4.18(a) and (b), regarding the R_{total} and R''_{total}, despite the LHPs developed here did not work as well as the mini-LHPs, they presented good results. One reason for this relatively poor result is that the mini-LHPs reported by the other authors

use ammonia as working fluid which, due to its thermal properties, is considered the best working fluid for capillary pumping systems.

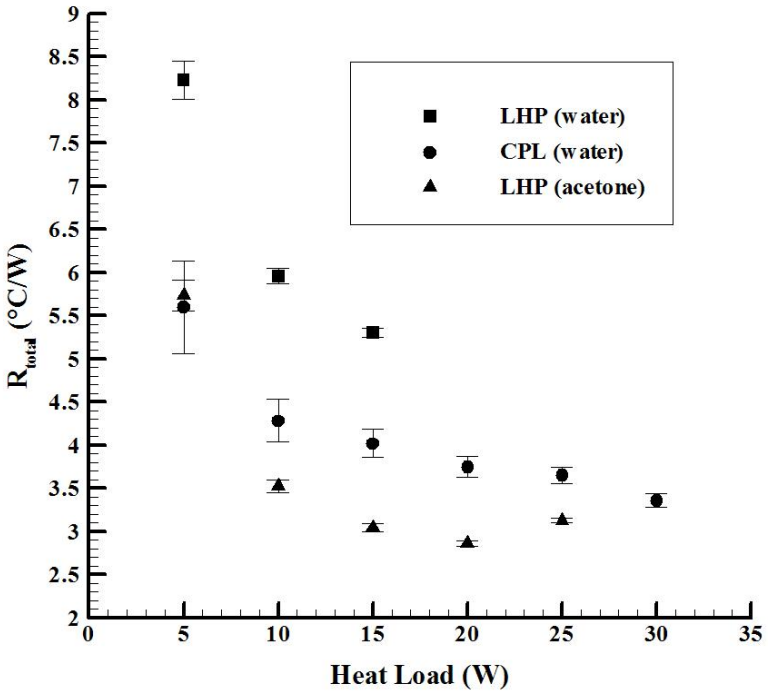

(a)

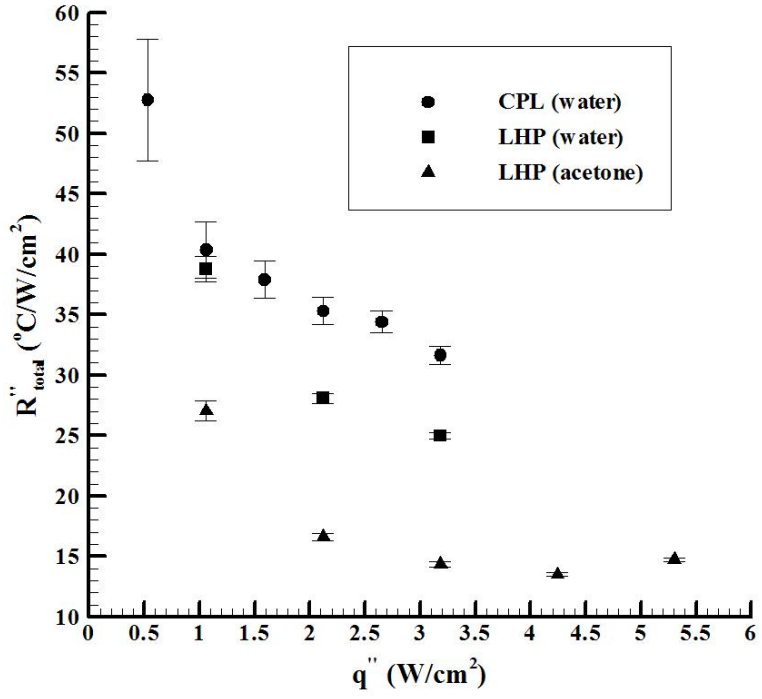

(b)

Figure 4.16 – (a) Total thermal resistance vs. heat load and (b) total thermal resistance per square centimeter vs. heat flux for both LHPs and CPL with water, with 130% load.

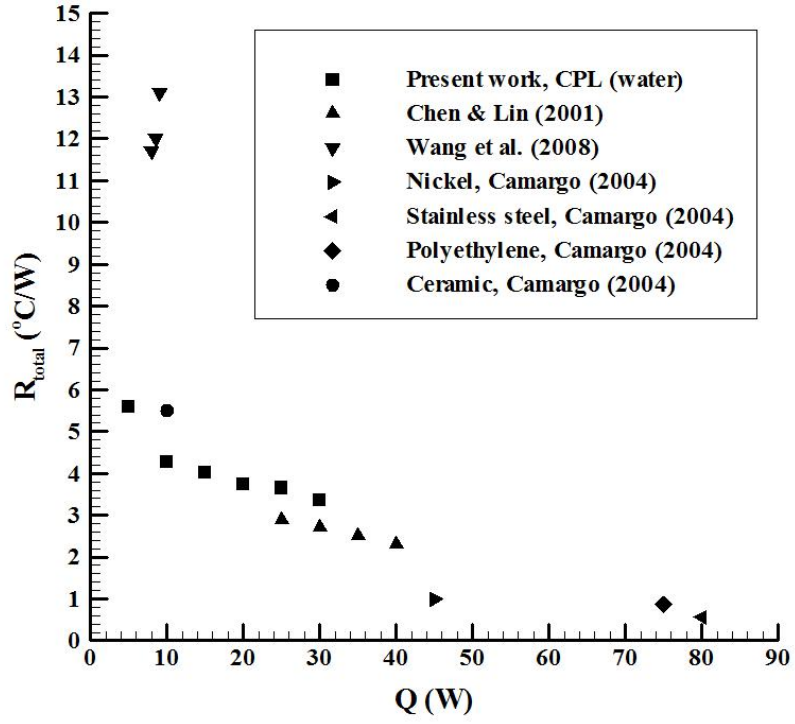

(a)

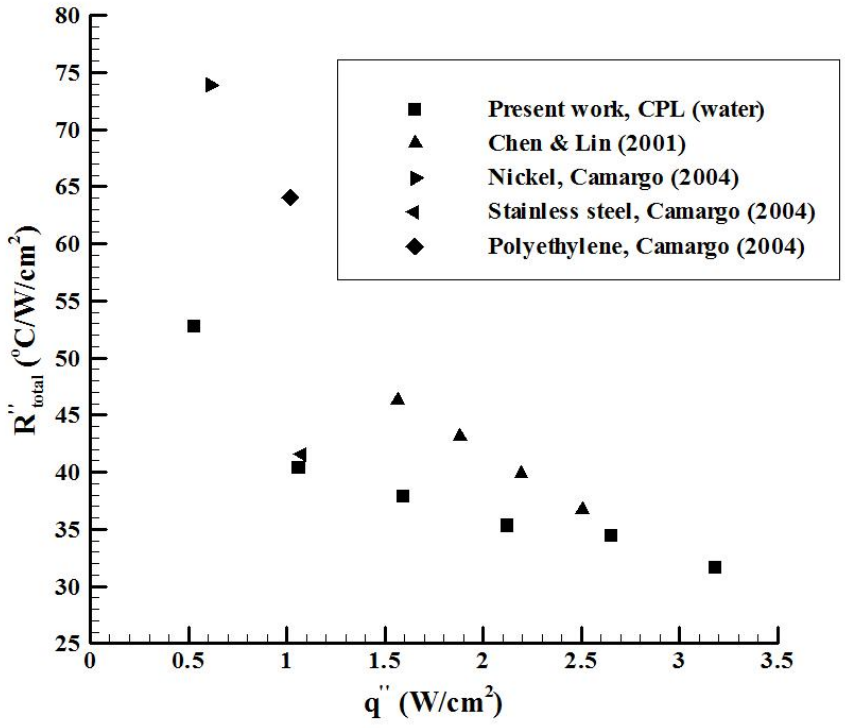

(b)

Figure 4.17 – (a) Total thermal resistance vs. heat load and (b) total thermal resistance per square centimeter vs. heat flux for the CPLs.

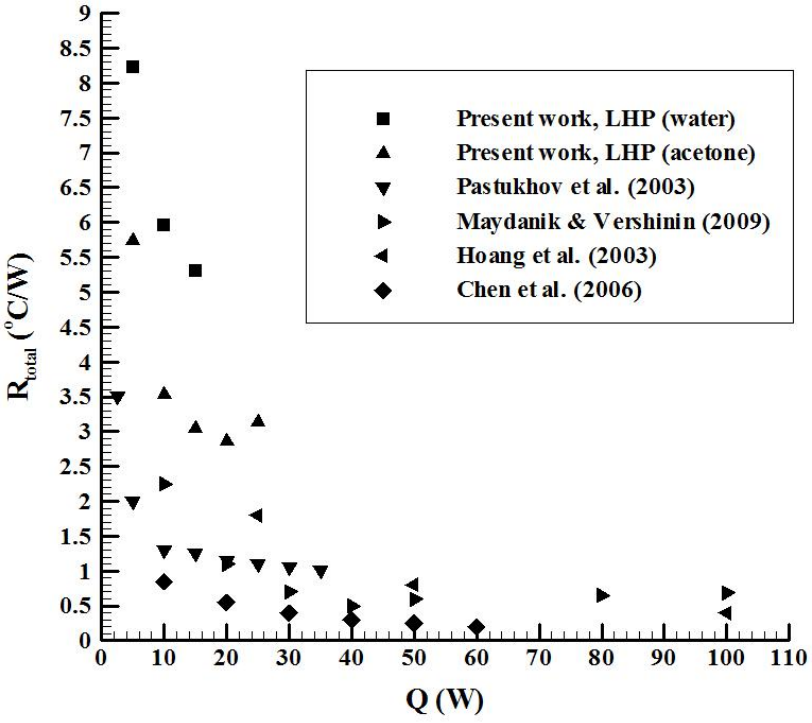

(a)

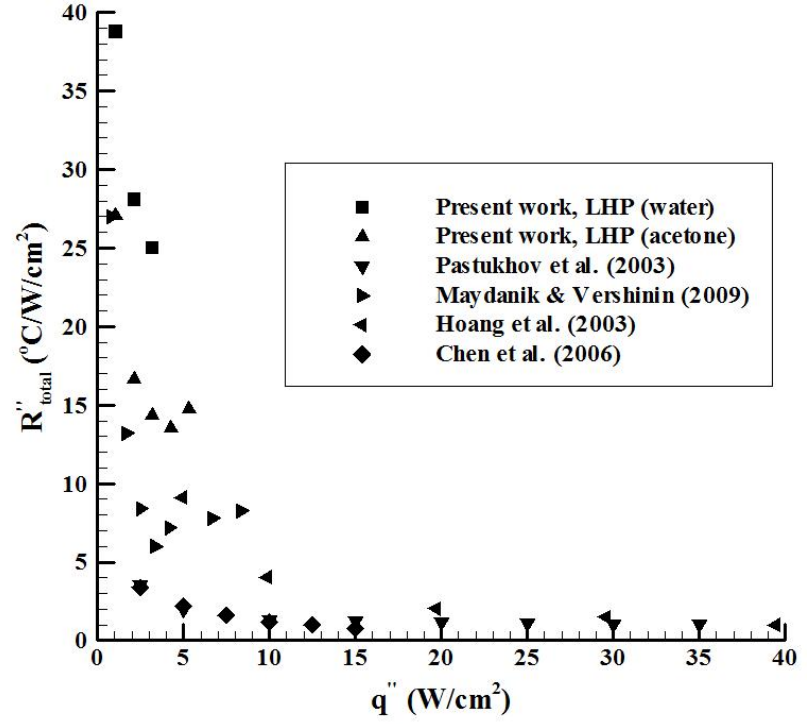

(b)

Figure 4.18 – (a) Total thermal resistance vs. heat load and (b) total thermal resistance per square centimeter vs. heat flux for the LHPs.

4.6 Capillary Limit Analysis of the LHPs and the CPL

The main operational limits of capillary pumping systems (CPL and LHP) are the boiling and capillary limits. In this section, the capillary limit will be explored basing the analysis on the experimental results. As explained before, the condition for both CPL and LHP work is that the total system pressure drop does not exceed the maximum pressure that the porous wick can provide. Due to the vapor penetration through the porous wick, the operating temperature of the system has a sudden increase when the capillary limit is exceeded. So, the capillary pumping system operation requires that the sum of the pressure drops in the components and in the transport lines must be smaller than the maximum capillary pressure head developed by the wick, *i.e.*,

$$\Delta p_{cap,\max} \geq \Delta p_{\mathrm{evap}} + \Delta p_{\mathrm{cond}} + \Delta p_{\mathrm{v}} + \Delta p_{\mathrm{l}} + \Delta p_{\mathrm{g}} \tag{4.3}$$

In the following, the total pressure drop will be estimated based on the measurements and compared to the expected maximum capillary limit.

4.6.1 Mass Flow Rate

The mass flow rate can be approximately obtained from the energy balance in the compensation chamber and capillary evaporator assembly during steady-state operation. During typical LHP operation, according to Fig. 4.19, heat is applied uniformly to the evaporator (Q_{app}). The majority of the overall applied heat load (Q_{evap}) vaporizes the liquid on the outer surface of the porous wick and superheats the vapor in the vapor channel up to the outlet of the evaporator. The other part of the applied heat load is transferred through the metallic structure of the assembly to the compensation chamber, where one part is transferred to the ambient ($Q_{cc,amb}$), and the other part is transferred to the vapor transport line.

Here, the heat transfer to the vapor transport line will be neglected. Thus, the energy balance in the compensation chamber and evaporator requires:

$$Q_{app} = Q_{evap} + Q_{cc,amb}, \tag{4.4}$$

where

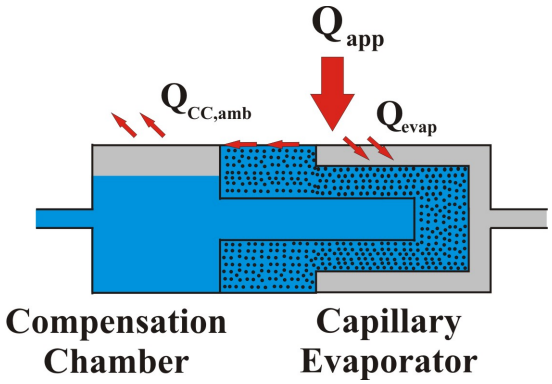

Figure 4.19 – Scheme of energy balance in the compensation chamber and capillary evaporator assembly.

$$Q_{evap} = \dot{m}\ h_{lv} + \dot{m}\ c_{p,v}\ (T_{evap,out} - T_{evap,sat}) + \dot{m}\ c_{p,l}\Delta T_{subcooled}, \tag{4.5}$$

where $T_{evap,out}$ is the temperature of the vapor in the evaporator outlet, $T_{evap,sat}$ is the saturation temperature of the vapor in the evaporator, $\dot{m}$ is the mass flow rate of vapor and $\Delta T_{subcooled}$ is the liquid temperature difference between the condenser outlet and compensation chamber inlet.

The heat transfer from the compensation chamber surface to the ambient, $Q_{cc,amb} = h_{cc,amb}A_{cc,out}(T_{cc}^{w} - T_{amb})$, is assumed to be by natural convection and the heat transfer coefficient by convection ($h_{cc,amb}$) of a horizontal cylinder to the ambient can be estimated from (INCROPERA; DEWITT, 2003),

$$h_{cc,amb} = \frac{\lambda_{air} Nu_{cc,amb}}{d_{cc}}, \tag{4.6}$$

where $d_{cc,out}$ is the outer diameter of the compensation chamber, λ_{air} is the air thermal conductivity and $Nu_{cc,amb}$ is the nusselt number which can be estimated as,

$$Nu_{cc,amb} = \left\{ 0.60 + \frac{0.387Ra^{1/6}}{\left[1 + (0.559/\,\mathrm{Pr}_{air})^{9/16}\right]^{8/27}} \right\}^{2}; \quad Ra \leq 10^{12} \tag{4.7}$$

where Ra is the Rayleigh number which is calculated as,

$$Ra = \frac{g\beta_{air}\,(T_{cc} - T_{amb})\,L_{cc}}{\nu_{air}\alpha_{air}}, \tag{4.8}$$

where g is the acceleration due to gravity, $\nu_{air} = 1/T_f$ is the thermal expansion coefficient, α_{air} is the thermal diffusivity and ν_{air} is the kinematic viscosity of the air and T_f is the

film temperature. All properties of the air were evaluated at the film temperature (T_f).

The effects of the sensible heat in the mass flow rate are only secondary in most cases and can be neglected ($\dot{m}\ h_{lv} \gg \left[\dot{m}\ c_{p,l}\ (T_{evap,out} - T_{evap,sat}) + \dot{m}\ c_{p,l}\Delta T_{subcooled}\right]$). From the applied heat (Q_{app}), the mass flow rate can be estimated from,

$$Q_{app} = \dot{m}\ h_{lv} + \ h_{cc,amb}A_{cc,out}(T_{cc} - T_{amb}) \tag{4.9}$$

where T_{cc} is the temperature measured at the wall of the compensation chamber, T_{amb} is the ambient temperature measured and $A_{cc,out}$ is the external area of the compensation chamber.

Since the reservoir in CPL is separated from the evaporator and assuming that there is no heat transfer from the evaporator to the ambient (due to insulation of the evaporator), the mass flow rate can be estimated from $Q_{app} = \dot{m}\ h_{lv}$.

4.6.2 Fluid Properties

The fluid properties used in this work were obtained from the software Engineering Equation Solver (EES) and Peterson (1994). These properties include saturation pressure, latent heat, liquid and vapor densities, liquid and vapor viscosities, liquid and vapor thermal conductivities, liquid and vapor specific heats and liquid surface tension. Further information regarding the fluid properties, used in the present model for the estimation of the pressure drop of the capillary pumping systems under study, can be found in Appendix D.

4.6.3 Single-Phase Pressure Drop

Single-phase flow is assumed to prevail along the grooves, vapor and liquid transport lines, liquid feeding channel and through the porous wick. The single-phase viscous pressure drop can be estimated from the Darcy-Weisbach equation,

$$\Delta p = f\left(\frac{L}{d_h}\right)\left(\frac{\rho v^2}{2}\right) \tag{4.10}$$

where f is the Darcy (or Moody) friction factor. For laminar flow in circular tubes, $f\mathrm{Re} = 64$. For turbulent flow in smooth tubes, the solution proposed by H. Blasius, $f = 0.316\mathrm{Re}^{-0.25}$ for $4000 < Re < 10^5$, is used.

The flow in the grooves can be shown to be laminar. The friction factor is given by

$f\mathrm{Re} = constant$, where the Reynolds number is defined in terms of the hydraulic diameter given by

$$d_h = \frac{2h_{groove}w_{groove}}{(h_{groove} + w_{groove})} \tag{4.11}$$

where h_{groove} and w_{groove} are the height and width of the grooves, respectively. For the grooves of the evaporator of interest, $h_{groove} = 1$ mm and $w_{groove} = 1$ mm, and therefore, $f\mathrm{Re} = 57$ (INCROPERA; DEWITT, 2003).

The pressure drop in the porous wick, according to Darcy's law, can be written as,

$$v_{w,l} = -\frac{K_w}{\mu_l}\frac{dp}{dr}$$

or

$$\dot{m}_l = \rho_l v_{w,l} A_w = -\frac{\rho_l 2\pi r L_w K_w}{\mu_l}\frac{dp}{dr}, \tag{4.12}$$

where ρ_l is the liquid density, $v_{w,l}$ is the liquid velocity that flows throug the wick and A_w is the transversal area of the wick.

Integrating Eq. 4.12 from $r_{w,in}$ to $r_{w,out}$, assuming μ_l, ρ_l and K_w are constants, the pressure drop in the porous wick can be calculated from,

$$\Delta p_w = \frac{\dot{m}_l \mu_l}{\theta \rho_l L_w K_w} \ln\left(\frac{r_{w,out}}{r_{w,in}}\right), \tag{4.13}$$

where $\theta = 2\pi\left(\frac{N_{groove}w_{groove}}{2\pi r_{w,out}}\right)$ is the angle comprehended by the grooves and N_{groove} is the number of the grooves in the wick.

4.6.4 Condenser of LHP

In general, the condensers of CPLs and LHPs present superheated vapor, two-phase and subcooled liquid regions which depend on the heat load. According to Ku (1994, 1999) and Maydanik (2005), when the heat load is low (less than ~ 50 W for their LHPs), the vapor enters the condenser in saturate state and only a small area is necessary to occur the phase change of the working fluid. Thus, for low heat load, the condenser presents only two regions: two-phase and subcooled liquid. As the heat load of experiments presented here (LHPs and CPL) are low, the temperature measured at the wall of condenser inlet was assumed as the temperature of the vapor in saturated state that enters the condenser

of the LHPs, since the pressure of the LHPs was not measured. On the other hand, the pressure of the CPL was measured and this assumption was not needed. This assumption used for the LHPs is discussed in detail in Appendix D.

Figure 4.20 shows schematically the condenser with finned tube of the LHPs. The three regions mentioned before are presented, but here the region of superheated vapor is neglected due to the low heat load supplied to the LHPs. So, the length of condenser can be divided in: $L_{cond} = L_{cond,l} + L_{cond,lv}$.

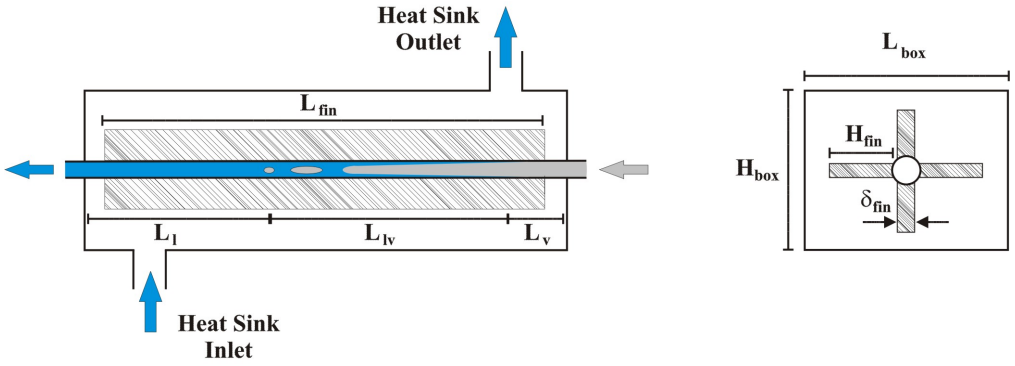

Figure 4.20 – Schematic diagram of the condenser for the LHPs with finned tube.

The lenght of two-phase ($L_{cond,lv}$) and liquid ($L_{cond,l}$) regions must be determined in order to estimate the pressure drop along the condenser. First, an energy balance is applied in the two-phase region of the condenser, schematically shown in Fig. 4.20.

The energy balance in the two-phase region provides:

$$\dot{m}\, h_{lv} = (UA)_{cond,lv}\, \Delta T_{lm}^{cond,lv}, \tag{4.14}$$

where,

$$\Delta T_{lm}^{cond,lv} = \frac{\Delta T_1^{cond,lv} - \Delta T_2^{cond,lv}}{\ln\left(\Delta T_1^{cond,lv} \Big/ \Delta T_2^{cond,lv}\right)}$$

$$\Delta T_1^{cond,lv} = T_{cond,sat} - T_{HS,out}$$

$$\Delta T_2^{cond,lv} = T_{cond,sat} - T_{HS,in}$$

$$(UA)_{cond,lv} = \frac{1}{\frac{1}{h_{cond,lv}\left(\pi d_{cond,in} L_{cond,lv}\right)} + \frac{\ln\left(d_{cond,out}/d_{cond,in}\right)}{2\pi\lambda_{SS} L_{cond,lv}} + \frac{1}{\eta_{fin,0} h_{HS} A_t}}. \quad (4.15)$$

A finned tube is used in the condenser section and the overall surface efficiency of the fin ($\eta_{fin,0}$) may be determined from

$$\eta_{fin,0} = 1 - \left(1 - \eta_{fin}\frac{A_{fin}}{A_u}\right) \quad (4.16)$$

where the finned (A_{fin}), unfinned (A_u) and total(A_t) areas and the fin efficiency (η_{fin}) are defined as,

$$A_{fin} = N_{fin} L_{fin}\left(2H_{fin} + \delta_{fin}\right) \quad (4.17)$$

$$A_u = \pi d_{cond,out} L_{fin} - N_{fin} L_{fin} \delta_{fin} \quad (4.18)$$

$$A_t = A_u + A_{fin} \quad (4.19)$$

$$\eta_{fin} = \frac{\tanh\left(mH_{fin}\right)}{mH_{fin}}; \quad \delta_{fin} \ll H_{fin}, \quad (4.20)$$

where $m = \sqrt{\frac{2h_{HS}}{\delta_{fin}\lambda_{fin}}}$; $\delta_{fin} \ll H_{fin}$. δ_{fin} is the thickness, H_{fin} is the height and L_{fin} is the lenght of the retangular, uniform section fin, presented in Fig. 4.20.

The heat transfer coefficient of the water flow in the heat sink (h_{HS}) is estimated from

$$h_{HS} = \frac{Nu_{HS}\lambda_{water}}{d_e}, \quad (4.21)$$

where the equivalent diameter (d_e), based on the heat transfer area, is defined as,

$$d_e = \frac{4A_c}{P_h}. \quad (4.22)$$

The heat transfer perimeter (P_h) and the net cross sectional free-flow area (A_c) with longitudinal finned tube are given by,

$$P_h = \pi d_{cond,out} + 2H_{fin}N_{fin} \tag{4.23}$$

$$A_c = H_{cond,box}L_{cond,box} - \left(\pi\frac{d_{cond,out}^2}{4} + N_{fin}\delta_{fin}H_{fin}\right) \tag{4.24}$$

The empirical correlation proposed by Sieder and Tate (KAKAC; LIU, 2002) is used to predict the mean Nusselt number for the water flow in the heat sink,

$$Nu_{HS} = 1.86\left(Pe_{HS}\frac{d_h}{L_{fin}}\right)^{1/3}\left(\frac{\mu_{water}}{\mu_{wall,water}}\right)^{0.14}, \tag{4.25}$$

where $Pe_{HS} = \mathrm{Re}_{HS}\,\mathrm{Pr}_{HS}$ and the dynamic viscosity of the water in contact with the wall of the finned tube ($\mu_{wall,water}$) is a function of the mean temperature,

$$\bar{T}_{wall,water} = \frac{1}{2}\left(\frac{T_{cond,in} + T_{cond,out}}{2} + \frac{T_{HS,in} + T_{HS,out}}{2}\right). \tag{4.26}$$

Equation 4.25 is valid for laminar flow, $0.48 < \mathrm{Pr}_{water} < 16700$ and,

$$\left(Pe_{HS}\frac{d_h}{L_{fin}}\right)^{1/3}\left(\frac{\mu_{water}}{\mu_{wall,water}}\right)^{0.14} \geq 2.$$

The Reynolds number is determined as,

$$\mathrm{Re}_{HS} = \frac{\rho_{water}v_{HS,water}d_h}{\mu_{water}}, \tag{4.27}$$

where the equivalent diameter (d_h), based on the pressure drop, is defined as,

$$d_h = \frac{4A_c}{P_{wetted}}. \tag{4.28}$$

The wetted perimeter (P_{wetted}) of a tube with longitudinal fins is given by,

$$P_{wetted} = 2H_{cond,box} + 2L_{cond,box} + \pi d_{cond,out} + 2H_{fin}N_{fin}. \tag{4.29}$$

There are several available correlations to estimate the two-phase heat transfer coefficient ($h_{cond,lv}$). Here, the correlation proposed by Cavallini and Zecchin (KAKAC; LIU, 2002) is used to determine the two-phase heat transfer coefficient,

$$h_{cond,lv} = 0.05\mathrm{Re}_{eq}^{0.8}\mathrm{Pr}_l{}^{0.33}\frac{\lambda_l}{d_{cond,in}}, \tag{4.30}$$

where $\mathrm{Re}_{eq} = \mathrm{Re}_v^{lv}\left(\frac{\mu_v}{\mu_l}\right)\left(\frac{\rho_l}{\rho_v}\right)^{0.5} + \mathrm{Re}_l^{lv}$. ${Re_l}^{lv}$ and ${Re_v}^{lv}$ are calculated by,

$$\mathrm{Re}_v^{lv} = \frac{\rho_v v_v x d_{cond,in}}{\mu_v} \tag{4.31}$$

$$\mathrm{Re}_l^{lv} = \frac{\rho_l v_l \left(1-x\right) d_{cond,in}}{\mu_l}. \tag{4.32}$$

The value of the Re_{eq} varies along the condenser due to the variations in the vapor fraction (x). In order to arrive at an averaged heat transfer coeficient along the two-phase region ($\bar{h}_{cond,lv}$), a model for the variation of x along the condenser is needed. Here, it will be assumed that the fluid pressure remains approximately constant along the two-phase region such that the ΔT for heat transfer is constant and the rate of condensation also remains constant. Therefore, it will be imposed that,

$$x = 1 - \frac{z}{L_{cond,lv}},$$

where z is a local coordinate along the two-phase region. With this hypothesis, the averaged heat transfer for the two-phase region is obtained from,

$$\bar{h}_{cond,lv} = \frac{1}{L_{cond,lv}} \int_0^{L_{cond,lv}} h_{cond,lv} dz.$$

Using Eqs. 4.30 to 4.32, the averaged heat transfer coeficient for the two-phase region becomes,

$$\frac{\bar{h}_{cond,lv} d_{cond,in}}{\lambda_l} = 0.028\mathrm{Pr}_l{}^{0.33}\left(\mathrm{Re}_v \frac{\mu_v}{\mu_l}\sqrt{\frac{\rho_l}{\rho_v}} - \mathrm{Re}_l\right)^{0.8}. \tag{4.33}$$

After the determination of the two phase length in the condenser, the liquid length is determined as $L_{cond} = L_{cond,lv} + L_{cond,l}$.

The two-phase pressure drop consists of gravitational pressure drop, frictional pressure drop, and acceleration pressure drop. Since the condenser is placed horizontally, the gravitational pressure drop in the condenser is identically zero. The pressure drop of the two-phase zone in the condenser is estimated using

$$\left(\frac{dp}{dL}\right)_{lv} = \phi_{lv}^2 \left(\frac{dp}{dL}\right)_{liq}, \tag{4.34}$$

where ϕ_{lv} is the two-phase multiplier and $\frac{dp}{dL}$ is the pressure drop in the two-phase ($_{lv}$) and liquid ($_{liq}$) zones.

The single-phase pressure drop for liquid flow in the tube can be written as:

$$\left(\frac{dp}{dL}\right)_{liq} = -\frac{f_{liq}}{d_{cond,in}} \frac{(1-x)^2}{2\rho_{liq}} \left(\frac{\dot{m}}{A_{cond}}\right)^2, \tag{4.35}$$

where the liquid-phase friction factor (f_{liq}) can be calculated from the Reynolds number as discussed previously for single-phase pressure drop. The Reynolds number of the liquid phase can be calculated as:

$$\mathrm{Re}_{liq} = \frac{4\,\dot{m}\,(1-x)}{\pi \mu_{liq} d_{cond,in}}. \tag{4.36}$$

Substituting Eq. 4.35 into Eq. 4.34 and applying the chain rule, the two-phase pressure drop becomes a function of vapor fraction (x) as,

$$\left(\frac{dp}{dx}\right)_{lv} = -\phi_{lv}^2 \frac{f_{liq}}{d_{cond,in}} \frac{(1-x)^2}{2\rho_{liq}} \left(\frac{\dot{m}}{A_{cond}}\right)^2 \left(\frac{dL}{dx}\right) \tag{4.37}$$

Assuming again that there is a linear vapor fraction (x) variation from 1 to 0 over the lenght of the two-phase region and integrating the Eq. 4.37 over the two-phase length, we obtain,

$$\Delta p_{lv} = \int_{x=0}^{x=1} \left[-\phi_{lv}^2 \frac{f_{liq}}{d_{cond,in}} \frac{(1-x)^2}{2\rho_{liq}} \left(\frac{\dot{m}}{A_{cond}}\right)^2 \left(\frac{dL}{dx}\right) \right] dx, \tag{4.38}$$

where the two-phase multiplier can be determined by,

$$\phi_{lv} = \left(1 + \frac{C}{X} + \frac{1}{X^2}\right)^{0.5} \tag{4.39}$$

and the Martinelli parameter X can calculated as,

$$X = \left(\frac{f_{liq}}{f_{vap}}\right)^{0.5} \left(\frac{\rho_{vap}}{\rho_{liq}}\right)^{0.5} \left(\frac{1-x}{x}\right). \tag{4.40}$$

The constant (C) in Eq. 4.39 is dependent on the flow regime and is associated with

the single flow of the vapor and the liquid in the pipe. Table 4.3 indicates the value of the constant for four different possible combinations.

Equation 4.38 is solved numerically for the conditions of interest.

Table 4.3 – Value of the constant (C) in the two-phase correlation proposed by Lockhart and Martinelli (KAKAC; LIU, 2002).

Liquid	Vapor	C
Turbulent	Turbulent	20
Laminar	Turbulent	12
Laminar	Turbulent	10
Laminar	Laminar	5

4.6.5 Condenser of CPL

Two finned air coolers were used to cool the condenser section of the CPL. In this type of coolers, the fan is mounted on top of the fin assembly and pushes air over the fin spacing. There is very little information that can be used to estimate the heat transfer coefficient for this situation. Therefore, here it is assumed that the air flow passes through the fins as shown in Fig. 4.21. This assumption can overestimate or subestimate the value of the heat transfer coefficient, thus, an evaluation of this estimation of heat transfer coefficient is presented in Appendix D.

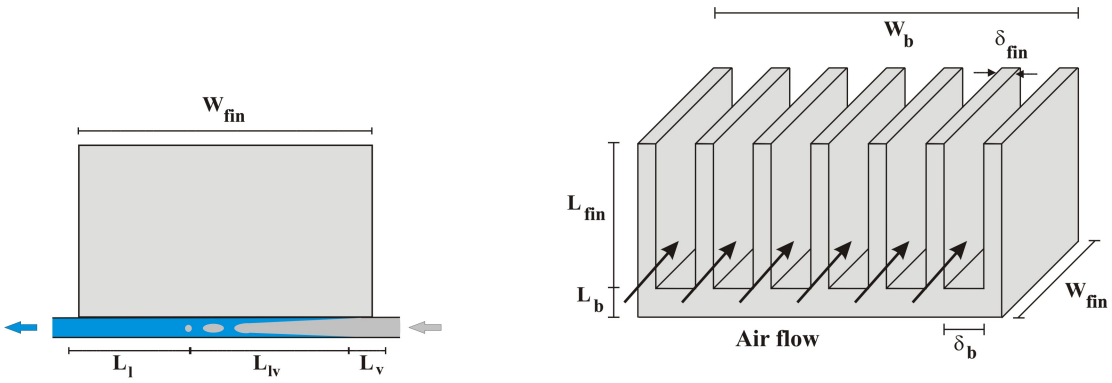

Figure 4.21 – Schematic diagram of the finned condenser for the CPL.

The lenght of two-phase ($L_{cond,lv}$) and liquid ($L_{cond,l}$) regions must be determined in order to estimate the pressure drop along the condenser as in the previous section.

The energy balance in the two-phase region provides:

$$\dot{m}\, h_{lv} = (UA)_{cond,lv}\, \Delta T_{lm}^{cond,lv}, \tag{4.41}$$

where,

$$\Delta T_{lm}^{cond,lv} = \frac{\Delta T_1^{cond,lv} - \Delta T_2^{cond,lv}}{\ln\left(\Delta T_1^{cond,lv} \Big/ \Delta T_2^{cond,lv}\right)}$$

$$\Delta T_1^{cond,lv} = T_{cond,sat} - T_{amb}$$

$$\Delta T_2^{cond,lv} = T_{cond,sat} - T_{amb}$$

$$(UA)_{cond,lv} = \frac{1}{\frac{1}{h_{cond,lv}\left(\pi d_{cond,in} L_{cond,lv}\right)} + \frac{\ln\left(d_{cond,out}/d_{cond,in}\right)}{2\pi\lambda_{SS} L_{cond,lv}} + \frac{1}{\eta_{fin,0} h_{air} A_t}}. \quad (4.42)$$

A finned tube is used in the condenser section and the overall surface efficiency of the fin ($\eta_{fin,0}$) may be determined from

$$\eta_{fin,0} = 1 - \left(1 - \eta_{fin}\frac{A_{fin}}{A_u}\right) \quad (4.43)$$

where the finned (A_{fin}), unfinned (A_u) and total(A_t) areas and the fin efficiency (η_{fin}) are defined as,

$$A_{fin} = N_{fin} 2 W_{fin}\left(L_{fin} + \frac{\delta_{fin}}{2}\right) \quad (4.44)$$

$$A_u = \left(N_{fin} - 1\right)\delta_b W_{fin} \quad (4.45)$$

$$A_t = A_u + A_{fin} \quad (4.46)$$

$$\eta_{fin} = \frac{\tanh\left(mL_{fin}\right)}{mL_{fin}}; \quad \delta_{fin} \ll L_{fin}, \quad (4.47)$$

where $m = \sqrt{\frac{2h_{air}}{\delta_{fin}\lambda_{fin}}}$; $\delta_{fin} \ll L_{fin}$. δ_b is the thickness of the base fin spacing, W_b is the width and L_b is the height of the fin base, δ_{fin} is the thickness, W_{fin} is the lenght and L_{fin} is the height of the retangular, uniform section fin, presented in Fig. 4.21.

The heat transfer coefficient of the air flow in the outer side of the condenser (h_{air}) is

estimated from,

$$h_{air} = \frac{Nu_{air}\lambda_{air}}{d_h}, \tag{4.48}$$

where d_h is the hydraulic (equivalent) diameter and it is defined as,

$$d_h = \frac{4A_c}{P_{fin}}, \tag{4.49}$$

where the fin perimeter (P_{fin}) and the net cross sectional air flow area (A_c) are given by,

$$P_{fin} = 2\left(L_{fin} + \delta_b\right) \tag{4.50}$$

$$A_c = L_{fin}\delta_b. \tag{4.51}$$

For the turbulent fully developed flow, the Nusselt number (Nu_{air}) can be estimated using the correlation proposed by Dittus-Boelter as,

$$Nu_{air} = 0.023(Re_{air})^{4/5}(Pr_{air})^{0.4}, \tag{4.52}$$

where Pr_{air} is the Prandtl number and Re_{air} is Reynolds number,

$$Re_{air} = \frac{\rho_{air}v_{air}d_h}{\mu_{air}}. \tag{4.53}$$

The two-phase heat transfer coefficient ($h_{cond,lv}$) was estimated using the same equations introduced in the previous section (Condenser of LHP).

4.6.6 Results

The pressure drop of the capillary pumping systems here under study (two LHPs and one CPL) were evaluated for the maximum heat load applied to the system (15 W for the LHP (water), 25 W for the LHP (acetone) and 30 W for the CPL). The thermodynamic properties of the working fluid were determined at the saturation temperature of the vapor within the condenser. For the CPL, the saturation temperature was estimated using the measured pressure at the system. However, for the LHPs, since the pressure was not measured, the temperature of the condenser inlet ($T_{cond,in}$) was assumed as the saturation temperature. Further explanations regarding this assumption can be found in Appendix

D. The Table 4.4 summarizes the estimated results, taking into account the dimensions for both LHPs and the CPL tested in the lab. Further results are presented in Appendix D.

Table 4.4 – Pressure drop of the LHPs and CPL.

	LHP (Water)		LHP (Acetone)		CPL (Water)	
Components	Δp (Pa)	%	Δp (Pa)	%	Δp (Pa)	%
Vapor grooves	77.84	7.04	47.673	0.723	1.38×10^3	15.76
Vapor line	38.89	3.52	30.654	0.465	206.3	2.36
Porous wick	987.42	89.25	6.511×10^3	98.688	7.13×10^3	81.63
Liquid line	0.46	0.04	2.363	0.036	2.15	0.02
Two phase	1.69	0.15	5.863	0.089	19.89	0.23
Δp_{total}	1.106×10^3	100.00	6.598×10^3	100.00	8.74×10^3	100.00
Capillary limit	41.78×10^3	—	11.5×10^3	—	45.14×10^3	—
$\Delta p_{total}/p^*_{cap,max}$	0.03	—	0.574	—	0.19	—

* is the maximum capillary pressure which is estimated using the Eq. 1.2 ($p_{cap,max} = \frac{2\sigma}{r_p}$).

Note in Table 4.4 that the total pressure drop (Δp_{total}) of all systems is smaller than the capillary limit. It is noticed that the contribution of the pressure drop in the vapor and liquid transport lines and in the two phase zone of condenser are much smaller than the pressure drop in the porous wick. The total pressure drop of the CPL (water) is greater than the LHP (water) due to the greater mass flow rate and the greater number of grooves in the evaporator of the CPL. It can also be noticed the total pressure drop of all capillary pumping systems is up to 57.4% of the capillary limit, showing that, considering this limit, all capillary pumping systems are capable of transfering heat over longer distances.

According to Ku (1994, 1999), Maydanik (2005) and others, the pressure drop across the two phase zone in the condenser can be neglected when compared with the total pressure drop of the capillary pumping systems. As it can be noticed in Table 4.4, the two phase pressure drop in the condenser is very small representing less than 0.5%, due to the low mass flow rates. Therefore, uncertainties in the evaluation of this contribution are not very relevant.

4.7 Comparison Between the Experimental and Theoretical Results

This section presents a comparison between the experimental and theoretical results obtained with the model presented in Chapter 2. The curves of the critical nondimensional

average radius at $z^* = 1.0$ and $r^* = 0.0$ as a function of the nondimensional inlet heat flux for two porous wick with one-layer and two layers are compared to the experimental nondimensional average radius for each heat flux applied to the capilary pumping systems tested in this work. Figure 4.22 presents this comparison.

The experimental nondimensional average radius was estimated for average pore radius of 3 μm and permeability of 1.5×10^{-14} m^2. The input heat fluxes (q_{in}) for each capillary pumping system tested here were estimated as,

$$q_{in} = \frac{Q_{app}}{N_{fin} A_{fin}},$$

where Q_{app} is the heat transfer rate applied to the capillary evaporator, N_{fin} is the number of fins in the capillary evaporator and A_{fin} is the area of one fin.

The input heat fluxes (q_{in}) for the experiments varied from 5.3×10^3 to 53.1×10^3 W/m^2 and they are related to the heat loads from 5 to 15 W for the LHP (water), heat loads from 5 to 25 W for the LHP (acetone) and heat loads from 5 to 30 W for the CPL (water). The nondimensional input heat fluxes (q^*_{in}) varied from 1.3 to 13.3.

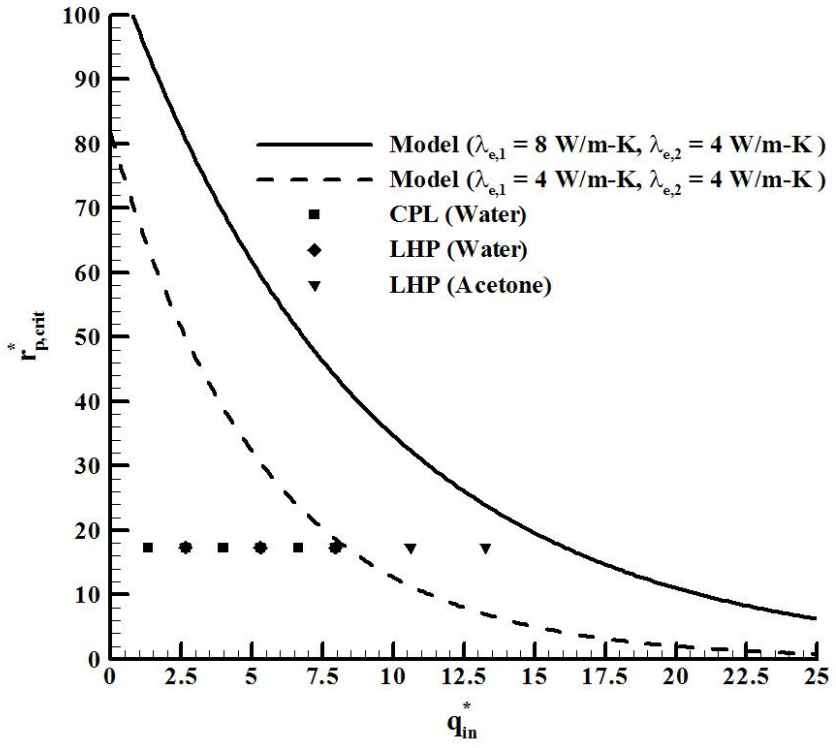

Figure 4.22 – Comparison between the experimental and theoretical results.

It is noticed in Fig. 4.22 that only the results of the LHP (acetone) reached the capillary limit for a porous wick with one-layer. Despite the LHP (acetone) has reached the capillary limit, it continued working for heat loads of 20 and 25 W. So, according

to the model (presented in Chapter 2), the evaporation front invaded the porous wick and stablished a stable position within it. However, this comparison should be taken only as a first approximation since the theoretical model does not reproduce completely the geometry of the tested CPL and LHPs. Nevertheless, the physical trends remain the same.

It is also noticed in Fig. 4.22 that, if a porous wick with two-layers with different thermal conductivity was used, the capillary limit would increase, showing that the high thermal conductivity underneath the fin are desirable for capillary pumping systems.

5 Conclusions and Recommendations for Future Work

In this last chapter, the general conclusions obtained in this thesis as well as proposals for development of future works in modeling and design of LHP and CPL are presented.

5.1 General Conclusions

This study presents a theoretical and experimental study of two LHPs and one CPL. Regarding the modeling of the heat and mass transfer problem in capillary evaporators, a criterion for wick dry-out was proposed. Regarding the development of capillary evaporators of LHP and CPL, a new ceramic porous wick is proposed as an alternative to wicks made of metal and plastic. These evaporators produced showed reliable operations for LHP and CPL applications.

5.2 Modeling Conclusions

In Chapter 2, two models for the heat and mass transfer problem within the porous wick of flat capillary evaporators are presented. First, a simplified model allowed analytical solutions for the velocity and temperature fields within the porous wick of a flat capillary evaporator. The analytical solution by separation of variables was possible after simpler boundary conditions are applied and this model was based on the model reported by Cao & Faghri (1994a). Then, an improved model followed by its numerical solution is presented. The improved model allowed to simulate the heat and mass transfer within a wick with two layers with different thermophysical properties and to verify the effect of design variables, dimensions, permeability, average pore radius and thermal conductivity of the wick in the performance of the flat capillary evaporator. Furthermore, the improved model also allowed to test the onset of drying underneath the fin, defining the limit for the application of the model which considers the wick fully saturated with liquid.

5.2.1 Simplified Model

With the simplified model, it was possible to analyze different types of porous wicks, working fluids and the variation of some geometric parameters. This analysis provided important information such as: the decrease of the wick thickness increased the capillary limit, however increased both the temperature in the area close to the fin and the heat flux to the feeding liquid channel. Also, as expected, it was noticed that the smaller the thermal conductivity of the porous wick, the greater the temperatures in the area underneath the fin. Therefore, the main conclusions from the variation of the parameters, thickness and thermal conductivity obtained in the simplified model indicate that a good design must seek:

1. an optimum thickness and a high permeability so that the heat flux to the feeding liquid channel is minimized and the pressure losses remain low;

2. a porous material with optimum thermal conductivity so that the temperature in the area underneath the fin is minimized, at the same time that the temperature in the surface of the liquid channel is also limited. This contraditory need was also observed by Figus *et al.* (1999) that recomended the use of a double layered porous wick.

The analysis of the simplified model also revealed that the boundary conditions should be improved to match better with the expected physics of the problem. This model also allows no conclusions regarding the attainment of a capillary limit. Thus, it was verified that:

1. the outlet velocity field is not uniform but it must result in higher velocities closer to the fin;

2. the liquid channel surface temperature must be smaller than the vapor temperature.

5.2.2 Improved Model

With the improved model, it was possible to simulate the heat and mass transfer within the porous wick with more than one layer with different thermophysical properties. This improved model also provided a condition for dryout. The analysis of the porous wick with one and two layers showed that the wick with two layers is better than with one layer regarding the onset of drying underneath the fin. Other conclusions are:

1. The capillary limit, or onset drying, stablishes a relation between the pore size (and all medium properties) and the heat flux. If this limit is reached, the evaporation front may penetrate within the porous wick. This can be used as a criterium for the specification of the maximum heat flux allowed during operation in steady-state.

2. The larger the thermal conductivity of the porous wick 1 (underneath the fin), the smaller is the heat transfer to the liquid feeding channel, causing a smaller increase of the inlet temperature. The increase of the thermal conductivity of the porous wick 1 causes the increase of the capillary limit, avoiding the onset of drying of the region underneath the fin. The increase of the thermal conductivity also decreases the mass flow rate, causing the decrease of the pressure losses through the porous wick.

3. Finally, the dimensions of the bi-layered wick ($R = 15$ mm, $R^{'} = 7.5$ mm, $L_{z,1} = 4$ mm, $L_{z,2} = 6$ mm) and its thermophysical properties can be used for a design of a flat capillary evaporator.

5.3 Experimental Results and Conclusion

Most LHPs and CPLs use polyethylene or metallic porous wicks and the application of ceramic porous wicks into the evaporators of capillary pumping systems is scarce. The ceramic wick proposed here proved to be a reliable alternative for its applications in LHPs and CPLs. Performance tests of two LHPs using acetone and water as working fluids were carried out for power inputs up to 25 W, taking into account the steady state condition, the changes in the heat sink temperature and also different slopes in relation to the horizontal position of the LHPs. Performance tests of one CPL using water were also carried out for power inputs up to 30 W.

The LHP with acetone and water worked satisfactorily in the ranges from 5 to 25 W and from 5 to 15 W, respectively. Considering the limit temperature of 100 ^{o}C, the maximum power inputs were 25 W for acetone and 15 W for water. In spite of the LHPs have worked satisfactorily, a high temperature difference between the evaporator outlet and the heat sink was measured, varying from 40 to 80 ^{o}C for water and from 30 to 78 ^{o}C for acetone. The use of acetone as a working fluid ensured better results as compared with water.

The CPL (water) worked satisfactorily in the range from 5 to 30 W. The limit temperature of 100 ^{o}C (assumed for safety reasons) was not reached at the outlet evaporator ($T_{evap.out}$) even for 30 W power input.

The total thermal resistance was maximum for a heat load of 5 W (8.2 ^{o}C/W for LHP using water and 5.7 ^{o}C/W for LHP using acetone) and it was minimum for a heat load of 20 W (2.9 ^{o}C/W for LHP using acetone). The operation with water resulted in a minimum total thermal resistance of 5.3 ^{o}C/W for a heat load of 15 W. The smaller the total thermal resistance, the greater the heat transfer between the hot (evaporator surface) and cold (heat sink) sources of the capillary pumping systems for a given temperature difference.

Despite the quality of LHPs and CPLs has been customarily expressed by the total thermal resistance (R_{total}), the results obtained with R''_{total} showed more reliable for comparison of different systems. The results obtained with R''_{total} for the CPL (water) were larger than the both LHPs, *i.e.*, the LHPs worked better than the CPL (water). The R''_{total} was larger for heat flux of 0.53 W/cm^2 (52.8 ^{o}C/W/cm^2 for CPL using water) and heat flux of 1.06 W/cm^2 (38.8 ^{o}C/W/cm^2 for LHP using water and 27.0 ^{o}C/W/cm^2 for LHP using acetone) and it reached the lowest values in the range measured for heat flux of 3.18 W/cm^2 (31.7 ^{o}C/W/cm^2 for CPL and 25.0 ^{o}C/W/cm^2 for LHP, both using water) and heat flux of 5.3 W/cm^2 (14.7 ^{o}C/W/cm^2 for LHP using acetone).

Comparing the results of the present work with the results reported in the literature regarding the R''_{total}, the CPL (water) worked better than all CPLs reported in the literature reviewed in this work. On the other hand, despite the LHPs did not work as well as the mini-LHPs, they presented satisfactory results. One possible reason for this relatively poor result is that the mini-LHPs reported by the other authors used ammnonia as working fluid which, due to its thermal properties, is considered the best working fluid for capillary pumping systems.

The total pressure drop of all systems were estimated and no systems reached the capillary limit. It was noticed that the contribution of the pressure drop in the vapor and liquid transport lines and in the two phase zone of condenser were much smaller than the pressure drop in the porous wick. Besides, the total pressure drop of the CPL (water) was greater than the LHP (water) due to the greater mass flow rate and the greater number of grooves in the evaporator of the CPL. As it could be noticed in the results, the two phase pressure drop in the condenser was very small representing less than 0.5%, due to the low mass flow rates. Therefore, uncertainties in the evaluation of this contribution were not very relevant.

The experimental results were compared with the theoretical results obtained with the model. Only the results of the LHP (acetone) reached the capillary limit for a porous wick with one-layer. Despite the LHP (acetone) has reached the capillary limit, it continued working for heat loads of 20 and 25 W. So, according to the model (presented in Chapter

2), the evaporation front invaded the porous wick and stablished a stable position within it. However, this comparison should be taken only as a first approximation since the theoretical model does not reproduce completely the geometry of the tested CPL and LHPs. Nevertheless, the physical trends remain the same. If a porous wick with two-layers with different thermal conductivity was used instead of a porous wick with one-layer, it was observed that the higher the thermal conductivity underneath the fin the higher the capillary limit.

Finally, further research is still required in order to reduce the operation temperature, evaluating changes related to the properties of the ceramic wick (porosity, pore size and thermal conductivity) and improvements in the whole design of LHPs and CPL.

5.4 Future Works

This study initiated the research at LabCET (Laboratory of Combustion and Thermal Systems Engineering, Federal University of Santa Catarina in Brazil) and IKE (Institute of Nuclear Technology and Energy Systems, Stuttgart University in Germany) regarding the feasibility of the ceramic wick application in LHP and CPL using water as working fluid. The main objectives of this work, the application of a ceramic wick in capillary pumping systems (LHPs and CPLs) and the mathematical model which allow to determine the vapor invasion threshold of the porous wick, were attained, however future research is need. In the author's opinion, the following research directions can be investigated in the future:

- Adaptation of the model for the actual cylindrical geometry of the capillary evaporators tested here.
- Design mini-LHPs and mini-CPLs in order to apply them in notebooks and desktops.
- Design and manufacture a LHP and/or CPL with devices to measure pressure drops along the system and temperature distribution inside the capillary evaporator.
- Test the LHP and the CPL in microgravity environment for space application.
- Manufacture a ceramic wick with higher thermal conductivity, changing for instance the percentage of mullite from 80 to 20% and alumina from 20 to 80%.

References

ARPACI, V. S. *Conduction Heat Transfer*. [S.l.]: Addison-Wesley Publishing Company, 1966.

BERTI, L.; SANTOS, P. H. D.; JANSSEN, R.; BAZZO, E.; HOTZA, D.; RAMBO, C. Evaluation of permeability constants of ceramic wick structures for two phase heat transfer devices. *Topics in Chemistry and Material Science*, v. 01, p. 131–137, 2010.

BERTI, L. F. *Characterization of Ceramic Wicks for Application in Capillary Pumping Systems (in portuguese)*. Dissertação (Mestrado) — Federal University of Santa Catarina, 2008.

CAMARGO, H. V. R. *Experimental and Theoretical Evaluation of Porous Wicks Applied to Capillary Pumping Systems (in portuguese)*. Tese (Doutorado) — Federal University of Santa Catarina, 2004.

CAO, Y.; FAGHRI, A. Analytical solution of flow and heat transfer in a porous structure with partial heating and evaporation on the upper surface. *International Journal of Heat and Mass Transfer*, v. 37, p. 1525 – 1533, 1994.

CAO, Y.; FAGHRI, A. Conjugate analysis of a flat-plate type evaporator for capillary pumped loops with three-dimensional vapor flow in the groove. *International Journal of Heat and Mass Transfer*, v. 37, p. 401–409, 1994.

CHEN, P. C.; LIN, W. K. The application of capillary pumped loop for cooling of electronic components. *Applied Thermal Engineering*, v. 21, p. 1739–1754, 2001.

CHEN, Y.; GROLL, M.; MERTZ, R.; MAYDANIK, Y. F.; VERSHININ, S. Steady-state and transient performance of a miniature loop heat pipe. *International Journal of Thermal Science*, v. 45, p. 1084–1090, 2006.

CHERNYSHEVA, M. A.; VERSHININ, S. V.; MAYDANIK, Y. F. Operating temperature and distribution of a working fluid in lhp. *International Journal of Heat and Mass Transfer*, v. 50, p. 2704–2713., 2007.

CHUANG, P. Y. A. *An Improved Steady-State Model of Loop Heat Pipe Based on Experimental and Theoretical Analyses*. Tese (Doutorado) — Pennsylvania State

University, 2003.

DEMIDOV, A. S.; YATSENKO, E. S. Investigation of heat and mass transfer in the evaporation zone of a heat pipe operating by the inverted meniscus principle. *International Journal of Heat and Mass Transfer*, v. 37, p. 2155–2163, 1994.

EçA, L.; HOEKSTRA, M. Code verification of unsteady flow solvers with method of manufactured solutions. *International Journal of Offshore and Polar Engineering*, v. 18, p. 120–126, 2008.

EçA, L.; HOEKSTRA, M. Evaluation of numerical error estimation based on grid refinement studies with the method of the manufactured solutions. *Computers & Fluids*, v. 38, p. 1580–1591, 2009.

FAGHRI, A. *Heat Pipe Science And Technology*. [S.l.]: Taylor and Francis, 1995.

FIGUS, C.; BRAY, Y. L.; BORIES, S.; PRAT, M. Heat and mass transfer with phase change in a porous structure partially heated: continuum model and pore network simulation. *International Journal of Heat and Mass Transfer*, v. 42, p. 2557 –2569, 1999.

GRAY, W. G. A derivation of the equations for multi-phase transport. *Chemical Engineering Science*, v. 30, p. 229–233, 1975.

HADLEY, G. R. Thermal conductivity of packed metal powders. *International Journal of Heat and Mass Transfer*, v. 29, p. 909–920, 1986.

HOANG, T. T.; O'CONNELL, T. A.; KU, J.; BUTLER, C. D. Miniature loop heat pipes for electronic cooling. In: *International Electronic Packaging Technical Conference and Exhibition, Maui, Hawaii, USA*. [S.l.: s.n.], 2003.

IEC751. Industrial platinum resistance thermometer sensors. In: *IEC*. [S.l.: s.n.], 1983.

INCROPERA, F. P.; DEWITT, D. P. *Fundamentals of Heat and Mass Transfer*. [S.l.]: John Wiley & Sons, Inc., 2003.

ISO. Guide to the expression of uncertainty in measurement. In: *GUM*. [S.l.: s.n.], 2008.

JANSSEN, R.; SCHEPPOKAT, S.; CLAUSSEN, N. Tailor-made ceramic-based components - advantages by reactive processing and advanced shaping techniques. *Journal of the European Ceramic Society*, v. 28, p. 1369–1379, 2008.

KAKAC, S.; LIU, H. *Heat Exchangers Selection, Rating, and Thermal Design*. [S.l.]:

CRC, 2002.

KAVIANY, M. *Principles of Heat Transfer in Porous Media*. [S.l.]: Springer-Verlag, 1995.

KAYA, T.; GOLDAK, J. Numerical analysis of heat and mass transfer in the capillary structure of a loop heat pipe. *International Journal of Heat and Mass Transfer*, v. 49, p. 3211–3220, 2006.

KU, J. Thermodynamic aspects of capillary pumped loop operation. In: *Proceedings of the 6th AIAA/ASME Joint Thermophysics and Heat Transfer Conference, AIAA-94-2059, Colorado Springs, USA, pp.1-11.* [S.l.: s.n.], 1994.

KU, J. Operating characteristics of loop heat pipes. In: *Proceedings of the 29th International Conference on Enviromental System, 1999-01-2007, Denver, Colorado, USA.* [S.l.: s.n.], 1999.

KU, J.; KROLICZEK, E. J. Analytical modeling of the capillary pumped loop. In: *6th International Heat Pipe Conference, Grenoble, France.* [S.l.: s.n.], 1987.

KU, J.; OTTENSTEIN, L.; BIRUR, G. Thermal performance of a multi-evaporator loop heat pipe with thermal masses and thermal electrical coolers. In: *Proceedings of the 13th International Heat Pipe Conference (IHPC), Shanghai, China.* [S.l.: s.n.], 2004.

LAURINDO, J. B.; PRAT, M. Numerical and experimental net-work study of evaporation in capillary porous media: phase distributions. *Chemical Engineering Science*, v. 23, p. 5171–5185, 1996.

LI, T.; OCHTERBECK, J. M. Effect of wick thermal conductivity on startup of a capillary pumped loop evaporator. *AIAA*, v. 993446, p. 10–20, 1999.

MALISKA, C. R. *Computational Heat and Mass Transfer and Fluid Mechanic (in portuguese).* [S.l.]: Livros Técnicos e Científicos Editora, 2004.

MARCHI, C. H.; SILVA, A. F. C. Unidimensional numerical solution error estimation for convergent apparent order. *Numerical Heat Transfer - Part B Fundamentals*, v. 42, n. 2, p. 167–188, ago. 2002.

MARCHI, C. H.; SILVA, A. F. C. Multi-dimensional discretization error estimation for convergent apparent order. *Journal of the Brazilian Society of Mechanical Engineering*, v. 27, n. 4, p. 432–439, out.-dez. 2005.

MAYDANIK, Y. F. State-of-the-art of cpl and lhp technology. In: *Proccedings of the 11th International Heat Pipe Conference, Tokyo, Japan*. [S.l.: s.n.], 1999.

MAYDANIK, Y. F. Loop heat pipes - review. *Applied Thermal Engineering*, v. 25, p. 635–657., 2005.

MAYDANIK, Y. F.; FERSHTATER, Y. G.; GONCHAROV, K. A. Capillary-pump loop for the systems of thermal regulation of sapcecraft. In: *Proceedings of the 4th European Symposium on Space Environmental and Crontrol Systems, Florance, Italy, pp. 87-92.* [S.l.: s.n.], 1991.

MAYDANIK, Y. F.; VERSHININ, S. Development and tests of ammonia miniature loop heat pipes with cylindrical evaporators. *Applied Thermal Engineering*, v. 29, p. 2297–2301, 2009.

NICHOLAS, J. V.; WHITE, D. R. *Traceable Temperatures - An Introduction to Temperature Measurement and Calibration*. [S.l.]: John Wiley & Sons Ltd, England, 2005.

NIKITKIN, M.; CULLIMORE, B. Cpl and lhp technologies: What are the differences, what are the similarities? *SAE Paper*, No. 981587, 1998.

OLIVEIRA, P. A. *Modeling and Numerical Analisys of Flow and Heat Transfer in Active Magnetic Regenerators (in protuguese)*. Dissertação (Mestrado) — Federal University of Santa Catarina, 2008.

PASTUKHOV, V.; MAYDANIK, Y. F. Low-noise cooling system for pc on the base of loop heat pipes. *Applied Thermal Engineering*, v. 27, p. 894–901, 2007.

PASTUKHOV, V. G.; MAYDANIK, Y. F.; VERSHININ, S. V.; KORUKOV, M. A. Miniature loop heat pipes for electronics cooling. *Applied Thermal Engineering*, v. 23, p. 1125–1135, 2003.

PATANKAR, S. V. *Numerical Heat Transfer and Fluid Flow*. [S.l.]: Hemisphere Publishing Corporation, 1980.

PETERSON, G. *An Introduction to Heat Pipes*. [S.l.]: John Wiley & Sons, Inc., New York, 1994.

PRAT, M. Percolation model of drying under isothermal conditions in porous media. *International Journal of Multiphase Flow*, v. 19, p. 691–704, 1993.

PRAT, M. Isothermal drying of non-hygroscopic capillary porous materials as an invasion percolation process. *International Journal of Multiphase Flow*, v. 21, p. 875–892, 1995.

RASSAMAKIN, B. M.; PISMENNY, Y. N.; KHAYRNASOV, S. M.; YE, Y.; SMIRNOV, G. F. Research and development of aluminum loop heat pipes operation characteristics. In: *Proceedings of the 12 th IHPC, Moscow*. [S.l.: s.n.], 2002.

REIMBRECHT, E. G. *Manufacturing, Geometric Characterization and Determination of Hydraulic Properties of Porous Wicks for Using in Capillary Pumps (in portuguese)*. Tese (Doutorado) — Federal University of Santa Catarina, 2004.

REIMBRECHT, E. G.; FREDEL, M. C.; BAZZO, E.; PEREIRA, F. M. Manufacturing and microstructural characterization of sintered nickel wicks for capillary pump. *Materials Research*, v. 2, p. 225–229, 1999.

RHI, S. H. Operation and characteristics of a loop heat pipe. In: *Proceedings of the 8th International Heat Pipe Symposium, Kumamoto, Japan*. [S.l.: s.n.], 2006.

ROACHE, P. J. *Verification and Validation in Computational Science and Engineering*. [S.l.]: Hermosa, Albuquerque, New Mexico, U.S.A., 1998.

SANTOS, P. H. D.; BAZZO, E. Thermohydraulic analysis of two-phase capillary pumping systems for industrial design and space applications. In: *Proccedings of the 19th International Congress of Mechanical Engineering (COBEM), Brasília, Brazil*. [S.l.: s.n.], 2007.

TAKAHASHI, A. R. *Analisys of Heat and Mass Transfer with Phase Change into Porous Wicks Regarding its Optimization for Application in Capillary Pumps (in portuguese)*. Dissertação (Mestrado) — Federal University of Santa Catarina, 2002.

UDELL, K. S. Heat transfer in porous media heated from above with evaporation, condensation and capillary effects. *ASME*, v. 105, p. 485–492, 1983.

WANG, C.; LEU, T.; LAI, T. Micro capillary pumped loop system for a cooling high power device. *Experimental Thermal and Fluid Science*, v. 32, p. 1090–1095, 2008.

WHITAKER, S. Simultaneous heat, mass, and momentum transfer in porous media: A theory of drying. *Advances in Heat Transfer*, v. 13, p. 119–203, 1977.

APPENDIX A

Volume Averaged Equations of Energy and Mass Conservation

This appendix presents the volume averaged equations of energy and mass conservation used in the formulation of the model presented in Chapter 2. For the modeling, the porous wick is a flat circular disc and is assembled between the liquid feeding channel and the vapor chamber. Figure A.1 presents a rendering of the porous wick modeled. The upper part of the wick is heated by an external heat flux. The evaporation process that takes place in the wick of the capillary evaporator depends on the applied thermal load on the system and it is assumed that it may occur in three regimes: microfilm evaporation, evaporation at the external surface of the wick and evaporation within the wick.

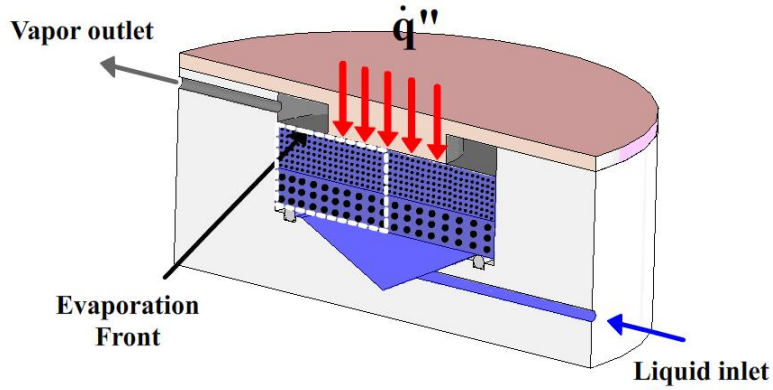

Figure A.1 – Cross-section view of the flat capillary evaporator with cylindrical geometry.

Figure A.2 presents a unit cell formed by a half of a single fin and the region of the porous wick bounded by the two symmetry surfaces. In Fig. A.2(a), an external heat flux is supplied to the capillary evaporator and a liquid microfilm is formed between the external surface of the porous wick and the vapor grooves as modeled by Demidov & Yatsenko (1994). Since the inner surface temperature of the fin is higher than the liquid temperature, the liquid microfilm tends to dry out. After the microfilm dries out, the evaporation interface migrates to the external surface of the porous wick, as depicted in

Fig. A.2(b). If the thermal load continues increasing, a capillary pressure threshold is reached and the evaporation front moves to within the porous wick, as shown in Fig. A.2(c). Here, only the evaporation regime in the external surface of the wick is studied. Following Li & Ochterbeck (1999), this is the safest operation condition.

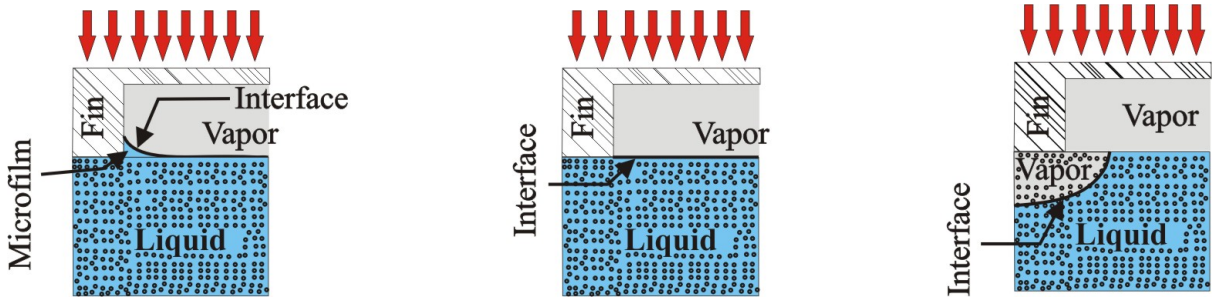

Figure A.2 – (a) Microfilm evaporation (b) evaporation at the outer surface and (c) evaporation within the porous wick.

A.1 Local Problem

Assuming the existence of a liquid-vapor interface, according to Fig. A.3, in which the mass flow rate of liquid, that flows by capillary action through the porous wick, becomes vapor and flows via the grooves forward the condenser. This interface is composed by several menisci.

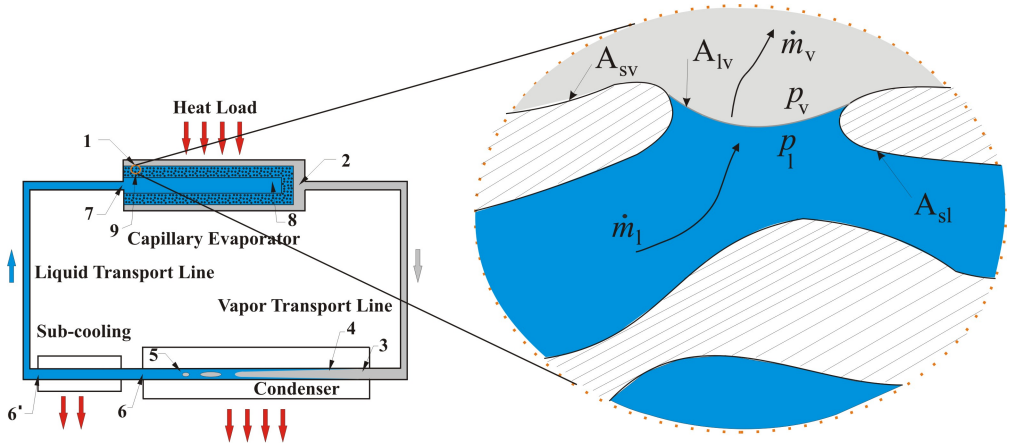

Figure A.3 – The local problem of phase change within porous wick of a capillary pumping system. Rendering of the surface of the porous wick during evaporation.

Since in this work the attention is focused on the evaporation of the liquid in the upper surface of the porous wick, the porous medium is sutarated with liquid and the evaporation only takes place in the boundary of the domain. The phase solid of the porous wick is inert and impermeable to the fluid phases. The conservation equations

that govern the phenomena are presented as follows. The mass conservation equation for liquid phase:

$$\frac{\partial\left(\rho_l\right)}{\partial t}+\nabla\cdot\left(\rho_l\mathbf{v}_l\right)=0 \tag{A.1}$$

The energy equation for the liquid and solid phases are:

$$\frac{\partial\left(\rho_l c_{p,l}T_l\right)}{\partial t}+\nabla\cdot\left(\rho_l\mathbf{v}_l c_{p,l}T_l\right)=-\nabla\cdot\mathbf{q}_l \tag{A.2}$$

$$\frac{\partial\left(\rho_s c_{p,s}T_s\right)}{\partial t}=-\nabla\cdot\mathbf{q}_s \tag{A.3}$$

The conduction heat fluxes in the solid and liquid phases are given by Fourier's Law as,

$$\mathbf{q}_s=-\lambda_s\nabla T_s$$

$$\mathbf{q}_l=-\lambda_l\nabla T_l$$

The momentum conservation equation (Navier-Stokes) for a compressible flow for the liquid phase:

$$\rho_l\left(\frac{\partial\mathbf{v}_l}{\partial t}+\mathbf{v}_l\cdot\nabla\mathbf{v}_l\right)=-\nabla p_l+\mu\nabla^2\mathbf{v}_l+\rho_l\mathbf{f} \tag{A.4}$$

The boundary conditions for the interface solid-liquid may be represented as:

$$\mathbf{v}_l=0\quad\text{on}\quad A_{sl} \tag{A.5}$$

$$\lambda_l\nabla T_l\cdot\hat{\mathbf{n}}_{ls}=\lambda_s\nabla T_s\cdot\hat{\mathbf{n}}_{sl}\quad\text{on}\quad A_{sl} \tag{A.6}$$

$$T_l=T_s\quad\text{on}\quad A_{sl} \tag{A.7}$$

The boundary conditions for the interface liquid-vapor in the upper surface of the porous wick may be represented as:

$$\rho_l\left(\mathbf{v}_l\right)\cdot\hat{\mathbf{n}}_{lv}+\rho_v\left(\mathbf{v}_v\right)\cdot\hat{\mathbf{n}}_{vl}=0\quad\text{on}\quad A_{lv} \tag{A.8}$$

$$T_l = T_v \quad on \quad A_{lv} \tag{A.9}$$

$$p_{cap} = p_v - p_l \quad \text{on} \quad A_{lv} \tag{A.10}$$

The analysis of heat and mass transfer in porous wicks is a difficult task, because there are limitations, even using modern computers, in the calculation of the detailed profiles of the variables such as: temperature, pressure and velocities. There are two methods which have been more used for solving the heat and mass transfer problem with phase change in porous wick: volume averaging method (continuum approach) and pore network method. Here, only the volume averaging method will be presented. Further information about the application of pore network method for solving the heat and mass transfer problem in porous wick can be found in Figus *et al.* (1999). The set of equations, presented above, is solved using the volume averaging method.

A.2 Volume Averaging Method

The fields of temperature, pressure and velocities can be obtained with the macroscopic model using the volume averaging method. This method will be applied to the govern equations of the heat and mass transfer phenomena in porous wick with phase change, which takes place in the external surface of the porous wick. For the volume averaging method, first it is necessary to choose a representative elementary volume (REV), as shown in Fig. A.4. REV is the smallest differential volume that results in statistically meaningful local average properties, *i.e.*, a small increase in the REV does not change the averaged properties. This requires that,

$$d_p \ll l_{REV} \ll L_{wick}$$

where d_p is the pore characteristic diameter, l_{REV} is the characteristic length of the REV and L_{wick} is the largest characteristic length of the problem.

Some definitions and theorems are presented here to better understand the volume averaging method. First, applying the volume average to the temperature of the solid phase for example:

$$\langle T_s \rangle = \frac{1}{V} \int_V T_s dV \tag{A.11}$$

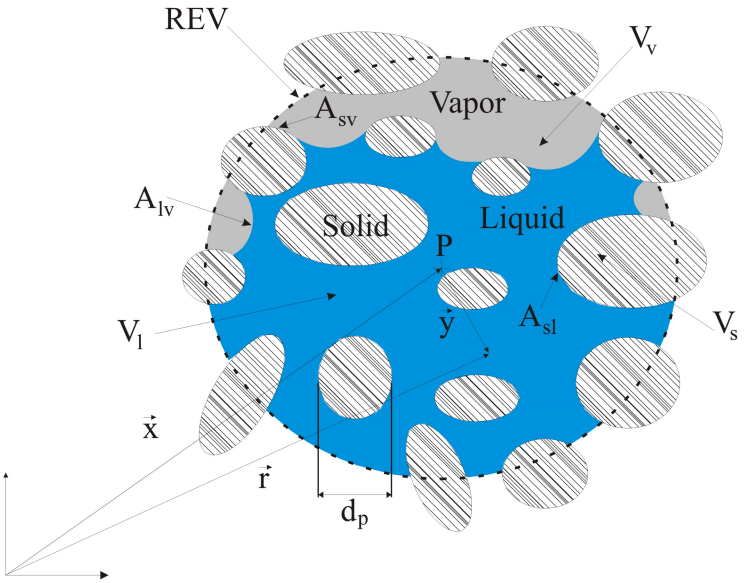

Figure A.4 – Schematic averaging volume

Since T_s is defined only in the solid phase and is zero in all other phases, Eq. A.11 reduces to

$$\langle T_s \rangle = \frac{1}{V} \int_{V_s} T_s dV \tag{A.12}$$

The disadvantage of the phase average is when the T_s is constant, because the phase average value is not equal to this constant value of T_s. Then a quantity more representative for the temperature of the solid is the intrinsic phase average, which is given by

$$\langle T_s \rangle^s = \frac{1}{V_s} \int_{V_s} T_s dV \tag{A.13}$$

The volume fraction for the liquid and solid phases are defined as

$$\varepsilon_s = \frac{V_s}{V} \tag{A.14}$$

$$\varepsilon_l = \frac{V_l}{V} \tag{A.15}$$

$$\varepsilon_s + \varepsilon_l = 1 \tag{A.16}$$

The relation between the phase average and the intrinsic phase average is given by

$$\varepsilon_s \langle T_s \rangle^s = \langle T_s \rangle \tag{A.17}$$

The averaging theorem is an important tool in the formulation of volume averaged equations and is given by

$$\langle \nabla T_s \rangle = \nabla \langle T_s \rangle + \frac{1}{V} \int_{A_{sl}} T_s \hat{\mathbf{n}}_{sl} \, dA \tag{A.18}$$

The Reynolds transport theorem is also used in the volume averaging method and is defined for the liquid phase as,

$$\frac{1}{V} \int_{V_l} \left(\frac{\partial \rho_l}{\partial t} \right) dV = \frac{d}{dt} \left[\frac{1}{V} \int_{V_l} \rho_l \, dV \right] - \frac{1}{V} \int_{A_{ls}} \rho_l \mathbf{v}_l \cdot \mathbf{n}_{ls} \, dA \tag{A.19}$$

A.2.1 Energy Equation for the Solid Phase in Volume Average

Applying the volume averaging method to the Eq. A.3 for the solid phase,

$$\left\langle \frac{\partial \left(\rho_s c_{p,s} T_s \right)}{\partial t} \right\rangle = - \langle \nabla \cdot \mathbf{q}_s \rangle \tag{A.20}$$

Applying the averaging theorem, defined in Eq. A.18, in Eq. A.20 and next substituting the intrinsic phase average, given in Eq. A.13, the energy equation for the solid phase in volume average is obtained,

$$\frac{\partial \left(\rho_s c_{p,s} \varepsilon_s \langle T_s \rangle^s \right)}{\partial t} = \nabla \cdot \left\{ \lambda_s \left[\nabla \left(\varepsilon_s \langle T_s \rangle^s \right) + \frac{1}{V} \int_{A_{sl}} T_s \mathbf{n}_{sl} \, dA \right] \right\} - \frac{1}{V} \int_{A_{sl}} \mathbf{q}_s \mathbf{n}_{sl} \, dA \tag{A.21}$$

A.2.2 Mass Conservation Equation for the Liquid Phase in Volume Average

Applying the volume averaging method to the mass conservation equation as applied to the energy equation for the solid phase, we have:

$$\left\langle \frac{\partial \left(\rho_l \right)}{\partial t} \right\rangle + \langle \nabla \cdot \left(\rho_l \mathbf{v}_l \right) \rangle = 0 \tag{A.22}$$

Using the Reynolds transport theorem, defined in Eq. A.19, in the first term of Eq. A.22 and the averaging theorem, defined in Eq. A.18, in the second term of of Eq. A.22, then

$$\frac{\partial}{\partial t}\left(\frac{1}{V}\int_{V_l}\rho_l\,dV\right)-\frac{1}{V}\int_{A_{ls}}\rho_l\mathbf{v}_l\cdot\mathbf{n}_{ls}\,dA+\nabla\cdot\langle\rho_l\mathbf{v}_l\rangle+\frac{1}{V}\int_{A_{ls}}\rho_l\mathbf{v}_l\cdot\mathbf{n}_{ls}\,dA=0 \quad \text{(A.23)}$$

According to the boundary condition in the interface liquid-solid presented in the Eq. A.5, which states that at a solid boundary the liquid velocity relative to the boundary is zero, then the Eq. A.23 becomes,

$$\frac{\partial\langle\rho_l\rangle}{\partial t}+\nabla\cdot\langle\rho_l\mathbf{v}_l\rangle=0 \quad \text{(A.24)}$$

Applying the volume fraction for the liquid phase defined in Eq. A.15 and assuming incompressible flow, we have the final form of the mass conservation equation for the liquid phase in volume average:

$$\frac{\partial\varepsilon_l}{\partial t}+\nabla\cdot\langle\mathbf{v}_l\rangle=0 \quad \text{(A.25)}$$

A.2.3 Energy Equation for the Liquid Phase in Volume Average

Now applaying the volume averaging method to the energy equation for liquid phase, then the Eq. A.2 becomes:

$$\left\langle\frac{\partial\left(\rho_l c_{p,l}T_l\right)}{\partial t}\right\rangle+\langle\nabla\cdot\left(\rho_l\mathbf{v}_l c_{p,l}T_l\right)\rangle=-\langle\nabla\cdot\mathbf{q}_l\rangle \quad \text{(A.26)}$$

Applying the Renolds transport and averaging theorems to the first and second terms of the Eq. A.26, respectively, we have:

$$\frac{\partial}{\partial t}\left(\frac{1}{V}\int_{V_l}\rho_l c_{p,l}T_l\,dV\right)-\frac{1}{V}\int_{A_{ls}}\rho_l c_{p,l}T_l\mathbf{v}_l\cdot\mathbf{n}_{ls}\,dA+\nabla\cdot\langle\rho_l\mathbf{v}_l c_{p,l}T_l\rangle$$

$$+\frac{1}{V}\int_{A_{ls}}\rho_l c_{p,l}T_l\mathbf{v}_l\cdot\mathbf{n}_{ls}\,dA=-\langle\nabla\cdot\mathbf{q}_l\rangle \quad \text{(A.27)}$$

Again according to the boundary condition in the interface liquid-solid presented in the Eq. A.5 ($\mathbf{v}_l=0$), considering $c_{p,l}$ and ρ_l constant and using the averaging theorem in the last term of the Eq. A.27, then

$$\rho_l c_{p,l}\frac{\partial\langle T_l\rangle}{\partial t}+\rho_l c_{p,l}\nabla\cdot\langle\mathbf{v}_l T_l\rangle=$$

$$\nabla \cdot \left\{ \lambda_l \left[\nabla \left(\varepsilon_l \left\langle T_l \right\rangle^l \right) + \frac{1}{V} \int_{A_{ls}} T_l \mathbf{n}_{ls} \, dA \right] \right\} - \frac{1}{V} \int_{A_{ls}} \mathbf{q}_l \mathbf{n}_{ls} \, dA \tag{A.28}$$

According to Whitaker (1977), the term $\nabla \cdot \langle \mathbf{v}_l T_l \rangle$ should be represented in terms of $\langle T_l \rangle^l$ and $\langle \mathbf{v}_l \rangle$. In order to accomplish this, it is necessary to represent the point functions T_l and $\mathbf{v}_l$ in terms of the average values and deviations from these average values. Here, it will be used the Gray's decomposition as follows,

$$T_l = \langle T_l \rangle^l + T_l^{'} \tag{A.29}$$

$$\mathbf{v}_l = \langle \mathbf{v}_l \rangle + \mathbf{v}_l^{'} \tag{A.30}$$

where $T_l^{'}$ and $\mathbf{v}_l^{'}$ are the deviations from average values. Applying the Eqs. A.29 and A.30 in the second term of Eq. A.28, we have:

$$\nabla \cdot \langle \mathbf{v}_l T_l \rangle = \langle T_l \rangle^l \nabla \cdot \langle \mathbf{v}_l \rangle + \langle \mathbf{v}_l \rangle \cdot \nabla \langle T_l \rangle^l + \nabla \cdot \left\langle \mathbf{v}^{'} T_l^{'} \right\rangle \tag{A.31}$$

Substituting the intrinsic phase average for liquid temperature ($\langle T_l \rangle = \varepsilon_l \langle T_l \rangle^l$) and the Eq. A.31 in the Eq. A.28, we have

$$\varepsilon_l \rho_l c_{p,l} \frac{\partial \langle T_l \rangle^l}{\partial t} + \left(\frac{\partial \varepsilon_l}{\partial t} + \nabla \cdot \langle \mathbf{v}_l \rangle \right) \rho_l c_{p,l} \langle T_l \rangle^l + \rho_l c_{p,l} \langle \mathbf{v}_l \rangle \cdot \nabla \langle T_l \rangle^l + \rho_l c_{p,l} \nabla \cdot \left\langle v_l^{'} T_l^{'} \right\rangle$$

$$= \nabla \cdot \left\{ \lambda_l \left[\nabla \left(\varepsilon_l \left\langle T_l \right\rangle^l \right) + \frac{1}{V} \int_{A_{ls}} T_l \mathbf{n}_{ls} \, dA \right] \right\} - \frac{1}{V} \int_{A_{ls}} \mathbf{q}_l \mathbf{n}_{ls} \, dA \tag{A.32}$$

Finally, substituting the mass conservation equation for the liquid phase in volume average presented in Eq. A.25, $\frac{\partial \varepsilon_l}{\partial t} + \nabla \cdot \langle \mathbf{v}_l \rangle = 0$, in the second term of Eq. A.32, we have

$$\varepsilon_l \rho_l c_{p,l} \frac{\partial \langle T_l \rangle^l}{\partial t} + \rho_l c_{p,l} \langle \mathbf{v}_l \rangle \cdot \nabla \langle T_l \rangle^l + \rho_l c_{p,l} \nabla \cdot \left\langle v_l^{'} T_l^{'} \right\rangle$$

$$= \nabla \cdot \left\{ \lambda_l \left[\nabla \left(\varepsilon_l \left\langle T_l \right\rangle^l \right) + \frac{1}{V} \int_{A_{ls}} T_l \mathbf{n}_{ls} \, dA \right] \right\} - \frac{1}{V} \int_{A_{ls}} \mathbf{q}_l \mathbf{n}_{ls} \, dA \tag{A.33}$$

A.2.4 Total Energy Equation in Volume Average

Whitaker (1977) states that in many processes the temperature of the liquid phase is different from the temperature of the solid phase. However in drying processes, the temperature of the liquid phase is equal to the solid one due to the relatively low convective transport rates. Under these circumstances one is encouraged to assume that conductive transport is sufficient to eliminate significant tamperature differences between the separate phases. Then, in order to obtain the total energy equation in volume average for solid and liquid phases, it is reasonable to assume the local thermal equilibrium between the phases, *i.e.*, the temperatures in each phase are equal ($\langle T_l \rangle^l = \langle T_s \rangle^s = \langle T \rangle$). Now adding the Eqs. A.21 and A.33, we have

$$\left(\varepsilon_s \rho_s c_{p,s} + \varepsilon_l \rho_l c_{p,l}\right) \frac{\partial \langle T \rangle}{\partial t} + \left(\rho_l c_{p,l} \langle \mathbf{v}_l \rangle\right) \cdot \nabla \langle T \rangle + \rho_l c_{p,l} \nabla \cdot \left\langle v_l{}' T_l{}' \right\rangle =$$

$$\nabla \cdot \left[\lambda_s \left(\varepsilon_s \nabla \langle T_s \rangle^s + \langle T_s \rangle^s \nabla \varepsilon_s \right) + \lambda_l \left(\varepsilon_l \nabla \langle T_l \rangle^l + \langle T_l \rangle^l \nabla \varepsilon_l \right) + \frac{\lambda_s}{V} \int_{A_{sl}} T_s \mathbf{n_{sl}} \, dA + \frac{\lambda_l}{V} \int_{A_{ls}} T_l \mathbf{n}_{ls} \, dA \right]$$

$$- \frac{1}{V} \int_{A_{sl}} \mathbf{q}_s \mathbf{n}_{sl} \, dA - \frac{1}{V} \int_{A_{ls}} \mathbf{q}_l \mathbf{n}_{ls} \, dA \tag{A.34}$$

From the volume-averaging theorem applied to the phase indicator (GRAY, 1975), it is possible to show that,

$$\nabla \varepsilon_s = - \frac{1}{V} \int_{A_{sl}} \mathbf{n}_{sl} \, dA \tag{A.35}$$

According to Kaviany (1995) in the hipothesis of local thermal equilibrium it can also assume that $T_s{}'$ and $T_l{}'$ are equal. Since unitary normal vectors are opposite ($\mathbf{n}_{sl} = -\mathbf{n}_{ls}$) and applying the Gray's decomposition ($T_l = \langle T_l \rangle^l + T_l{}'$ and $T_l = \langle T_s \rangle^s + T_s{}'$) and the Eqs. A.6 and A.35 to Eq. A.34, we have

$$\left(\varepsilon_s \rho_s c_{p,s} + \varepsilon_l \rho_l c_{p,l}\right) \frac{\partial \langle T \rangle}{\partial t} + \left(\rho_l c_{p,l} \langle \mathbf{v}_l \rangle\right) \cdot \nabla \langle T \rangle + \rho_l c_{p,l} \nabla \cdot \left\langle v_l{}' T_l{}' \right\rangle$$

$$= \nabla \cdot \left[\left(\lambda_s \varepsilon_s + \varepsilon_l \lambda_l \right) \nabla \langle T \rangle + \left(\lambda_s - \lambda_l \right) \frac{1}{V} \int_{A_{sl}} T_s{}' \mathbf{n}_{sl} \, dA \right] \tag{A.36}$$

The problem is closed proposing a set of closure constitutive equations that, in general, is related to the local deviation of the variable to the gradient of its average such as,

$$T_s^{'} = \mathbf{b}_s \cdot \nabla \langle T \rangle \tag{A.37}$$

With this approximation the term involving $\left\langle \mathbf{v}_l^{'} T_l^{'} \right\rangle$ can be expressed as, (KAVIANY, 1995),

$$\left\langle \mathbf{v}_l^{'} T_l^{'} \right\rangle = \mathbf{D}^d \cdot \nabla \langle T_l \rangle^l \tag{A.38}$$

where $\mathbf{D}^d = -\frac{1}{V_l} \int_{V_l} \mathbf{v}_l^{'} \mathbf{b}_s \, dV$ is the dispersion tensor.

The effective thermal conductivity tensor λ_e is defined as,

$$\lambda_e = (\lambda_s \varepsilon_s + \varepsilon_l \lambda_l) \, \mathbf{I} + (\lambda_s - \lambda_l) \, \frac{1}{V} \int_{A_{sl}} \mathbf{b}_s \cdot \mathbf{n_{sl}} \, dA \tag{A.39}$$

where $\mathbf{I}$ is the unit tensor.

The total energy equation in volume average for liquid and solid phases is obtained by substituting of the Eqs. A.37, A.38 and A.39 in the Eq. A.36,

$$(\varepsilon_s \rho_s c_{p,s} + \varepsilon_l \rho_l c_{p,l}) \, \frac{\partial \langle T \rangle}{\partial t} + (\rho_l c_{p,l} \langle \mathbf{v}_l \rangle) \cdot \nabla \langle T \rangle = \nabla \cdot \left[\left(\lambda_e + \rho_l c_{p,l} \mathbf{D}^d \right) \cdot \nabla \langle T \rangle \right] \tag{A.40}$$

A.2.5 Semiheuristic Momentum Equationin Volume Average

The semiheuristic momentum equation was developed in order to have an equivalent equation to the Navier-Stokes equation that could describe the flowing through porous media. The momentum equation can be written in volume average as,

$$\frac{\rho_l}{\varepsilon_l} \left(\frac{\partial \langle \mathbf{v}_l \rangle^l}{\partial t} + \langle \mathbf{v}_l \rangle^l \cdot \nabla \langle \mathbf{v}_l \rangle^l \right) =$$

$$-\nabla \langle p \rangle^l + \rho_l \mathbf{f} + \frac{\mu}{\varepsilon_l} \nabla^2 \langle \mathbf{v}_l \rangle^l - \frac{\mu}{\mathbf{K}} \langle \mathbf{v}_l \rangle^l - \frac{C_E}{\mathbf{K}^{1/2}} \rho_l \left| \langle \mathbf{v}_l \rangle^l \right| \langle \mathbf{v}_l \rangle^l \tag{A.41}$$

The first terms on the left hand side of the Eq. A.41 represent the macroscopic inertial forces. On the right hand side of the Eq. A.41, the first term represents the pore pressure gradient, the second one represents the body force, the third represents the macroscopic shear stress diffusion (Brinkman viscous term), the fourth represents the microscopic viscous shear stress (Darcy term) and the fifth represents the microscopic

inertial force (Forscheimer term). When $\varepsilon_l \rightarrow 1$ and $\mathrm{K} \rightarrow \infty$ the Navier-Stokes equation is recovered.

APPENDIX B

Verification Study of the Numerical Code and Solution

This appendix presents a verification study of the numerical code and solution, which was obtained with the model presented in Chapter 2. Grid refinement tests were performed in order to evaluate the quality of the numerical code and solution. First, the numerical code is analyzed using a methodology of manufactured solution, which was proposed by Eça & Hoekstra (2008). Next, the numerical solution is analyzed using the Richardson extrapolation in order to estimate the uncertainties of the numerical solution, which was proposed by Marchi & Silva (2002, 2005) and also implemented by Oliveira (2008).

B.1 Verification of the Numerical Code

The maturing of Computational Fluid Dynamics (CFD) codes for pratical calculations in engineering implies the need to stablish the credibility of the results by verification and validation (EçA; HOEKSTRA, 2008). The verification of calculations is a purely mathematical exercise that intends to show that we are solving correctly the equations of the model. On the other hand, the validation is a science and engineering activity that intends to show that we are solving the right equations for the model. Here, only the verification is presented.

According to Roache (1998), the verification of the calculations is composed of two different processes: i) Code verification - verify that a given code solves correctly the equations and that there are not any errors in the code or inconsistences in the algorithm solution; and ii) Solution Verification - quantify the numerical erros in the computational simulation.

The exact solution of the mathematical model or of a manufactured solution can be used for the code verification. In the Method of Manufactured Solution (MMS), first a

continuum solution is constructed. In general, this constructed solution will not satisfy the governing equations (continuity and momentum) because of the arbitrary nature of the choice. But by adding an appropriate source term, which removes any imbalance caused by the choice of the continuum solution, the governing equations are forced to become a model for the constructed solution. Further information about the MMS method can be found in Eça & Hoekstra (2008, 2009). Here, the exact solution of the methamatical model will be used for the code verification.

Two models were presented in Chapter 2: Simplified and Improved Models. It was developed an exact solution for the simplified model and a numerical solution for the improved model. A CFD code was developed in FORTRAN 90 for the numerical solution of the improved model. In order to verify this CFD code, the boundary conditions of the improved model were changed for the boundary conditions of the simplified model, which was analytically solved. That is, the CFD code solved the simplified model numericaly for six different grids. The monitoring of the errors was done using the Root Mean Squared (RMS) error as,

$$RMS(e_\phi) = \sqrt{\frac{\sum_{i=1}^{Nr}\sum_{j=1}^{Nz}\left(\phi_{i,j}^{Num} - \phi_{exact}\right)^2}{Nr \times Nz}}, \tag{B.1}$$

where $RMS(e_\phi)$ is the RMS error of the variable ϕ (T - temperature or p - pressure), Nr and Nz are the numbers of nodes of the grid in the r and z directions, respectively. i and j are the nodes counters, $\phi_{i,j}^{Num}$ is the numerical solution for the node counter and ϕ_{exact} is the exact solution.

The RMS errors of the temperature $RMS(e_T)$ and pressure $RMS(e_p)$ are presented in Fig. B.1 for a grid refinement and heat flux of 4.0×10^4 W/m^2.

Six grids were used and they are identified as ($\eta_{50\times50}$), ($\eta_{100\times100}$), ($\eta_{150\times150}$), ($\eta_{200\times200}$), ($\eta_{250\times250}$) and ($\eta_{300\times300}$). In this notation, $\eta_{N_r\times N_z}$ represents a grid with N_r and N_z points. Figure B.1 presents in the abscissa, a relative ratio between the six grids (η_i) and the coarse grid ($\eta_{50\times50}$). It can be noticed in both figures that the more refined the grid, the smaller the RMS errors for both variables. It can also be noticed that the curves of $RMS(e_T)$ and $RMS(e_p)$ present an assymptotic behavior and the errors of the $RMS(e_T)$ was 0.00054 ^{o}C ($0,054\%$) and the $RMS(e_p)$ was 0.0140 Pa (1.40%) for a grid of $\eta_{150\times150}$. Therefore, since the RMS errors were estimated below 2% for both fields of temperature and pressure, the grid ($\eta_{150\times150}$) was chosen.

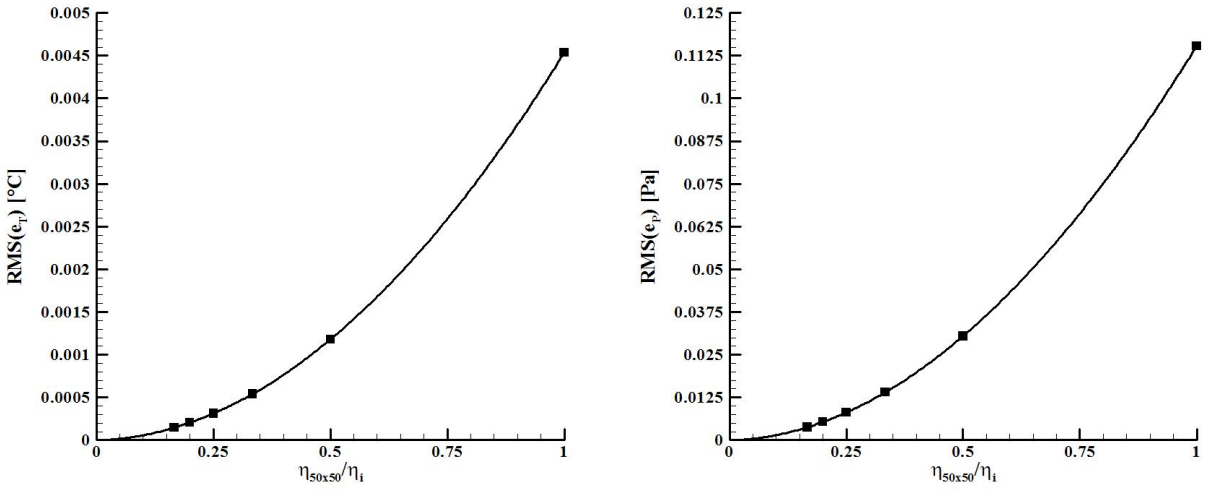

(a) (b)

Figure B.1 – (a) RMS error of the temperature and (b) pressure as a function of grid refinement.

B.2 Verification of the Numerical Solution

The analysis of the numerical solution was accomplished by the successive refinements of the grids. Figures B.2 and B.3 present the grid refinements for the temperature and pressure fields, respectively, at two locations in the computational domain ($z = L_z$ and $z = L_z/2$) and for the same heat flux of 4.0×10^4 W/m^2. Five grids are shown and it is noticed that the more refined the grid, the smaller becomes the difference between the results. For instance, the differences among the results of the grids ($\eta_{150\times150}$), ($\eta_{200\times200}$) and ($\eta_{250\times250}$) are almost indistinguishable.

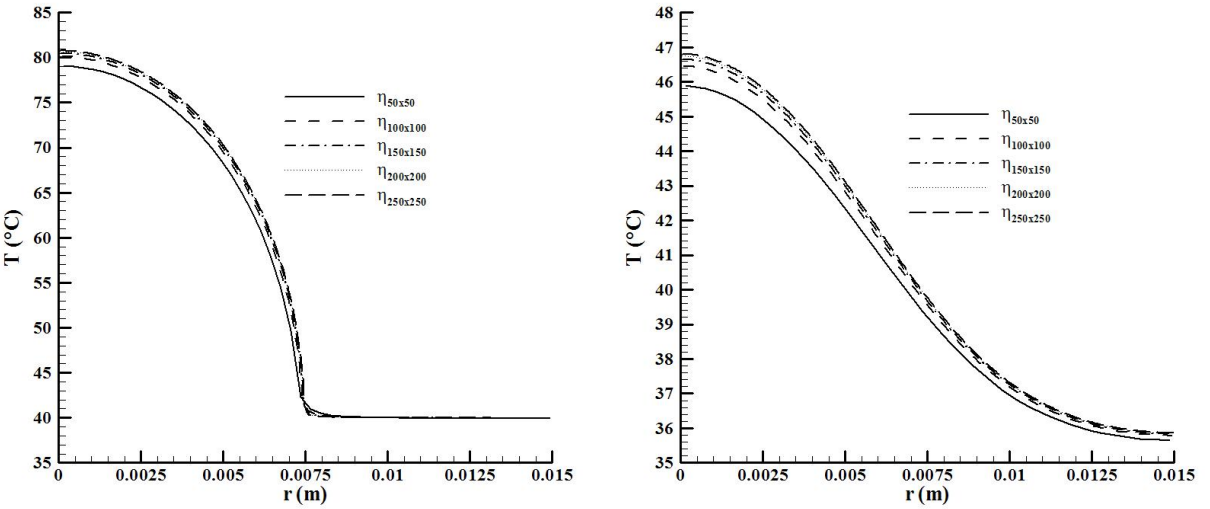

(a) (b)

Figure B.2 – Temperature distribution along r at $z = L_z$ (a) and (b) at $z = L_z/2$ for a heat flux of 4.0×10^4 W/m^2 and different grids.

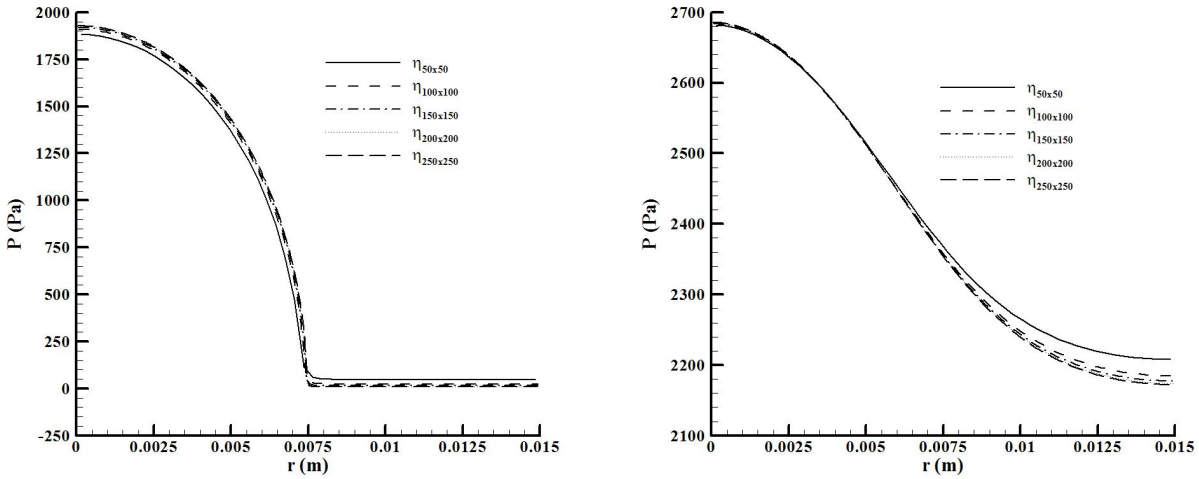

Figure B.3 – Pressure distribution along r at $z = L_z$ (a) and (b) at $z = L_z/2$ for a heat flux of 4.0×10^4 W/m^2 and different grids.

A methodology for estimating the uncertainties of the numerical solution is applied as follows. Oliveira (2008) presents in detail a methodology for estimating the uncertainties of numerical solutions, which is based on the Richardson Error Estimator following Marchi & Silva (2002, 2005). This methodology is briefly presented as follows. First, the area averaged temperature and pressure are determined as,

$$\bar{T} = \frac{1}{A}\int_0^{L_z}\int_0^{r} T(r,z)rdrdz \tag{B.2}$$

$$\bar{p} = \frac{1}{A}\int_0^{L_z}\int_0^{r} p(r,z)rdrdz. \tag{B.3}$$

Next, seven grids, ($\eta_{50\times50}$), ($\eta_{100\times100}$), ($\eta_{150\times150}$), ($\eta_{200\times200}$), ($\eta_{250\times250}$), ($\eta_{300\times300}$) and ($\eta_{400\times400}$) were used for calculating the average temperature and pressure. Tables B.1 and B.2 present the average temperature and pressure, respectively, the grid refinement ratio (Γ), the percentage of variation of the averaged values of T and p when compared to the previous grid and the CPU time for each grid. These results were used in the calculation of the numerical uncertainties.

Assuming that the possible mistakes made during the development of the CFD code and the errors of iteration are small, the true discretization error $E(\phi)$ of any variable of interest (ϕ) can be defined as the difference between the numerical (ϕ_{num}) and exact (ϕ_{exact}) solutions,

$$E(\phi) = \phi_{num} - \phi_{exact} \tag{B.4}$$

Table B.1 – Grid refinement of the numerical solution for the average temperature.

Grid ($\eta_{r\times z}$)	Γ	$\bar{T}$ (^{o}C)	Percentage (%)	CPU time
$\eta_{50\times50}$	—	38.08412	—	7.98s
$\eta_{100\times100}$	2.00	38.26033	0.463	2.21min
$\eta_{150\times150}$	1.50	38.32008	0.156	16.22min
$\eta_{200\times200}$	1.33	38.35015	0.078	56.73min
$\eta_{250\times250}$	1.25	38.36826	0.047	2.09h
$\eta_{300\times300}$	1.20	38.37936	0.029	4.48h
$\eta_{400\times400}$	1.20	38.39222	0.034	8.20h

Table B.2 – Grid refinement of the numerical solution for the average pressure.

Grid ($\eta_{r\times z}$)	Γ	$\bar{p}$ (Pa)	Percentage (%)	CPU time
$\eta_{50\times50}$	—	2271.187	—	7.98s
$\eta_{100\times100}$	2.00	2275.576	0.193	2.21min
$\eta_{150\times150}$	1.50	2277.658	0.091	16.22min
$\eta_{200\times200}$	1.33	2278.835	0.052	56.73min
$\eta_{250\times250}$	1.25	2279.590	0.033	2.09h
$\eta_{300\times300}$	1.20	2280.102	0.022	4.48h
$\eta_{400\times400}$	1.33	2280.721	0.027	8.20h

In order to determine the true discretization error through Eq. B.4 requires knowing the exact analytical solution (ϕ_{exact}). Unfortunately, in most practical problems, ϕ_{exact} is unknown. In such cases, the concept of estimated error or uncertainty $U(\phi)$ of the numerical solution can be expressed by,

$$U(\phi) = \phi_{est} - \phi_{num}, \tag{B.5}$$

where ϕ_{est} is an estimated analytical solution and ϕ_{num} is the numerical solution of any variable of interest (ϕ).

According to Marchi & Silva (2005), among the estimators found in the literature for estimating the discretization error, the generalized Richardson extrapolation is a good choice. The estimated analytical solution (ϕ_{est}), using the generalized Richardson extrapolation, can be obtained by,

$$\phi_{est} = \phi_1 + \frac{\phi_1 - \phi_2}{\Gamma^{\Lambda} - 1}, \tag{B.6}$$

where ϕ_1, ϕ_1 and ϕ_3 (it will be shown next) are the numerical solutions obtained, respectively, with the fine, coarse and supercoarse grids, Γ is the grid refinement ratio between the grids and Λ is the order of the discretization error.

Marchi & Silva (2005) classify the convergency order of the discretization error in:

- Theoretical (or real) order (Λ_t) - its value depends on the extrapolation functions used in the discretization of the mathematical model;
- Apparent order (Λ_{app}) - its value is a function of the numerical solution obtained, at least, with three different grids;
- Asymptotic order (Λ_{as}) - value for which the apparent order (Λ_{app}) converges when the volumes of the grid tend to zero.

The apparent order (Λ_{app}) can be calculated with the following equation for situations where the grid refinement ratio (Γ) between three grids is either constant or variable.

$$\Lambda_{app} = \frac{\ln\left(\dfrac{\phi_2 - \phi_3}{\phi_1 - \phi_2}\right)}{\ln(\Gamma)} \Rightarrow (\Gamma_{3,2} = \Gamma_{2,1} = \Gamma) \tag{B.7}$$

$$\Lambda_{app} = \frac{\ln\left[\left(\dfrac{\phi_2 - \phi_3}{\phi_1 - \phi_2}\right)\left(\dfrac{\Gamma_{2,1}^{\Lambda_{app}} - 1}{\Gamma_{3,2}^{\Lambda_{app}} - 1}\right)\right]}{\ln(\Gamma_{2,1})} \Rightarrow (\Gamma_{3,2} \neq \Gamma_{2,1}) \tag{B.8}$$

Marchi & Silva (2002) identify two types of behavior for Λ_{app} when the volumes of the grid are decreased: subconvergent and superconvergent intervals as it is shown in Fig. B.4.

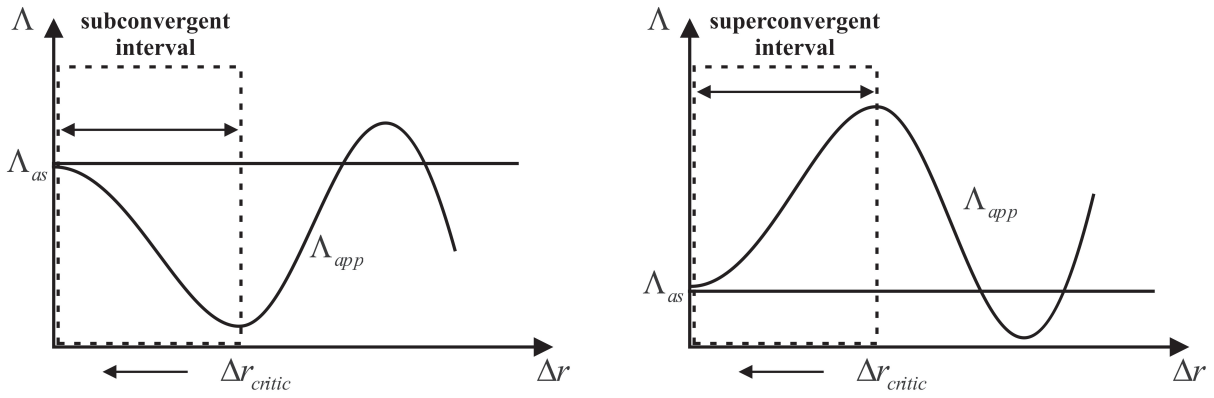

Figure B.4 – (a) Definition of the subconvergent interval and (b) superconvergent interval of the apparent order. Source: adapted from Oliveira (2008).

Figure B.4(a) presents the subconvergent interval, in which as the volumes of the grid are decreased in respect to a critical value (Δr_{critic}), the values of the apparent order (Λ_{app}) are positive, increasing and lower than the value of the asymptotic order (Λ_{as}). On

the other hand, Fig. B.4(b) presents the superconvergent interval, in which the values of the apparent order (Λ_{app}) are positive, decreasing and greater than the value of the asymptotic order (Λ_{as}). For solutions of complex problems, Λ_{app} does not reach exactly Λ_{as} since for that it would be necessary an infinite number of control volumes.

If the apparent order (Λ_{app}) is monotonic convergent, as it is presented in Figs. B.4(a) and (b) within the dashed area, then the exact analytical solution (ϕ_{exact}) will be bound between $\phi_{est}(\Lambda_{as})$ and $\phi_{est}(\Lambda_{app})$ and they can be estimated as,

$$\phi_{est}\left(\Lambda_{as}\right) = \phi_1 + \frac{\phi_1 - \phi_2}{\Gamma^{\Lambda_{as}} - 1} \tag{B.9}$$

$$\phi_{est}\left(\Lambda_{app}\right) = \phi_1 + \frac{\phi_1 - \phi_2}{\Gamma^{\Lambda_{app}} - 1} \tag{B.10}$$

According to Marchi & Silva (2005), Eqs. B.9 and B.10 are the generalized Richardson extrapolation. Replacing them in Eq. B.5, the uncertainty or estimated error of the numerical solution for the apparent and asymptotic orders is obtained as,

$$U_{Ri}\left(\Lambda_{as}, \phi_1\right) = \frac{\phi_1 - \phi_2}{\Gamma^{\Lambda_{as}} - 1} \tag{B.11}$$

$$U_{Ri}\left(\Lambda_{app}, \phi_1\right) = \frac{\phi_1 - \phi_2}{\Gamma^{\Lambda_{app}} - 1}, \tag{B.12}$$

which represent the estimated errors of the numerical solution ϕ_1 according to the Richardson error estimator (U_{Ri}) (MARCHI; SILVA, 2005).

Marchi & Silva (2005) demonstrate that the discretization error of a given numerical solution (ϕ_1) is bound between the values of $U_{Ri}(\Lambda_{as}, \phi_1)$ and $U_{Ri}(\Lambda_{app}, \phi_1)$ for the subconvergent and superconvergent as follows,

$$\frac{U_{Ri}\left(\Lambda_{as}, \phi_1\right)}{E(\phi_1)} \leq 1 \leq \frac{U_{Ri}\left(\Lambda_{app}, \phi_1\right)}{E(\phi_1)} \tag{B.13}$$

$$\frac{U_{Ri}\left(\Lambda_{app}, \phi_1\right)}{E(\phi_1)} \leq 1 \leq \frac{U_{Ri}\left(\Lambda_{as}, \phi_1\right)}{E(\phi_1)} \tag{B.14}$$

The value of the uncertainty is considered reliable when the ratio between U_{Ri} and E is equal or greater than unit. Since the accuracy of the uncertainty depends on the difference between Λ_{app} and Λ_{as}, the more the value of Λ_{app} approaches the value of Λ_{as}, the values of $\frac{U_{Ri}\left(\Lambda_{as}, \phi_1\right)}{E(\phi_1)}$ and $\frac{U_{Ri}\left(\Lambda_{app}, \phi_1\right)}{E(\phi_1)}$ tend to unity and the estimate of the discretization

error becomes more accurate (MARCHI; SILVA, 2005).

Since the equations of the numerical model for solving the energy and the momentum problems were discretized using central discretization scheme (CDS), Marchi & Silva (2005) suggest that the asymptotic order (Λ_{as}) should be equal to 2.0. Table B.3 presents the estimated variables for the calculation of the numerical uncertainties using the generalized Richardson extrapolation. It is noticed that as the grid is refined, the values of the apparent order (Λ_{app}) tend monotonically to the values of the asymptotic order ($\Lambda_{as} = 2.0$) in a subconvergent interval. So, the discretization error is within the interval ($U_{Ri}(\Lambda_{as}, \phi_1) \leq E(\phi_1) \leq U_{Ri}(\Lambda_{app}, \phi_1)$) when the Λ_{app} is within the subconvergent interval. The upper limit of this interval is the numerical uncertainty obtained with the fine grid (ϕ_1) of each group analyzed composed by three grids, which are presented in Tables B.1 and B.2.

Table B.3 – Estimated variables for the calculation of the uncertainty U using the generalized Richardson extrapolation.

Estimated variables	Grid 50,100,150	Grid 100,150,200	Grid 150,200,250	Grid 200,250,300	Grid 250,300,400
$\Gamma_{2,1}$	1.50	1.33	1.25	1.20	$1,33$
$\Gamma_{3,2}$	2.00	1.50	1.33	1.25	1.20
$\frac{\phi_2 - \phi_3}{\phi_1 - \phi_2}$	2.95(2.11)	1.99(1.77)	1.66(1.56)	1.56(1.48)	$0,86(0,83)$
Λ_{ap}	0.97(0.37)	0.96(0.63)	1.03(0.78)	1.18(0.92)	1.30(1.11)
$I_{Ri}(\Lambda_{as}, \phi_1)$	0.048(1.66)	0.039(1.53)	0.03(1.34)	0.03(1.16)	0.02(0.80)
$I_{Ri}(\Lambda_{ap}, \phi_1)$	0.12(12.55)	0.095(5.99)	0.07(4.00)	0.05(2.80)	0.03(1.65)
$I(\phi_1)$	0.12(12.55)	0.095(5.99)	0.07(4.00)	0.05(2.80)	0.03(1.65)
$\frac{U_{Ri}(\Lambda_{app}, \phi_1)}{U_{Ri}(\Lambda_{as}, \phi_1)}$	2.59(7.54)	2.44(3.92)	2.19(2.99)	1.83(2.41)	$1,72(2,06)$

Note: the values within parentheses ( ) refer to the pressure field presented in Table B.2.

Since that there are no analytical solutions for the temperature and pressure fields, according to Oliveira (2008), the methodology proposed by Marchi & Silva (2002) can be used when the values of apparent order (Λ_{app}) approach or, at least, tend to the values of the asymptotic order (Λ_{as}), that is, the estimate of the error is more accurate and the ratio between estimated uncertainty and the real error tend to unit, making the estimate more reliable.

In the lack of analytical solutions, the ratio $\frac{U_{Ri}(\Lambda_{app}, \phi_1)}{U_{Ri}(\Lambda_{as}, \phi_1)}$ indentifies when the numerical solution is accurate and reliable. From Table B.3, we can also notice that the values of this ratio tend to unit as the grid is refined and that the values for the temperature field are more accurate than those for pressure.

Figure B.5 presents a rendering of relative values of the variables used in the verification of the numerical solution, as explained above, for the subconvergent interval of apparent order of error discretization.

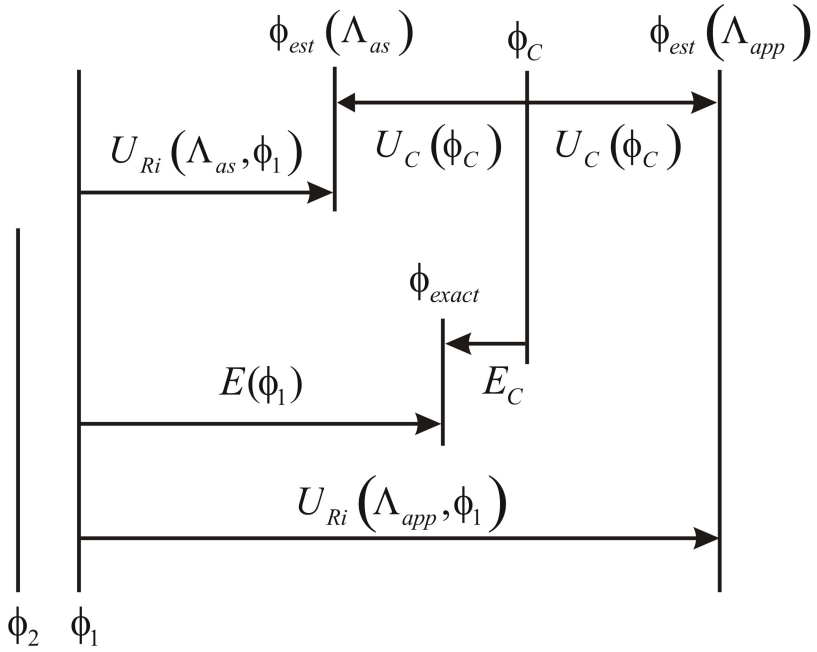

Figure B.5 – Schematic diagram of the convergent solution ϕ_C in the subconvergent interval of Λ_{app}. Source: adapted from Oliveira (2008).

From this diagram, the convergent numerical solution can be expressed as,

$$\phi_C = \frac{|\phi_{est}(\Lambda_{as}) + \phi_{est}(\Lambda_{app})|}{2}, \tag{B.15}$$

where $\phi_{est}(\Lambda_{as})$ and $\phi_{est}(\Lambda_{app})$ are obtained from the Richardson extrapolation, Eqs. B.9 and B.10. For ϕ_C, the numerical solution of the variable of interest (ϕ) should be presented or reported as (MARCHI; SILVA, 2005),

$$\phi_1 = \phi_C \pm U_C(\phi_C). \tag{B.16}$$

According to Marchi & Silva (2005), the estimated error of ϕ_C, $U_C(\phi_C)$, is equal to the modulus of half of the interval between $\phi_{est}(\Lambda_{as})$ and $\phi_{est}(\Lambda_{app})$, that is,

$$U_C(\phi_C) = \frac{|\phi_{est}(\Lambda_{as}) - \phi_{est}(\Lambda_{app})|}{2} \tag{B.17}$$

According to Marchi & Silva (2002, 2005), within the convergent interval of apparent order (Λ_{app}), it is advisable to use the convergent numerical solution (ϕ_C) instead of the calculated numerical solution (ϕ_1), because the true discretization error of ϕ_C, $E(\phi_C)$, is

smaller than the true discretization error of ϕ_1, $E(\phi_1)$. Table B.4 presents the estimated numerical solutions for apparent and asymptotic orders, the convergent numerical solution and the uncertainties of numerical solution by the convergent estimator.

Table B.4 – Estimated uncertainties U using the generalized Richardson extrapolation.

Estimated variables	Grid 50,100,150	Grid 100,150,200	Grid 150,200,250	Grid 200,250,300	Grid 250,300,400
$\phi_{est}\,(\Lambda_{as})$	38.37(2279)	38.39(2280)	38.40(2281)	38.41(2281)	38.409(2281.53)
$\phi_{est}\,(\Lambda_{app})$	38.44(2290)	38.45(2285)	38.44(2284)	38.43(2283)	38.421(2282.38)
ϕ_C	38.41(2285)	38.42(2283)	38.42(2282)	38.42(2282)	38.415(2281.95)
$U_C\,(\phi_C)$	0.038(5.443)	0.028(2.232)	0.019(1.328)	0.010(0.818)	0.006(0.425)

Note: the values within parentheses ( ) refer to the pressure field presented in Table B.2.

From these results, it is noticed that the values of the numerical uncertainties decrease slightly with the grid refinement. The uncertainties are lower than 0.5% for all groups of grids. Now, if we look back in the CPU time column of Table B.1, we will notice that the time difference for obtaining the numerical solutions between the grids ($\eta_{150\times150}$) and ($\eta_{400\times400}$) is greater than 8h. That is, as the grids are refined, a significant increasing of the CPU time is observed, although the uncertainties do not decrease significantly. Therefore, the grid ($\eta_{150\times150}$) was chosen in order to decrease the CPU time for obtaining the numerical solutions. For that grid, the numerical solutions for the temperature and pressure fields are $\phi_T = 38.41 \pm 0.038$ ^{o}C and $\phi_p = 2285 \pm 5.443$ Pa, respectively.

APPENDIX C

Measurement Uncertainty Analysis

This appendix deals with the measurement uncertainty analysis regarding the expirements accomplished at LabCET/UFSC in Brazil and at IKE/Stuttgart University in Germany. First is presented the theory for the measurement uncertainty analysis, which is based on the Guide to the Expression of Uncertainty in Measurement, ISO (2008). Next, it is separately presented the assessing of uncertainties for the temperature and power input measurements at both laboratories.

C.1 Theory of Assessing Uncertainty

Uncertainty exists in the measurements and the degree to which the uncertainty affects the conclusion is an important issue. According to ISO (2008), the objective of a measurement is to determine the value of the measurand, that is, the value of the particular quantity to be measured. A measurement, therefore, begins with an appropriate specification of the measurand, the method of measurement and the measurement procedure. In general, the result of a measurement is only an approximation or estimate of the value of the measurand and, thus, it will be complete only when accompanied by a statement of the uncertainty of that estimate.

The simplest way of assessing uncertainty is to make many measurements and to use the obtained results to estimate the range of possible values. Uncertainties estimated in this way, using actual measurement and statistical analysis, are called Type A uncertainties. On the other hand, when statistical sampling is impractical and the information for the analysis is brought by physical theory, information from handbooks or varying degrees of experience of similar situations, these uncertainties are called Type B uncertainties. Here, both types of uncertainty are used.

C.1.1 Standard Uncertainty

The standard uncertainty (u) of a source of uncertainties is defined as uncertainty of the result of a measurement expressed as a standard deviation. The estimation of standard uncertainty related to a source of uncertainties can be done through statistic procedures or by others means.

There are several situations where the experimental standard deviation associated to a source of uncertainties can be estimated from values of repeated observation of the measurand. According to ISO (2008), uncertainties estimated in this way are called Type A uncertainties.

Suppose that a random variable $\mathbf{q}$ represents the effects of a source of uncertainties regarding the measurement result. The experimental standard deviation of this variable $\mathbf{q}$ is determined from n values independently obtained for the variable $\mathbf{q}$, *i.e.*, $\mathbf{q_k}$ (where $k = 1, 2, ..., n$). So, the arithmetic mean of variable $\mathbf{q}$ can be expressed as:

$$\bar{q} = \frac{1}{n} \sum_{k=1}^{n} q_k. \tag{C.1}$$

The experimental standard deviation (s) of variable $\mathbf{q}$ is estimated as,

$$s\left(q\right) = \sqrt{\frac{\sum_{k=1}^{n} \left(q_k - \bar{q}\right)^2}{n-1}} \tag{C.2}$$

This estimate of the experimental standard deviation $s\left(q\right)$ characterizes the variability of the observed values q_k, or more specifically, their dispersion about their mean $\bar{q}$. If only one measurement is done, the standard uncertainty is expressed by: $u(q) = s(q)$. However, if n measurements are done and their mean value is used for the calculation of the measurement result, the standard uncertainty corresponds to the standard deviation of the mean of the n measurements, *i.e.*,

$$u\left(q\right) = s\left(\bar{q}\right) = \frac{s\left(q\right)}{\sqrt{n}} \tag{C.3}$$

Type B uncertainties are those determined by other than statistical means. There are several situations where it is not practical or possible to use estatistical procedures for estimation of the experimental standard deviation related to a source of uncertainties. So, according to Nicholas & White (2005), the evaluation of the uncertainties can be based on theoretical models of the measurement, information from handbooks and data sheet,

the work of other experiments, calibration certificates, even intution and experience.

According to ISO (2008), the proper use of available information for the Type B evaluation of standard uncertainty calls for insight based on experience and general knowledge. It should be recognized that the Type B evaluation of standard uncertainty can be as reliable as the Type A evaluation, especially in a measurement situation where the Type A evaluation is based on a comparatively small number of statistically independent observations.

If the error estimate is taken from a manufacturer's specification, calibration certificate, handbook, or other source and its quoted uncertainty is stated to be a particular multiple of a standard deviation, the standard uncertainty is simply the value of error divided by the multiplier. According to ISO (2008), the normal probability distribution is assumed for type A uncertainties and the multiplier is one (1). On the other hand, the rectangular probability distribution is assumed for type B uncertainties and the multiplier is the square root of three ($\sqrt{3}$). Here in this work, it is made the same assumptions as made by ISO (2008), *i.e.*, normal probability distribution is assumed for type A and rectangular probability distribution for type B.

C.1.2 Combined Standard Uncertainty

The variables of input quantities that contribute for the uncertainties can be correlated or uncorrelated. The random variables are called statisticaly independent (or uncorrelated) when there is not any relation between the random increasing of one and the random increasing (or decreasing) of another. On the other hand, the random variables are called statisticaly interdependent (or correlated) when there is a noticable relation between the random increasing of one and the random increasing (or decreasing) of another in a proportional way to the first one. Here, all contributing uncertainties are uncorrelated (or independent) and the equations for estimation of that uncertainties are presented as follows.

In most measurements there is more than one source of uncertainty. Assuming that a determined measurand $\mathbf{z}$ is not measured directly, but is determined from independent (or uncorrelated) random variables x, y and other variables through a functional relationship f:

$$z = f(x, y, ...). \tag{C.4}$$

The standard uncertainty of z, where z is the estimate of the measurand $\mathbf{z}$ and thus

the result of the measurement, is obtained by appropriately combining the standard uncertainties of the input estimates x, y and other variables of function f. The combined standard uncertainty of the estimate z is denoted by $u_c(z)$ according to ISO (2008) and it can be expressed by

$$u_c\left(z\right) = \sqrt{\sum_{i=1}^{n} \left(\frac{\partial f}{\partial x}\right)^2 u^2\left(x\right) + \left(\frac{\partial f}{\partial y}\right)^2 u^2\left(y\right) + ...}, \tag{C.5}$$

where $u(x)$, $u(y)$ and other variables are the standard uncertainties of each source of uncertainty.

C.1.3 Effective Number of Degrees of Freedom

The number of degrees of freedom is used in statistical distributions (*e.g.*, in Student's t-distribution) to account the number of random uncorrelated variables used to calculate the variance. In general, the degrees of freedom of an estimate (ν) is equal to the number of independent variables used to calculate the experimental standard deviation minus one, *i.e.*,

$$\nu = n - 1. \tag{C.6}$$

Equation C.6 should be used for the calculation of number of degrees of freedom for type A uncertainties. On the other hand, for the type B uncertainties, in which is assumed to have rectangular probability distribution, according to ISO (2008), the number of degrees of freedom should be infinite.

According to Nicholas & White (2005), when the standard uncertainty of several sources of uncertainties are considered to estimate the combined standard uncertainty, the number of degrees of freedom resultant from the combined standard uncertainty should be also estimated. This can be done by Welch-Satterthwaite equation,

$$\frac{u_c^4}{\nu_{eff}} = \frac{u_1^4}{\nu_1} + \frac{u_2^4}{\nu_2} + ... + \frac{u_p^4}{\nu_p}, \tag{C.7}$$

where ν_1, ν_2, ..., ν_p are the numbers of degrees of freedom and u_1, u_2, ..., u_p are the standard uncertainties of each p sources of uncertainties.

C.1.4 Expanded Uncertainty

According to ISO (2008), although the combined standard uncertainty (u_c) can be universally used to express the uncertainty of a measurement result, it is necessary to give a measure of uncertainty that defines an interval concerning the measurement result that may be expected to encompass a large fraction of the distribution of values that could reasonably be attributed to the measurand. The additional measure of uncertainty that meets the requirement of providing this interval is called expanded uncertainty (U).

In engineering applications is common to design within levels of confidence of 95%. For that, the combined standard uncertainty (u_c) should be multiplied by a coverage factor k (Student coefficient) for obtaining the expanded uncertainty (U). According to ISO (2008), this coverage factor is commonly represented by the symbol $k_{95\%}$ for confidence level of 95%. The expanded uncertainty ($U_{95\%}$) corresponds to a range of values that encompass the uncertainty with confidence leval of about 95% and it is estimaded by:

$$U_{95\%} = k_{95\%} u_c. \tag{C.8}$$

C.2 Assessing Uncertainties of the Temperature Measurements at IKE/Stuttgart University

In this work, all tests of LHPs were carried out at Institute of Nuclear Technology and Energy Systems (IKE) of Stuttgart University in Germany. Here, it is presented the assessing of uncertainties of these experiments for the temperature measurements. Both types of uncertainties are evaluated here, *e.g.*, the type A uncertainties which are due to the repeatability errors of the temperature measurements (u_{Re}) and the type B uncertainties (obtained by catalogs and norms), which are due to the errors of the data logger (u_{DL}) and the temperature sensors (u_{Pt100}).

C.2.1 Type A Uncertainties

The type A uncertainties were evaluated due to the repeatability errors of the temperature measurements. The temperatures along the LHP were measured for a steady state condition for each step of heat load. n measurements of temperature were collected in steps of time of 30 s during 20 min for each sensor and each step of heat load. Thus, according to Eqs. C.1, C.2 and C.3, the uncertainty due to the repeatability errors (u_{Re}) can estimated as,

$$\bar{T} = \frac{1}{n}\sum_{k=1}^{n} T_k \tag{C.9}$$

$$s\left(T\right) = \sqrt{\frac{\sum_{k=1}^{n}\left(T_k - \bar{T}\right)^2}{n-1}} \tag{C.10}$$

$$u_{Re} = \frac{s\left(T\right)}{\sqrt{n}}, \tag{C.11}$$

where n is equal to 40 measurements, T_k are the n measurements of the measurand T and $\bar{T}$ is the arithmetic mean.

All temperature sensors used for the temperature measurements along the LHPs were evaluated in order to estimate the uncertainty due to the repeatability errors, however for simplifying reasons, only the greatest standard uncertainty among the temperature sensors is presented in Table C.1.

C.2.2 Type B Uncertainties

The type B uncertainties (obtained by catalogs and norms) are due to the errors of the data logger (u_{DL}) and the temperature sensors (u_{Pt100}). The temperature distribution along the LHP was measured using temperature sensors (RTDs) of type Pt100 delivered with an accuracy of class A. Regarding to international norm IEC751 (1983), the error of the RTDs can be estimated by following equation:

$$u_{Pt100} = 0.15 + 0.002\mathrm{T}, \tag{C.12}$$

where T is the operation temperature of the Pt100, which range from -100 to $+450$ ^{o}C. Here, this error was evaluated for limiting operation temperature of 100 ^{o}C and the result is presented in Table C.1.

The error of the temperature measurement for RTDs at the data logger(u_{DL}) was obtained in the accuracy specification of the catalog of the Agilent 34970A (Data Acquisition/Switch Unitsare), which is estimated as 0.06 ^{o}C.

C.2.3 Combined Standard Uncertainty

The sources of uncertainties mentioned before - repeatablility, data logger and temperature sensors - are composed by uncorrelated variables. So, the combined standard

uncertainty for the temperature measurements, according to Eq. C.5, can be expressed as,

$$u_c(T) = \sqrt{\left(\frac{\partial T}{\partial T_{\mathrm{Re}}}\right)^2 u_{\mathrm{Re}}^2(T_{\mathrm{Re}}) + \left(\frac{\partial T}{\partial T_{DL}}\right)^2 u_{DL}^2(T_{DL}) + \left(\frac{\partial T}{\partial T_{Pt100}}\right)^2 u_{Pt100}^2(T_{Pt100})}, \tag{C.13}$$

where $\frac{\partial T}{\partial T_{\mathrm{Re}}} = \frac{\partial T}{\partial T_{DL}} = \frac{\partial T}{\partial T_{Pt100}} = 1$ and Eq. C.13 becomes,

$$u_c(T) = \sqrt{u_{\mathrm{Re}}^2(T_{\mathrm{Re}}) + u_{DL}^2(T_{DL}) + u_{Pt100}^2(T_{Pt100})}. \tag{C.14}$$

C.2.4 Expanded Uncertainty

For the estimation of the expanded uncertainty, it is necessary to determine the coverage factor (k) which is function of the confidence level and the effective number of degrees of freedom (ν_{eff}). It assumed the confidence level of 95% and the effective number of degrees of freedom is estimated using the Eq. C.7. In ISO (2008), there is a Table with the values of coverage factor (k) from a statistical distribution which is function of degrees of freedom (ν) for different levels of confidence. Usually when the effective number of degrees of freedom (ν_{eff}) is great, the coverage factor ($k_{95\%}$) is equal to 2.0 for a confidence level of 95%.

C.2.5 Results

Table C.1 presents the summary of standard uncertainty components for the temperature measurement. It is noticed that the number of degrees of freedom is great ($\nu_{eff} = 2.57 \times 10^{11}$) and the $k_{95\%}$ is equal to 2.0. Therefore, the expanded uncertainty for the temperature measurement is estimated as ± 0.41 ^{o}C.

C.3 Assessing Uncertainties of the Temperature Measurements at LabCET/UFSC

The tests of the CPL were carried out at Laboratory of Combustion and Engineering of Thermal Systems (LabCET) of Federal University of Santa Catarina in Brazil. Here, it is presented the assessing of uncertainty of this experiment for the temperature measurements. It was accomplished the same procedure that was presented in previous section. Both types of uncertainties are evaluated, however in the type A uncertainties is included

Table C.1 – Summary of standard uncertainty for the temperature measurement at IKE/Stuttgart University

Standard uncertainty component	Source of uncertainty	Value of errors	Type of Distribution	Divider	Value of standard uncertainty	Degrees of freedom
u_{Re}	Repeatability	0.005	Normal	1.0	0.005	39
u_{DL}	Data Logger	0.06	Rectangular	$\sqrt{3}$	0.035	∞
u_{Pt100}	RTD Pt10	0.35	Rectangular	$\sqrt{3}$	0.202	∞
u_c	Combined standard uncertainty	—	Normal	—	0.205	2.57×10^{11}
$U_{95\%}$	Expanded uncertainty (95%)	—	Normal	—	0.41	—

the uncertainty (u_{Cal}) due to the errors of thermocouples calibration for the temperature measurements.

C.3.1 Type A Uncertainties

The type A uncertainties were evaluated due to the errors of repeatability (u_{Re}) and thermocouples calibration (u_{Cal}) for the temperature measurement. The temperatures along the CPL were measured for a steady state condition for each step of heat load. n measurements of temperature were collected in steps of time of 30 s during 20 min for each sensor and each step of heat load. The uncertainty due to the repeatability errors (u_{Re}) was estimated using Eqs. C.1, C.2 and C.3. Again, all thermocouples used for the temperature measurements along the CPL were evaluated, however for simplifying reasons, only the greatest standard uncertainty among the thermocouples is presented in Table C.2.

The thermocouples calibration was done using a reference thermometer which has the operation range from -10 to $+100$ ^{o}C and accuracy of 0.01 ^{o}C. The thermocouples and the reference thermometer were imersed in a heat sink, which used water as working fluid. The heat sink temperature was varied in a range from 10 to 80 ^{o}C in steps of 5 ^{o}C. The results of the temperature measurements with the thermocouples were compared with the reference thermometer results. Finally, the experimental standard deviations for each thermocouple was calculated. All thermocouples were evaluated based on the experimental standard deviation, but only the greatest standard uncertainty (u_{Cal}) among the errors of thermocouples calibration is presented in Table C.2.

C.3.2 Type B Uncertainties

The type B uncertainties (obtained only by catalogs) are due to the errors of the data logger (u_{DL}) and the termocouples ($u_{Thermocouple}$). The temperature distribution along the CPL was measured using thermocouples type T and their errors are estimated as 1.0 ^{o}C according to Omega Engineering Inc. The error of the temperature measurement for thermocouples at the data logger (u_{DL}) was obtained in the accuracy specification of the catalog of the Agilent 34970A (Data Acquisition/Switch Unitsare), which is estimated as 1.0 ^{o}C.

C.3.3 Combined Standard Uncertainty

The sources of uncertainties (repeatablility, calibration, data logger and thermocouple) are composed by uncorrelated variables. So, the combined standard uncertainty for the temperature was estimated using Eq. C.5.

C.3.4 Expanded Uncertainty

It was also assumed the confidence level of 95% for the estimation of the expanded uncertainty.

C.3.5 Results

Table C.2 presents the summary of standard uncertainty components for the temperature measurement. It is also noticed that the number of degrees of freedom is great ($\nu_{eff} = 2.49 \times 10^{8}$) and the $k_{95\%}$ is equal to 2.0. Therefore, the expanded uncertainty for the temperature measurement is estimated as $\pm$1.77 ^{o}C.

C.4 Assessing Uncertainties of the Power Input Measurements at IKE/Stuttgart University

The electrical power input for the two cartridge heaters is controlled by the measurement software via the data acquisition system, sending the target value to the power supply units. Only the type B uncertainties were evaluated for the power suply and its errors is estimated as 0.2% (by catalog) for the voltage of inputs and outputs. Each cartridge heater provides 12.5 W for the maximum power input of 25 W (value obtained with the LHP using acetone as working fluid). As each cartridge heater has an electrical

Table C.2 – Summary of standard uncertainty for the temperature measurement at LabCET/UFSC

Standard uncertainty component	Source of uncertainty	Value of errors	Type of Distribution	Divider	Value of standard uncertainty	Degrees of freedom
u_{Re}	Repeatability	0.11	Normal	1.0	0.011	39
u_{Cal}	Calibration	0.32	Normal	1.0	0.322	∞
u_{DL}	Data Logger	1.00	Rectangular	$\sqrt{3}$	0.577	∞
$u_{Thermocouple}$	Thermocouple	1.00	Rectangular	$\sqrt{3}$	0.577	∞
u_c	Combined standard uncertainty	—	Normal	—	0.878	2.49×10^8
$U_{95\%}$	Expanded uncertainty (95%)	—	Normal	—	1.77	—

resistance of 7.76 Ω, for the the maximum power input of 12.5 W, the voltage of each cartridge is equal to 9.85 V. Thus, if the voltage error is 0.2% of the voltage of each cartridge, it means that the voltage error for the input and output is 0.0197 V.

With a maximum power input of 25 W (value obtained with the LHP using acetone as working fluid), *i.e.*, 12.5 W for each cartridge heater. As each cartridge heater has an electrical resistance of 7.76 Ω, for the the maximum power input of 12.5 W, the voltage of each cartridge is equal to 9.85 V. Thus, if the voltage error is 0.2%, it means that the voltage error for the input and output is 0.0197 V.

The power input is a function of the electrical resistance and the voltage measured in the power supply unit. Since there are two cartridge heaters, the total power input is estimated as,

$$Q_{app} = Q_{app,CH1} + Q_{app,CH2} = \frac{(V_{CH1})^2}{R_{CH1}} + \frac{(V_{CH2})^2}{R_{CH2}} \tag{C.15}$$

where Q_{app} is the power input, V is the voltage, R is the electrical resistance, $CH1$ and $CH2$ are the cartridge heaters 1 and 2, respectively.

The combined standard uncertainty for the total power input is estimated using the Eq. C.5 as,

$$u_c\left(Q_{app}\right) = \sqrt{\left(\frac{\partial Q_{app}}{\partial V_{CH1}}\right)^2 u_{CH1}^2\left(V_{CH1}\right) + \left(\frac{\partial Q_{app}}{\partial V_{CH2}}\right)^2 u_{CH2}^2\left(V_{CH2}\right)}, \tag{C.16}$$

where $\dfrac{\partial Q_{app}}{\partial V_{CH1}} = \dfrac{2V_{CH1}}{R}$ and $\dfrac{\partial Q_{app}}{\partial V_{CH2}} = \dfrac{2V_{CH2}}{R}$.

The uncertainies $u_{CH1}\,(V_{CH1})$ and $u_{CH2}\,(V_{CH2})$ are equal to the combined standard uncertainty due to the measurement of the voltage of input and output ($u_c(V) = 0.016$ V) presented in Table C.3.

Table C.3 – Summary of standard uncertainty for the voltage measurement at IKE/Stuttgart University

Standard uncertainty component	Source of uncertainty	Value of errors	Type of Distribution	Divider	Value of standard uncertainty	Degrees of freedom
$u_{V,in}$	Voltage output	0.0197	Rectangular	$\sqrt{3}$	0.0114	∞
$u_{V,out}$	Voltage input	0.0197	Rectangular	$\sqrt{3}$	0.0114	∞
u_c	Combined standard uncertainty	—	Normal	—	0.016	∞

The Table C.4 presents the summary of standard uncertainty for the power input measurement at IKE/Stuttgart University. For the maximum power input of 25 W, the expanded uncertainty for the measurement of the power input is estimated as ±0.1155 W.

Table C.4 – Summary of standard uncertainty for the power input measurement at IKE/Stuttgart University

Standard uncertainty component	Source of uncertainty	Value of uncertainty	Derivative	Value of derivative	degrees of freedom
$u_{CH1}\,(V_{CH1})$	CH1	0.016	$\frac{\partial P}{\partial V_{CH1}} = \frac{2V_{CH1}}{R}$	2.539	∞
$u_{CH2}\,(V_{CH2})$	CH2	0.016	$\frac{\partial P}{\partial V_{CH2}} = \frac{2V_{CH2}}{R}$	2.539	∞
u_c	Combined standard uncertainty	0.0574	—	—	∞
$U_{95\%}$	Expanded uncertainty (95%)	0.1155	—	—	—

CH1 and CH2 are the cartridge heaters 1 and 2, respectively.

C.5 Assessing Uncertainties of the Power Input Measurements at LabCET/UFSC

The electrical power input for the heating system of the CPL was controlled by the direct measurement in the power supply unit (Agilent N6700B). The errors of the power supply unit are given for the voltage as $0.1\% + 100$ mV and for the current as $0.15\% + 6$ mA. The power input is a function of the current (I) and the voltage (V) measured in the power supply unit and it is estimated as,

$$Q_{app} = VI, \tag{C.17}$$

where Q_{app} is the power input, V is the voltage and I is the current.

The combined standard uncertainty for the power input is estimated using the Eq. C.5 as,

$$u_c\left(Q_{app}\right) = \sqrt{\left(\frac{\partial Q_{app}}{\partial V}\right)^2 u^2\left(V\right) + \left(\frac{\partial Q_{app}}{\partial I}\right)^2 u^2\left(I\right)}, \tag{C.18}$$

where $\frac{\partial Q_{app}}{\partial V} = I$ and $\frac{\partial Q_{app}}{\partial I} = V$.

For the maximum power input of 30 W, it was measured at the power supply unit a current of 1.366 A and a voltage of 21.96 V. It is assumed a rectangular distribution for the uncertainties due to the errors of the measurements in the power supply units of the current and the voltage.

Table C.5 – Summary of standard uncertainty for the power input measurements at LabCET/UFSC

Standard uncertainty component	Source of uncertainty	Value of errors	Type of Distribution	Divider	Value of uncertainty	degrees of freedom
$u\left(V\right)$	Voltage	0.122	Rectangular	$\sqrt{3}$	0.0704	∞
$u\left(I\right)$	Current	0.008	Rectangular	$\sqrt{3}$	0.0046	∞
u_c	Combined standard uncertainty	—	Normal	—	0.1395	∞
$U_{95\%}$	Expanded uncertainty (95%)	—	Normal	—	0.2790	—

The Table C.5 presents the summary of standard uncertainty for the power input measurement at LabCET/UFSC. For the maximum power input of 30 W, the expanded

uncertainty for the measurement of the power input is estimated as ±0.2790 W.

C.6 Assessing Uncertainties of the Pressure Measurements at LabCET/UFSC

Here, it is presented the assessing of uncertainty of pressure measurements at the CPL. It was accomplished the same procedure that was presented in previous sections. Both types of uncertainties are evaluated.

C.6.1 Type A Uncertainties

The type A uncertainty was evaluated due to the errors of repeatability (u_{Re}) for the pressure measurement. The pressure at the liquid line of the CPL was measured for a steady state condition for each step of heat load. n measurements of pressure were collected in steps of time of 30 s during 20 min for each step of heat load. The uncertainty due to the repeatability errors (u_{Re}) was estimated using Eqs. C.1, C.2 and C.3. Here, only the greatest standard uncertainty among each step of heat load is presented in Table C.6.

C.6.2 Type B Uncertainties

The type B uncertainties (obtained only by catalog) are due to the errors of the pressure transducer ($u_{Pressure}$). The pressure at the liquid line of the CPL was measured using a steel transducer type PX309-030A5V and their errors are estimated as 2% of the measurements according to Omega Engineering Inc.

C.6.3 Combined and Expanded Uncertainties

The sources of uncertainties (repeatablility and transducer) are composed by uncorrelated variables. So, the combined standard uncertainty for the pressure was estimated using Eq. C.5. It was assumed the confidence level of 95% for the estimation of the expanded uncertainty.

C.6.4 Results

Table C.6 presents the summary of standard uncertainty components for the pressure measurement. It is also noticed that the number of degrees of freedom is great ($\nu_{eff} =$

7.2×10^2) and the $k_{95\%}$ is equal to 2.0. Thus, the expanded uncertainty for the temperature measurement is estimated as ±345.22 Pa.

Table C.6 – Summary of standard uncertainty for the pressure measurement at LabCET/UFSC

Standard uncertainty component	Source of uncertainty	Value of errors	Type of Distribution	Divider	Value of standard uncertainty	Degrees of freedom
u_{Re}	Repeatability	83.78	Normal	1.0	83.78	39
$u_{Pressure}$	Transducer	261.39	Rectangular	$\sqrt{3}$	150.91	∞
u_c	Combined standard uncertainty	—	Normal	—	172.61	7.2×10^2
$U_{95\%}$	Expanded uncertainty (95%)	—	Normal	—	345.22	—

APPENDIX D

Hydrodynamic Model for Pressure Drop

This appendix presents the reasons for the assumptions taken for the hydrodynamic model presented in Chapter 4. The data input, the thermophysical properties and the main results of the hydrodynamic model for each capillary pumping systems (Two LHPs and one CPL) are also presented.

D.1 Introduction

The main operational limit of capillary pumping systems (CPL and LHP) are the boiling and capillary limits. Here, the capillary limit will be explored basing the analysis on the experimental results. The condition for both CPL and LHP work is that the total system pressure drop does not exceed the maximum pressure that the porous wick can provide. So, the capillary pumping system operation requires that the sum of the pressure drops in the components and in the transport lines must be smaller than the maximum capillary pressure head developed by the wick, *i.e.*,

$$\Delta p_{cap,\max} \geq \Delta p_{\text{evap}} + \Delta p_{\text{cond}} + \Delta p_{\text{v}} + \Delta p_{\text{l}} + \Delta p_{\text{g}}$$

In order to estimate the total pressure drop of the LHPs and CPL, a hydrodynamic model was developed based on the measurements and the results were compared to the expected maximum capillary limit. The hydrodynamic model is composed by the set of equations already presented in Chapter 4. For the LHPs, this set of equations is solved according to the following steps:

(1) Input data such as the LHP dimensions, working fluid, Q_{app}, T_{CC}, T_{amb}, $T_{Cond,in}$, $T_{Cond,out}$, $T_{HS,in}$, $T_{HS,out}$ and $\dot{m}_{HS}$ are supplied to the model.

(2) The thermophysical properties of the working fluid are estimated as a function of the working fluid saturation temperature in the condenser. Next, the mass flow rate is

calculated using Eqs. 4.1 to 4.9.

(3) The pressure drops in the porous wick - Eqs. 4.10 and 4.13 - and in the grooves - Eqs. 4.10 and 4.11 - as well as in the vapor transport line, Eq. 4.10, are estimated.

(4) The condenser two-phase region lenght ($L_{cond,lv}$) is estimated using the Eqs. 4.14 to 4.33. Next, the length of liquid region ($L_{cond,l}$) is estimated subtracting the two-phase length ($L_{cond,lv}$) from the total condenser length (L_{cond}).

(5) The pressure drop in the liquid transport line is estimated using Eq. 4.10.

(6) The condenser two-phase region pressure drop is estimated using Eqs. 4.34 to 4.40.

Considering now the CPL, the set of equations is solved as follows:

(1) Input data such as the CPL dimensions, Q_{app}, T_{amb}, P_{Sensor}, $T_{Cond,in}$ and $T_{Cond,out}$ are supplied to the model.

(2) The working fluid thermophysical properties are estimated as a function of the saturation temperature, which was calculated regarding the pressure measured with the pressure sensor. Next, the mass flow rate is calculated by $Q_{app} = \dot{m}\ h_{lv}$.

(3) The pressure drops in the porous wick, Eqs. 4.10 and 4.13, in the grooves, Eqs. 4.10 and 4.11, and in the vapor transport line, Eq. 4.10, are estimated.

(4) The condenser two-phase region lenght ($L_{cond,lv}$) is estimated using the Eqs. 4.41 to 4.53. Next, the length of liquid region ($L_{cond,l}$) is estimated subtracting the two-phase length ($L_{cond,lv}$) from the total condenser length (L_{cond}).

(5) The pressure drop in the liquid transport line is estimated using Eq. 4.10.

(6) The condenser two-phase region pressure drop is estimated using Eqs. 4.34 to 4.40.

D.2 Saturation Temperature of the CPL and LHPs

From the previous section, one can notice that the saturation temperature is needed in step (2) in order to estimate the working fluid thermophysical properties to be used in both CPL and LHPs models. On the one hand, for the CPL model, the system pressure was measured and its saturation temperature could be determined. On the other hand, for the LHP model, it was not possible to determine the saturation temperature in the condenser (or in any other component) based only on temperature measurements at LHP walls. Thus, the working fluid saturation temperature was assumed as the temperature

measured at the wall of the condenser inlet. The reasons for that assumption are presented as follows.

The LHP startup occurs when the temperature measured at the condenser inlet increases suddenly. Figure D.1, which was already presented in Chapter 4 and is repeated here for didactical purposes, shows the steady state of LHP (using water as working fluid) for an increasing heat load. As the heat load is applied, it is noticed that the evaporator outlet temperature increases. After some seconds, the condenser inlet temperature increases suddenly as well, showing that the LHP has started up. It should be observed that the condenser inlet temperature presents an unstable behavior only for the 5 W heat load, probably due to the formation and possible colapse of bubbles before the condenser inlet. As the heat load increases to 10 W, that behavior disappears. To some extend, the presence of this instability indicates that vapor enters the condenser at saturated state.

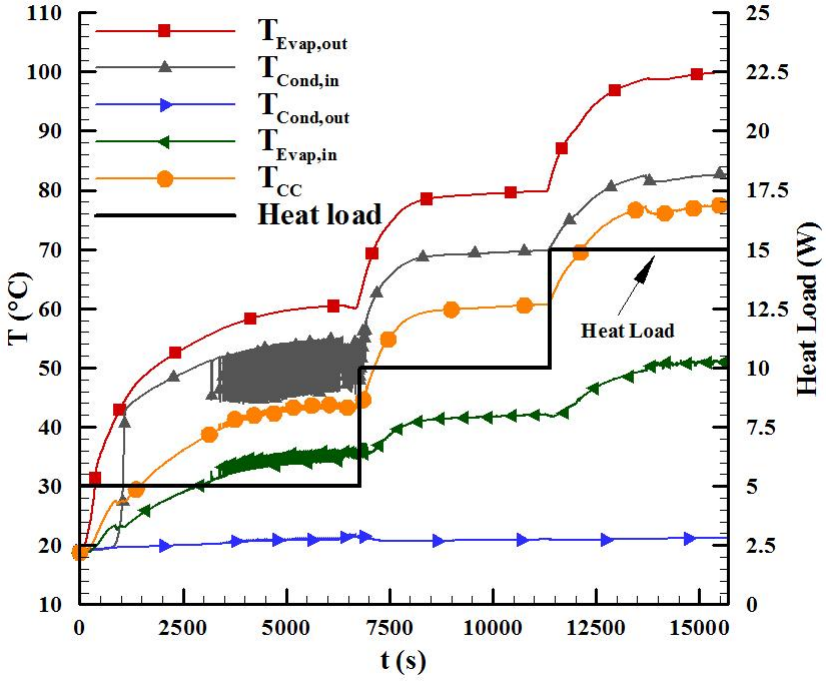

Figure D.1 – Temperatures of LHP (water) for heat loads increasing at horizontal position and at heat sink temperature of 20 ^{o}C (Already presented in Chapter 4).

Figure D.2 presents the results for temperatures along the CPL and the pressure measured at the liquid line for three different heat loads (Q_{app} = 10, 20 and 30 W). The mean pressure was 8.22, 11.61 and 13.23 kPa for heat load of 10, 20 and 30 W, respectively.

Based on the results presented in the previous figure, the saturation temperature was estimated as a function of the mean pressure. Figure D.3 presents this temperature, the condenser inlet temperature and their correspondent uncertainties. The results show that the temperatures are in the range of the uncertainty. Therefore, the assumption that the saturation temperature becomes closer to the temperature measured at the condenser

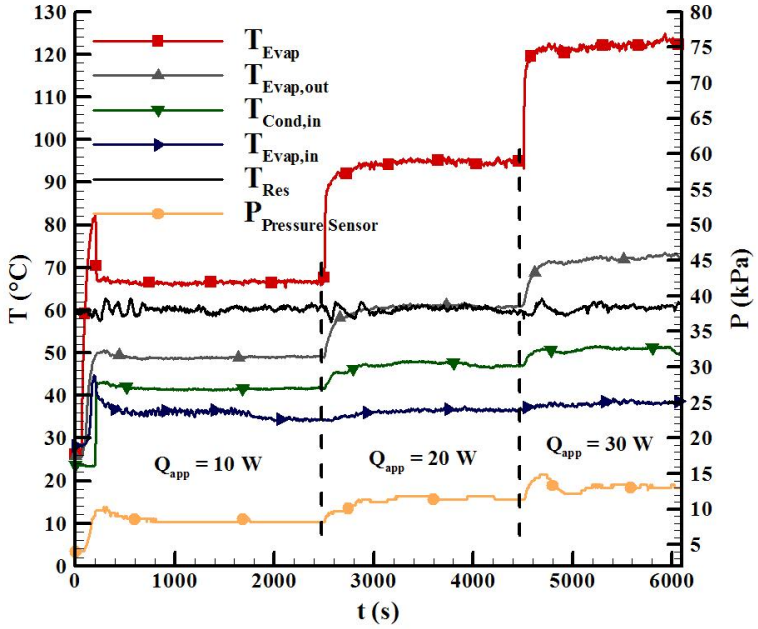

Figure D.2 – Temperatures and pressure of the CPL for heat loads increasing at horizontal position and with 130% load.

inlet does not involve great errors. It should be addressed that this assumption was taken only for the LHPs.

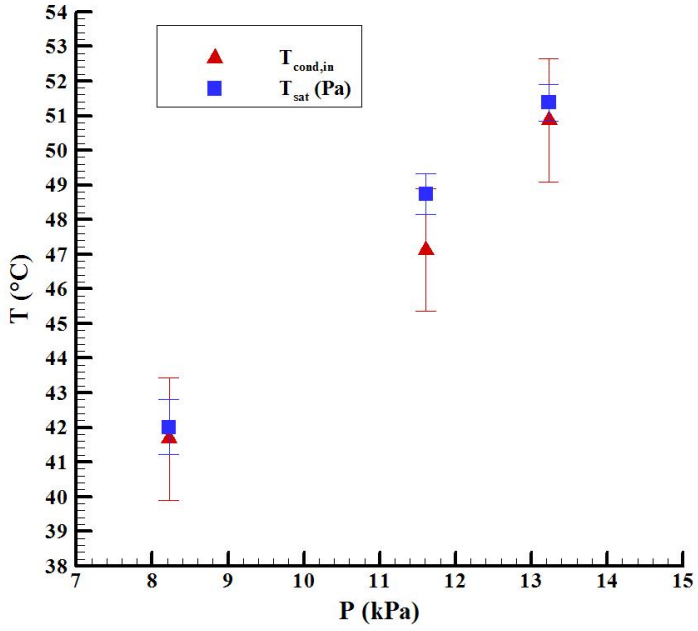

Figure D.3 – Saturation temperature (as a function of the mean measured pressure), condenser inlet temperature and their correspondent uncertainties.

For the CPL model, the saturation temperature in the condenser was estimated as a function of the pressure measured. Since the pressure sensor is located at the liquid line, the saturation temperature in the condenser is different from the saturation temperature estimated as a function of the pressure. This difference was estimated using the Clausius-

Clapeyron equation, as follows,

$$(T_{cond,sat} - T_{sensor,sat}) = \Delta p \frac{T_{sensor,sat} v_{lv}}{h_{lv}}, \tag{D.1}$$

where $T_{cond,sat}$ is the condenser saturation temperature, $T_{sensor,sat}$ is the saturation temperature estimated as a function of the pressure measured with the sensor, Δp is the pressure drop between the condenser inlet and the location of the pressure sensor at the liquid line.

The results obtained with Eq. D.1 showed that the difference between the saturation temperatures was less than 0.05% for the maximum heat load of 30 W.

D.3 Heat Transfer Coeffient of the Air Flow in the Condenser of the CPL

Two finned air coolers were used to cool the condenser section of the CPL. In this type of coolers, the fan is mounted on top of the fin assembly and pushes air over the fin spacing. There is very little information that can be used to estimate the heat transfer coefficient for this situation. Therefore, here it is assumed that the air flow passes through the fins as shown in Fig. D.4.

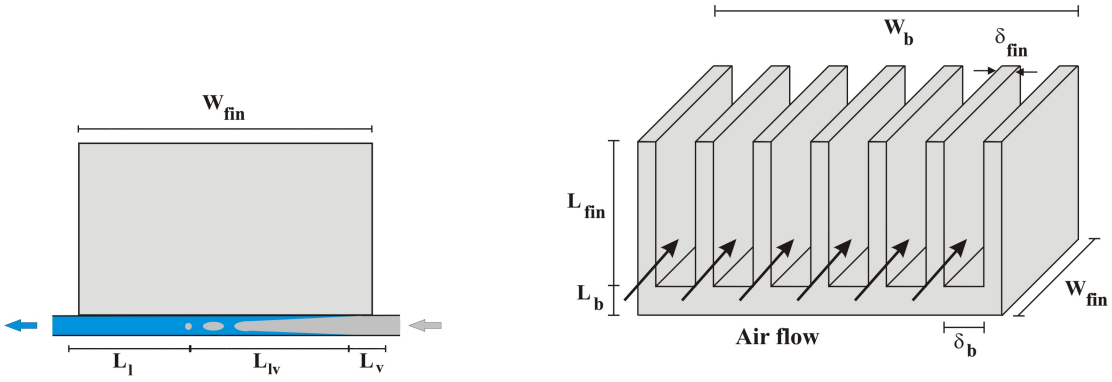

Figure D.4 – Schematic diagram of the finned condenser for the CPL.

This assumption can overestimate or subestimate the value of the heat transfer coefficient. In order to evaluate its influence on the total pressure drop of the CPL, the heat transfer coefficient of the air flow was varied. Table D.1 shows the results of the two-phase length, two-phase region pressure drop and its percentage as well as the total CPL pressure drop as a function of the air flow heat transfer coefficient.

Despite all the parameters decreased with the heat transfer coefficient increase, the total CPL pressure drop decayment was relative small and the equations presented in

Table D.1 – Evaluation of the air flow heat transfer coefficient.

h_{air} (W/m-K)	L_{lv} (mm)	Δp_{lv} (Pa)	Percentage (%)	Δp_{total} (Pa)
30	90.4	35.54	0.41	8.754×10^3
50	65.1	25.59	0.29	8.744×10^3
100	53.8	21.15	0.24	8.740×10^3
160	50.5	19.85	0.23	8.738×10^3

Chapter 4 to estimate the air flow heat transfer coefficient can be applied without involving significant errors.

D.4 Data Inputs and Themophysical Properties

This section presents the input data and the thermophysical properties which were determined as a function of the saturation temperature in the condenser. The LHPs and CPL dimensions were already presented in Tables 3.1 and 3.3 in Chapter 3, respectively. The input data for the LHPs and CPL are shown in Tables D.2 and D.3, respectively.

Table D.2 – Input data for the LHPs hydrodynamic models.

		LHP (Water)	LHP (Acetone)
Q_{app}	(W)	15.00	25.00
T_{CC}	(^{o}C)	75.00	52.50
T_{amb}	(^{o}C)	20.00	20.00
$T_{Cond,in}$	(^{o}C)	80.00	71.70
$T_{Cond,out}$	(^{o}C)	21.20	21.57
$T_{HS,in}$	(^{o}C)	20.25	20.14
$T_{HS,out}$	(^{o}C)	20.28	20.21
$\dot{m}_{HS}$	(kg/s)	0.0273	0.0274
r_{pore}	(μm)	3.0	3.0
K_{wick}	(m^2)	1.5×10^{-14}	1.5×10^{-14}

Table D.3 – Input data for the CPL hydrodynamic model.

		CPL (Water)
Q_{app}	(W)	30.00
T_{amb}	(^{o}C)	23.00
p_{sensor}	(kPa)	13.23
$\dot{m}_{air}$	(kg/s)	0.028
r_{pore}	(μm)	3.0
K_{wick}	(m^2)	1.5×10^{-14}

The thermophysical properties for the LHPs and CPL are presented in Tables D.5 and D.4, respectively.

Table D.4 – Thermophysical properties for the LHPs hydrodynamic models.

		LHP (Water)[a]	LHP (Acetone)[b]
$T_{cond,sat}$	(^{o}C)	80.00	71.70
h_{lv}	(J/kg)	2.30×10^6	0.51×10^6
ρ_{liq}	(kg/m^3)	971.79	731.23
ρ_{vap}	(kg/m^3)	0.2934	3.285
μ_{liq}	(kg/m-s)	354.5×10^{-6}	206.7×10^{-6}
μ_{vap}	(kg/m-s)	11.6×10^{-6}	9.3×10^{-6}
λ_{liq}	(W/m-K)	0.6562	0.1637
λ_{vap}	(W/m-K)	0.0230	0.0154
σ	(N/m)	0.0627	0.0173
Pr_{liq}	—	2.266	2.96
Pr_{vap}	—	0.999	0.87
ρ_{water}	(kg/m^3)	998.2	998.2
μ_{water}	(kg/m-s)	1002.0×10^{-6}	1002.0×10^{-6}
$\mu_{wall,water}$	(kg/m-s)	713.5×10^{-6}	743.2×10^{-6}
λ_{water}	(W/m-K)	0.5861	0.5861
Pr_{water}	—	7.152	7.152
$\lambda_{fin,copper}$	(W/m-K)	401.8	401.8

[a] the properties of the water were obtained by the software Engineering Equation Solver (EES).
[b] the properties of the acetone were obtained from Faghri (1995).

Table D.5 – Thermophysical properties for the CPL hydrodynamic model.

		CPL (Water)[a]
$T_{cond,sat}$	(^{o}C)	51.38
h_{lv}	(J/kg)	2.38×10^6
ρ_{liq}	(kg/m^3)	987.4
ρ_{vap}	(kg/m^3)	0.0886
μ_{liq}	(kg/m-s)	534.63×10^{-6}
μ_{vap}	(kg/m-s)	10.66×10^{-6}
λ_{liq}	(W/m-K)	0.632
λ_{vap}	(W/m-K)	0.0205
σ	(N/m)	0.0677
Pr_{liq}	—	3.537
Pr_{vap}	—	1.001
ρ_{air}	(kg/m^3)	1.213
μ_{air}	(kg/m-s)	18.39×10^{-6}
λ_{air}	(W/m-K)	0.0254
Pr_{water}	—	0.7285
$\lambda_{fin,aluminum}$	(W/m-K)	236

[a] the properties of the water were obtained by the software Engineering Equation Solver (EES).

D.5 Results of the Hydrodynamic Model for the LHPs and CPL

This section presents the results for the LHPs and CPL hydrodynamic models. Tables D.6 and D.7 show the main output variables obtained.

Table D.6 – Output variables of the LHPs hydrodynamic models.

		LHP (Water)	LHP (Acetone)
$h_{cc,amb}$	(W/m^2-K)	34.05	31.86
$Q_{cc,amb}$	(W)	2.47	1.37
$\dot{m}$	(kg/s)	5.43×10^{-6}	46.18×10^{-6}
h_{HS}	(W/m^2-K)	109.3	108.9
$h_{cond,lv}$	(W/m^2-K)	1.06×10^3	872.8
$L_{cond,lv}$	(mm)	28.5	107
$L_{cond,l}$	(mm)	91.5	13

Table D.7 – Output variables of the CPL hydrodynamic model.

$\dot{m}$	(kg/s)	12.61×10^{-6}
h_{air}	(W/m^2-K)	158.1
$h_{cond,lv}$	(W/m^2-K)	2.69×10^3
$L_{cond,lv}$	(mm)	50.6
$L_{cond,l}$	(mm)	334.4

Table D.8 presents the pressure drop of the capillary systems here under study for the maximum heat load applied to the capillary systems, 15 W for the LHP (water), 25 W for the LHP (acetone) and 30 W for the CPL. Note in Table D.8 that the total pressure drop (Δp_{total}) of all systems is smaller than the capillary limit. It is noticed that the contribution of the pressure drop in the vapor and liquid transport lines and in the two phase zone of condenser are much smaller than the pressure drop in the porous wick. The total pressure drop of the CPL (water) is greater than the LHP (water) due to the greater mass flow rate and the greater number of grooves in the evaporator of the CPL. It can also be noticed the total pressure drop of all capillary pumping systems is up to 57.4% of the capillary limit, showing that, considering this limit, all capillary pumping systems are capable of transfering heat over longer distances.

Table D.8 – Pressure drop of the LHPs and CPL.

	LHP (Water)		LHP (Acetone)		CPL (Water)	
Components	Δp (Pa)	%	Δp (Pa)	%	Δp (Pa)	%
Vapor grooves	77.84	7.04	47.673	0.723	1.38×10^3	15.76
Vapor line	38.89	3.52	30.654	0.465	206.3	2.36
Porous wick	987.42	89.25	6.511×10^3	98.688	7.13×10^3	81.63
Liquid line	0.46	0.04	2.363	0.036	2.15	0.02
Two phase	1.69	0.15	5.863	0.089	19.89	0.23
Δp_{total}	1.106×10^3	100.00	6.598×10^3	100.00	8.74×10^3	100.00
Capillary limit	41.78×10^3	—	11.5×10^3	—	45.14×10^3	—
$\Delta p_{total}/p^*_{cap,max}$	0.03	—	0.574	—	0.19	—

* is the maximum capillary pressure which is estimated using the Eq. 1.2 ($p_{cap,max} = \frac{2\sigma}{r_p}$).